CRANFIELD UNIVERSITY

Xiuyuan Yang

THE INFLUENCE OF SURFACE DETERMINATION IN X-RAY COMPUTED TOMOGRAPHY

School of Aerospace, Transport and Manufacturing

PhD in Manufacturing

PhD

Academic Year: 2018 - 2022

Academic Supervisor: Dr Claudiu Giusca

Industrial Supervisor: Dr Wenjuan Sun

October 2022

CRANFIELD UNIVERSITY

School of Aerospace, Transport and Manufacturing
PhD in Manufacturing

PhD

Academic Year 2018 - 2022

Xiuyuan Yang

THE INFLUENCE OF SURFACE DETERMINATION IN X-RAY COMPUTED TOMOGRAPHY

Academic Supervisor: Dr Claudiu Giusca
Industrial Supervisor: Dr Wenjuan Sun
October 2022

This thesis is submitted in partial fulfilment of the requirements for the degree of PhD

© Cranfield University 2022. All rights reserved. No part of this publication may be reproduced without the written permission of the copyright owner.

ABSTRACT

X-ray computed tomography (XCT) is a non-destructive technique that enables the dimensional inspection of the internal and external features of modern components. All dimensional attributes, including form, size and surface texture, are derived from the surface of the component, therefore, surface determination (SD) is a critical step in X-ray computed tomography (XCT) for dimensional metrology. Threshold-based and gradient-based algorithms are widely used. However, these algorithms are often sensitive to systematic errors and can be largely influenced by the input parameters selected by operators.

Current research gaps include the limited knowledge related to the quantifiable impact of SD algorithms on the traceability of the XCT geometric measurements and to the SD algorithm robustness to threshold setting. It was postulated here that Marker-controlled watershed (MCW), successfully applied in the medical field, can overcome the potential threshold errors encountered with current SD algorithms and provide robust results even in the presence of typical XCT errors.

As a result, this thesis presents the development of a robust SD algorithm for XCT based on the MCW method, which combined weighted gradient voxel refinement and automated marker generation. The validation and comparison of MCW were accomplished by employing calibrated workpiece for experimental XCT scanning, and simulation.

The work has further evaluated the performance of MCW algorithm and two commonly applied SD algorithms, Canny and ‘advanced mode in VGStudio’ (VG) algorithms, under beam hardening and noise effect. SD thresholding parameters were optimised by Taguchi methods when evaluating different types of surface conditions, including smooth and rough surfaces.

Canny presented the worst performance during the measurement of rough surfaces but performed well in smooth surface measurement cases. VG performed worst in bi-directional measurement under the influence of beam hardening but successfully computed the rough surface when beam hardening was corrected. The proposed MCW demonstrated that it is an all-rounded

algorithm. Compared to other surface determination algorithms, the MCW algorithm presented consistent results with little influence from the beam hardening, noise and threshold settings. This demonstrates a great potential that the proposed SD algorithm can be fully automated in XCT.

Keywords:

X-ray computed tomography, marker-controlled watershed, surface determination, dimensional metrology, surface texture measurement, coordinate measuring machine, contact stylus, traceability

ACKNOWLEDGEMENTS

Hereby I gratefully like to thank my supervisors, Dr Claudiu Giusca (Cranfield University) and Dr Wenjuan Sun (National Physical Laboratory), for their generous support during my whole period of PhD study.

All collaborators during my PhD study are sincerely thanked for their grateful help in academic support. In no particular order: Dr Carsten Bellon (BAM, Germany), Mr Stephen Brown (National Physical Laboratory), Dr Shada Kazemi (University of Surrey), Ms Xiao Chen (PhD student, University of Huddersfield), Dr Jian Qiu (Visiting researcher, National Physical Laboratory), Dr Joseph Lifton (A*STAR, Singapore).

I hereby would like to thank every internal colleague in DIMMET group in National Physical Laboratory for the support of my fieldwork in the team. I also would like to thank Mr David Flack, Dr Christopher Jones, and Dr Daniel O'Connor for reviewing my conference and journal paper.

I am grateful to my family and my friends, and they help me a lot during my PhD study.

The author is grateful to the National Measurement System Programme for Engineering & Flow Metrology, and Centre for Doctoral Training in Ultra Precision Engineering for the financial support to this project.

TABLE OF CONTENTS

ABSTRACT i
ACKNOWLEDGEMENTS iii
LIST OF FIGURES viii
LIST OF TABLES xv
LIST OF EQUATIONS xvi
LIST OF ABBREVIATIONS xviii
1 Introduction 3
1.1 Surface Determination process in dimensional measurement context 8
1.2 Terminology 10
1.3 Thesis structure, aim and objectives 12
2 Literature review 13
2.1 Introduction of metrology 14
2.1.1 Measurement uncertainty 16
2.1.2 Uncertainty evaluation 20
2.2 Basic concept of XCT 25
2.2.1 X-ray source 27
2.2.2 Interaction between X-ray and material 29
2.2.3 X-ray detector 29
2.3 Dimensional XCT 32
2.3.1 Roughness, waviness, and form 37
2.3.2 Coordinate Measurement Machine (CMM) 39
2.3.3 CS machine and traceability 42
2.4 Available standards for XCT dimensional metrology 44
2.5 Surface determination algorithm 46
2.5.1 Global threshold algorithm 46
2.5.2 Local adaptive threshold algorithm 47
2.6 Watershed segmentation 52
2.6.1 Watershed algorithm and XCT 55
2.7 Conclusion and research justification 57
3 MCW implementation 59
3.1 3D marker generation 59
3.1.1 Initial thresholding 59
3.1.2 3D Closing operation [263] of the initial marker 60
3.1.3 3D object marker erosion 61
3.1.4 Creation of 3D background marker 62
3.1.5 Combination of the object and background marker 63
3.2 Gradient transformation 64
3.3 Geodesic transformation 65
3.4 Watershed transformation over gradient volume data with geodesic transformation 67

3.5 Voxel refinement 68
4 Preliminary MCW results – 2D bi-directional measurement case 69
4.1 Methodology 69
4.2 Monochromatic and polychromatic XCT measurement regime. 72
4.3 Noise effect 74
4.4 Influence of marker size and position 77
4.5 Influence of interpolation ratio 80
4.6 Additional considerations 86
4.7 Conclusion 89
5 Evaluation of the effect of SD algorithms on bi-directional measurements (smooth surfaces) 91
5.1 Methodology 92
5.1.1 Measurement 92
5.1.2 Simulation scanning 93
5.1.3 Reconstruction 95
5.1.4 SD implementation 95
5.1.5 Radius calculation 98
5.2 Results and Discussions 98
5.2.1 Measurement data 99
5.2.2 Monochromatic simulations data 101
5.2.3 Polychromatic simulations data – no filters 101
5.2.4 Polychromatic simulations data – with filters and BHC 104
5.2.5 Comparison between measurement and simulations before BHC 105
5.2.6 Comparison between measurement and simulations after BHC 105
5.3 Limitation 106
5.4 Summary and Conclusions 106
6 SD effect on surface texture 109
6.1 Materials 111
6.1.1 Measured sample 111
6.2 Stylus morphological transformation 115
6.2.1 Synthetic data 116
6.3 Results and discussion 119
6.3.1 Experimental optimisation results 119
6.3.2 Discussion of experimental results 125
6.3.3 Similarity comparison 129
6.3.4 Residual comparison 131
6.3.5 Limitation 134
6.3.6 Synthetic Result 134
6.4 Conclusion 139
7 Conclusion, thesis summary and future work 141
REFERENCES 149
8 APPENDICES 173

Appendix A Fourier Beam Hardening Correction 173
Appendix B The result of SD optimisation for 3DRS sample 182
Appendix C 3DRS sample rotation 194
Appendix D Residual results for synthetic data 197
Appendix E Stylus morphological transformation algorithm (written in Matlab) 201

LIST OF FIGURES

Figure 1-1: The diagram of the working principle of industrial X-ray computed tomography [2] 4

Figure 1-2: A: The reconstruction of National Physical Laboratory (NPL)'s AM measurement standard; B. A cross section of the sample showing the position of the determined edge relative to the background and the object. Hereby red dots are the sampling of the measured cylinder 5

Figure 1-3: The Ishikawa diagram showing the main factors involved in XCT dimensional metrology [10, 23] 6

Figure 1-4: The artefact caused by beam hardening for the two-sphere sample, showing the 'streak' artefacts on the side of the spheres. Surfaces are determined using the advantage threshold algorithm in VGStudio Max 3.2.5 9

Figure 1-5: (a) The XCT Stedman [85, 88]. (b): Stedman diagram [85] for: Atomic force microscopes (AFM), Scanning probe microscopes (SPM), XCT, optical methods (optical profilometry, confocal microscopy and interferometry), and tactile instruments. 10

Figure 2-1: Early example of measurement devices [97] 14

Figure 2-2 The error and uncertainty source [104] 19

Figure 2-3 The diagram of the relationship between accuracy and precision ... 20

Figure 2-4: The X-ray spectrum with incident electron energy of 120 keV (red) and 100 keV (blue). This plot is generated using aRTist, X-ray tube [125, 126]. A. Bremsstrahlung; B. Characteristic radiation; C. Interaction with nuclear 27

Figure 2-5: The typical structure of X-ray source [2] 28

Figure 2-6: Left: Semiconductor detector [2]; Right: Scintillation detector [2, 138] 31

Figure 2-7: The workflow of complete XCT dimensional measurement [20] 33

Figure 2-8: Uni-directional and bi-directional distance 35

Figure 2-9: Form and roughness illustration 37

Figure 2-10: Profile figures [309] 38

Figure 2-11: The typical probing system of CMM [160] 40

Figure 2-12: Description of overhang problem in CMM measurement 42

Figure 2-13: The typical structure of contact stylus from ISO 3274 [170] 43

Figure 2-14: Upper image: The effect of peak round-off and reduced depth when measuring the valley. Lower image: the limited “re-entrant” feature [162, 172] 44

Figure 2-15: The histogram of a reconstructed XCT image with a total number of pixels N, showing the calculation of Otsu threshold and ISO50 threshold. The grey value is shown in ‘float 32’ format 47

Figure 2-16: Canny edge detection with inappropriate threshold selection 48

Figure 2-17: The underlying digital grid G with 4 or 8 connectivity (2D image) and 6, 18 and 26 connectivity (3D) [248] 53

Figure 2-18: Description of paths under 4 and 8 connectivity 54

Figure 2-19: The description of minimums and the associated catchment basins and watershed lines [178] 54

Figure 3-1: The diagram of the initial thresholding process used to generate initial object marker 60

Figure 3-2: 3D closing operation to eliminate the imperfections, such as holes, within the object. Note that this is the sketch of the cross section of the volume data (white area). A. Volume data before closing; B. Volume data after closing 61

Figure 3-3: The volume data after erosion while N = 20. B. The volume data after erosion while N = 40 62

Figure 3-4: 3D background marker ($\boldsymbol{VBCe}$, the white area in this image) after complement, closing and erosion process. 63

Figure 3-5: The combination of the 3D object and background marker ($\boldsymbol{VBOM}$). A. with size of a kernel of 20. B. size of a kernel of 40. 64

Figure 3-6: The volume data after gradient transformation using the Sobel operator 64

Figure 3-7: The geodesic transformation. The rectangular black dash box indicates the position and size of markers; solid blue plot indicates the original plot (*f*); green dotted plot (*f'*) indicates the plot after geodesic transformation from f 65

Figure 3-8: Topographic map of gradient image: Left: before geodesic transformation; Right: After geodesic transformation 66

Figure 3-9: The watershed segmentation volume data 67

Figure 3-10: The point cloud data of the 3D MCW surface 68

Figure 4-1: The overlapped tube reference sample: A. The drawing of radius of the CAD model B. Positions of 2D cross-section images considered along the vertical axis 70

Figure 4-2: The signal-to-noise ratio (SNR) of the projection without any objects under different voltages and currents 71

Figure 4-3: The error of radius for simulation set 1 (benchmark, monochromatic, no beam hardening) and simulation set 2 (polychromatic, beam hardening), noise factor = 0, Interpolation ratio p = 0.1, mean radius value and error bars are based on five individual MCW and Canny applications over five slices within the range of ± 10 layers around each benchmark (L3-H3) layers.... 73

Figure 4-4: The surface determined with watershed algorithm for the comparison of simulation with beam hardening (dash line) and without beam hardening (solid line) conditions 74

Figure 4-5: Surface point clouds determined by MCW under simulation set 2: Polychromatic. Left column: Without noise. Right column: with noise. Slice height index: L2, Interpolation ratio p = 0.1. The corresponding polar plot and the histogram of the residual (in pixels) are shown in E (without noise) and F (with noise) 76

Figure 4-6: The radius error result for simulation set 2 (SNR = inf) and simulation set 3 (SNR = 155), polychromatic, Interpolation ratio p = 0.1, mean radius value and error bars are based on 5 individual MCW and Canny applications over 5 slices within the range of ±10 layers around each benchmark (L3-H3) layers. Error bars indicate the standard deviation for each radius value.... 77

Figure 4-7: A. Markers by auto-selection; B. Watershed surface based on the geodesic transformed representation with auto-selected markers; C. Markers by random-selection; D. Watershed surface based on the geodesic transformed representation with randomly selected marker 79

Figure 4-8: Surface point clouds determined by MCW under simulation set 2: Polychromatic, no noise. Outer Circle; Slice height index: L2, Interpolation ratio p = 0.1 (blue dot), p = 0.2 (orange dot), p = 0.5 (cyan dot) and p = 1 (no interpolation, green dot), red line = nominal circle 81

Figure 4-9: The polar plot of the residual of point cloud calculated by MCW algorithm at four different interpolation ratios. Simulation set 2: Polychromatic, without noise. Outer Circle; Slice height index: L2. Solid red line is the nominal circle..... 82

Figure 4-10: The scatter plot of the relationship between p and RMS of the residual against fitted circle, Simulation set 2: Polychromatic, without noise. 83

Figure 4-11: The radius deviation of fitting circle against the nominal radius value under different interpolation ratio p value: A. Simulation set 2, polychromatic, with noise; B. Simulation set 3, polychromatic, SNR = 155. Mean radius value and error bars are based on five individual watershed surface applications over 5 slices within the range of ±10 layers around each benchmark (L3-H3) layers. Error bars indicate the standard deviation for each radius value.... 85

Figure 4-12: The edge determined using automatic marker-controlled watershed and Canny algorithm. The number in the square brackets indicate the threshold in the canny edge determination algorithm in MATLAB, and each number is within (0,1). The image is acquired under the CT simulation with noise 87

Figure 4-13: The comparison between 3D MCW and 3D canny surfaces for surface roughness analysis over the experimental reference sample 88

Figure 4-14: The comparison between the MCW and 'advanced mode' in commercial VGStudio software in dealing with 'streak' artefact caused by beam hardening 88

Figure 5-1 The two-sphere reference sample, and the drawing of the two sphere 93

Figure 5-2 The two-sphere CAD model 94

Figure 5-3: The histogram and initial thresholding settings within VGStudio MAX 3.2.5 [284] 96

Figure 5-4: Summary of SD optimisation results of S1 (measurement), S2 (simulation) 99

Figure 5-5: Canny optimisation results applied to the measured data. 100

Figure 5-6: (A) Simulation 1 – Monochromatic and (B) Simulation 2 – polychromatic simulations reconstruction result. 102

Figure 5-7: Canny trials results on Simulation 2 (O) 103

Figure 5-8: VG threshold trials for simulation 3 103

Table 5-8Figure 5-9: The comparison between C5, all MCW trials and VG1 on the streak artefact area 104

Figure 5-10:A Polychromatic with Cu filter without BHC; B. Polychromatic with Cu filter with BHC reconstruction result 105

Figure 6-1: The problem of the VG algorithm in non-smooth surface detection. The search distance is set as four voxels, 0.08 mm. 110

Figure 6-2 The photo of the 3DRS reference sample (left) and the sketch picture, including the CS measuring position. Down: SEM image of the 3DRS surface 112

Figure 6-3: Top crest search strategy 113

Figure 6-4: The watershed point cloud of Face A, S1, S2 and S4 within the coordinate system before (upper image) and after transformation (lower image). The figure is generated using MATLAB R2019b. Red line indicates the extracted profile position. 114

Figure 6-5: The schematic diagram of stylus morphological transformation. The stylus is exaggerated for description only 116

Figure 6-6: The synthetic encoded depth image PGGAN [290, 295] and its corresponding CAD models converted using Image2Surface. A: Downskin surface (S_a = 20 μm); B. Top surface (S_a = 5 μm); C. Upskin surface (S_a = 15 μm) 117

Figure 6-7: SD profiles without morphological filter and without BH (white dots) and CS (red dash line). The solid rectangular indicates the location of Figure 6-13; rectangular dash region indicates the location of Figure 6-14 120

Figure 6-8: SD profiles with morphological filter and without BH (white dots) and CS (red dash line)..... 121

Figure 6-9: MCW and VG roughness profiles (dot yellow: without BHC; solid white: with BHC) and CS profile (dash red). 122

Figure 6-10: The R_a value of the XCT profiles under different surface determination algorithms (MCW, C7 and VG3) without BHC. The red line indicates the R_a value of CS's profile..... 123

Figure 6-11: The R_q value of the XCT profiles under different surface determination algorithms (MCW, C7 and VG3). The red line indicates the R_q value of CS's profile..... 123

Figure 6-12: R_a and R_q results for MCW and VG, with and without BHC. The red line indicates the corresponding CS values. The table displays the corresponding values..... 124

Figure 6-13: The SD results of C2, C7, VG1, VG4, MCW on surface texture before and after BHC. The white dots correspond to SD profiles and red dash line is the CS profile. The XCT reconstructed slices are shown as the background. The image was captured from the solid rectangular region of Figure 6-7 127

Figure 6-14: The SD results of C2, C7, VG1, VG4, MCW on surface texture before and after BHC. The white dots correspond to SD profiles and red dash line is the CS profile. The XCT reconstructed slices are shown as the background. The image was captured from the dashed rectangular region of Figure 6-7 128

Figure 6-15: The systematic sketch of *diff* metric between XCT (while solid line) and CS profile (red dash line). The morphological profile of high and low *diff* corresponds to VG1 and MCW without BHC individually. 129

Figure 6-16: The similarity comparison results between XCT and CS profiles. The *diff* range is limited to (0 to 55) μm. 130

Figure 6-17: First image: The superimposed image containing the morphological profile of XCT with MCW SD algorithm (solid white line), CS profile (red dash

line), without BHC. The second to the sixth image: the plot of $\boldsymbol{yi} - \boldsymbol{yi}$ with the selected optimised SD algorithms. All images are aligned horizontally. .. 133

Figure 6-18: The box plot describing the distribution of the deviation of the point clouds from the mesh surface for the down-skin surface (S_a = 20 μm). Each box plot reports the median, interquartile range, whiskers, and outliers (red plus sign). 136

Figure 6-19: The box plot describing the distribution of the deviation of the point clouds from the mesh surface for the top surface (S_a = 5 μm). Each box plot reports the median, interquartile range, whiskers, and outliers (red plus sign). 137

Figure 6-20: The box plot describing the distribution of the deviation of the point clouds from the mesh surface for the up-skin surface (S_a = 15 μm). Each box plot reports the median, interquartile range, whiskers, and outliers (red plus sign)..... 138

Figure 8-1: The flow chart of calculation of polychromatic beam intensity..... 175

Figure 8-2: The comparison of the intensity of the polychromatic photons with a spectrum between 0 to 140 keV ($\boldsymbol{Ipt}$ dashed line) and monochromatic photons μ = 8 ($\boldsymbol{Imt}$ continuous line) after attenuation passing through a Cu. 176

Figure 8-3: Upper: Sixth degree polynomial regression plot. Lower: Regression residual plot, and 'I_after_attenuation_with_inco_sum' is equal to $\boldsymbol{Ip}$ in this plot..... 178

Figure 8-4: Upper: Six degree Fourier regression plot. Lower: Regression residual plot, and 'I_after_attenuation_with_inco_sum' is equal to $\boldsymbol{Gp}$ in this plot..... 179

Figure 8-5: A: Projection image without BHC; B: BHC image using $\boldsymbol{F6}$ regression transfer function; C. Exponential regression result of the plot indicated by yellow line in A; D. Exponential regression result of the plot indicated by yellow line in B 182

Figure 8-6: The optimisation result without BHC using VG SD algorithm. White dots- XCT surface; red line: CS data 183

Figure 8-7: The optimisation result without BHC using VG SD algorithm after applying morphological filter. White dots- XCT surface after morphological filter; red line: CS data 184

Figure 8-8: The optimisation result with BHC using VG SD algorithm. White dots- XCT surface; red line: CS data 185

Figure 8-9: The optimisation result with BHC using VG SD algorithm after applying morphological filter. White dots- XCT surface after morphological filter; red line: CS data 186

Figure 8-10: The optimisation result without BHC using Canny SD algorithm (C5 returns no surface data and not shown here). White dots: XCT surface; red line: CS data 187

Figure 8-11: The optimisation result without BHC using Canny SD algorithm after applying morphological filter (C5 returns no surface data and not shown here). White dots- XCT surface after morphological filter; red line: CS data 188

Figure 8-12: The optimisation result with BHC using Canny SD algorithm (C5 returns no surface data and not shown here). White dots: XCT surface; red line: CS data 189

Figure 8-13: The optimisation result with BHC using Canny SD algorithm after applying morphological filter (C5 returns no surface data and not shown here). White dots- XCT surface after morphological filter; red line: CS data 190

Figure 8-14: The optimisation result without BHC using MCW SD algorithm before and after applying morphological filter. White dots- XCT surface (after morphological filter); red line: CS data 191

Figure 8-15: The optimisation result with BHC using MCW SD algorithm before and after applying morphological filter. White dots- XCT surface (after morphological filter); red line: CS data 192

Figure 8-16: The residual of the surface point cloud against the mesh surface of downskin sample 198

Figure 8-17: The residual of the surface point cloud against the mesh surface of upskin sample 199

Figure 8-18: The residual of the surface point cloud against the mesh surface of side sample 200

LIST OF TABLES

Table 2-1 The seven base units and two additional units [97, 101] 15

Table 2-2 The seven base physical constants in the new SI system [102]..... 16

Table 2-3: The relationship between the roughness cut-off wavelength $\boldsymbol{\lambda c}$, tip radius and the maximum sampling spacing distance according to ISO 3274 [170]..... 39

Table 4-1: Settings of simulation. 70

Table 4-2: The comparison of computing time with different marker-selection methods (based on 0.1 interpolation ratio). The processor was Intel Xeon CPU E5-2630 v2 2.60GHz..... 80

Table 5-1 The reference data of the two-sphere reference sample calibrated using the Zeiss F25 CMM with a standard uncertainty 50 nm (k = 1) [76]. 93

Table 5-2: The experimental scanning parameter of the two-sphere sample... 93

Table 5-3: Simulation conditions 94

Table 5-4: The control parameters and levels for VG..... 96

Table 5-5: Taguchi orthogonal array for VG 97

Table 5-6: The threshold settings for 3D Canny algorithm 97

Table 5-7: Parameter setting for 3D MCW algorithm..... 98

Table 5-8: Relative radius errors between the polychromatic and monochromatic simulations in best- and worst- scenarios..... 104

Table 6-1: CT scanning parameters of 3DRS (Ti64) sample..... 113

Table 6-2 The general setting of simulations..... 117

Table 6-3: Settings for four simulation scanning..... 118

Table 6-4: The mean and standard deviation of residual, where minus means towards the material 134

LIST OF EQUATIONS

(2-1)..... 20
(2-2)..... 21
(2-3)..... 21
(2-4)..... 21
(2-5)..... 22
(2-6)..... 22
(2-7)..... 22
(2-8)..... 22
(2-9)..... 23
(2-10)..... 23
(2-11)..... 23
(2-12)..... 23
(2-13)..... 24
(2-14)..... 24
(2-15)..... 24
(2-16)..... 25
(2-17)..... 25
(2-18)..... 25
(2-19)..... 29
(2-20)..... 41
(3-1)..... 59
(3-2)..... 60
(3-3)..... 61
(3-4)..... 62
(3-5)..... 62
(3-6)..... 63
(3-7)..... 63
(3-8)..... 64

(6-1)..... 115
(6-2)..... 115
(6-3)..... 129
(8-1)..... 176
(8-2)..... 177
(8-3)..... 177

LIST OF ABBREVIATIONS

BHC	Beam Hardening Correction
MCW	Marker-Controlled Watershed
SD	Surface Determination
CMM	Coordinate Measurement Machine
CS	Contact Stylus
VG	VGStudio
Ti64	Ti6Al4V
NPL	National Physical Laboratory
GUM	Guide to the Expression of Uncertainty in Measurement
NDT	Non-destructive testing
AM	Additive Manufacturing
FDD	Focal spot to detector distance
FOD	Focal spot to object distance

1 Introduction

X-ray computed tomography (XCT), also known as X-ray CT or CT, is a radiographic technique that was invented by Hounsfield and Cormack who were awarded the Nobel Prize for Physiology and Medicine in 1979 [1,2]. Since then, apart from its use in medicine [3,4], XCT has been used in industry as a non-destructive testing (NDT) [4,5] and, more recently, for dimensional metrology.

The automotive, aerospace and additive manufacturing (AM) sectors increasingly employ XCT as an NDT technology to inspect the internal and external geometry of components with complex structures [1-3]. In recent years XCT has been proven to be especially useful in additive manufacturing (AM) field, where the need for precise dimensional measurement is growing [2, 4]. AM samples have complex internal structures and as such conventional and traceable contact and optical dimensional measuring systems often require destructive testing for a complete investigation [2, 5-9]. Previous studies show the confidence of XCT in quality control of complex features of AM, including internal or 'hidden features' in a 'near-net-shape' manner, which can aid the further development of AM technique [5-7, 10-18].

XCT instruments capture a series of radiographic projections of an object/component at multiple angular positions that are subsequently used to reconstruct a three-dimensional (3D) representation of that object. The design of XCT is based on the attenuation of X-rays going through a measured sample. In a typical cone beam XCT system, the object is positioned on a rotary table between the X-ray source and the detector, as shown in Figure 1-1. The detector captures thousands of projection images while the object is rotating. Reconstruction, which normally uses Feldkamp algorithm [19], is then applied to generate the 3D representation of the object. According to Nyquist-Shannon sampling theorem [10], the sampling frequency should be larger than twice the highest frequency included in a signal, otherwise the signal cannot be reconstructed as continuous. Optimising the number of projections per required CT scan reduces both aliasing artefacts and noise [10].

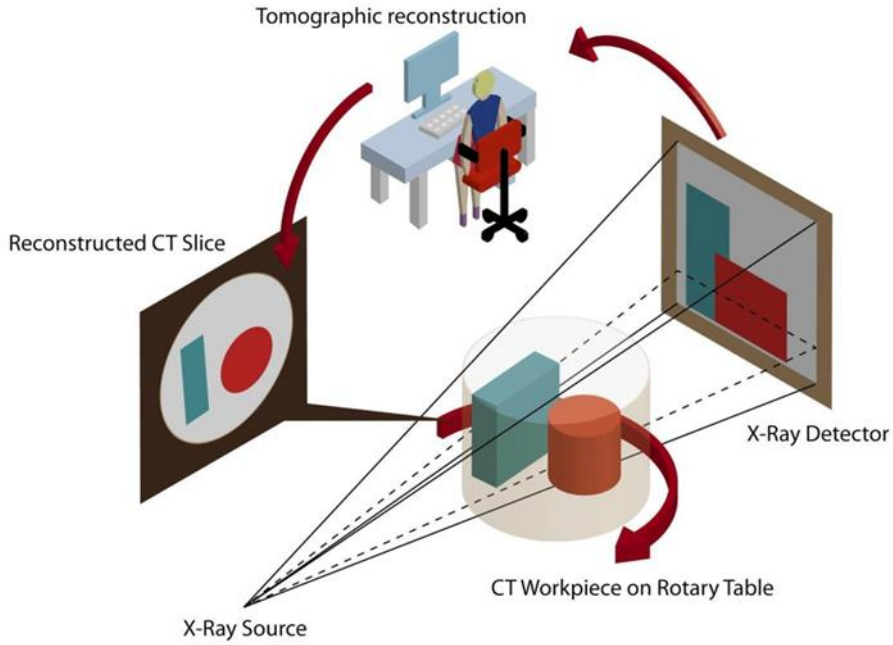

Figure 1-1: The diagram of the working principle of industrial X-ray computed tomography [2]

As shown in Figure 1-2A, the 3D representation associated with object consists of a cluster of voxels of grey values of different intensities compared to the intensity of the voxels corresponding to the background.

In the example shown in Figure 1-2, dark grey shade voxels represent the background and the light grey shade voxels represent the object (or foreground). The dimensional measurements are derived from the surface of the object, which is established from the 3D representation of the object.

Due to its ability to measure internal features, XCT is complementing traditional dimensional inspection methods, such as optical and tactile coordinate measuring techniques, which have limited access to internal surfaces [20].

However, XCT implementation in the industry trails behind contending technologies as it is not yet capable of providing dimensional measurement results with adequate confidence in traceability. There is a lack of international measurement standards able to provide a guideline for the use of XCT as a traceable dimensional measurement tool [10]. The main reasons are the relative

novelty of the use of XCT as a dimensional measurement tool [10] and the difficulties in modelling the X-Ray measurement process from X-ray generation and penetration, to the surface determination (SD) within the voxelated data [10].

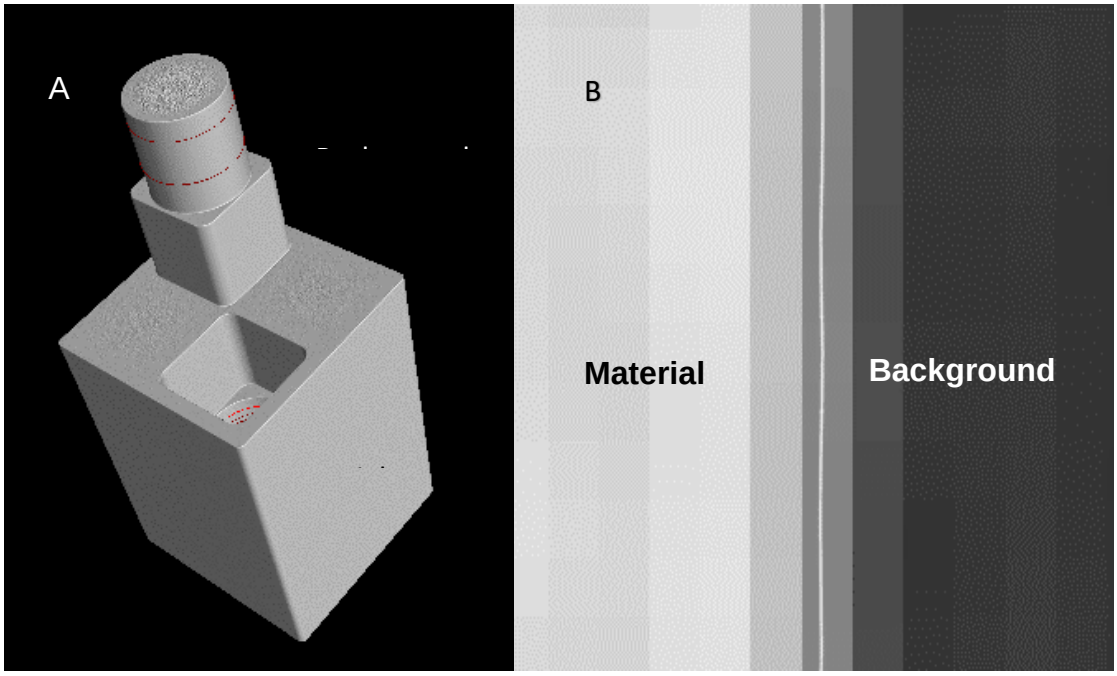

Figure 1-2: A: The reconstruction of National Physical Laboratory (NPL)'s AM measurement standard; B. A cross section of the sample showing the position of the determined edge relative to the background and the object. Hereby red dots are the sampling of the measured cylinder.

Establishing a calibration and measurement standard in line with the Guide to the Expression of Uncertainty in Measurement (GUM) requires a large amount of research given the complexity of the XCT measurement illustrated in Ishikawa diagram presented in Figure 1-3.

From the initial projections to the final geometrical evaluation, there are various factors that affect the dimensional measurement results, such as instrument alignment, focus spot stability, user-defined scanning parameters, material, geometry, photon-material interaction, orientation of the component, reconstruction and the SD algorithm [21, 22]. However, for the purpose of this thesis, the errors can be clustered into two main groups:

- Errors introduced by systematic effects during the scanning process. This includes XCT scanning and reconstruction, hereby called ‘scanning introduced error’
- Errors introduced by surface determination algorithms and the associated SD settings, hereby called ‘SD introduced error’

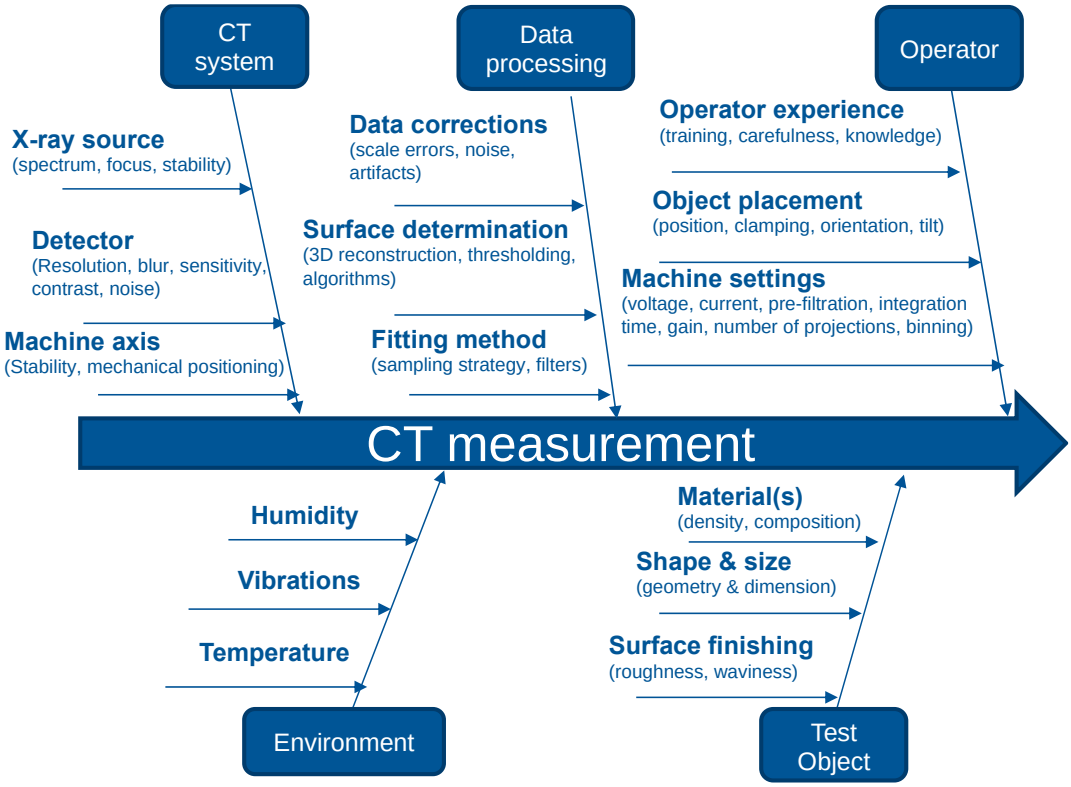

Figure 1-3: The Ishikawa diagram showing the main factors involved in XCT dimensional metrology [10, 23]

Previous research related to XCT’s error evaluation in dimensional metrology was focused on X-ray source [24, 25], reconstruction [26], detector [27], etc. However, only few research [22, 34] covered the influence of SD algorithm which is yet to be investigated systematically.

SD plays a critical role in the XCT measuring model as it affects the way the other factors influence dimensional measurements, *i.e.,* their associated sensitivity coefficients [28]. The role of SD algorithms is to find, often with sub-voxel resolution, the boundary situated in the transition area between the background and the object (the white line in Figure 1-2-B) that is associated with the surface

of the object. Hence, any errors introduced by SD algorithms lead to significant errors in the dimensional measurement [22, 23, 29-37].

Despite the importance of the SD process, commercial software does not provide sufficient transparency – i.e., SD is regarded as a black box, impeding the development of complete uncertainty models.

1.1 Surface Determination process in dimensional measurement context

Different SD algorithms react differently to the XCT scanning errors. A typical example of the scanning introduced error is the beam hardening [38-51] and beam scattering [52-71]. Beam hardening appears during reconstruction process when the attenuation coefficient is assumed to be independent of the photon energy. However, the ejected photons from the gun are polychromatic and their attenuation coefficient is an 'energy-dependent' physical quantity. Based on this improper assumption, the reconstruction process can generate unwanted artefacts, which can seriously affect the SD afterwards [41, 42, 47, 49, 50, 72, 73]. To understand the effect of BH in SD context, an example of real measurement of two closely positioned spheres and the associated SD process performed with VGStudio MAX version 3.2.5 in "advanced mode" is shown in Figure 1-4. Here, beam hardening produces 'streak' artefacts [74] causing severe deviations of the surfaces (inset B and C for 2D case and inset D for 3D case).

All dimensional metrology tools are trying to find the spatial location of the surface [10, 75]. However, this may be affected by other error sources. For shorter wavelength surface texture, detector resolution, the finite X-ray focal spot size, X-ray beam collimation, precision of the translational and rotational movement controllers, and blurs, can introduce uncertainty in the determination of the spatial location of the real surface [2, 10, 76]. In ISO 14660-1, the '*real surface'* is defined as the '*set of features which physically exist and separate the entire workpiece from the surrounding medium' [23, 77]*. Defining the spatial location of the real surface is very important because all elements for defining the geometrical attributes, such as size and shape, and surface texture are based on the determined surface [10]. The XCT surface is registered as a point cloud of spatial coordinates calculated from XCT volume data using a SD algorithm, which is part of Data Processing described in the Ishikawa diagram.

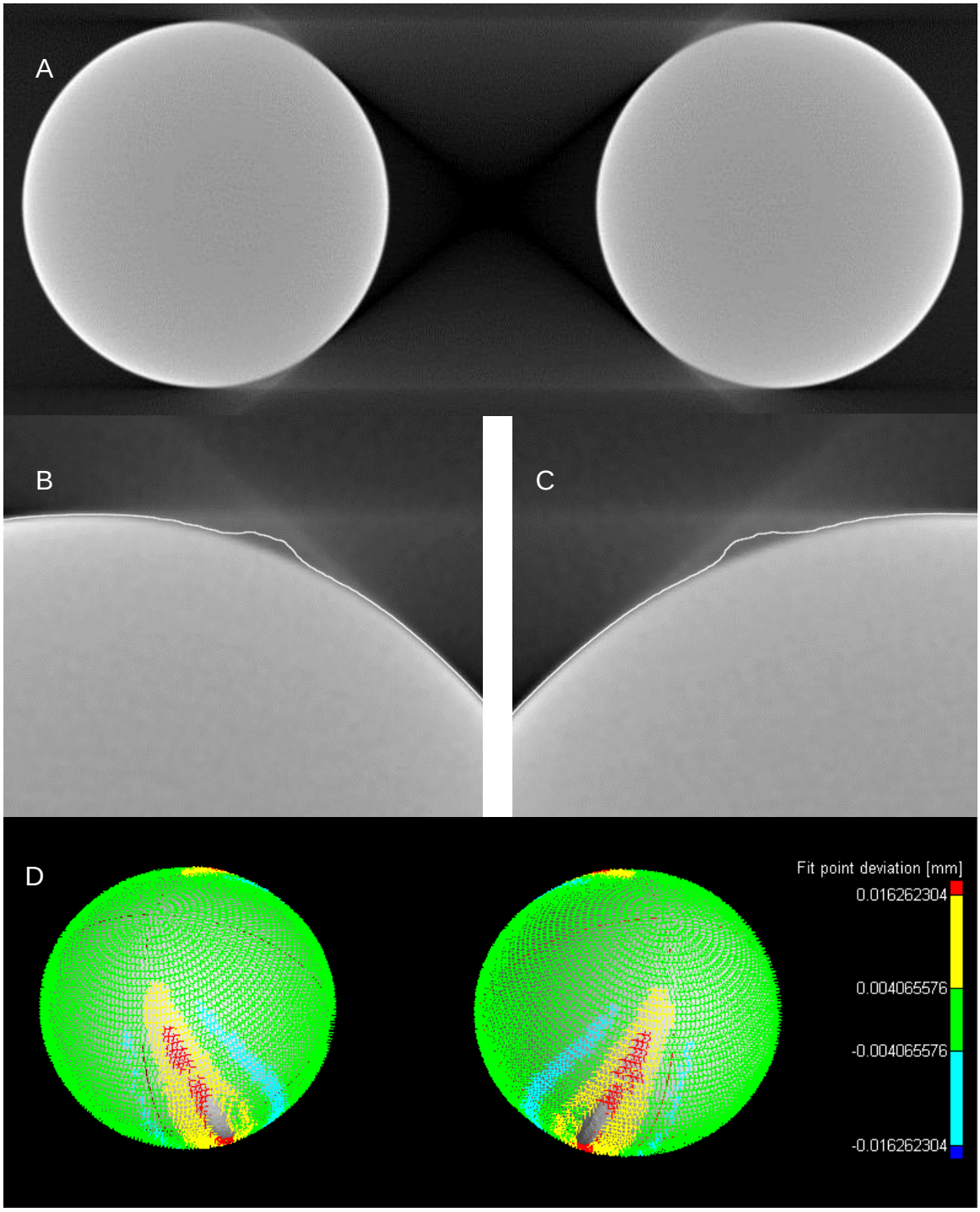

Figure 1-4: The artefact caused by beam hardening for the two-sphere sample, showing the 'streak' artefacts on the side of the spheres. Surfaces are determined using the advantage threshold algorithm in VGStudio Max 3.2.5

1.2 Terminology

In the XCT field, the term ‘threshold’ is commonly used to define the grey value that characterises the edge between material and background, or between materials [10]. The threshold selection can significantly impact the overall accuracy of the XCT dimensional measurement. One of the metrological characteristics which are immediately affected by the threshold is ‘structural resolution’, or ‘spatial resolution’, which is defined as the smallest structure size that can be dimensionally measured [2, 10]. The study of spatial resolution in XCT is currently an active research topic [78-84].

A comprehensive way to demonstrate the spatial resolution limits of XCT is the use of an amplitude-wavelength (AW) map or ‘Stedman diagram’ [85]. The AW map of a measuring instrument, see Figure 1-5-A, is a polygonal area showing the capabilities of the instruments of detecting the amplitude (A) of the surface spatial frequencies as a function of their wavelength W [10, 86, 87], where: R_h and R_v represent the maximum component size in horizontal and vertical direction, respectively; r_h and r_v are the minimum resolution limits; S_{max} is the maximum slope; and R_{min} is the minimum measurable curvature.

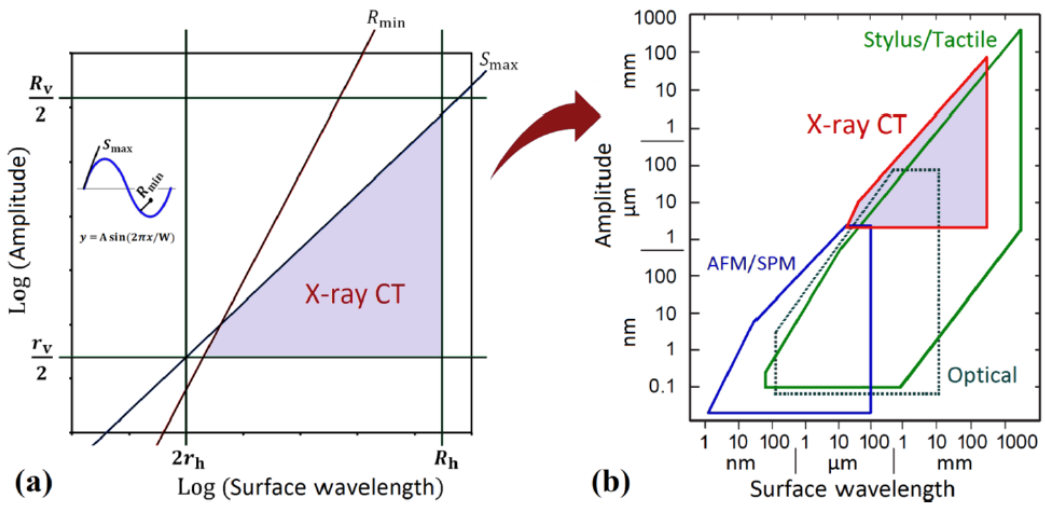

Figure 1-5: (a) The XCT Stedman [85, 88]. (b): Stedman diagram [85] for: Atomic force microscopes (AFM), Scanning probe microscopes (SPM), XCT, optical

methods (optical profilometry, confocal microscopy and interferometry), and tactile instruments.

Contact stylus instruments, which include Coordinate Measurement Machine (CMM) and Contact Stylus profilometer (CS), require mechanical contact between the probe and the surface of the component [89], see also section 2.3.2 and 2.3.3. CMM is usually used to evaluate the geometrical attributes of the component [90], whereas CS is used to evaluate the surface texture [91]. Both CMM and CS are used to provide traceable measurements in industry, however they are limited by their measurement speed and the probe size, typical (8 to 1) mm sphere radius and (2.5 to 0.1) μm conisphere radius, respectively. Surface wavelengths smaller than 2.5 μm are measured traceably using atomic force microscopy (AFM).

In comparison to other dimensional measuring techniques, contact and non-contact, the XCT covers a restricted domain in AW space, but it can access internal geometrical structures and measure out-of-sight features. In the XCT case, which is shown in Figure 1-5-B, the smallest measurable surface wavelength is restricted to approximately (5-10) μm and depends strongly on the SD method, which is often used in conjunction with interpolations techniques to find the position of the surface within the voxel. Often increasing the magnification, i.e. decreasing the physical dimension of the voxel, is not always possible due to the hardware limitation or penumbra effect [92-95]. Nevertheless, SD algorithm also can affect the spatial resolution [2]. Therefore, a more advanced digitization approach, such as the SD algorithm, is potentially beneficial to offset the magnification limitations.

1.3 Thesis structure, aim and objectives

The overall aim of the study is to evaluate the role of the SD algorithms in the uncertainty associated with the XCT dimensional measurements.

The objectives are listed below:

Objective 1: To propose an automated robust SD algorithm for the need for XCT dimensional metrology for both form and surface texture measurement

Objective 2: Investigation of the influence of 2D SD algorithm for bi-directional measurement in XCT dimensional metrology

Objective 3: Optimisation and comparison of 3D SD parameters for bi-directional measurement related to smooth surface (low spatial frequency)

Objective 4: Optimisation and comparison of SD parameters for bi-directional measurement related to rough surface (high spatial frequency)

Chapter 2 provides a review of the basic concepts of metrology, XCT traceability, SD in XCT dimensional metrology, for both smooth and rough surfaces. Chapter 3 presents a robust surface determination algorithm by employing marker-controlled watershed, which is linked to Objective 1. Chapter 4 and 5 describe the performance of 2D and 3D MCW algorithm for dimensional measurement for smooth surfaces (surface wavelengths greater than 100 μm) by employing simulation data, which are linked to Objective 2 and 3 respectively. Chapter 6 focuses on the 3D MCW algorithm for surface texture metrology (wavelength lower than 100 μm) by using both simulation and experimental data, which are linked to Objective 4. Chapter 7 presents the overall conclusion and future work.

2 Literature review

As mentioned in the introduction, precision dimensional (length) measurements are needed in all areas of manufacturing, quality control and scientific research to determine the **size** and **position** of the features of interest [96]. Especially in manufacturing, dimensional measurements are essential in assuring tolerance specifications, which is the total amount that a specific dimension can vary [97]. Geometric Dimensioning and Tolerancing (GD&T) ASME Y14.5-2018 [98] defines five different types of tolerance, form, profile, orientation, location, and runout, which can be evaluated using a wide variety of measuring instruments and devices, including ordinary rulers, steel rules, Vernier calliper, micrometre (not the unit!), gauge blocks, etc [96]. All dimensional measurements are affected by a range of errors, such as Abbe [97] and temperature distortion errors. Hence, the true value of the measurands is not possible to know [96]. Nevertheless, what is important is to establish the confidence level in the measurement results or their *traceability.* According to International vocabulary of basic and general terms in metrology (VIM) [99], traceability is “the property of the result or the value of a standard whereby it can be related to stated references, usually national or international standards, through an unbroken chain of comparisons all having stated uncertainties” [97, 99]. “Unbroken chain”, and “national or international standards” are two essential elements of traceability. The measurement traceability is established via the *calibration* process, which consists of [97]:

- Identifying the factors resulting in measurement uncertainty.
- Evaluating the magnitude of each of these factors.
- Determining their effect on the measurement capability.

The next section of the literature review will explore the general metrology concepts and the dimensional traceability of the XCT.

2.1 Introduction of metrology

Metrology is the science of measurement, and measurement is the language of science [97]. According to the **Guide to the expression of uncertainty in measurement (GUM) [28]**, **measurand** is the 'particular quantity subject to measurement', and **measurement** is defined as 'a set of operations having the object of determining a value of a quantity' [28]. In the International vocabulary of basic and general terms in metrology (VIM) [99], the term **metrology** is defined as 'field of knowledge concerned with **measurement**, and it includes all theoretical and practical aspects of measurement, whichever the **measurement uncertainty** and field of application'. The book 'Fundamentals of Dimensional metrology' [97] listed three reasons why it is necessary to do the measurement:

- Measurement is needed to manufacture things, regardless of the ownership of the design.
- Measurement is needed to control and evaluate the way other people make things.
- Measurement is needed for description in the scientific aspect.

Throughout history, the techniques and the standards for conducting the measurement have changed significantly [100]. Figure 2-1 gives examples of the metrology techniques in a very early era.

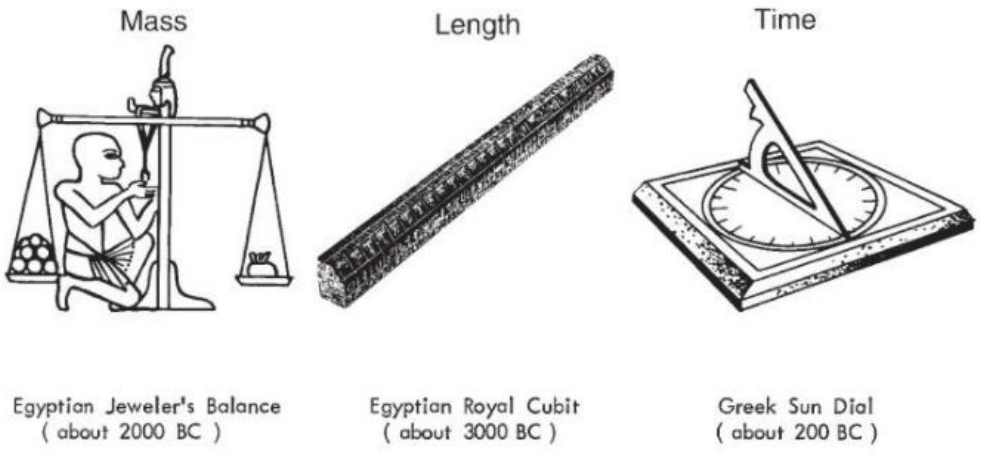

Figure 2-1: Early example of measurement devices [97]

The basic concepts that are extensively accepted for modern measurement systems were initially introduced in France in 1799, known as ‘Système International d'Unités’ (SI) in French, and ‘International System of Units’ in English [100, 101]. At the time of the French Revolution, the SI created the Decimal Metric System, and used two platinum reference standards to represent the meter and kilogram [101]. This was the first step towards the modern SI system.

Throughout the following two centuries, the SI had experienced several major changes. In 1960, at the 11th Conférence Générale des Poids et Mesures (CGPM), the name of Système International d'Unités’ and its abbreviations of SI were formally given, with six base units [101]. The 14th Conférence Générale des Poids et Mesures (CGPM) in 1971, along with adding the unit of *mole* as the base unit of the amount of substance, established the complete SI system which included seven base units: metre, kilogram, second, ampere, kelvin, Candelaa and mole [97, 101]. Then the derived units were defined by employing the seven base units.

Table 2-1 The seven base units and two additional units [97, 101]

QUANTITY	SYMBOL	NAME
Length	*l*	Metre (m)
Mass	*m*	Kilogram (kg)
Time	*t*	Second (s)
Electric Current	*I*	Ampere (A)
Temperature	*T*	Kelvin (K)
Luminous Intensity	*I*	Candela (cd)
Amount of Substance	*m*	Mole (mol)
Plane Angle		Radian (rad)
Solid Angle		Steradian (sr)

The **second** [101] was defined as ‘the duration of 9 192 631 770 periods of the radiation corresponding to the transition between the two hyperfine levels of the ground state of the caesium 133 atom’. With a well-defined **second,** the definition of **metre** [101] became ‘the length of the path travelled by light in vacuum during a time interval of 1/299 792 458 of a **second**’ instead of relying on a physical artefact. However, the base unit of mass, **kilogram** [101], was defined as ‘the

mass of the international prototype of the kilogram (IPK)', which was an alloy cylinder with a 90% mass fraction of platinum and 10% mass fraction of iridium.

In May 2019, the SI was revised [102] and is now based on seven physics constants, which are listed in Table 2-2. The SI base units are determined solely on physical constants, finally moving the definition of the kilogram away from IPK to one based on a physical constant: "by taking the fixed numerical value of the Planck constant h to be $6.62607015 \times 10^{-34}$ when expressed in the unit J s, is equal to $kg\ m^2 s^{-1}$, where the meter and the second are defined in terms of c and Δv_{Cs} [102].

Table 2-2 The seven base physical constants in the new SI system [102]

Name	Symbol	Value
Unperturbed ground state hyperfine transition frequency of the caesium -133 atom	ΔVC_s	9,192,631,770 Hz
Speed of light in vacuum	c	299,792,458 m/s
Planck constant	h	$6.62607015 \times 10^{-34}\ J\ s$
Elementary charge	e	$1.602176634 \times 10^{-19}\ C$
Boltzmann constant	k	$1.380649 \times 10^{-23}\ J/K$
Avogadro constant	N_A	$6.02214076 \times 10^{-23}\ mol^{-1}$
The luminous efficacy of monochromatic radiation of frequency $\mathbf{540 \times 10^{12}\ Hz}$	K_{cd}	683 lm/W

2.1.1 Measurement uncertainty

Each measurand always has the '**true value**' ultimately [99], which is defined as [28]

value consistent with the definition of a given particular quantity

Obtaining the true value is the ultimate goal of all measurements, but it is an unfulfillable task, as it cannot be known [99]. This is because all measurement techniques and equipment have limitations, and all measurement results are solely an estimate of the true value [97]. Thus, current measurement techniques and instruments always yield **errors** [97, 99], where the **error** is defined as

difference of quantity value obtained by measurement and true value of the measurand

There are two types of errors: systematic and random error [28]:

- Systematic error is the element of errors that reflect the fixed systematic effects of the measurement technique or equipment, or as a simple work, the systematic error cannot be reduced by repeated measurements.
- Random error is the component of errors that are generally affected by unpredictable factors, for example, temperature variation, humidity variation, vibrations, etc. Unlike systematic error, random error can be reduced by repeated observations and measurements. GUM [28] clarifies that random error is the error minus systematic error.

Thus, knowing that it is impossible to obtain the measurand's true value and 'true error', it is important to understand the degree of credibility of the measurement results, or measurement estimations. In this situation, each measurement result needs the report of the uncertainty with the degree of credibility, or confidence level in the field of metrology. There are several definitions of the measurement uncertainty [28, 99]. In VIM [99], the term **measurement uncertainty** is defined as:

parameter that characterizes the dispersion of the quantity values that are being attributed to a measurand, based on the information used

GUM [28] declares the definition of uncertainty (of measurement) as follows:

parameter, associated with the result of a measurement, that characterises the dispersion of the values that could reasonable be attributed to the measurand

Both definitions emphasise the essential element of the uncertainty: dispersion of the quantity values. It reflects the random and systematic effects during the measurement [99]. In the beginner guide [103] published by National Physical Laboratory (NPL), the source of error and uncertainty mainly results from the following factors:

- **The measurement instrument** – this could come from aging, corrosion, lack of calibration, limited resolution, noises, and all other factors related to a measurement instrument
- **The item being measured** – for example, thermal expansion, bending, heterogeneous of the sample, etc
- **Measurement process** – the measurement process is hard to design and control. For example, the measurement of the bird's weight, which has difficulty cooperating.
- **'Imported' uncertainties** – the uncertainty due to the calibration process which can introduce the final measurement uncertainty
- **Operator skills** – the ability of the operator to do the measurement task is also essential to the uncertainty, for example, the reaction time for the operator to operate a stopwatch
- **Sampling issue** – improper sampling location (hereby broadly speaking) could cause the error and uncertainty. For example, if investigating the mean population density of a country, the sampling location should not be only within big cities like New York or L.A.
- **The environment** – it mainly refers to the environmental fluctuations, like temperature, humidity, and air pressure that affect the measurement instrument or measuring object.

Another example describing the source of error and uncertainty is from ISO 14253-2 [104]. This document provides a simplified and iterative way to calculate and estimate the uncertainty (standard uncertainty and expanded uncertainty), and is also used for measuring equipment calibration and product verification, in accordance with GUM [28, 104]. Although this document is not commonly used as the demonstrated simplified way and often results in overestimation of the uncertainty, the listing of sources of error and uncertainty provided in this document is a good summary, which is illustrated in Figure 2-2. It classifies the uncertainty components into ten groups.

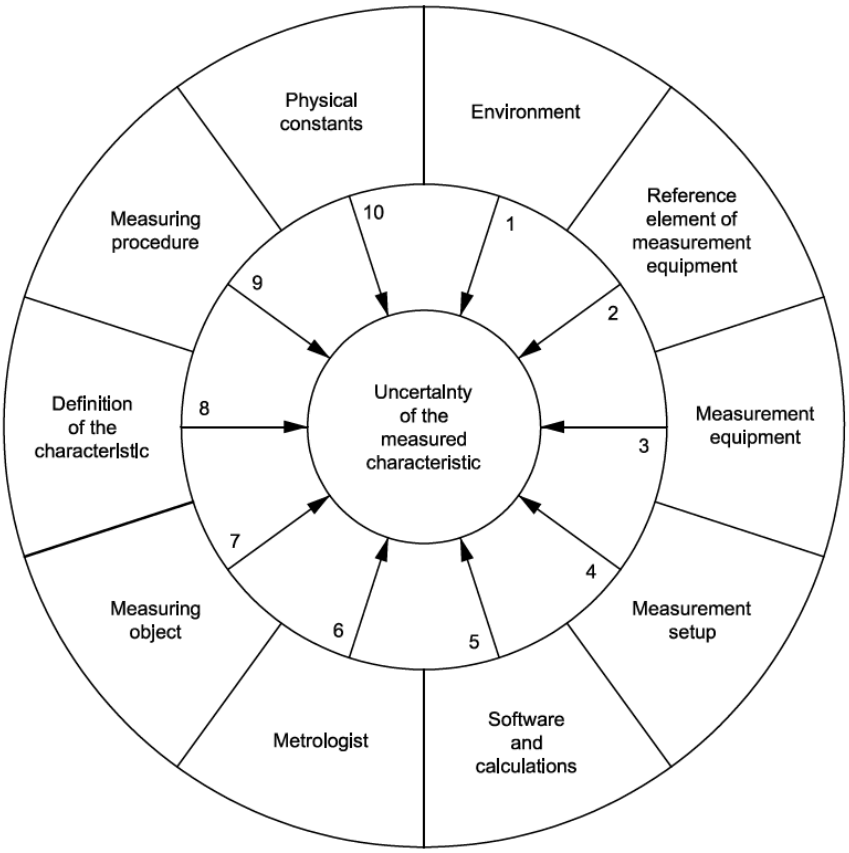

Figure 2-2 The error and uncertainty source [104]

The other two concepts often used in metrology are: accuracy and precision. In daily life, the concept boundary between accuracy and precision is ambiguous. However, in the metrology area, those concepts should not be mixed up. VIM [99] demonstrated those concepts in a more scientific way. **Accuracy (of measurement)** is defined as [99]

closeness of agreement between a quantity value obtained by measurement and the true value of the measurand

whereas **(measurement) precision** is

closeness of agreement between quantity values obtained by replicate measurement of a quantity, under specified conditions

Figure 2-3 describes the relationship between accuracy and precision, using the example of the target practice. In the left picture, the mean of the bullet position

is close to the centre, but their dispersion (precision) of the individual locations is large, resulting in low overall accuracy. The middle picture shows that the dispersion of the individual location is low, but the bias is high. The term bias is the 'estimate of a systematic measurement error' [99]. The right picture illustrates the example of high accuracy, low bias, and high precision.

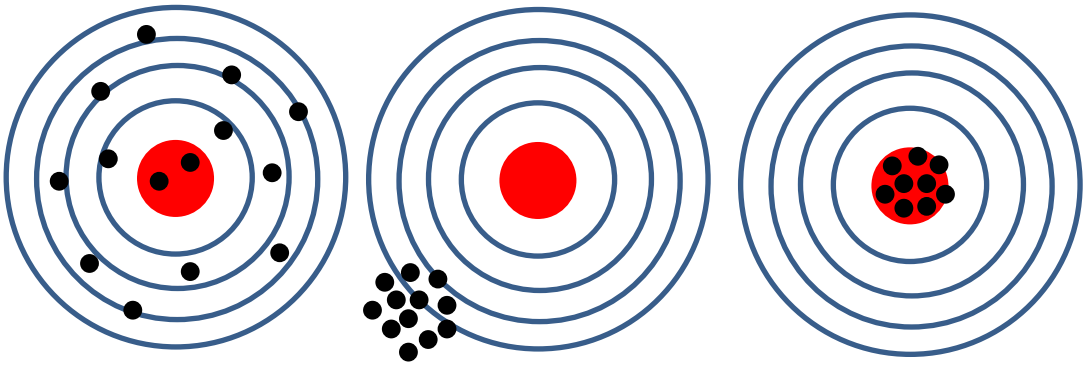

Figure 2-3 The diagram of the relationship between accuracy and precision

It is important to note that accuracy demonstrates the measurement result qualitatively, and it cannot be expressed using the numerical value [99]. While precision is normally expressed using the value of imprecision, such as standard deviation, variance, coefficient of variation, etc. [99].

2.1.2 Uncertainty evaluation

Giving the measurement value is not complete until a report of the uncertainty with traceability is accomplished [28, 99, 100, 103], and the final measurement result expression is as follows

$$Y = y \pm U \tag{2-1}$$

where y is the mean value of the measurement result, and U is the expanded measurement uncertainty. For example, a typical measurement result of the length of a sample can be expressed as follows

$$(30.02 \pm 0.02)\ \text{mm, with 95 \% level of confidence} \quad \textbf{(2-2)}$$

This result expression means that the possibility of the true value of the length of the sample lying between 30.00 mm and 30.04 mm should be 95 %.

A general guidance for evaluating the standard uncertainty is given in GUM [28]. Following steps are shown below:

- Modelling the measurement [105]

It is important to note that most of the measurands are not determined directly. Instead, many measurements are completed using the functional relationship between the measurands and input quantities [28, 105]. A typical functional relationship between measurand Y and input quantities, $X_1, X_2, X_3, \dots, X_N$, is shown below [28, 105]:

$$Y = f(X_1, X_2, X_3, \dots, X_N) \quad \textbf{(2-3)}$$

The measurement model can be simple or complex. Regarding the form, it can also be the mathematical formula, step-by-step calculation method, computer software, etc. [100]. Also, each input quantity can be regarded as an individual measurand related to other input quantities, including correction of systematic errors [28]. The relationship between the estimate of the measurand and input quantities is illustrated below [28, 105]:

$$y = f(x_1, x_2, x_3, \dots, x_N) \quad \textbf{(2-4)}$$

A detail of the development of the measurement model related to GUM is illustrated in JCGM GUM-6:2020 [105]. It points out that most of the models are hybrid models, which combine the aspects of theoretical and empirical models [105].

- Probability distribution function (PDF) assignment for each input quantities

This step is to estimate the PDF of each input quantity, such as Gaussian distribution, rectangular distribution, triangle distribution, t-distribution, etc. Based on the measurement model, the PDF of Y at y can be determined using the PDF

of each input quantity X_i. Generally, to propagate the uncertainty of input quantities to the output measurand, standard uncertainty should be worked out. In the GUM uncertainty framework [28], there are two types of evaluation of standard uncertainty: Type A and Type B of standard uncertainty. In type A, the information of the input quantity X_i is estimated by repeated measurements. The mean value, x_i, or estimate of quantity X_i is determined by J measurements

$$x_i = \frac{1}{J}\sum_{k=1}^{J} x_{i,k} \tag{2-5}$$

where k=1,2,…,J. The standard uncertainty with an estimate of x_i, is given by

$$u(x_i) = \sqrt{\frac{1}{J(J-1)}\sum_{k=1}^{J}\left(x_{i,k} - x_i\right)^2} \tag{2-6}$$

Hereby, the degree of freedom is

$$v = J - 1 \tag{2-7}$$

Type B standard uncertainty evaluation is based on the methods that are not related to repeated observations. To estimate the input quantity X_i, all the information related to the expectation and uncertainty is acquired by scientific judgement based on the pool of information on the possible variability of X_i [28]. GUM listed the resource of the information such as previous measurement data, manufacturer's specification, calibration certificate, etc.

- Determine the combined standard uncertainty of Y with an estimate of y

Under the condition of the non-correlated input quantities $X_1, X_2, X_3, \ldots, X_N$, the combined standard uncertainty is calculated as follows [28]:

$$u_c^2(y) = \sum_{i=1}^{N}\left(\frac{\partial f}{\partial x_i}\right)^2 u^2(x_i) \tag{2-8}$$

In this equation, $c_i \equiv \left(\frac{\partial f}{\partial x_i}\right)$ is called the sensitivity of coefficient related to the input quantity X_i with the estimate of x_i, as is based on the first-order Taylor series

approximation [28]. The sensitivity coefficient [28] reflects the extent of the contribution of each input quantity to the combined standard uncertainty. Equation (2-8) is only valid if the input quantities are independent. For correlated input quantities, the combined standard uncertainty is expressed in the following equation [28]:

$$u_c^2(y) = \sum_{i=1}^{N} \left(\frac{\partial f}{\partial x_i}\right)^2 u^2(x_i) + 2\sum_{i=1}^{N-1}\sum_{j=i+1}^{N} \frac{\partial f}{\partial x_i}\frac{\partial f}{\partial x_j} u(x_i, x_j) \quad \textbf{(2-9)}$$

where $u(x_i, x_j)$ is the estimated covariance associated with estimates of x_i, x_j. In reality, the correlation coefficient is estimated using the flowing expression [28]:

$$r(x_i, x_j) = \frac{u(x_i, x_j)}{u(x_i)u(x_j)} \quad \textbf{(2-10)}$$

where $-1 \leq r(x_i, x_j) \leq 1$, and equation (2-9) can be written as [28]:

$$u_c^2(y) = \sum_{i=1}^{N} \left(\frac{\partial f}{\partial x_i}\right)^2 u^2(x_i) + 2\sum_{i=1}^{N-1}\sum_{j=i+1}^{N} \frac{\partial f}{\partial x_i}\frac{\partial f}{\partial x_j} u(x_i)u(x_j)r(x_i, x_j) \quad \textbf{(2-11)}$$

If input quantities are completely uncorrelated, $r(x_i, x_j) = 0$, the combined standard uncertainty calculation should be performed using equation (2-11).

- Calculation of the expanded uncertainty U

  The expanded uncertainty U is calculated by multiplying $u_c(y)$ by coverage factor k, which is shown as follows [28]:

  $$U = ku_c(y) \quad \textbf{(2-12)}$$

  In most research studies, the reported expanded uncertainty is commonly under the condition of the coverage interval of 95% approximately, which gives the coverage factor $k = 2$. However, technically, it is only valid when the degree of freedom $\nu = +\infty$, according to Table G.2 in GUM [28]. In reality, for most Type A uncertainties, the number of repeated measurements is limited, which denotes the finite degree of freedom, leading to variations in the choice of the coverage factor to get 95% confidence level uncertainty. Thus, the

effective degree of freedom should be calculated prior to the determination of coverage factor using the Welch-Scatterthwaite formula [28]:

$$\nu_{eff} = \frac{u_c^4(y)}{\sum_{i=1}^{N} \frac{u_i^4(y)}{\nu_i}} \quad \textbf{(2-13)}$$

where $u_c^2(y) = \sum_{i=1}^{N} u_i^2(y)$. For most Type A evaluations, $\nu_i = J - 1$, where J is the number of repeated measurements. For Type B evaluations, in practice, $\nu_i \to \infty$. After determining the effective degree of freedom, the expanded standard uncertainty can be determined by

$$U_p = k_p u_c(y) \quad \textbf{(2-14)}$$

where k_p can be found in Table G.2 in GUM.

Finally, the measurement result can be reported as

$$y \pm U_p \quad \textbf{(2-15)}$$

with the level of confidence of 95% based on t-distribution with the coverage factor of k_p under an effective degree of freedom of ν_{eff}.

2.2 Basic concept of XCT

The discovery of X-ray by Wilhelm Conrad Röntgen, who won the first Nobel Prize for Physics in 1901 [75], has led to the development of a large amount of NDT techniques and medical instrumentation [6, 10, 75, 106-111].

X-ray is an electromagnetic wave that has the ability to penetrate a range of materials, from biological tissues to metals, and X-ray's energy is proportional to its frequency (or with inverse proportion to the wavelength) [75]:

$$E = h\nu = \frac{hc}{\lambda} \quad \textbf{(2-16)}$$

where h is the Planck's constant ($6.63 \times 10^{-34}\ J\ s$), c is the light speed ($3 \times 10^{8}\ m/s$), and λ is the wavelength of the X-ray beam, which ranges from (0.01 to 10) nm [75, 112-114]. Hence, X-ray energy ranges from 100 eV to 1 MeV [75], where 1 eV is defined as the kinetic energy of a single electron ($1.6 \times 10^{-19}\ C$ of charge) that passes the electric potential difference of one volt in vacuum [75]. The X-rays are classified as soft X-ray (normally wavelength larger than 0.1 nm) and hard X-ray with shorter wavelengths.

A simple schema of the device that allows to produce X-rays is presented in Figure 2-5. The light is both electromagnetic wave and particles [23, 75, 110, 115-119]. The energy of a particle was calculated by Einstein in the Theory of Relativity to be [120]

$$E = \frac{mc^2}{\sqrt{1 - v^2/c^2}} \quad \textbf{(2-17)}$$

where m is the rest mass of the particle. A simple description of the expression of electron energy reaching the tungsten target is shown as follows [121]:

$$E_e = e\Delta V \quad \textbf{(2-18)}$$

where e is the electric charge of an electron, equal to $1.6 \times 10^{-19}\ C$, and ΔV is the potential difference to accelerate the electron before hitting the target. The target is then bombarded by the electrons causing several interactions. The X-ray

spectrum, and the diagram of the interaction between the accelerated electron and matter are illustrated in Figure 2-4. About 99% of the electron energy is transferred into heat, and the remaining 1% is emitted as X-rays by the following three interactions [75, 122, 123]:

- **Electron deceleration (**Figure 2-4**-A)**

  When a fast electron approaches the atom, it is decelerated by the Coulomb field of the atom, losing kinetic energy, and generating X-ray radiation. This process is called ***bremsstrahlung*** interaction [124]. The word ***bremsstrahlung*** is a combination of the German words ***bremsen*** (brake) and ***strahlung*** (deceleration radiation) [75]. The radiated X-ray photon energy in ***bremsstrahlung*** interaction is determined by the amount of energy converted during cascade deceleration. Only a proportion of electron energy transfers into photon energy. The distribution of the spectrum due to ***bremsstrahlung*** is continuous, as indicated in Figure 2-4.

- **X-ray emission due to the re-filling of a vacant place in the inner shell by an electron dropping from the outer shell of the atom (**Figure 2-4**-B)**

  These X-rays occur when the incident electron removes an electron on the inner shell of the target material, ionising the atom [124]. The electron vacancy is filled by an electron dropping down from one of the outer shells, generating X-rays with specific energies [124]. This process normally causes spikes within the spectrum, which is indicated in Figure 2-4, showing K_α, K_β. In most cases, the electron from adjacent shells has the most probability of filling the vacancy. In addition, the characteristic X-ray energy is determined by the binding energy [2].

- **X-ray emission due to the collision between electron and nucleus (**Figure 2-4**-C)**

  During this interaction, the entire energy of the incident electron transfers to the X-ray energy, however the probability of this interaction is low.

Due to the abovementioned electron-material interactions, the emitted X-ray beam consists of photons with variable energy values, leading to a polychromatic

spectrum, as shown in Figure 2-4. The continuous curve reflects the ***bremsstrahlung*** effect, whereas the spikes indicating with K_α, K_β show the emission due to the re-filling mechanism. For dimensional metrology, the polychromatic spectrum causes measurement errors, such as beam hardening effect, because the reconstruction software assumes a monochromatic beam, *i.e.* X-ray consisting of single-energy photons. The beam hardening effect can be neglected for low-density materials (medical field case) [39], however, the errors are significant for higher density materials, especially in high precision applications [43, 44, 51].

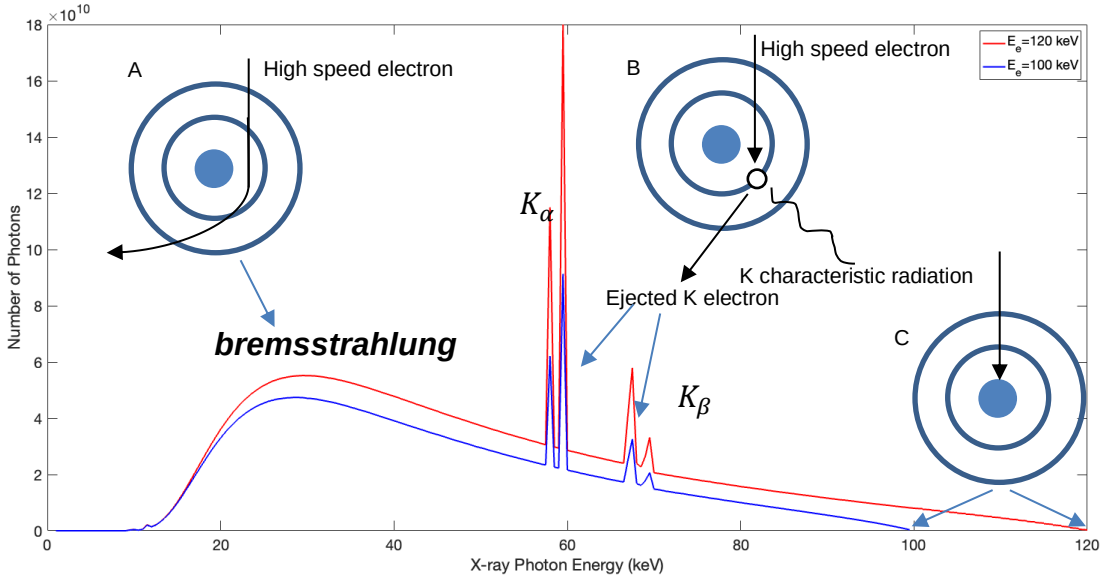

Figure 2-4: The X-ray spectrum with incident electron energy of 120 keV (red) and 100 keV (blue). This plot is generated using aRTist, X-ray tube [125, 126]. A. Bremsstrahlung; B. Characteristic radiation; C. Interaction with nuclear

2.2.1 X-ray source

A typical X-ray source structure is illustrated in Figure 2-5. The key elements of the X-ray tube are the filament (cathode) and target (anode) [2]. A vacuum chamber is needed (typically <0.1 μbar) to avoid the secondary electron with lower energy caused by the interaction of the electrons with the gas molecule [2, 75]. The filament is heated to approximately 2,400 K where the thermionic emission effect happens, allowing the electrons to escape the filament [75].

Tungsten is the common material used for the target, due to its physical properties, such as high melting points and X-ray generation efficiency [75]. Only less than 1% of the electron energy is transferred in the energy of X-rays, with the remaining energy being transferred into heat. Therefore, a cooling system is required [75].

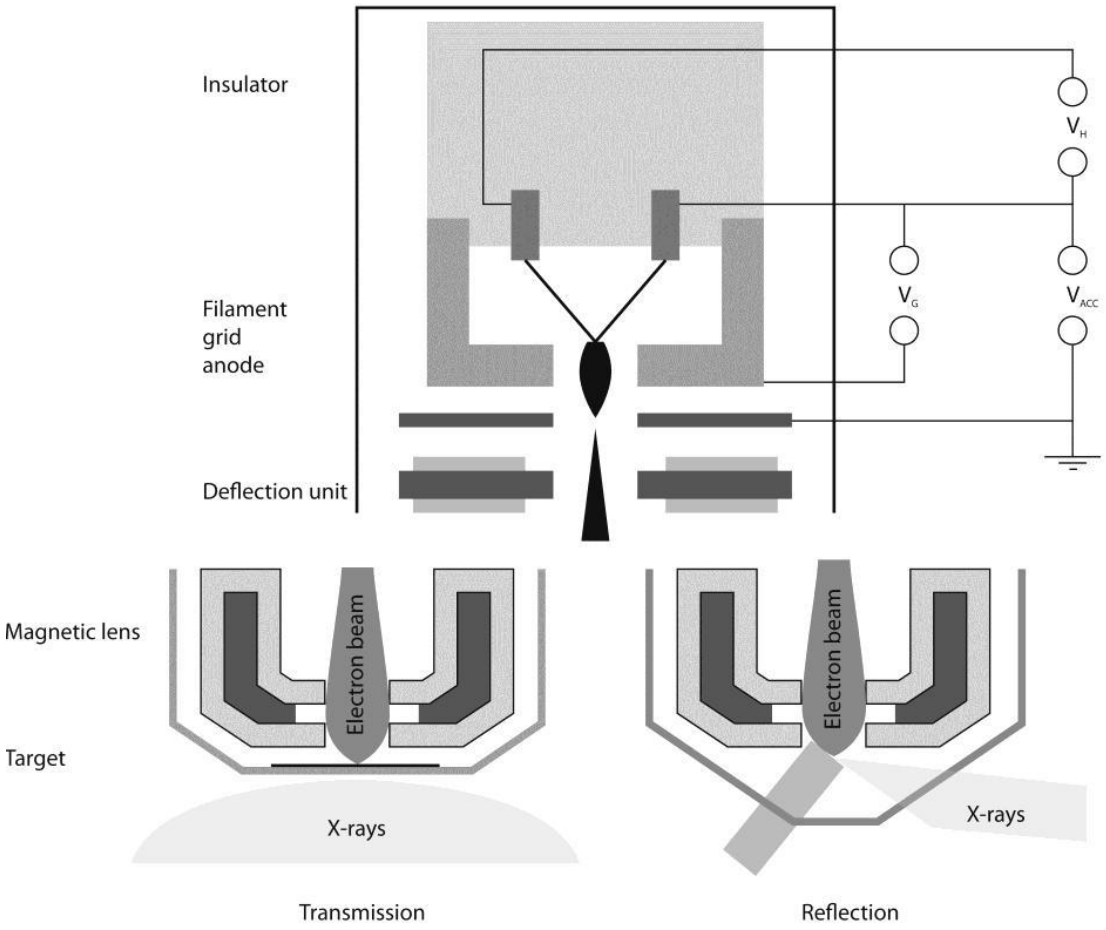

Figure 2-5: The typical structure of X-ray source [2]

The effective focal spot size, which significantly affects the image quality [22, 75, 95, 127-130], is related to the angle between the target collision surface and the electron beam [75]. The conventional XCT has a focal spot size of more than 1 mm [2]. For micro and nano focus XCT, the focal spots are between (1-1000) μm [2, 20] and below 1 μm [131, 132], respectively. Nano-focus systems are normally low-power systems [75]. As a rule of thumb, for each 1 W the focus spot size increases with a 1 μm [75].

2.2.2 Interaction between X-ray and material

After emission, the X-ray beam penetrates the material samples and gets linearly attenuated [133, 134]. Equation (2-19) provides the relationship between the attenuated intensity of an X-ray photon and the distance travelled by that photon through the material [135]:

$$I(x) = I_0 e^{-\mu x} \quad \textbf{(2-19)}$$

where:

$I(x)$: the intensity of the photon after travelling a distance of *x* in the attenuation

I_0: the initial intensity of the photon

μ: the linear attenuation coefficient

x: travel distance within the material

The linear attenuation coefficient is a function of the wavelength of the X-ray radiation and the material properties of the attenuated substance [136].

Equation (2-19) provides the mathematical foundation of the further reconstruction process, which relies on the thickness measurement derived from each radiogram (2D image) provided by the X-ray detector.

2.2.3 X-ray detector

The detector captures the attenuated photon and collects projection images from a different angle, either with a rotated sample or a rotated detector [2, 137]. There are many types of X-ray detectors which, according to ISO 15708, are classified into two main groups: ionization detectors or 'direct' detectors (for example, semiconductor detectors - Figure 2-6 left) and scintillation detectors or 'indirect' detectors [2] (Figure 2-6 right).

The semiconductor detector generates the current when exposed to the X-ray photon. In modern semiconductor detectors, the current is assembled within the thin film transistors (TFTs) [2]. TFTs have great sensitivity but can suffer from

overexposure when photon energy exceeds 20 keV - not the case of XCT dimensional metrology [2].

The scintillation detectors absorb the high-energy X-rays and transfer them into low-energy photons associated with the wavelength range of visible light, which is further captured by photomultiplier tubes or photodiodes [2]. The scintillation detectors are sensitive to low doses of X-ray [2].

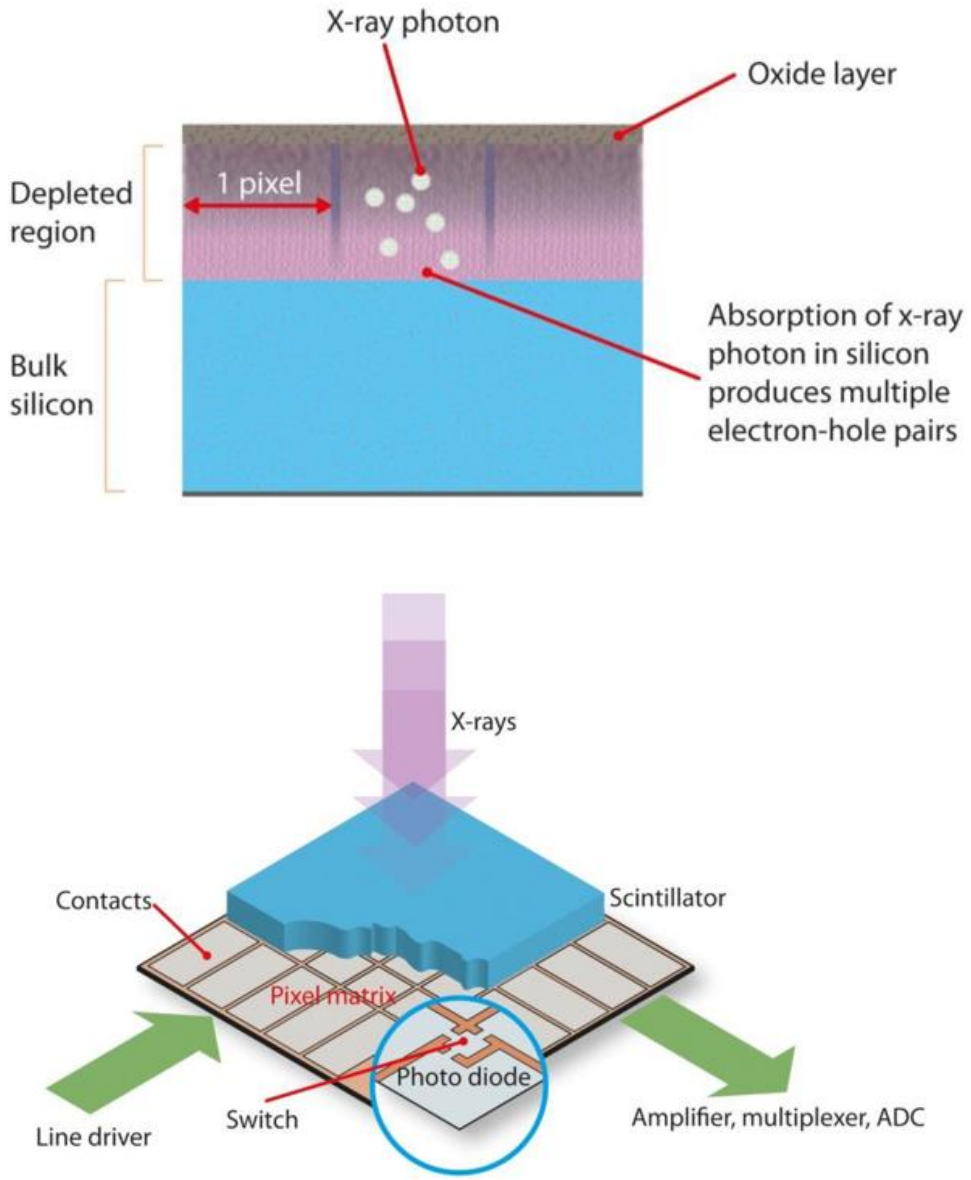

Figure 2-6: Left: Semiconductor detector [2]; Right: Scintillation detector [2, 138]

The radiogram is affected by the sensitivity of the detector, its field coverage, geometrical characteristics (size, pixels), quantum efficiency, spatial resolution, noise, dynamic range, uniformity, acquisition speed and frame rate [2].

2.3 Dimensional XCT

To achieve traceable XCT measurement results and to test its metrological capability, calibrated reference samples are often used [10]. CMM and CS are often used to provide traceable value for form and surface texture measurement, respectively [76]. This section reviews the concept and state-of-art of the traceability of the XCT.

The current knowledge about XCT use in dimensional metrology is largely based upon empirical studies [1, 2, 20, 27, 139, 140]. The first serious discussion and analysis regarding the use of XCT as a dimensional tool emerged during the 1990s [141]. This development culminated with the first commercial XCT system assigned exclusively for dimensional metrology, Werth Messtechnik, which was presented at Control Fair in Germany at the year of 2005 [20].

The complete measuring procedure is a combination of complex step chains. Kruth *et al*. [20] have proposed the systematic explanatory workflow during the CT dimensional measurement, including XCT measuring hardware (scale calibration, X-ray measurement process) and succedent data analysis process (raw data pre-processing, reconstruction to 3D models from 2D images, rescaling, thresholding, edge detection, voxel interpolation, geometrical determination, CMM software measurement evaluation, CAD comparison). The flow chart for accomplishing XCT dimensional measurement is illustrated in Figure 2-7.

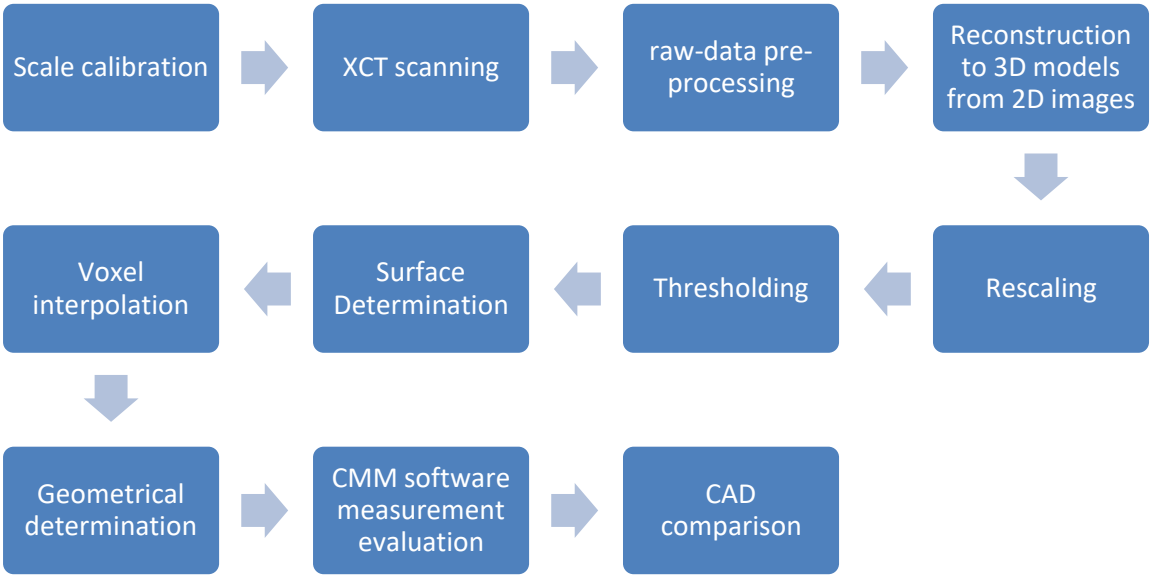

Figure 2-7: The workflow of complete XCT dimensional measurement [20]

The errors introduced at each step in the XCT measurement chain affect the outcome of measurement, and the accumulation of errors from one step to another causes significant deviations. Some common error sources of the XCT system have been understood [2, 20]:

- Beam drift is primarily caused by the thermal expansion of the X-ray tube in the X-ray generation process, where only 1-2% of the energy is transferred as the photon of the X-ray beam, and the remaining energy dissipation is the heat emission resulting in the increase of the temperature in the X-ray tube to distort the inner structure [2, 20]. Flay and Wenjuan [100, 142, 143] have assessed the focal spot drift (known as beam drift) with a novel design of a sample;
- Beam hardening is mainly caused by the polychromatic spectrum while reconstruction assumes linear attenuation [44]. Corcoran [144] attempted to evaluate the impact of beam hardening on the dimensional metrology with the different orientations of the workpiece;
- Ring artefacts are caused by the incorrect alignment of the object, focal spot and detector, and this error could lead to the sharper contrast rings on the sample around the centre of rotation [20];

- Other error sources could include SD, scattering, metal artefacts, noise, aliasing artefacts, sampling artefacts, filtering, rotation axis errors, adjustment errors, error from the wrong identification of rotation centre, and Feldkamp errors [20].

In addition to the error sources listed above, the operator can influence the measurement result by interfering with the XCT hardware and software:

- Hardware: voltage, current, position of detector and sample (FDD = focal spot to detector distance, FOD = focal spot to object distance), placement of the sample [20, 145, 146].
- Software: SD by the selection of voxel specimen in the raw data, geometry determination by selecting reference points on the determined surface.

The work on XCT dimensional measurement traceability often involves calibrated reference samples [10]. Interlaboratory comparisons [10, 147-149] addressing the overall ability of XCT to measure the shape and form of the objects, which were often characterised by smooth surfaces, used calibrated CMM to provide traceable reference measurements of the geometric features of the sample. The study used the local adaptive threshold within VG as the SD algorithm. However, the interlaboratory comparisons did not depict the individual influence of the SD algorithm in the XCT dimensional measurement.

Partly, the current SD research targets the measurements of the inner and outer features of cylinders [45, 150-153] because they are bi-directional [23] measurements, which are significantly impacted by SD. Figure 2-8 illustrates the difference between uni-directional and bi-directional distances and the impacts by surface determination thresholds. The surfaces from which the uni-directional distance is derived move in the same direction with the threshold position. However, for bi-directional distance measurement, there will be a great impact on the measurement results with different surface determination threshold values. Because surfaces upon which bi-directional distances were measured, for both inner and outer features, move to the opposite direction with the threshold position. Therefore, for inner and outer features, there will be opposite trends while changing the threshold value.

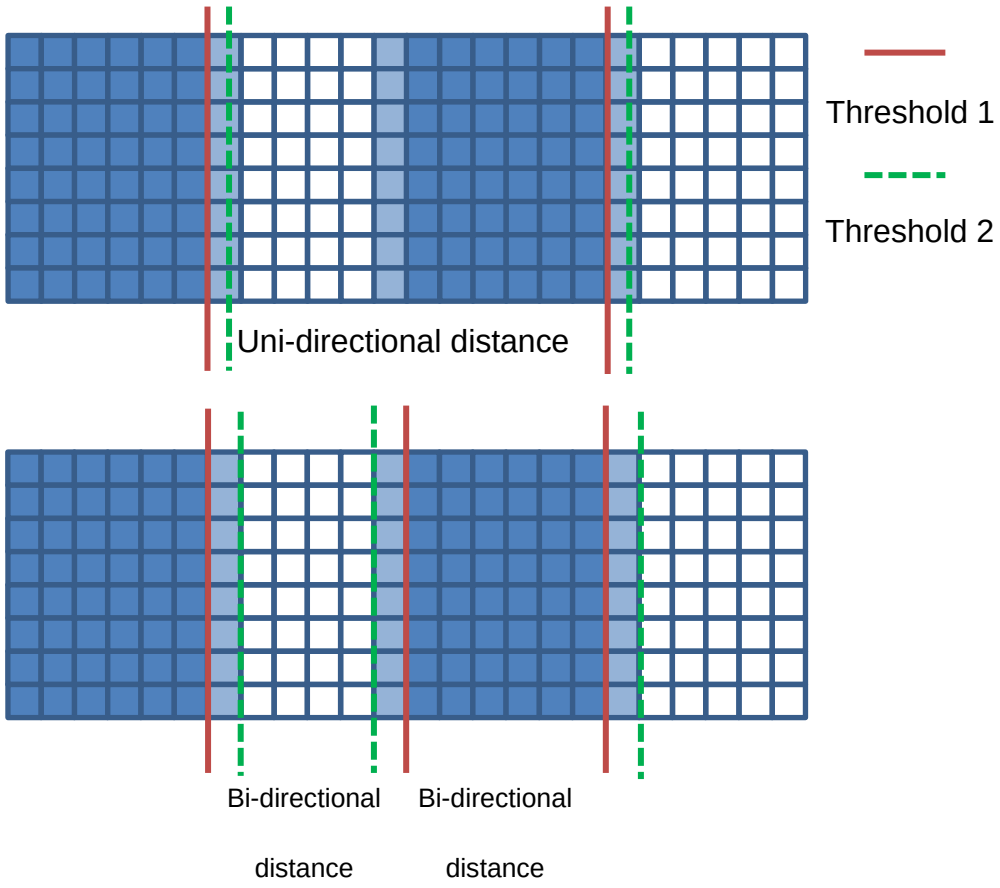

Figure 2-8: Uni-directional and bi-directional distance

A previous interlaboratory comparison showed that there was a limited impact of SD on the uni-directional measurement [150]. The reference sample was composed of the stack tubes with the same inner (ID) and outer diameter (OD). Measurands included ID, OD and length of the smaller tube. Hereby, both ID and OD are related to bi-directional distance, and length is uni-directional distance. This interlaboratory comparison also included the surface texture analysis. VG algorithm was used to extract the surface mesh data from the reconstructed volume data. However, in this paper, the term ‘surface determination correction’ is vague as it does not illustrate the concept of ‘surface determination correction’ in detail. For measuring OD and ID, the authors simply ‘removed’ the material: to increase ID and decrease OD which is called ‘surface determination correction’ in this paper. However, as described before, the VG algorithm is not transparent enough. Moreover, it was demonstrated that the material dilation as the result of

beam hardening artefacts does not strictly lead to less ID and more OD [154]. Therefore, the sensitivity of SD algorithms to beam hardening and noise needs further research.

Two Ti64 components were used in a surface texture interlaboratory comparison, which followed the ISO 25178-2 guidance [150, 155]. However, the study did not use a traceable reference instrument such as CS but used another XCT instrument, Nikon MCT225, to extract the reference roughness data. The intercomparison used once again the local adaptive threshold within VG and mentioned that a SD correction was applied without being specific about which specific correction was used.

Klingaa [156] used XCT to measure the surface texture of AlSi10Mg laser powder bed fusion channels and examined the influence of voxel. A 20 µm of voxel size led to an average residual error of 46.5 µm, approximately 230 % of voxel size, whilst applying a median filter before reconstruction to reduce the effect from noise.

Wenjuan [76] and Thompson [157] used VG to compare XCT with CS and coherence scanning instruments. Filippo [158] compared an optical profiler with the XCT measurement without beam hardening correction (BHC) of the Ti6Al4V sample manufactured using an AM technique. Once again, VG was used without providing details about the search distance and Region of Interest (ROI) selection.

Townsend [159] used VG and Otsu, and studied their effect on areal surface texture with no reference to traceable texture instruments.

2.3.1 Roughness, waviness, and form

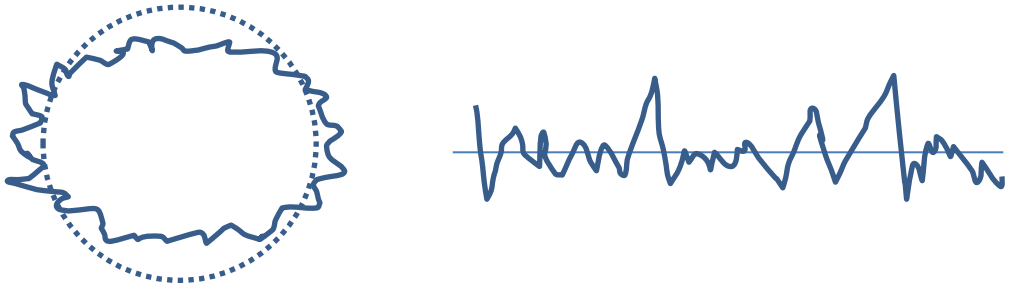

Form error Surface texture

Figure 2-9: Form and roughness illustration

Dimensional conformity/tolerance of a manufactured part is established by estimating the deviation from its intended design (nominal dimensional characteristics) in respect to the form and texture components. The form attributes describe the overall shape of the surface ignoring the roughness and waviness on the surface [162] (see Figure 2-9 -left where the overall form error exists as the shape deviates from perfect circle to ellipse) and is typically evaluated using coordinate measuring systems, see section 2.3.2.

Surface texture consists of topographical features present on the component after the removal of the overall form, as shown in the right figure in Figure 2-9. The surface texture normally consists of roughness and waviness. Roughness profile is defined as ‘the profile derived from the primary profile by suppressing the long wave component using a long wavelength (high pass) filter, with cut-off’ [162]. Waviness profile is ‘the profile derived by the application of a band pass filter to select the surface structure at rather longer wavelengths than the roughness’ [162].

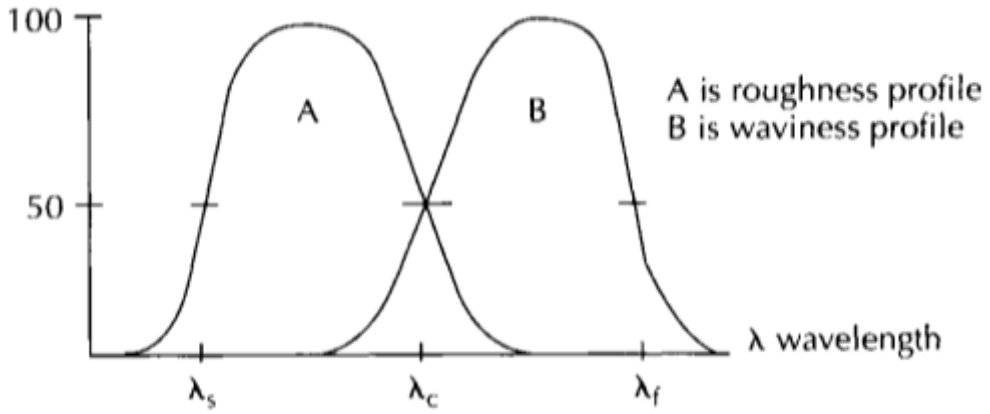

Figure 2-10: Profile figures [309]

In general, the roughness, waviness and form profiles are separated using different filtering and measurement conditions, as is shown in Figure 2-10.

λ_s profile filter defines the boundary between the **roughness** feature and the even smaller features such as microfracture marks [309];

λ_c profile filter defines the intersection between the **roughness** and **waviness** profiles at the cut off of 50 % [309];

λ_f profile filter determines the intersection between the **waviness** profile and the profile with longer wavelength such as **form** [309].

For example, in the case of a profile contact stylus measurement (see section 2.3.4), ISO 3274 [170] provides practical recommends for the selection of the filters cut-off, which depend on the maximum sampling spacing as well as maximum radius of the stylus tip. The relationship between the cut-off wavelength λ_c, the sampling distance and radius tip is shown in Table 2-3.

Table 2-3: The relationship between the roughness cut-off wavelength λ_c, tip radius and the maximum sampling spacing distance according to ISO 3274 [170]

$\lambda_c\ (mm)$	$\lambda_s\ (\mu m)$	λ_c/λ_s	$maximum\ r_{tip}\ (\mu m)$	Maximum sampling spacing μm
0.08	2.5	30	2	0.5
0.25	2.5	100	2	0.5
0.8	2.5	300	2	0.5
2.5	8	300	5	1.5
8	25	300	10	5

2.3.2 Coordinate Measurement Machine (CMM)

Classified as GPS measuring equipment [160], CMM is a 3D contact measurement technique based on a probing system, which is depicted in Figure 2-11, and three orthogonal reference axis (other axis configurations are also possible). The CMM measures the coordinates of a cluster of points on the surface of the component [160] by moving the probe along its reference axis. In practice, the axis and the probe are mounted in five configurations: cantilever, bridge, column, horizontal arm and gantry [97]. The cluster of points is used to determine the geometry features of the workpiece. The CMM presents several advantages [100]:

- Automated measurement process, with reduced operator requirements.
- Conduct multiple measurements on different industrial parts.
- Integrated technique to incorporate different metrological instruments.

The error sources affecting the CMM [161] fall into five categories:

- Hardware: machine design, probing system, reading system, probe tip size error, rotary axis errors, residual rigid-body geometric errors, environment affecting the machine structure, vibration, etc.
- Workpiece: form deviations, accessibility restrictions, clamping effects, elastic deformation due to contact between probe and workpiece.
- Sampling strategy: inadequate sampling, inadequate datums, interactions of sampling with complex forms.
- Fitting and evaluation algorithms: fitting algorithm selection, algorithm implementation
- Extrinsic factors: operators, cleanliness, filtering, fixturing variability.

Due to a large number of published standards, CMM was used in many task-specific experiments [76, 150, 159, 162-165]. As a mature measuring technique, the CMM benefits from a comprehensive standardisation framework under the ISO10360 [160] series and ISO 15530-3 [166], which cover in detail instrument specifications, measurement procedures, verification, calibration and traceability.

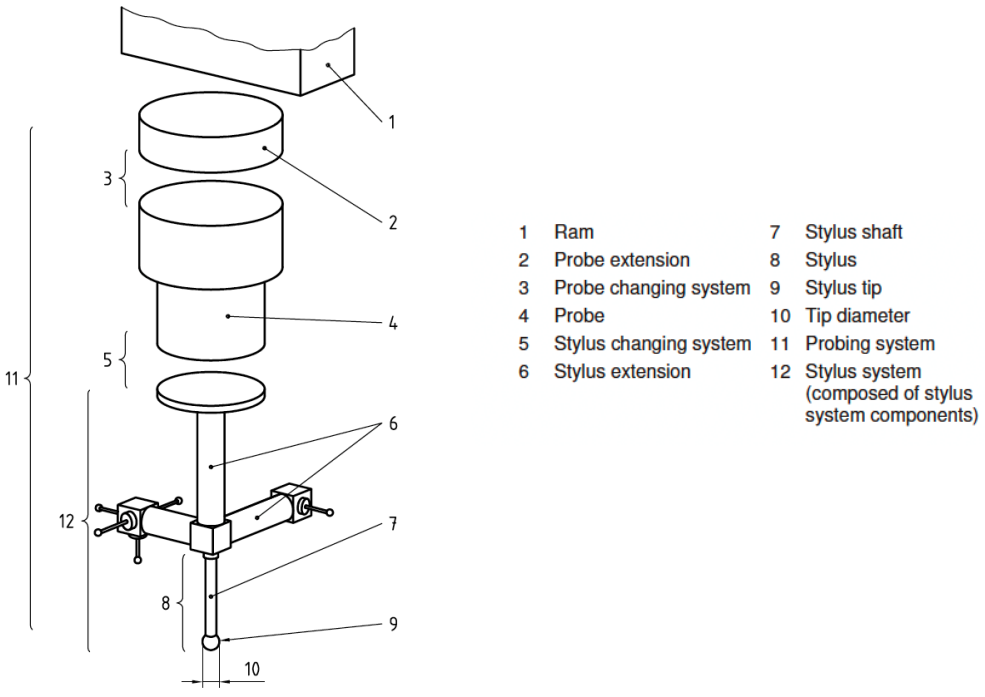

Figure 2-11: The typical probing system of CMM [160]

In practice, the measurement traceability is achieved by calibrating the CMM with a calibrated reference sample which has similar dimensional characteristics to the component under test [167]. The calibrated sample is often measured using equipment situating higher in the traceability hierarchy [28].

The expanded uncertainty is given by the equation [167]:

$$U = k \times \sqrt{u_{cal}^2 + u_p^2 + u_b^2 + u_w^2} \quad \textbf{(2-20)}$$

Where, u_p is the uncertainty related to the measurement procedure, for example, temperature of CMM, repeatability, which are all type A errors. u_{cal} is the uncertainty stated in the calibration certificate of the calibrated workpiece (type B). u_w is the standard uncertainty associated with the variations of a workpiece, for example, the thermal expansion (type A or B). $u_b$is the standard uncertainty associated with systematic error (type B).

Most of the CMM measurement limitations are related to the physical size and shape of the probe, as shown in Figure 2-12, which restricts the CMM access to out-of-sight features and narrow surface components. Similar limitations affecting the contact surface texture instruments (such as CS), but with a more significant impact on the targeted geometrical attributes, are explained in the next section.

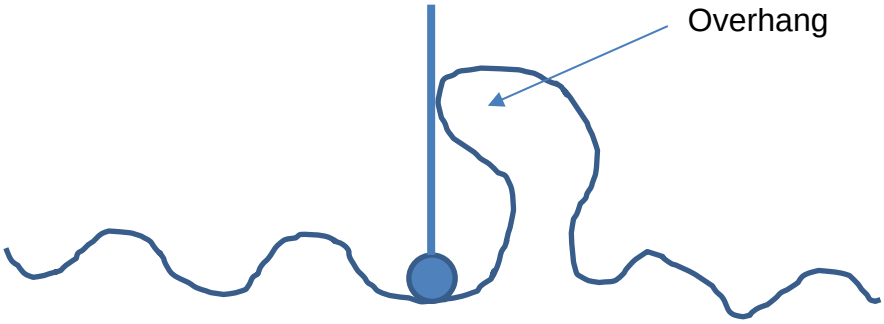

Figure 2-12: Description of overhang problem in CMM measurement

2.3.3 CS machine and traceability

CS was introduced in 1929 by Schmaltz [168]. The CS is a popular surface texture instrument [162] that provides traceable measurements [169]. Figure 2-13 shows the components of a typical contact stylus based on ISO 3274 [170]. The typical shape of the stylus is a cone-sphere with an opening angle of 60° or 90 and a tip radius of 1 μm, 2 μm, 5 μm or 10 μm (other stylus geometries are also possible). The sample under test is placed onto the fixture and the stylus is dragged across the surface along the linear guide presented in the drive unit.

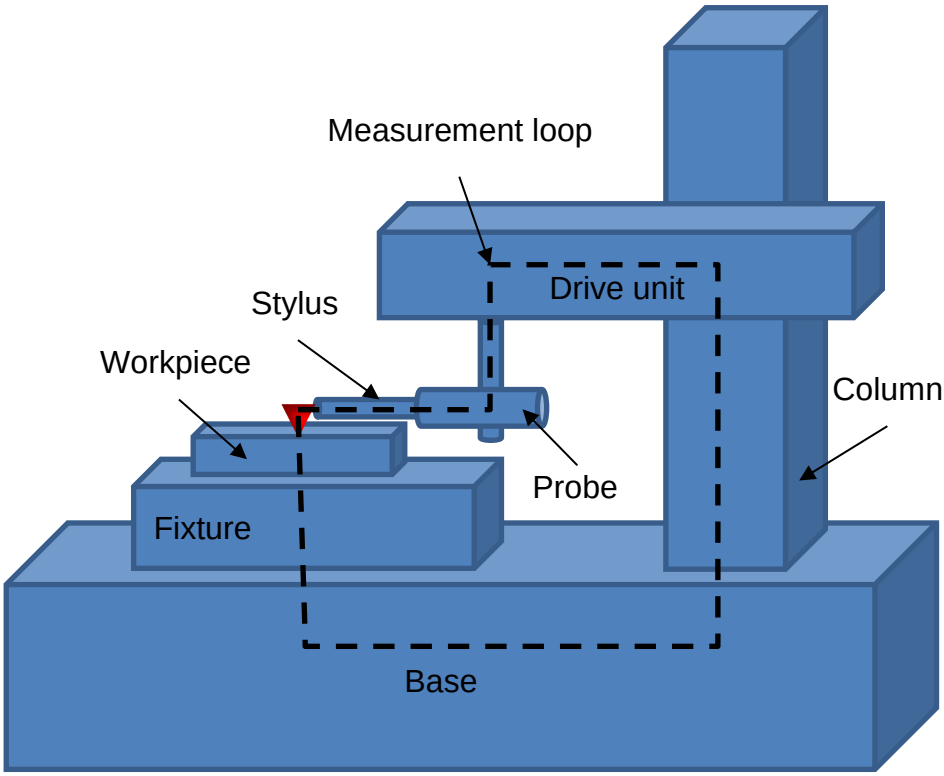

Figure 2-13: The typical structure of contact stylus from ISO 3274 [170]

When measuring the surface texture using a CS, the physical size and shape of the stylus will have an effect on the measured data, which will translate into reduced valleys depth and width, rounded peaks and unmeasured re-entrant features, as shown in Figure 2-14 [162]. These problems lead to a 'more smoothed surface' than the real one. In other words, the stylus tip applies a low pass filter on the true surface texture [171]. Other CS errors sources include:

Material hardness: when measuring a soft material, the contact stylus can plastically deform the surface [171]

Measuring force: the stylus can cause distortion of the weak feature [171]

Movement speed: increased stylus speed can act as a low pass filter [171]

Limited ability to generate areal surface texture: stylus instruments work in a raster fashion, therefore it takes time to cover large areas [171].

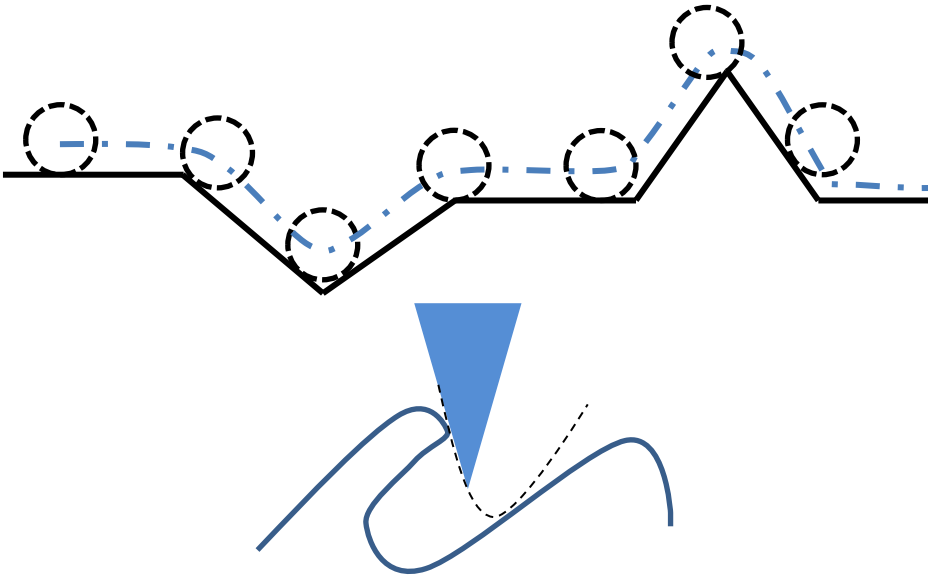

Figure 2-14: Upper image: The effect of peak round-off and reduced depth when measuring the valley. Lower image: the limited "re-entrant" feature [162, 172]

The CS traceability is detailed in reference [163]. The calibration is based on using various material measurement standards [173], which are themselves calibrated using traceable instrumentation. The calibration and performance evaluation of CS is described in [163] and relies on the evaluation of the following characteristics:

- Condition of the radius tip
- Linearity and amplification of the scales
- Spatial frequency response

2.4 Available standards for XCT dimensional metrology

Despite the lack of a clear uncertainty evaluation framework for XCT dimensional metrology, there are standards that are related to the XCT dimensional metrology. VDI/VDE 2630 [21] adapted the standards designed for CMM, such as ISO 15530-3 [166], to describes the influencing factors for both hardware and software aspects used in XCT dimensional metrology. In 2013, Japanese Standards Association Group has published the standard XCT dimensional metrology terminology in JIS B 7442 [303]. ISO 15708-2 [304] provides a

framework of XCT examination procedures and includes a list of data acquisition parameters, reconstruction parameters and image visualisation parameters, which can be applied to examine and develop the protocols [2].

A set of XCT related standard were developed in USA: ASTM E 1695 [305], ASTM E 1441 [306] and ASTM E 1570 [307]. ASTM E 1695 [305] provides the guidelines for evaluation of the spatial resolution and contrast sensitivity of XCT machine that can be used to provide the projection of uniform disk of material with reduced cupping effects. ASTM E 1441 [306] covers XCT for NDT testing, while focusing on spatial resolution, noise, and artefacts. ASTM E 1570 [307] describes the minimum requirements for XCT examination of test objects using fan beam systems. However, ASTM standards do not provide the specific guidance for XCT dimensional metrology purpose.

ISO 10360-11 [308], published in 2021, describes the metrological characteristics and methods for testing CMS that use the principle of XCT.

2.5 Surface determination algorithm

Back in the 1970s, most of the research targeted edge detection on 2D images [145, 174-206], including medical imaging and general images (RGB and grey images). Normally, edge detection in the medical area does not require the accuracy estimation of the edge itself [29], however, this is not the case in industrial XCT dimensional metrology. Only a few papers covered the development and verification of the XCT SD algorithm, and mostly, the investigation of image quality [29, 30, 183, 207-220].

SD algorithms can be classified into: (i) *global threshold methods* [35] and (ii) *local adaptive threshold methods* [36].

2.5.1 Global threshold algorithm

Otsu [35] and ISO50 [37] are the most common global threshold methods used to separate the background from the object. Both methods, represented pictorially in Figure 2-15, are histogram-based algorithms that return a single grey threshold value situated between the background and the object. Otsu's threshold value (T_{Otsu}) relies on the minimization of the between-class variance for the background and foreground [35], whereas ISO50 returns the threshold value (T_{ISO50}) at the midpoint between peaks of the object and background histograms (T1 and T2 in Figure 2-15). The voxels with higher intensities than the threshold value are classified as foreground, *i.e.* the object, and the rest as background. However, both methods are sensitive to errors present in the image. For example, Otsu method is affected by beam hardening [22, 221] and scattering that can lead to measurement errors as large as 9% [222]. Meanwhile, a single threshold value may not be able to determine the surface accurately (low adaptation) in some areas of the 3D representation of the object, due to the voxels' intensity variation along the boundary between the foreground and the background [22].

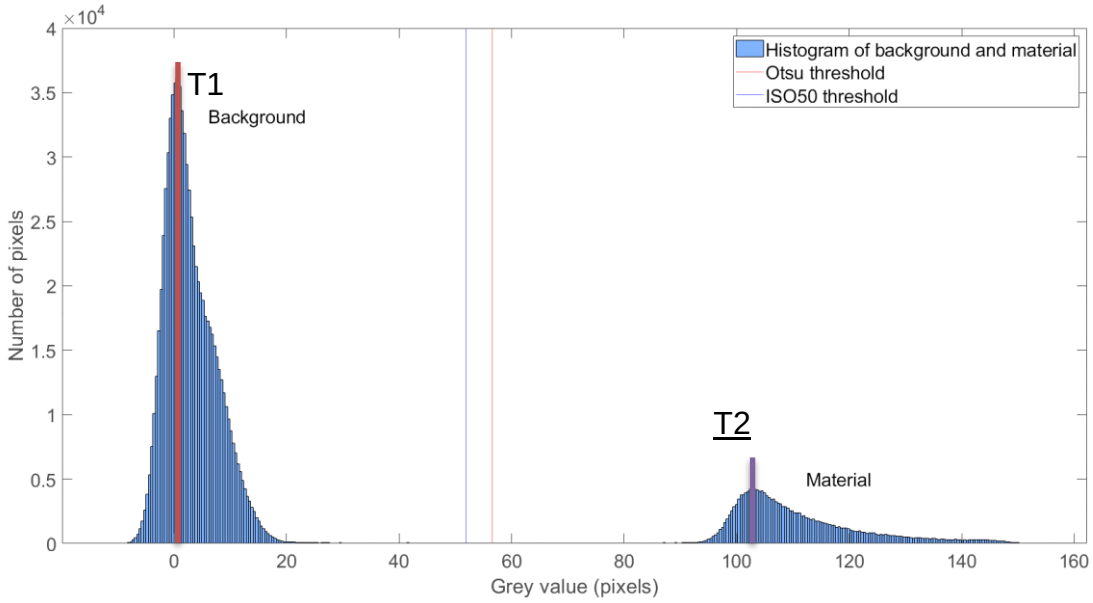

Figure 2-15: The histogram of a reconstructed XCT image with a total number of pixels N, showing the calculation of Otsu threshold and ISO50 threshold. The grey value is shown in 'float 32' format

2.5.2 Local adaptive threshold algorithm

In contrast to the global methods, local adaptive algorithms calculate the maximum local gradient [23]. Examples include Canny [31], Steinbess algorithm [223], Heinzl method [210], and advanced surface determination in VGStudio (VG).

Canny algorithm

Canny is a common SD algorithm capable of achieving good quality surface while reducing unnecessary information, such as noise [22, 29, 43, 44, 100, 224].

In the first step, Canny algorithm uses the non-maximum suppression technique to find all local maxima, which are defined as the pre-determined edge. In the following step, two thresholds, low and high, are set to select the desired edge from the pre-determined edge. Then, the pixels of the pre-determined edge that have an intensity greater than the high threshold value will be marked as the edge (hard edge). Meanwhile, the pre-determined edge pixels with an intensity smaller than the low threshold will be discarded. The pre-determined edge pixels between the high and low threshold values are marked as 'soft edge'. Lastly, the soft edge

connecting with the hard edge will be marked as the hard edge; otherwise, those soft edges will be discarded.

The main issue associated with Canny is that relevant thresholds have to be appropriately chosen to avoid broken-up and noisy surfaces [31]. For example, inappropriate threshold selection could result in omitting edges, as shown in Figure 2-16. The threshold for selecting the inner and outer cylinder surface can differ. Thus, it is common to lose weak edges while dealing with noise filtration.

Weibin [225] improved the Canny algorithm by introducing the concept of gravitational field intensity to substitute the image gradient and acquired the gravitational field intensity operator. The research also enhanced the threshold selection by associating with the mean of gradient magnitude and standard deviation and introduced two different threshold selection algorithms for ‘less’ and ‘rich’ edge information images. However, this advanced Canny algorithm has not been tested for XCT dimensional metrology purposes. Moreover, it did not declare a rigorous definition of the routine that defines images with ‘less’ and ‘rich’ edge information. For ‘low’ edge images, arbitrarily setting the low threshold value half of the high threshold value did not make the method sufficiently robust.

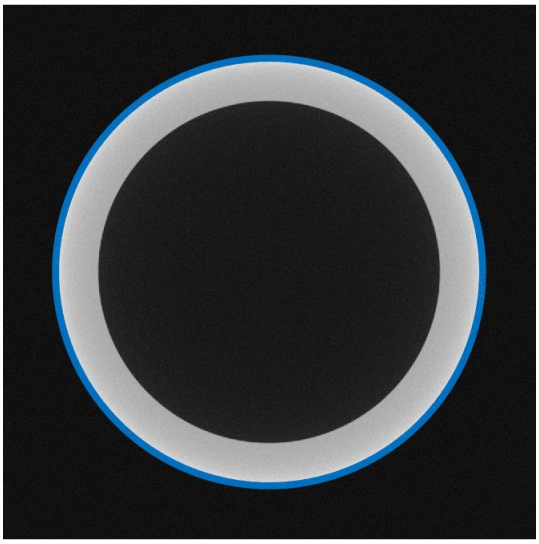

Figure 2-16: Canny edge detection with inappropriate threshold selection

VG

VG is a universal inspection tool for industrial CT analysis, and it was developed by Volume Graphics GmbH [36]. It provides the user-friendly interface and enables users to process the volume data, including Region of Interest (ROI) selection, porosity analysis, surface determination, geometry determination, etc. VG enable users to generate the boundary within the transition between the material and background, and it provides the global threshold and advanced mode.

The advanced SD method implemented within the VGStudio MAX (hereby Iterative algorithm) is commonly used for XCT dimensional metrology [37, 41, 43, 45, 74, 78, 150-153, 221, 226-239]. A major problem with VG algorithm in dimensional metrology is that it is not an open source. As described in (chapter 2.3.2), a complete measurement requires a full understanding of all influencing factors, including the SD algorithm. However, the VG algorithm is protected by a patent, and the mathematical calculation behind the algorithm is a black box for metrologists. Thus, when conducting metrology research in SD, traceability cannot be easily ensured when using VG algorithm. Also, as Figure 1-4 shows, the beam hardening results in the ‘streak’ artefacts, and the surface determined by VG algorithm deviates from the proposed sphere surface on the ‘streak’ region. Although it can be eliminated by adjusting the user parameters, it makes VG algorithm neither transparent nor robust.

Another example of the use of the VG for distance and diameter measurements, with uni-directional and bi-directional measurements, was documented in [154], which included the parameter settings of the VG algorithm and geometry determination, including starting contour, search distance (the author did not distinguish the surface determination search distance and geometry determination search distance in this table), maximum points, expand mode, etc. The most important parameters in VG algorithm were the starting contour and search distance. The starting contour determined the starting surface around which the final surface was determined within a searching distance. The starting contour was defined by voxels with a single threshold value established by the

histogram. The search distance was set as four voxels, while the term should be clear.

The weakness of VG algorithm on the non-smooth surface will be described in Chapter 6. Problems with the commonly used VG algorithm impede the uncertainty analysis due to its lack of transparency, less robustness in starting contour definition and search distance setting.

Heinzl algorithm

Heinzl algorithm sequentially applies an anisotropic diffusion filter, a gradient filter, and a watershed filter. The anisotropic diffusion filter reduces noise while preserving the specific image features, such as edges [240]. The gradient filter is employed to calculate the gradient data at each voxel by computing the directional derivative. The watershed filter segments the reconstructed data into groups based on the regional maximum gradient model to generate the edge data (for more details, see section 2.6). 'Flooding level' is controlled manually to avoid over-segmentation. However, the manual selection of the flooding level makes the Heinzl algorithm 'less robust'.

General characteristics of the local adaptive methods

Local adaptive methods have been proven to be more accurate than the global thresholding method [10, 22, 34, 46, 210]. However, some of the global methods, such as the Canny algorithm, are sensitive to noise [10]. Thus, most local adaptive algorithms employ various smoothing filters to reduce the noise effect [22, 31, 43, 210, 241, 242] and to obtain smooth surfaces, which also leads to errors associated with the operator. Korner and Staude et al. [241, 242] applied and compared several smoothing filters (e.g., 2D and 3D median filters implanted within Fiji, VGStudio and CT Pro) using the calotte cube (material: titanium alloy Ti-6Al-4V) to increase the signal-to-noise ratio and highlighted a depreciation in the resolution while applying a smoothing filter.

Some of the SD approaches have been proposed to reduce the artefact-related errors caused by beam hardening. A typical example of the study of the SD sensitivities of beam hardening was presented by several authors [43, 45, 49,

221], who demonstrated that compared with the global thresholding SD technique, local adaptive SD technique performed more effectively when addressing the ring artefact associated errors. Stolfi [243] compared seven SD algorithms: ISO50, Advanced mode, cutting out method, region growing method, histogram method, complement method and inverse method. The author applied those SD algorithms over multi-material step gauge assemblies composed of high-absorption material (hereby coded HAS) and low-absorption material (hereby coded LAS). It was found that when measuring the step gauge of all HASs, the ISO50 results deviated more than other results against the reference value; for all LASs' measurements, the differences were not as significant as the HASs' results. The author gave a possible explanation: when measuring LASs, HASs performed as the beam hardening filter, thus the difference between ISO50 and other SD results was not large; however, for HASs measurement, the LASs could not filter as effectively as what HASs did, therefore the ISO50 & other SD result differences became larger.

2.6 Watershed segmentation

The main purpose of the watershed algorithm (WA) is to segment the image (2D or 3D), which is a collection of topographic reliefs, into a series of partitions, or binarize the image [204, 205, 244-247].

To begin with, the domain of a greyscale 2D image *I* is defined as $D_I \subset \mathbb{Z}^2$. Let *G* denote an underlying digital grid and a subset of $\mathbb{Z}^2 \times \mathbb{Z}^2$, which can be any of the following types in 2D: a square grid with four pixels connected (edge neighbours – Figure 2-17: 4-connectivity) or eight (edge and vertex neighbours – Figure 2-17: 8-connectivity), in accordance with the connectivity of four or eight, respectively. Note that in 3D, the connectivity is defined around a cubic grid: six voxels connected (face neighbours – Figure 2-17: 6-connectivity), eighteen (face and edge neighbours – Figure 2-17: 18-connectivity) and twenty-six (face, edge and vertex neighbours – Figure 2-17: 26-connectivity). Hexagonal grids are possible [178], however, XCT only captures the images based on square pixels hence not discussed here.

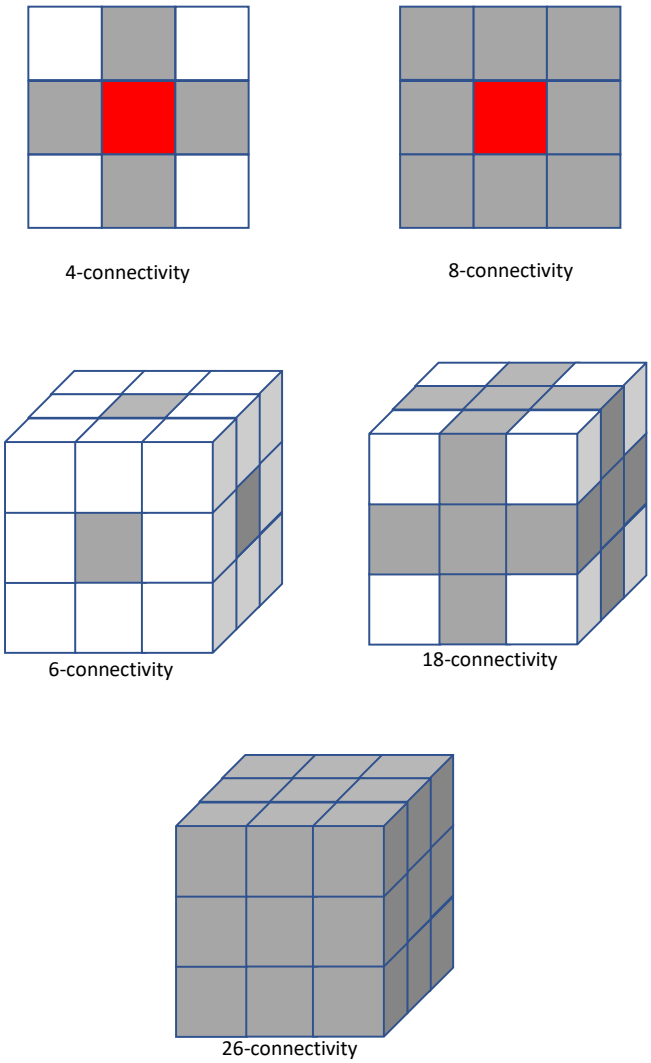

Figure 2-17: The underlying digital grid G with 4 or 8 connectivity (2D image) and 6, 18 and 26 connectivity (3D) [248]

The following definitions are fundamental in watershed segmentation.

Definition 1 [178]*: Path P with the length* $l(P)$ is the set of pixels $(p_0, p_1, p_2, \dots p_l)$ from pixel p to q, where $p_0 = p, p_l = q$, and $\forall k \in [1, l], (p_{k-1}, p_k) \in G$.

In other words, a path is a series of connected pixels or voxels that depends on the type of connectivity. Figure 2-18 provides an example of two different paths corresponding to four (only edge connected) and eight pixels connectivity (edge and vertex connected.

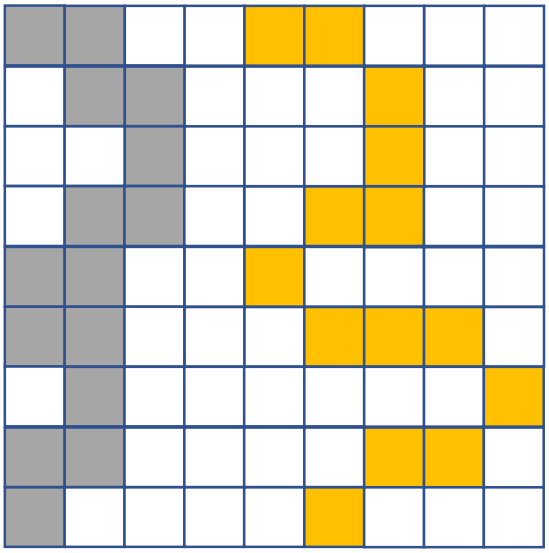

Figure 2-18: Description of paths under 4 and 8 connectivity

Definition 2 [178]*: Minimum M within I* is defined as the connected region from which the water droplet cannot reach another lower level without climbing [178]. M is a connected region characterised by a grey value (or altitude) lower than its neighbours, the region of connected pixels as darker than their neighbours (see Figure 2-19)

Definition 3 [178]*: Catchment basin C(M) associated with the minimum M* refers to the set of pixels from which the water flows down along the topographic relief and eventually reaches the minimum M. The edges separating different catchment basins are watershed lines, (see Figure 2-19).

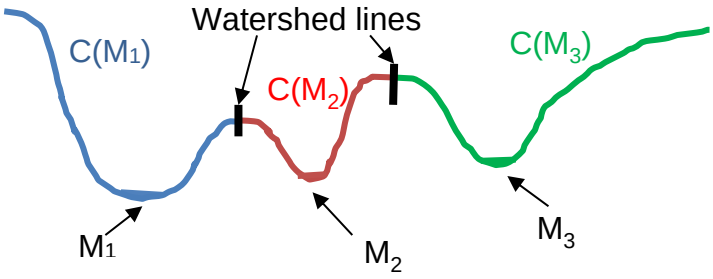

Figure 2-19: The description of minimums and the associated catchment basins and watershed lines [178]

There are two types of WA that are used to partition the image, one is based on flooding and was developed by Beucher [203, 204], and the other one is based on immersion and was proposed by Vincent [178]. All WA applied commonly in image segmentation [201], detect the regional minima and apply the flooding process. The outcome consists of a segmented region belonging to the associated minima, and the watershed edge. However, some algorithms, such as Bienick's [201], provided the segmented image without watershed edge.

Beucher [202] developed the first WA based on the immersion concept, pointing out that unlike the gradient (e.g., Canny [31] algorithm) and global threshold methods, which require the parameter of threshold(s) to define the edge, the WA is a non-parametric edge detection method. Based on the connectivity concept introduced in Figure 2-17 and Figure 2-18, the WA should provide a closed loop edge that separates the regions belonging to different catchment basins. WA segments the image and generates watershed lines, which do not belong to any catchment basins and indicates the ridge where water from different catchment basins meet.

WA is normally processed on the gradient image [186], because a high gradient value in a gradient image can indicate the edge between two regions with high grey value difference in original image, which is in accordance with the WA's process to segment different catchment basins based on immersion. A common problem with WA is over-segmentation in the presence of noise, which can increase the number of minima hence the number of catchment basins. Vincent [249, 250] successfully developed the process to transfer the image with a reduced number of catchment basins by combining it with markers, which were considered as the minimas only after transformation, and the local minimas that lead to over-segmentation were eliminated.

2.6.1 Watershed algorithm and XCT

The medical field has used WA extensively to extract the features of interests, often organs from XCT scans, and evaluate their size [251-254]. However, there are only a few studies [247, 255-261] related to the WA applied in the XCT industrial inspection of high-density materials that require higher penetration

energy, leading to additional errors, such as beam hardening. Previous studies of WA in dimensional industrial inspection [256] mainly focused on detecting freeform surface features, however, little attention was paid to WA's role in identifying the surface of the components from the XCT raw data, such as the inner features and surface texture.

[256] proved that the watershed technique could be implemented to segment the freeform surfaces of AM parts measured using XCT. However, watershed technique was used to divide the surface into a number of non-intersection regions and relied on already determined surface.

Hamdi [260] used the Threshold Curvelet to enhance the contrast of the input image, hence increasing the contrast of gradient image on which the watershed was applied. The study successfully reduced the over-segmentation problem, establishing the feasibility of Marker-controlled watershed in image segmentation. Nevertheless, Threshold Curvelet was not applied in industrial 2D or 3D XCT measurement.

2.7 Conclusion and research justification

This chapter reviewed the state-of-art XCT dimensional metrology and concluded that the influence of SD algorithms on measurement uncertainty is largely neglected in previous research. Most of the previous research used proprietary SD software, VGStudio Max, which does not provide sufficient transparency and is often treated as a black box.

In summary:

Section 2.1 reviewed the basic concepts of measurement and uncertainty, including the introduction of a new SI system.

Section 2.2 reviewed the working principle of XCT hardware, including the interaction between the polychromatic X-ray and matter, which is the main source of beam hardening. The BHC correction approach is discussed in Appendix A**.**

Section 2.3 reviewed the XCT measurement traceability in the context of dimensional metrology. This section pointed out that no comprehensive research on the influence of SD algorithms was studied for both bi-directional and surface texture measurements using XCT. This is a gap related to **Objectives 2** and **3**, and is addressed in **Chapters 4** and **5,** respectively.

Previous research related to surface texture measurement did not systematically investigate the effect of SD algorithms properly. This is a gap linked to **Objective 4** and addressed in **Chapter 6**.

Sections 2.3.2 and 2.3.3 reviewed the basic concepts and traceability of CMM and CS, respectively, which are used to provide the traceable reference value in **Chapters 5** and **6,** respectively. The re-entrant problem of CS has been identified as one of the major sources of discrepancies between CS and XCT and was addressed in **Chapter 6** by means of a morphological filter.

Section 2.5 reviewed the common SD algorithms applied in XCT dimensional metrology, including global threshold (ISO 50 [37] and Otsu [35]), and local adaptive threshold (Canny [31], VG [36], Heinzl [210]). Global threshold has been proven to be influenced significantly by artefacts related to XCT, whereas the

local adaptive method needs trial-and-error tests to reduce the noise and BHC artefacts. It was also found that user preference for parameters related to SD algorithm had a significant impact on the bias and uncertainty. Therefore, a robust threshold setting SD method is needed. This research gap is related to **Objective 1** and dealt with in **Chapter 3.**

Section 2.6 reviewed the basic concepts of image processing, as well as watershed segmentation. Previous studies [256, 262] mainly focused on using watershed method to segment surface features, including freeform surfaces. However, the ability to use watershed method to detect the surface from raw volume data, especially detecting inner features, has not been thoroughly explored. Over-segmentation is a common problem encountered by SD watershed-based methods, especially for XCT dimensional metrology. In response to these issues, the marker-control watershed (MCW) algorithm is proposed, which has been used successfully in the medical field [251, 252, 254] to extract the features of interest, often organs, and evaluate their nominal dimensions. So far, there is only few research related to the MCW algorithm applied in the XCT dimensional metrology field, which deals with the measurement of components with higher density, hence requiring higher penetration energy, leading to additional errors, such as beam hardening, not encountered with low-density objects measured at low photon energy. This is also linked to **Objectives 1,2 and 3**

3 MCW implementation

This chapter presents in detail the way in which the MCW is implemented to automate the SD for XCT dimensional application, combining the automated marker generation with voxel refinement in a transparent MATLAB script. Some of works [256, 262] discussed the use of watershed algorithm on free form surface segmentation, however, this is different from detecting the surface from the XCT volume data. This section is addressing the application of MCW in dimensional XCT metrology.

The aim of the automatic MCW process is to segment the material and provide the edge information for further geometry attribute analysis. MCW is a robust process with less input variables, which reduces the error associated with the operator. The 3D MCW process includes the following steps:

- 3D marker generation
- Gradient transformation over the 3D volume data, and the interpolation afterwards
- 3D geodesic transformation of the 3D gradient data based on the object and background markers
- 3D watershed transfer function

3.1 3D marker generation

3.1.1 Initial thresholding

The initial thresholding extracts the initial object marker. Figure 3-1-A shows the volume data to be segmented. Figure 3-1-B is the histogram of the volume data A. In the histogram there are two regions: background region on the left and object region on the right. If V_0 is set as the original volume data, then the initial marker volume data V_{I_M} is set as

$$\forall x \in [1,m], \forall y \in [1,n], \forall z \in [1,k], V_{IM}(x,y,z) = \begin{matrix} 1\ [V_0(x,y,z) \geq T] \\ 0\ [V_0(x,y,z) < T] \end{matrix} \quad \textbf{(3-1)}$$

where x, y, z denotes the coordinate of a single voxel within the volume data with the matrix size of $[m, n, k]$. T denotes the initial threshold value based on the

histogram. The initial threshold value can be estimated with the ISO50 method [34]. Figure 3-1-C presents the resultant binary volume data V_{I_M}..

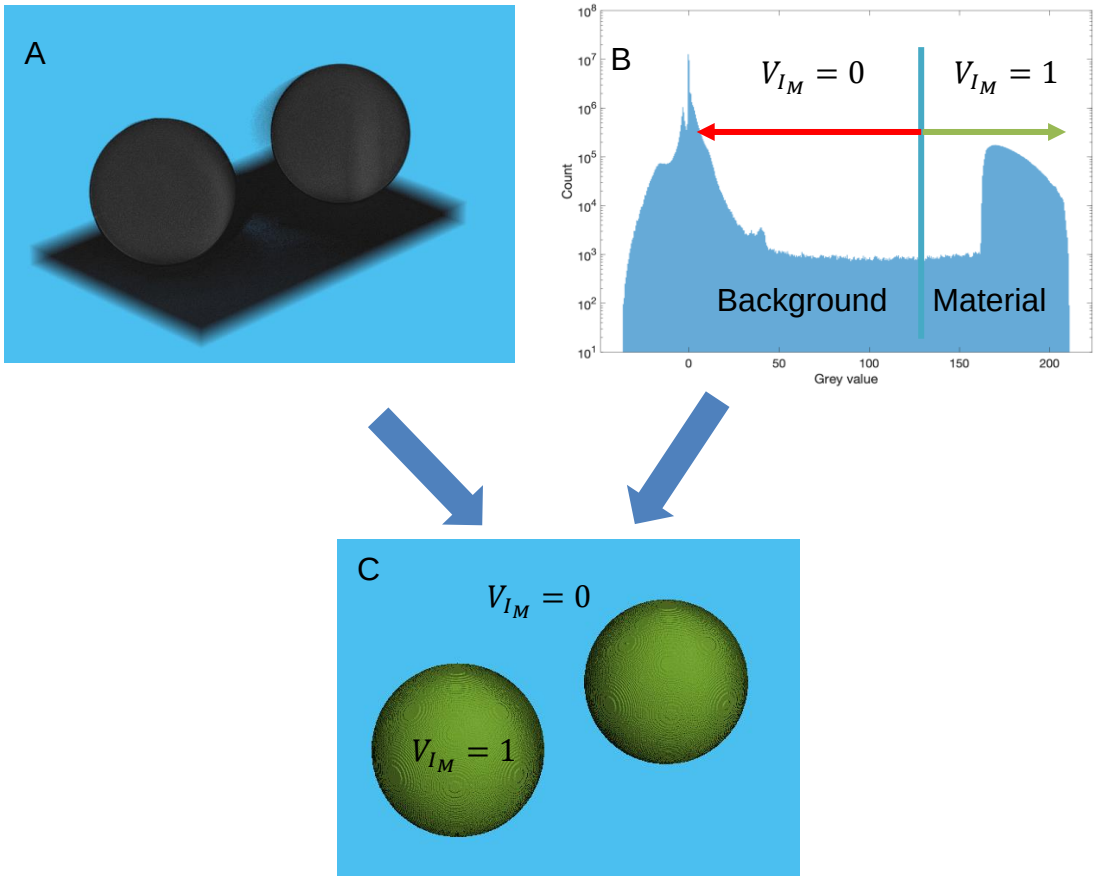

Figure 3-1: The diagram of the initial thresholding process used to generate initial object marker

3.1.2 3D Closing operation [263] of the initial marker

Imperfections in the volume data caused by the noise, cannot be eliminated after initial thresholding. However, it is essential to ensure that both the object and the background markers are continuous regions without any imperfections, like holes, for example, as it could cause unwanted edges, or, over-segmentation in watershed transformation. Thus, closing operation is needed. Closing operation for the initial marker volume data [263] is processed as follows:

$$V_{OC} = V_{IM} \bullet b = (V_{IM} \oplus b) \ominus b \qquad \textbf{(3-2)}$$

where V_{OC} is the marker volume data after closing process, b is the 3D structuring element, $\oplus$ is the dilation process and $\ominus$ is the erosion process. The closing process conducts the dilation operation followed by erosion, employing the same 3D operator b. In this case, b is a binary cube operator with the size of $N \times N \times N$, and all values are set to 1. Figure 3-2-A presents the cross section of the V_{IM} volume data, which reveals the holes within the initial object marker volume. The holes are eliminated after closing process and the closed object marker (Figure 3-2-B) is continuous without any holes inside.

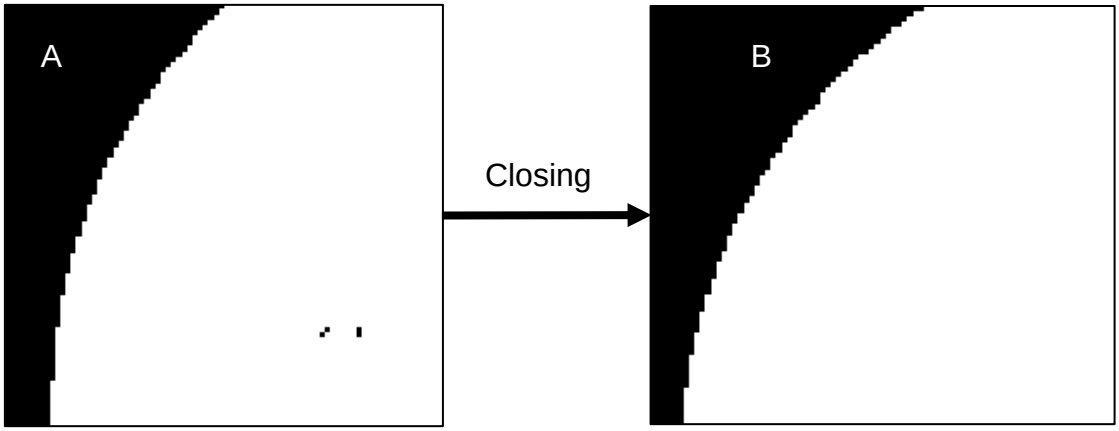

Figure 3-2: 3D closing operation to eliminate the imperfections, such as holes, within the object. Note that this is the sketch of the cross section of the volume data (white area). A. Volume data before closing; B. Volume data after closing

3.1.3 3D object marker erosion

Another requirement is that the markers cannot cover the corresponding location of the surface of the object Thus, erosion is employed to shrink the marker area. The equation is as follows

$$V_{OC}^{e} = V_{OC} \ominus c \qquad \textbf{(3-3)}$$

where V_{OC}^{e} is the volume data after erosion, and c is the 3D structuring element to operate erosion. Like structuring element b, c is also a binary cube data with $N \times N \times N$ of volume size. In this case, c can be the duplicate of b. Figure 3-3 shows that the erosion result for c is the $20 \times 20 \times 20$ ($N = 20$: A, B, C & D) binary matrix with all values of the object marker shrinks compared with the

marker before erosion, and V_{OC}^{e} does not overlap with the proposed MCW surface. As is shown in Figure 3-3, the marker size decreased by around 17 voxels when *N* = 20; while under $N = 40$, the marker shrunk by approximately 30 voxels. It is crucial to note that besides shrinking the marker, erosion can eliminate the scattered markers that are not connected with the object marker to avoid MCW over segmentation, but this is not indicated in this figure. The critical factor N controls the size of V_{OC}^{e} and should be carefully selected. If N is too large, V_{OC}^{e} could disappear; otherwise, if N is too small, the marker could be extremely close to the proposed surface and cause an error in watershed transformation. In most cases, $N = 20$ is appropriate but it should be adjusted according to the object size.

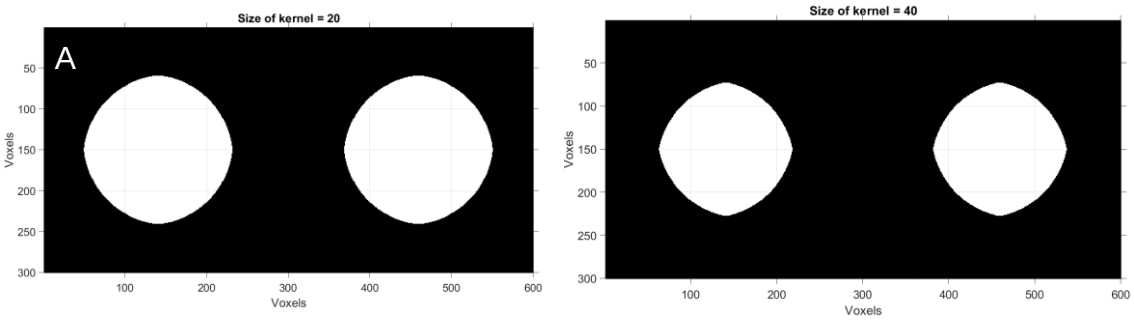

Figure 3-3: The volume data after erosion while N = 20. B. The volume data after erosion while N = 40

3.1.4 Creation of 3D background marker

Firstly, V_{BM} , the complement of the binary object marker after opening (V_{OC}) is created – 0 becomes 1 and 1 becomes 0.

Then, closing and erosion are applied on the V_{BM} as follows:

$$V_{BC} = V_{BM} \bullet b = (V_{BM} \oplus b) \ominus b \quad \textbf{(3-4)}$$

$$V_{BC}^{e} = V_{BC} \ominus c \quad \textbf{(3-5)}$$

Figure 3-4 shows the 3D background marker of V_{BC}^{e}. The background marker (white area) does not cover the proposed MCW surface.

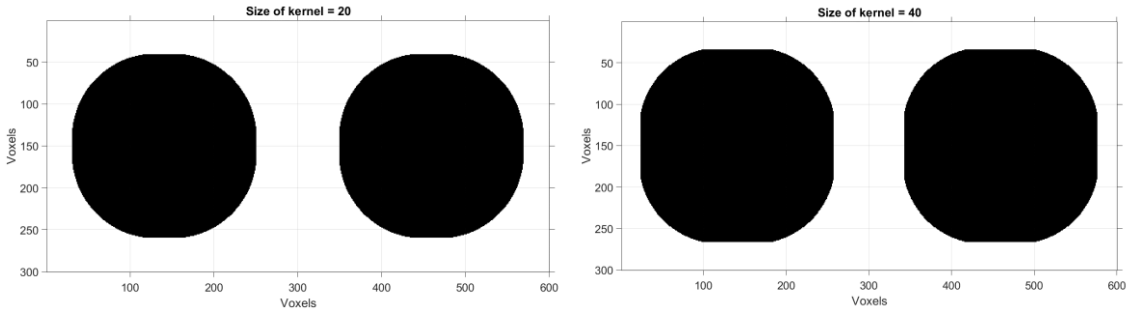

Figure 3-4: 3D background marker (V_{BC}^{e}, the white area in this image) after complement, closing and erosion process.

3.1.5 Combination of the object and background marker

In the final stage of marker generation, the algorithm generates the final marker matrix with the combination of the object and background marker defined as follows:

$$V_{BOM} = V_{OC}^{e} \vee V_{BC}^{e} \tag{3-6}$$

Hereby ∨ is the 'OR' operator symbol. It means that for voxels with the same location within V_{BOM}, V_{OC}^{e} and V_{BC}^{e}, 0 is given for V_{BOM} if both the corresponding V_{OC}^{e} and V_{BC}^{e} are 0; otherwise, it is 1. Or written as

$$\forall x \in [1,m], \forall y \in [1,n], \forall z \in [1,k], V_{BOM}(x,y,z) = \begin{matrix} 1\ [V_{OC}^{e}(x,y,z) OR\ V_{BC}^{e}(x,y,z) = 1] \\ 0\ [V_{OC}^{e}(x,y,z) AND\ V_{BC}^{e}(x,y,z) = 0] \end{matrix} \tag{3-7}$$

The volume data of V_{BOM} is displayed in Figure 3-5. Markers are shown in white colour (value is 1). It has the background marker and two object markers, and all of the markers are continuous without any holes within them. The black area is the corresponding gap region between markers, and within the original volume data, regions with the same location as the black regions are for surface detection. As **Figure 3-5-B** shows, the MCW surfaces (the blue line) are entirely located within the black region.

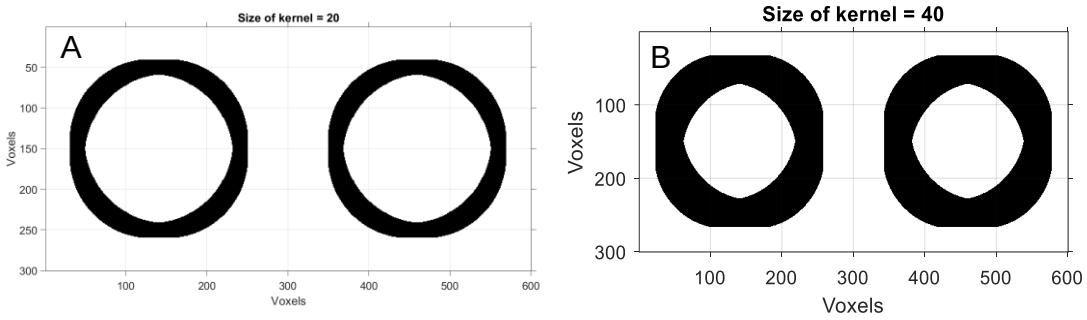

Figure 3-5: The combination of the 3D object and background marker (V_{BOM}). A. with size of a kernel of 20. B. size of a kernel of 40.

3.2 Gradient transformation

The gradient transformation employs the 3D Sobel operator [264] to transfer the original 3D volume data to gradient data. The Sobel operator is a matrix with a size of $3 \times 3 \times 3$. Considering that the volume data is associated with the coordinate system with X, Y, and Z axis, the Sobel operator in Z direction is:

$$G_{z1} = \begin{bmatrix} 1 & 3 & 1 \\ 3 & 6 & 3 \\ 1 & 3 & 1 \end{bmatrix}, G_{z2} = \begin{bmatrix} 0 & 0 & 0 \\ 0 & 0 & 0 \\ 0 & 0 & 0 \end{bmatrix}, G_{z3} = \begin{bmatrix} -1 & -3 & -1 \\ -3 & -6 & -3 \\ -1 & -3 & -1 \end{bmatrix} \quad \textbf{(3-8)}$$

Figure 3-6 shows the gradient volume data, hereby noted as V_G.

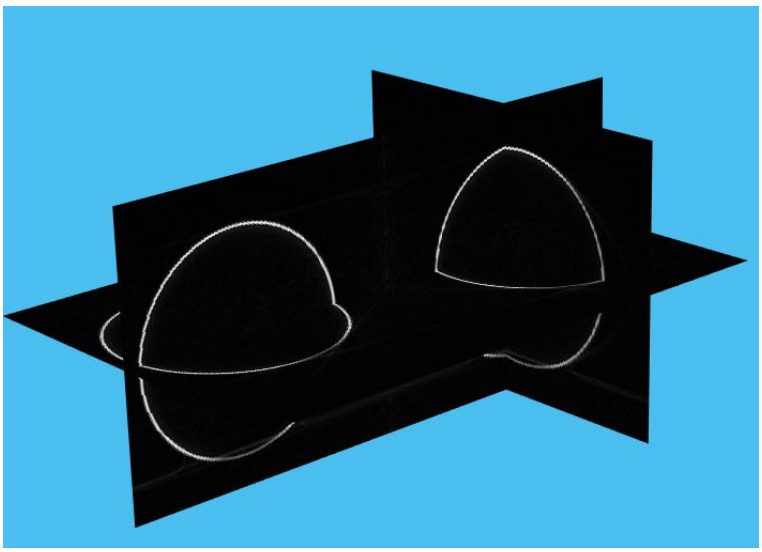

Figure 3-6: The volume data after gradient transformation using the Sobel operator

3.3 Geodesic transformation

To overcome the over-segmentation problem, a geodesic transformation [204] was applied to the gradient image produced at step 2 to reduce the number of minima [204] as a result of noise. The geodesic transformation process is illustrated in Figure 3-7. The black dash box marks the size and position of the marker; blue solid and green dash lines indicate the original plot (*f*) and geodesic transferred plot (*f'*), respectively. All the data points within the black dashed regions in Figure 3-7 were set to negative infinite, indicating the regions of minima.

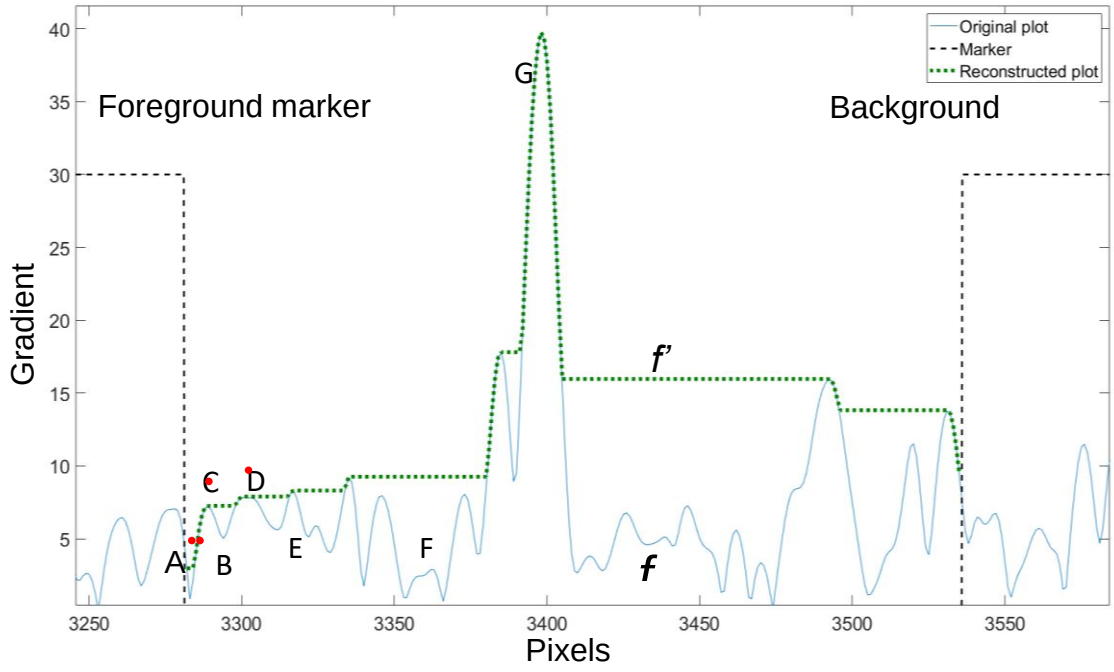

Figure 3-7: The geodesic transformation. The rectangular black dash box indicates the position and size of markers; solid blue plot indicates the original plot (*f*); green dotted plot (*f'*) indicates the plot after geodesic transformation from f

Starting from point A, which is the point of intersection between the boundary of the left-hand side marker and the line *f*, the geodesic transformation draws the line *f'* to point B, which has the same altitude as point A but is on the opposite side of the valley. The line *f'* takes the same values as *f* until the original plot reaches the peak point C. From point C, the line *f'* maintains the same value until it reaches point D at the opposite side of the valley. Concurrently, the same

process is started from the background marker and then moves towards the left. The line *f'* starts from the foreground marker boundary and goes up until point G in the graph, where it joins the plot started from the background marker. Thus, the line *f'* contains only the regional minima whose locations overlap with the markers' location. All other regional minima in the line *f* disappear, *i.e*. the valleys E and F will not be seen in the final line *f'*.

In the 2D range, Figure 3-8 describes the comparison of the 2D gradient image before and after geodesic transformation in topographic relief. Markers, or the local minima, are labelled to describe that, after geodesic transformation, the regions labelled by markers are assigned a negative infinite value. Before the geodesic transformation, there are numerical local minima within the topographic relief. After geodesic transformation, local minima are reduced to the region labelled by markers in the previous step, while all other pre-local minima regions are replaced by the plains. In other words, in topographic relief, every droplet in a random location within a catchment basin (e.g., the green dashed region in the figure on the next page) related to the local minima can flow to the local minima region without the need to climb up a hill.

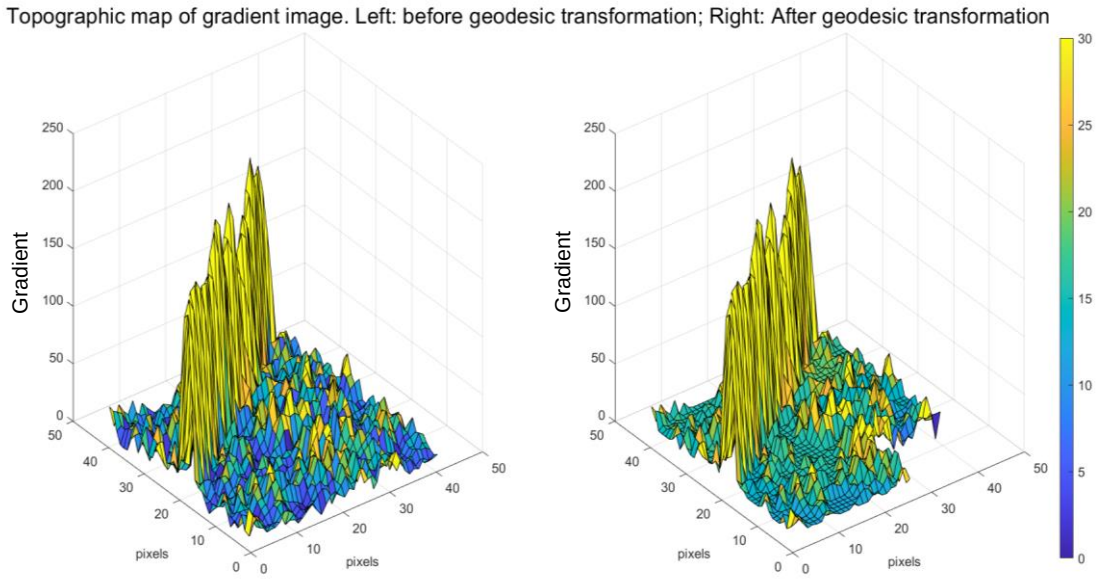

Figure 3-8: Topographic map of gradient image: Left: before geodesic transformation; Right: After geodesic transformation

Based on the above description, Meyer F [265] simply demonstrated the way to extend most transformations from 2D to 3D, including erosion, dilation, distance transformation and geodesic transformation. Here, MATLAB function *imimposemin(V_G, V_{BOM})* was used to calculate the gradient volume data. The voxel connectivity was set to 6.

3.4 Watershed transformation over gradient volume data with geodesic transformation

Finally, 3D watershed transformation [265, 266] was applied with 6 connectivity, which is the same connectivity setting as 3D geodesic transformation. Figure 3-9 displays the watershed results. The original volume data is segmented into three regions corresponding to background and two spheres. When referencing the marker volume data shown in Figure 3-5, it is intuitive to observe that the function of the marker volume data is to label the regions to be segmented within 3D MCW algorithm process. The black line is the 3D MCW surface, whose coordinate is extracted and generates the 3D point cloud data, as presented in Figure 3-10.

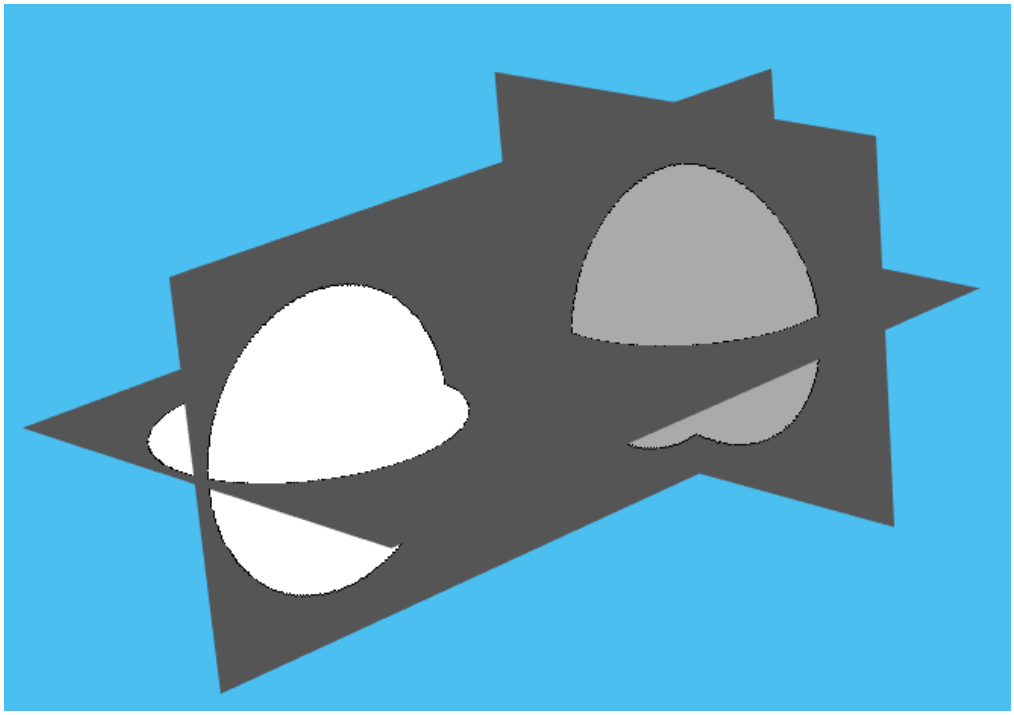

Figure 3-9: The watershed segmentation volume data

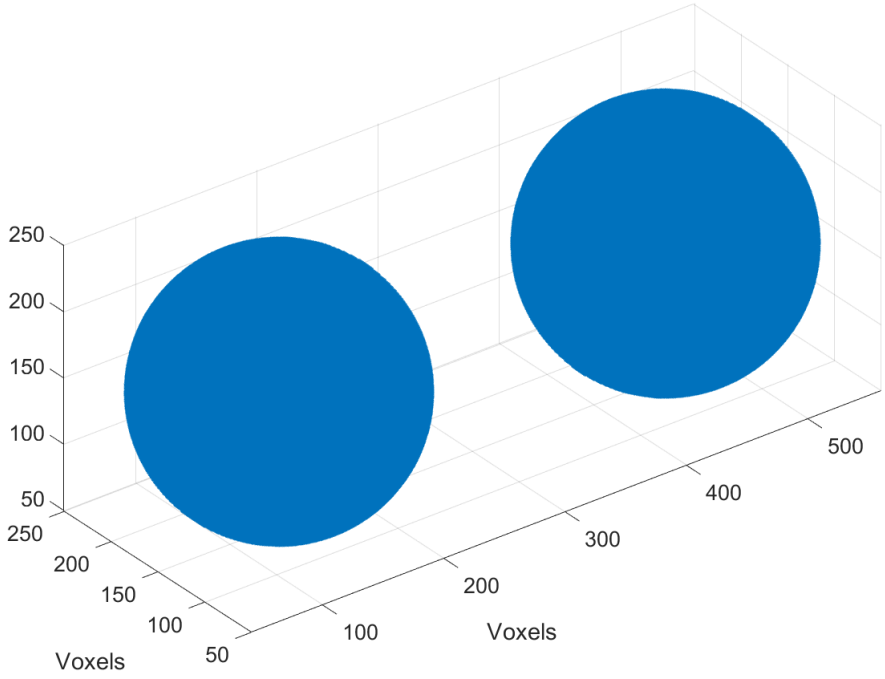

Figure 3-10: The point cloud data of the 3D MCW surface

Based on the point cloud data, further analysis, including geometry attribute determination, measurement and surface texture analysis can be performed, which will be discussed in the next section.

3.5 Voxel refinement

Sub-voxel refinement is based on the weighted algorithm used in [29]. For a single point cloud coordinate of $[i, j, k]$, the following equation was performed to obtain the refined coordinate of $[X'_{i,j,k}, Y'_{i,j,k}, Z'_{i,j,k}]$.

$$X'_{i,j,k} = \frac{\sum_{i-2}^{i+2}(X_{i,j,k} \times G_{X_{i,j,k}})}{\sum_{i-2}^{i+2} G_{X_{i,j,k}}},\ Y'_{i,j,k} = \frac{\sum_{j-2}^{j+2}(Y_{i,j,k} \times G_{Y_{i,j,k}})}{\sum_{j-2}^{j+2} G_{Y_{i,j,k}}},\ Z'_{i,j,k} = \frac{\sum_{k-2}^{k+2}(Z_{i,j,k} \times G_{Z_{i,j,k}})}{\sum_{k-2}^{k+2} G_{Z_{i,j,k}}}$$

where $G_{X_{i,j,k}}$, $G_{Y_{i,j,k}}$, $G_{Z_{i,j,k}}$ are absolute grey values of 3D gradient volume data on X, Y and Z directions for a surface point of $[i, j, k]$. This is the example for the kernel size of five.

4 Preliminary MCW results – 2D bi-directional measurement case

The work presented in this chapter has been published in NDT&E [3].

Here MCW is validated for the 2D case using both simulation and experimental data considered. The next section presents details about the exact methodology and methods used. Section 6.3 presents summary results and analysis of the effects of beam hardening and noise on the MCW surface, along with a discussion of the effect of markers selection and interpolation ratio. The last section, 6.4, provides a summary and conclusions, and signposts the future work.

4.1 Methodology

A 3D CAD model of a stacked cylinders sample was used to study the effect of MCW on 2D bi-directional measurements and subsequently compared with Canny and VG Studio. Similar to previous studies that used calibrated objects [32, 34, 37, 43, 45, 267], the design of the reference sample, presented in Figure 4-1, consists of cylinders with the following characteristics:

- The outer cylinder radius of the smaller tube is equal to the inner cylinder radius of the larger tube, allowing comparison of the results for inner and outer features,
- the reference sample has a simple structure with symmetry around the vertical axis [268], and
- the material considered is aluminium.

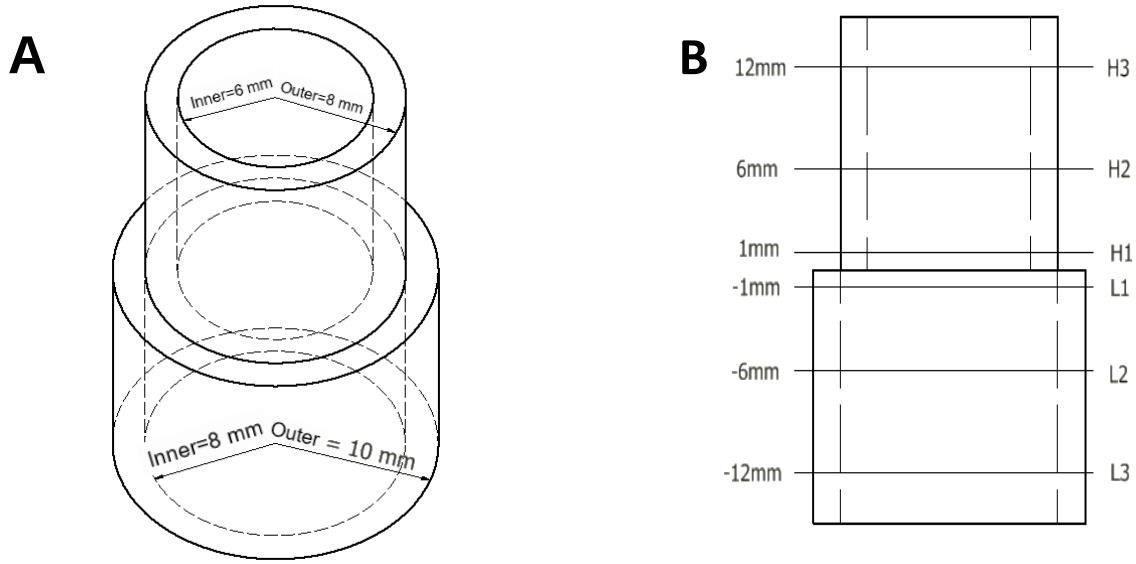

Figure 4-1: The overlapped tube reference sample: A. The drawing of radius of the CAD model B. Positions of 2D cross-section images considered along the vertical axis

The radii of each cylinder were determined at three positions (L1 to L3 and H1 to H3 in Figure 4-1-B). The least square circle fitting method (Pratt method) [269] was used here.

This study used simulated XCT projections to evaluate the quality of the MCW algorithm and investigate the influence of various parameters. The XCT projections of the reference sample were simulated using a commercial software package aRTist 2.10.4 [125], which is based on ray-tracing method. The parameters of simulations listed in Table 4-1 are commonly used in experimental work.

Table 4-1: Settings of simulation.

Voltage kV	Current µA	Number of projections	Magnification	Voxel size in µm	Multi-sampling
100	80	3143	8	25	3x3

This study considered three sets of XCT simulations:

- Set 1: Monochromatic scan, *i.e*. without beam hardening and noise, etc.
- Set 2: A scan that accounted for beam hardening (polychromatic) effects without noise;

- Set 3: A scan that included the effects of both beam hardening and noise.

To mimic experimental results, the signal-to-noise ratio of a real system has been studied. The XCT system considered is a Nikon XT H 225M cone beam system with a reflection target. The noise of the instrument has been evaluated, ranging between (75 to 150) kV and (60 to 100) µA, respectively. The signal to noise (SNR) ratio is shown in Figure 4-2. For 100 kV and 80 µA, the value of the SNR is approximately 155, which was subsequently used in simulations. It should be noted that this work did not consider scattering, as there is only slight scatter effect when X-ray penetrates aluminium.

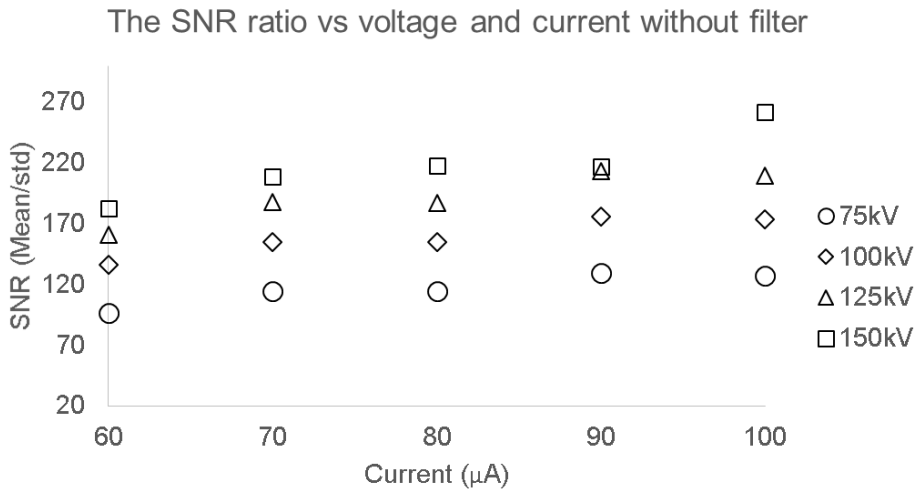

Figure 4-2: The signal-to-noise ratio (SNR) of the projection without any objects under different voltages and currents

The simulation projections were reconstructed with Feldkamp, Davis and Kless (FDK) algorithm [19] using CT Pro 3D version 5.4. For sub-pixel resolution purpose, a spline interpolation algorithm was used to subdivide the voxel in three interpolation ratios 0.1, 0.2, 0.5. $p = 1$ denotes that no interpolation was conducted before applying the watershed. In the case of $p = 0.1$, each voxel was subdivided into 100 voxels using spline interpolation.

For comparison with the MCW algorithm, a MATLAB [270] function that implements the Canny algorithm was used in this work to segment the 2D cross-section of reconstructed data. The *threshold* input variable is a two-element vector [*low, high*] which takes values in the range of [0,1] and is used to establish

the final edges. The *low* value provides the threshold below which all edges are discarded (weak edge) while the *high* value is the threshold above which all edges are preserved (strong edge). To ensure that all defined (strong) edges are connected, the edges situated between these two threshold values are labelled as strong edges if they are connected with a strong edge pixel and discarded otherwise. The *low* and *high* values are set by the operator using a trial-and-error method, as there are still no robust methods for the selection of the threshold input variable.

4.2 Monochromatic and polychromatic XCT measurement regime.

The results for monochromatic and polychromatic tests are shown in Figure 4-3. The errors (ε) were displayed in pixels to show the error relative to voxel size. For monochromatic (simulation set 1, no beam hardening) and polychromatic (simulation set 2, with beam hardening) cases, at $p = 0.1$. The errors are calculated as the difference between the measured radius and the nominal radius defined in the CAD model.

The monochromatic case shows that there is little difference between the ouput of the MCW and Canny algorithms, which demonstrates that both algorithms are equally effective in ideal measurement conditions. It is important to note that the error of the radii fitted to the inner and outer cylinders have different sign and magnitude, approximately + 0.4 % and – 1.1 % of pixels, respectively.

Compared with monochromatic results, the beam hardening effect had a marginal effect on the radius of the inner cylinders (less than 0.02 % of the error), which corroborates with the work of Lifton [43] and Villarraga-Gómez [23]. However, for the outer cylinders, the difference between monochromatic and polychromatic measurement results are as large as 3.3 % of pixels, which suggests that during the reconstruction process the beam hardening effect significantly altered the value of the pixels surrounding the edge of outer cylinders. It appears that the grey value can vary with different material thickness, but this assumption needs further attention.

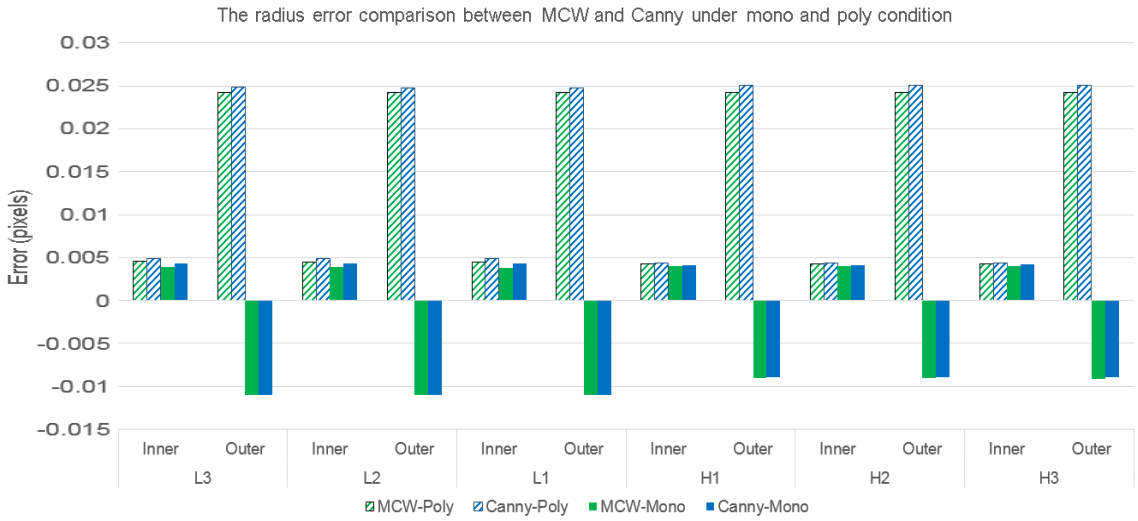

Figure 4-3: The error of radius for simulation set 1 (benchmark, monochromatic, no beam hardening) and simulation set 2 (polychromatic, beam hardening), noise factor = 0, Interpolation ratio p = 0.1, mean radius value and error bars are based on five individual MCW and Canny applications over five slices within the range of ± 10 layers around each benchmark (L3-H3) layers.

Figure 4-4 presents MCW results for polychromatic (dashed line) and monochromatic (solid line) X-ray spectrum effects of the measurement of the external cylinders. The results for polychromatic case, *i.e.* beam hardening, agrees with Villarraga-Gómez [23] findings, which concluded that the beam hardening shifts the surface point clouds of the external surfaces toward the background side. This explains the differences between radii calculations of the inner and outer cylinders in different XCT measurement conditions, that is to say, monochromatic and polychromatic.

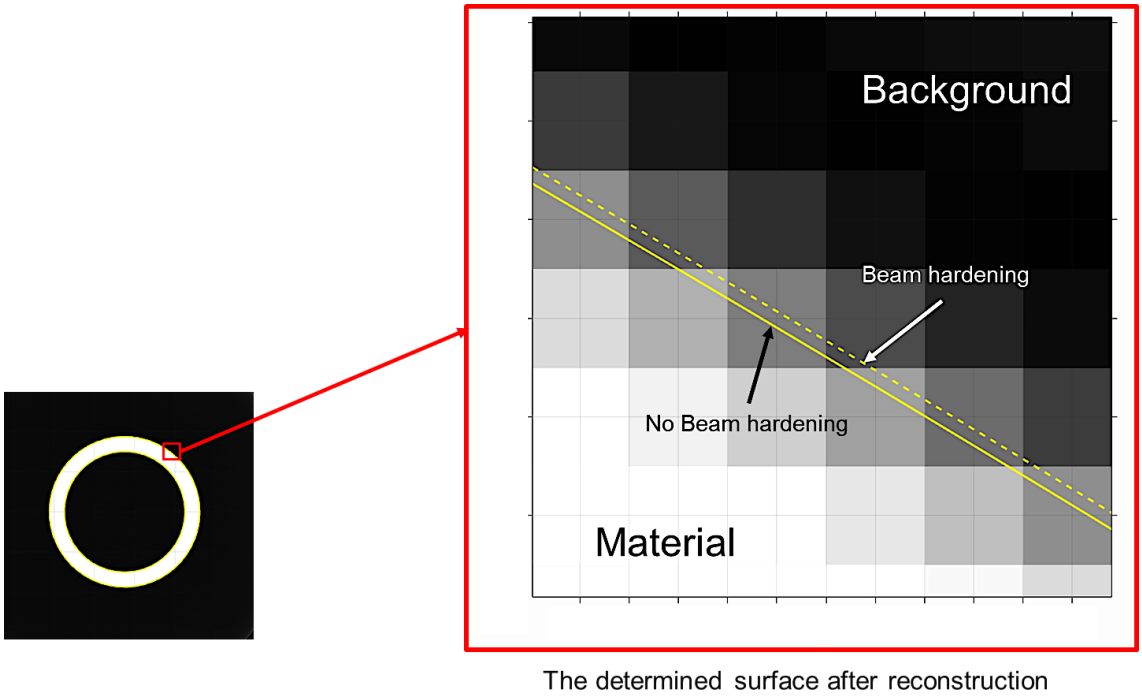

Figure 4-4: The surface determined with watershed algorithm for the comparison of simulation with beam hardening (dash line) and without beam hardening (solid line) conditions

4.3 Noise effect

Figure 4-5 allows comparison of the surface point cloud distribution without (left) and with (right) noise at $p = 0.1$. The solid red line represents the surface based on nominal data. In both cases, the MCW algorithm generated closed surfaces with no scattered points. In the absence of noise (Figure 4-5-E) the surface's point cloud remains within ± 10 % of the pixel away from the nominal data, whereas in the presence of noise (Figure 4-5-F) the point cloud errors from the nominal ranges within ± 20 % of the pixel size. This suggests that noise affects the gradient image, which consequently alters local maximum grey values detected by the watershed algorithm. The geodesic transformation eliminates most of the local minima in the gradient image and reduces over-segmentation, however, the magnitude and x and y position of the gradient maxima could still be affected by noise.

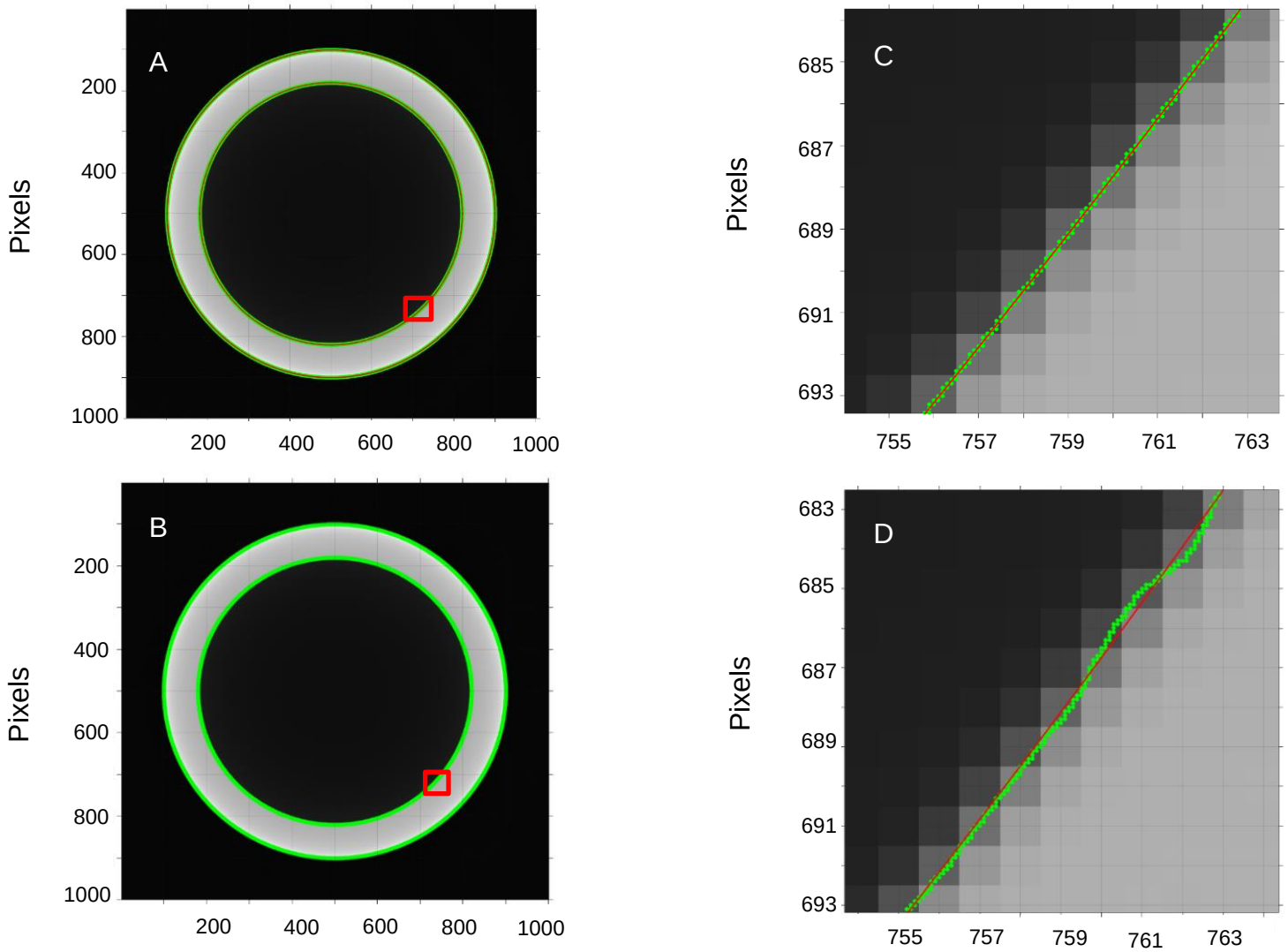
A
B
C
D
Pixels
Pixels
Pixels
Pixels
200
400
600
800
1000
200
400
600
800
1000
685
687
689
691
693
755
757
759
761
763
683
685
687
689
691
693
755
757
759
761
763

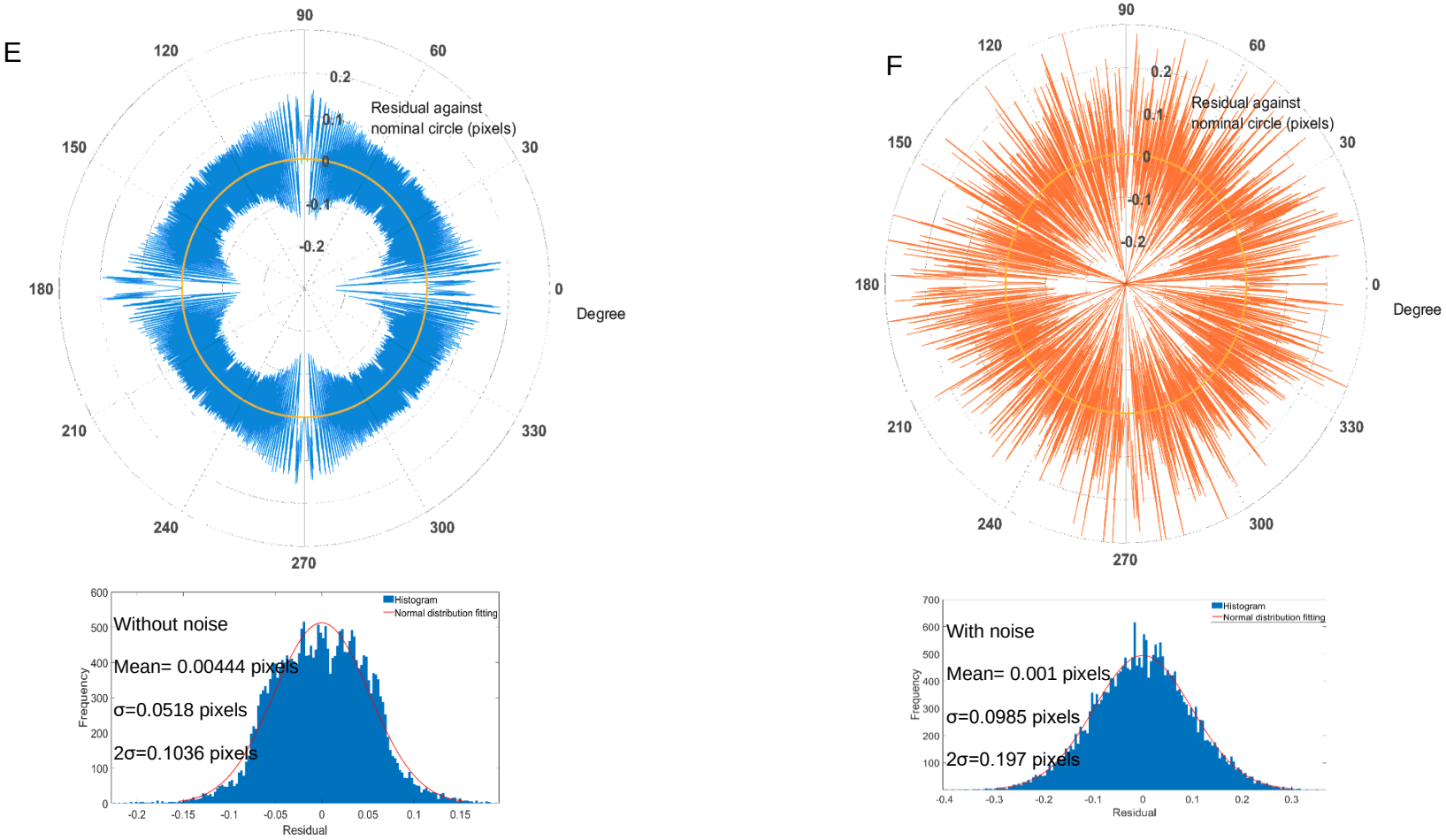

Figure 4-5: Surface point clouds determined by MCW under simulation set 2: Polychromatic. Left column: Without noise. Right column: with noise. Slice height index: L2, Interpolation ratio p = 0.1. The corresponding polar plot and the histogram of the residual (in pixels) are shown in E (without noise) and F (with noise)

The error chart presented in Figure 4-6 indicates that the mean radii of the inner cylinder measured with and without noise do not deviate by more than 0.5 % of pixels from their nominal size and the mean radius error of the outer cylinder is approximately +2.5 % of pixels. The standard deviation associated with the radius measurement of the inner cylinders of the tube is larger than the results on the outer cylinder. Whilst the outer diameter measurement results are affected by a larger bias, a better overall measuring accuracy of the inner diameters is observed.

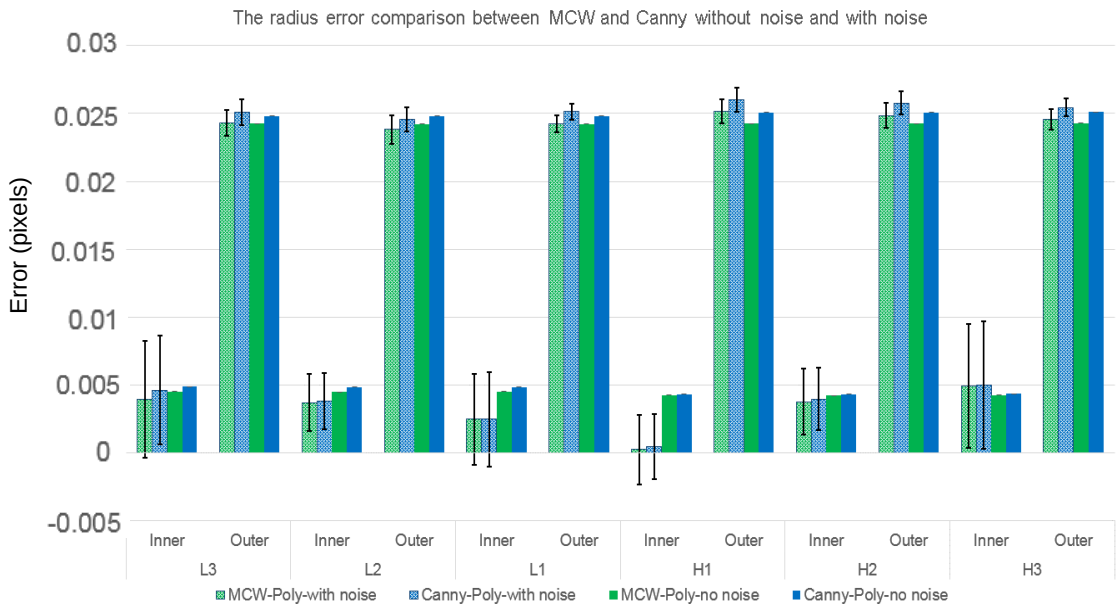

Figure 4-6: The radius error result for simulation set 2 (SNR = inf) and simulation set 3 (SNR = 155), polychromatic, Interpolation ratio p = 0.1, mean radius value and error bars are based on 5 individual MCW and Canny applications over 5 slices within the range of ±10 layers around each benchmark (L3-H3) layers. Error bars indicate the standard deviation for each radius value

4.4 Influence of marker size and position

According to Figure 4-7 C and D, both automatic [270] and manual MCW method generated closed surfaces. Comparing Figure 4-7 A and B, both methods have the following typical results:

- There is only one maker that labels the foreground.

- As the background is divided into two parts by the foreground, two markers label the background.
- Each marker is entirely within the range of the proposed segment: none of the marker intersects with the proposed watershed surface.
- The markers do not contain any gaps.

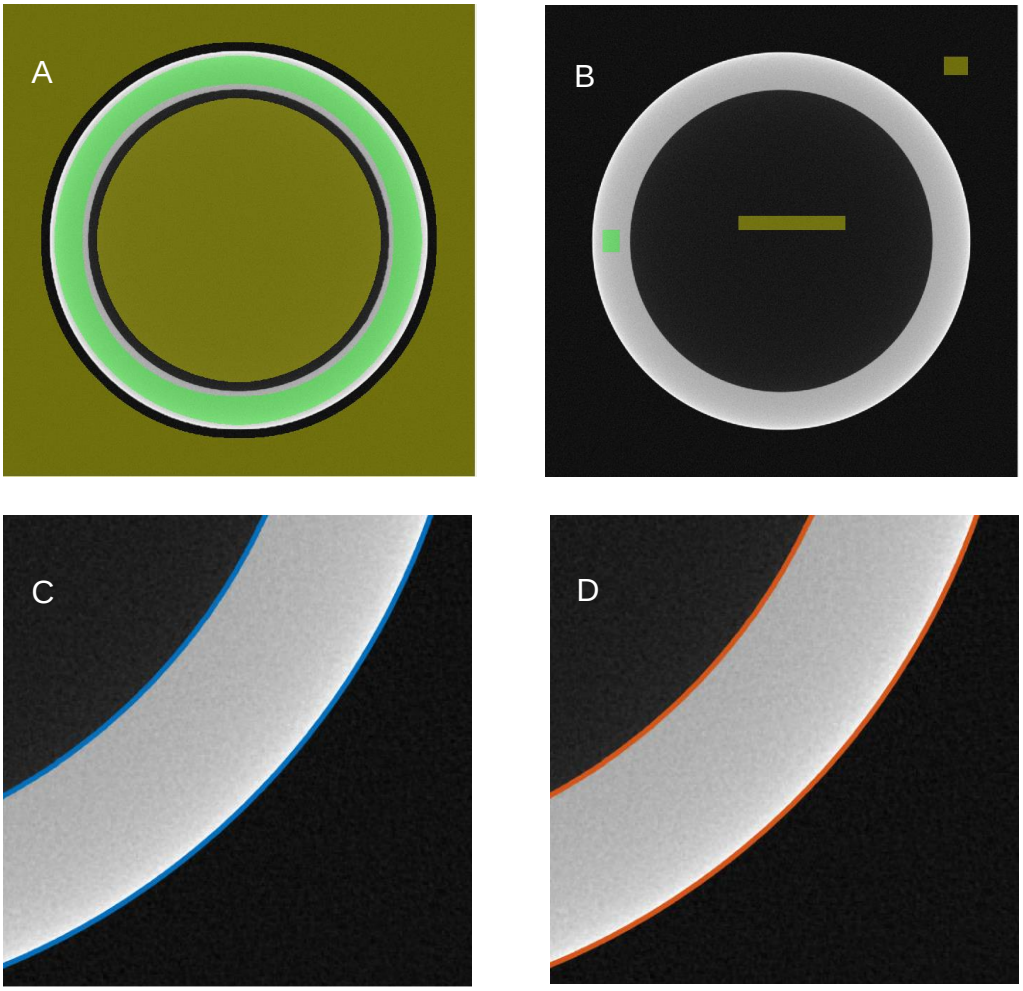

Figure 4-7: A. Markers by auto-selection; B. Watershed surface based on the geodesic transformed representation with auto-selected markers; C. Markers by random-selection; D. Watershed surface based on the geodesic transformed representation with randomly selected marker

However, differences in computational time are significant. Table 4-2 describes the computational time of the MCW algorithm in comparison to the Canny and ISO50 methods. According to Table 4-2, computing time based on manual selection was six times longer than the automatic selection. Smaller markers resulted in larger areas to assess during the geodesic and watershed transformations, increasing the computing time. Compared with the ISO50 algorithm, which only searches the pixels with the pre-defined single threshold value, the MCW's computation time drastically increased due to multiple image computations: marker generation, interpolation, gradient transformation, geodesic transformation, etc. Also, the Canny algorithm computation time is only

half of the automatic watershed. This study is yet to optimise the watershed computation time, and future work is mentioned in conclusion.

Table 4-2: The comparison of computing time with different marker-selection methods (based on 0.1 interpolation ratio). The processor was Intel Xeon CPU E5-2630 v2 2.60GHz

SD algorithms	Computing time (s)
Automatic MCW	32
Manual MCW	193
ISO 50	1
Canny	15

4.5 Influence of interpolation ratio

Figure 4-8 depicts the voxels sounding a portion of the outer cylinder surface from which outer cylinder was calculated and the point cloud associated with the cylinder surface at different interpolation ratios. Figure 4-9 shows the residual plots against the nominal circle at different interpolation ratios. Without interpolation, as $p = 1$, the radius calculations were affected by errors as large as 0.7 of the size of the pixel. For $p = 0.1$, most of the estimated surface points were distributed within a narrow band from the CAD data. Furthermore, the residuals against the nominal circle decreased, as evidenced in the polar plots presented in Figure 4-9. A common feature of the polar plots for all p levels was that the lowest residual errors were recorded at multiples of 90º on the polar plot, which correspond to pixel directions.

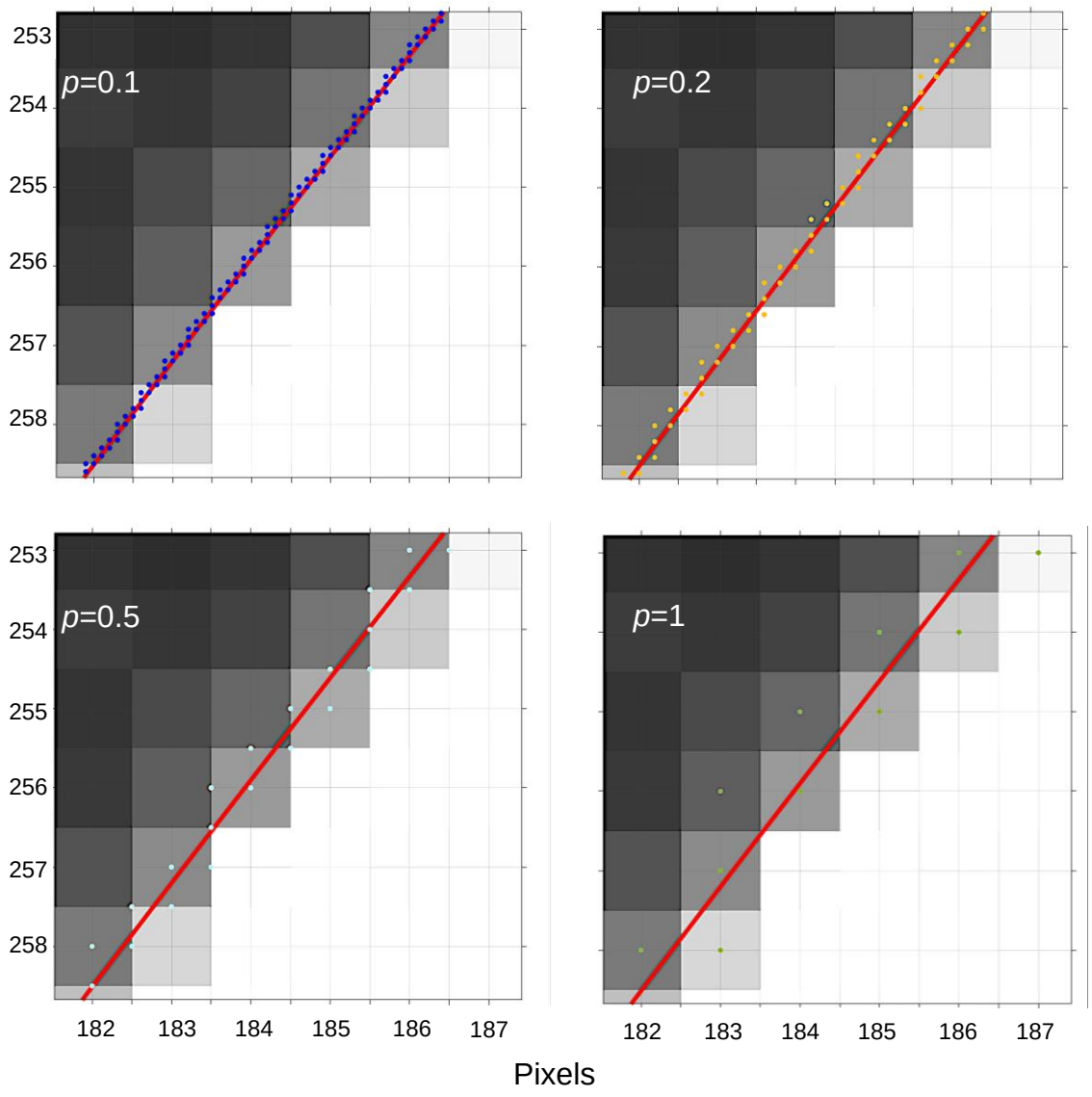

Figure 4-8: Surface point clouds determined by MCW under simulation set 2: Polychromatic, no noise. Outer Circle; Slice height index: L2, Interpolation ratio p = 0.1 (blue dot), p = 0.2 (orange dot), p = 0.5 (cyan dot) and p = 1 (no interpolation, green dot), red line = nominal circle

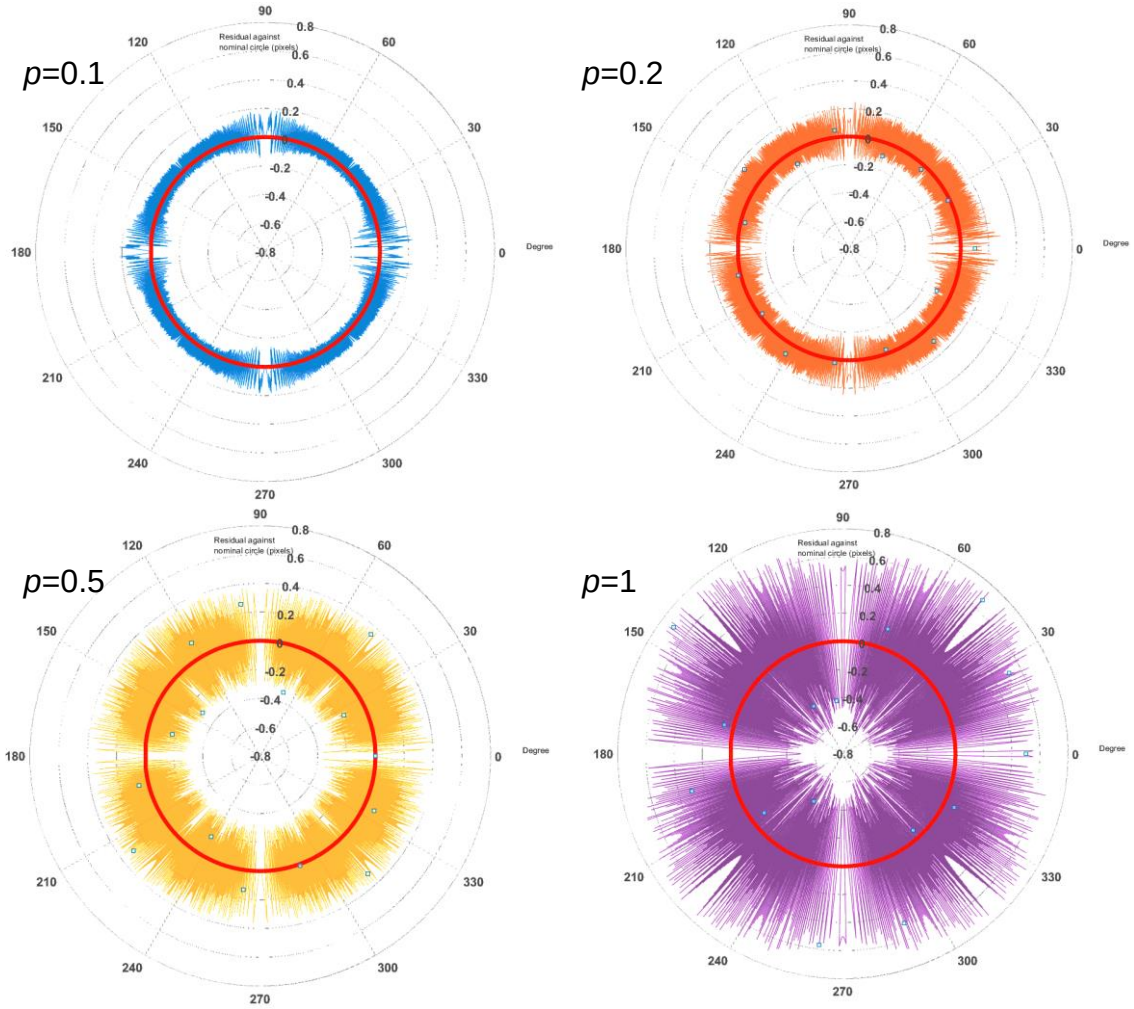

Figure 4-9: The polar plot of the residual of point cloud calculated by MCW algorithm at four different interpolation ratios. Simulation set 2: Polychromatic, without noise. Outer Circle; Slice height index: L2. Solid red line is the nominal circle

Figure 4-10 shows the relationship between the interpolation ratio *p* and root-mean-square deviation (RMS) value of the residual of the point clouds against the fitted circle. Decreasing *p* value (increasing interpolation ratio) reduces the standard deviation associated with circle fitting.

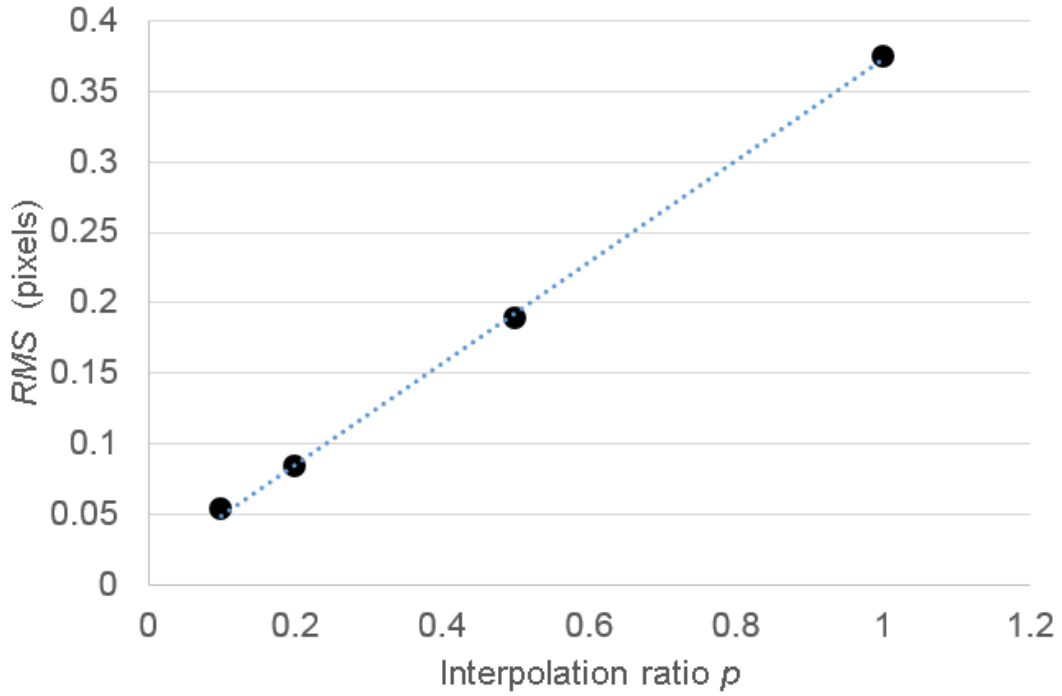

Figure 4-10: The scatter plot of the relationship between p and RMS of the residual against fitted circle, Simulation set 2: Polychromatic, without noise.

Figure 4-11 presents the mean radius errors and the associated standard deviations for different interpolation ratios and measurement conditions, *i.e.* with and without noise. The worse results were recorded for $p = 1$, meaning that the bias was significant without interpolation.

Excluding $p = 1$ case, for the inner cylinder, the best results calculated from the data without noise were obtained at $p = 0.2$. In polychromatic case, without noise and $p = 0.2$, the bias of the internal radius measurement did not exceed 0.4 % of the pixel size, but the outer cylinder radius bias was as large as 2.5 % of pixel size. The radius of the outer diameter was not significantly different for $p = 0.1$ and $p = 0.2$.

According to Figure 4-10, increasing interpolation resolution (lower p) can reduce the RMS of point cloud residuals. However, the errors of inner cylinders' radii at $p = 0.1$ for H1, H2 and H3 were larger than the bias recorded at $p = 0.2$ and 0.5. This result shows that the interpolation process can introduce additional errors.

As expected, the standard deviation of the measurement results that include noise effects were found to be larger than the one for the simulations without noise. The standard deviation associated with the inner cylinder measurements was significantly larger than the one associated with outer diameters, suggesting that the interpolation algorithm can cause additional systematic errors.

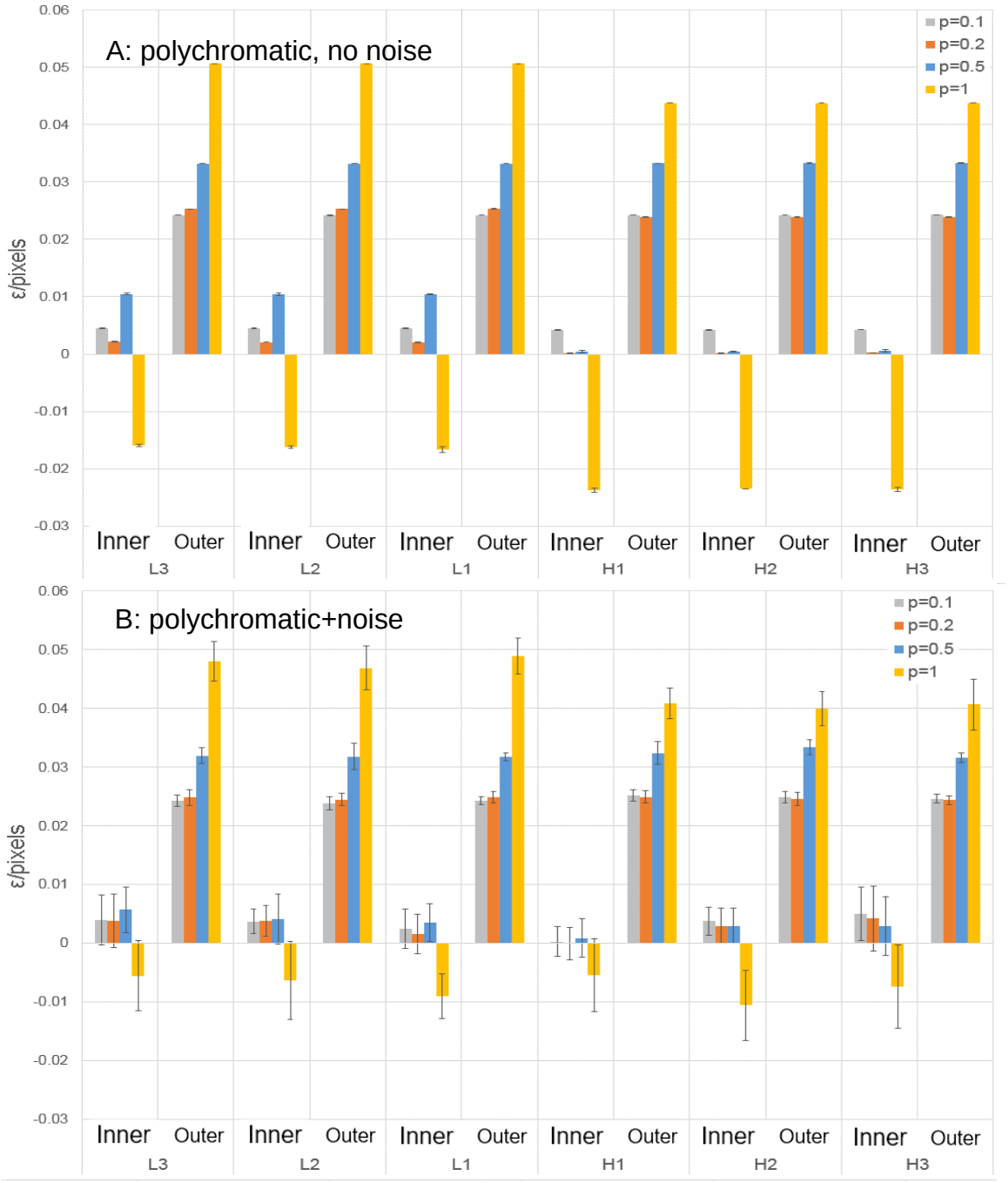

Figure 4-11: The radius deviation of fitting circle against the nominal radius value under different interpolation ratio p value: A. Simulation set 2, polychromatic, with noise; B. Simulation set 3, polychromatic, SNR = 155. Mean radius value and error bars are based on five individual watershed surface applications over 5 slices within the range of ±10 layers around each benchmark (L3-H3) layers. Error bars indicate the standard deviation for each radius value

4.6 Additional considerations

Figure 4-12 shows the comparison of the determined edges that are calculated by automatic MCW and the Canny algorithm. The Canny algorithm implementation can lead to different edge positions, which is also dependent on the selection of the thresholds. The Canny algorithm was run four times before achieving a clean edge for a *threshold* vector of [0.3 0.4]. [0.05 0.1] threshold settings lead to noisy edges, [0.2 0.9] only detected the outer circle edge, [0.7 0.9] detected half of the outer edge, [0.4 0.5] could establish the outer edge but lead to an intermittent inner circle edge, demonstrating that the selection of *threshold* values significantly impacts the edge result of the Canny algorithm.

In contrast, MCW computed a closed edge within a single trial. The foreground marker and the background marker were selected automatically. The watershed transformation segmented the geodesic transformed gradient image into partitions (material and background) whose edges are strictly closed. The result shows that the MCW can potentially be applied as an automated SD algorithm that does not require an educated input from the operator, hence reducing any associated operator errors.

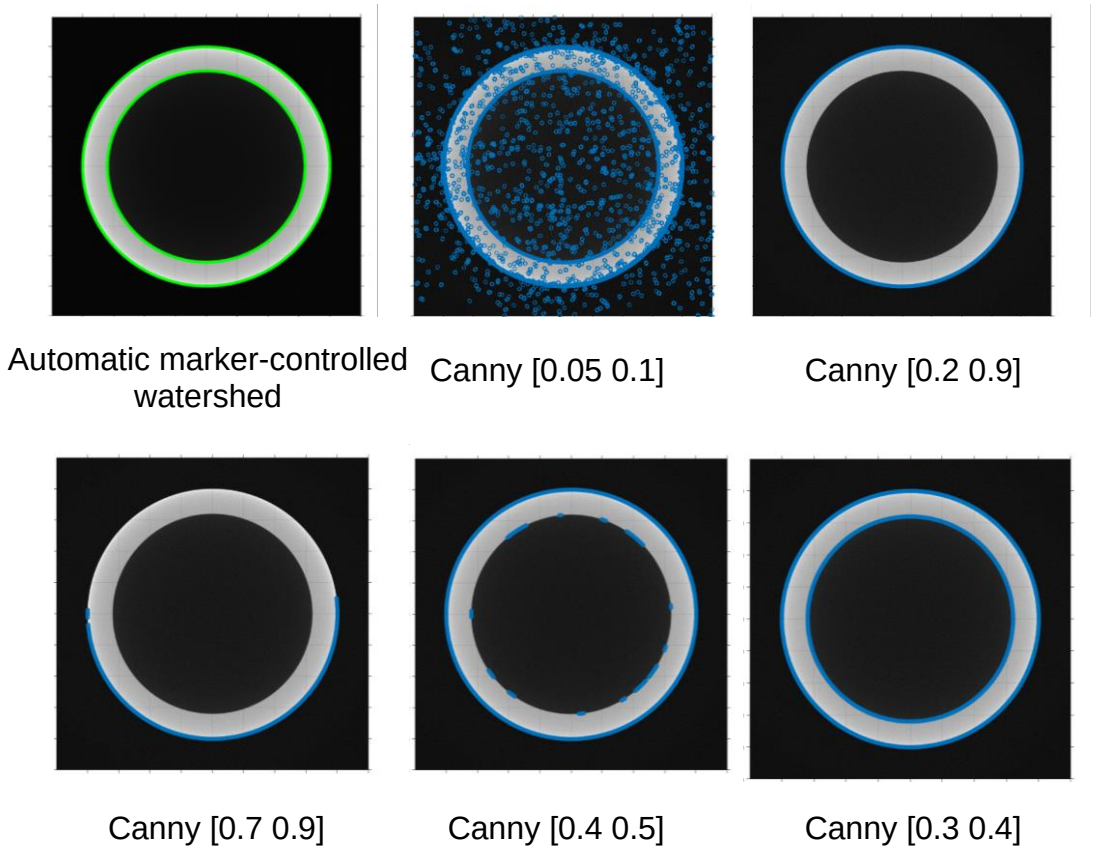

Figure 4-12: The edge determined using automatic marker-controlled watershed and Canny algorithm. The number in the square brackets indicate the threshold in the canny edge determination algorithm in MATLAB, and each number is within (0,1). The image is acquired under the CT simulation with noise

Despite the issues related to threshold selection in the Canny algorithm, the results presented until this point show that both methods, Canny and MCW provide equivalent results. This is because the surface of the object used in this research resembles an ideal situation, which is rarely met in practice. The difference between the MCW and Canny becomes visible when applied to real measurements of objects that are characterised by complex surface textures as shown in Figure 4-13 and Figure 4-14. Compared to the Canny algorithm, which generates disconnected edges nearby severe measuring artefacts, MCW

successfully provides only closed edges surrounding the feature of interests.

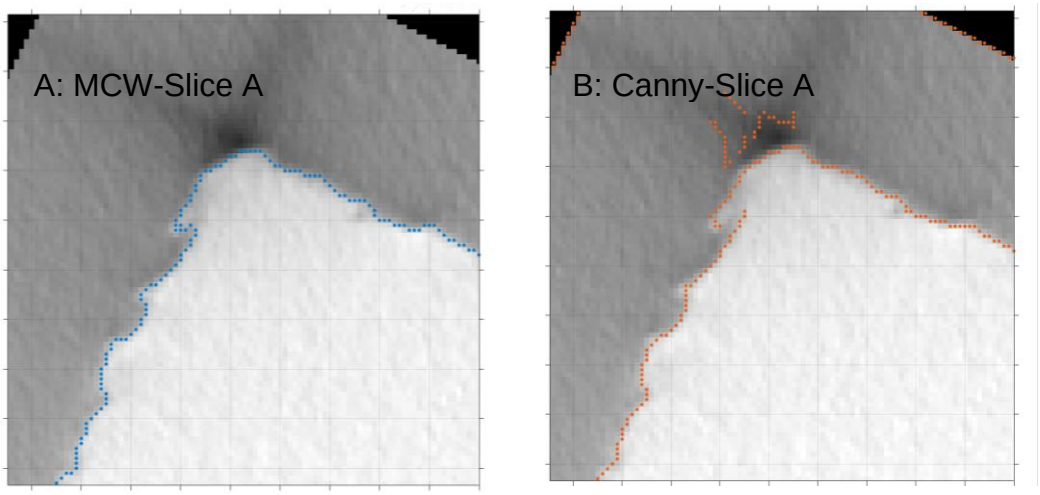

Figure 4-13: The comparison between 3D MCW and 3D canny surfaces for surface roughness analysis over the experimental reference sample

To conclude, Figure 4-14 presents the MCW results applied on the real measurement of the two spheres, introduced in Figure 1-4 is an example of 'streak' artefacts effect, highlighting once again the MCW resilience to common XCT measurement errors.

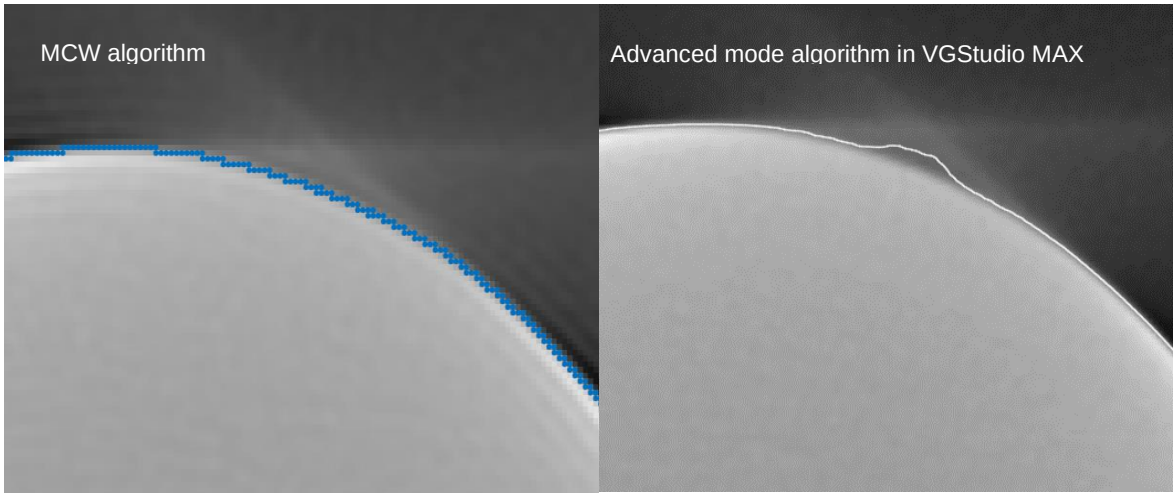

Figure 4-14: The comparison between the MCW and 'advanced mode' in commercial VGStudio software in dealing with 'streak' artefact caused by beam hardening

4.7 Conclusion

In summary, it has been identified that SD algorithms play an essential role in XCT measurements [20]. This chapter has addressed some of the issues encountered with the SD process: algorithm transparency, operator induced errors and the ability of the SD algorithms to avoid the effect of the noise and beam hardening that can lead to false edges. In order to reduce the operator's errors, an automatic SD algorithm based on the MCW algorithm that eliminates the over-segmentation issues has been proposed and evaluated for XCT inspection of samples with smooth and rough surfaces.

To recap, the MCW algorithm consists of four steps: marker selection; gradient transformation; geodesic transformation; watershed transformation. The main points to highlight here are:

- The foreground and background markers are determined automatically by combining the closing and erosion operators. Closing operator eliminates the small hole within the marker to avoid subsequent over-segmentation and erosion shrinks the marker area so that markers do not overlap with the pixels adjacent to the edges.
- The geodesic transformation removes the unwanted regional features present in the gradient image, which can lead to false edges.
- The watershed transformation produced a clean and closed surface without significant errors.

In conclusion, it is demonstrated that the MCW is an effective SD algorithm for XCT metrology and inspection purposes using simulations and a reference sample. Additionally, it was found that that:

- Compared to the Canny algorithm, the MCW algorithm can effectively provide closed inner and outer edges and avoids the errors attributed to the operator. At the same time, the MCW algorithm is easier to use compared to the Canny algorithm because it does not need to find the optimal thresholding conditions using 'trial and error' tests.
- Both automatic and manual marker selections lead to the same edge data.

- Interpolation is necessary to achieve sub-pixel (or sub-voxel) surface point clouds, however, there are no significant improvements below $p = 0.2$.
- At $p = 0.2$ and in polychromatic measurement conditions, the radius of the external cylinder is affected by an error that can be as large as 2.5 % of a pixel compared to 0.4 % in the case of the inner cylinder.
- The noise leads to twice as large residual errors associated with the circle fitting of the external features than the ones reported for the inner features (0.5% and 0.25% of pixel size, respectively).
- The geodesic transformation only eliminates most of the local minima that can lead to false edges.
- The MCW algorithm outperforms the Canny algorithm when used to determine the surface of measured objects with complex surfaces. Applied on real XCT measurements, MCW generated the closed edges around the feature of interests and the results were not affected by the surrounding measurement artefacts such as in the Canny algorithm case.
- Compared to commercial VG algorithm, MCW demonstrates resilience to common XCT measurement errors such as ‘streak’ artefacts.

5 Evaluation of the effect of SD algorithms on bi-directional measurements (smooth surfaces)

Chapter 4 demonstrates that, in comparison to Canny and VG, MCW can reduce the noise and eliminate operator factor in 2D. However, the 3D data poses additional challenges, such as algorithms implementation, computer memory and processing time. For example, the interpolation, which was introduced to obtain sub-pixel location of the surface, did not require a large amount of memory even for an interpolation ratio of 0.1, whereas the 3D interpolation with the ratio of 0.1 on the double-precision volume data of 500x500x500 requires the memory of 1TB. Hence, another approach to obtain the surface with sub-voxel refinement is required.

This chapter evaluates the effect of MCW, Canny and VG algorithms on the 3D bi-directional dimensional measurements. To this end, SD provides a point cloud, that is used to evaluate the dimensional conformity of the measured components [154], similar to measurement strategies originated from CMM [10]. Unlike the industry-accepted and traceable CMM measurements, the XCT measurement traceability is not established mainly because the effect of influencing factors, such as beam hardening, noise, SD, system stability, operator factor, *etc*., on the 3D point cloud is not rigorously investigated. Previous research only used the XCT point cloud affiliated with desired geometry [20, 37, 43, 100, 151, 154, 221, 234, 236, 271-274] and did not investigate the uncertainty associated with the position of each data point. As a result, some data affected by beam hardening and other errors, inevitably resulted in dimensional measurement deviations. Therefore, it is essential to evaluate the effect of the errors affecting the accuracy of the point cloud to distinguish the influence of the SD algorithms on any dimensional measurement.

Positional uncertainty of the point clouds has been investigated by multiple authors [94, 275-278], but not in the XCT context. All the previous examples imply that there is an urgent need to evaluate the point cloud error and uncertainty regarding XCT dimensional measurement.

The novelty of this work consists in the way SD algorithms are optimised and compared in the bidirectional dimensional measurement context.

The work methodology, including the measurement and simulations conditions, and the SD algorithms optimisation is presented in the flowing section. The results and discussions are covered in section 5.2. Section 0 summarises and concludes the chapter.

5.1 Methodology

In terms of investigating the influence of SD algorithms, the XCT measurement of a two-sphere sample and equivalent simulations were conducted. Each dataset was processed under VG, Canny and MCW with different parameter settings. The simulations were used to evaluate the effect of SD algorithms in well-defined conditions, which are practically impossible to control in a real measurement.

5.1.1 Measurement

For the experimental study, the two-sphere sample [76, 213, 279-281] shown in Figure 5-1 was used. The CMM calibrated values of the diameters of the spheres and of the unidirectional distance between the spheres are presented in Table 5-1. Two-sphere reference samples have been previously used to evaluate the performance of XCT and the uncertainty associated with instrument misalignment, and to derive error corrections [74, 78, 140, 211, 237, 242, 279, 282]. The distance between the centres of two spheres, a unidirectional measurement, was used to conduct the voxel calibration, which is essential in the adjustment and calibration of the sensitivity of the scales of the XCT [154, 227, 233]. The benefit of unidirectional measurements rests in their ability to minimise the effect of the errors introduced by the surface determination, and material effects, such as beam hardening [154, 227, 233].

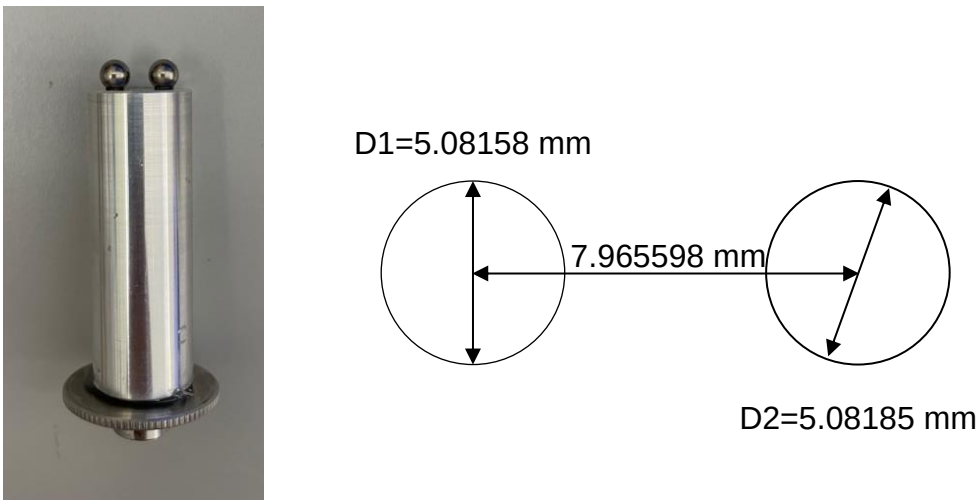

Figure 5-1 The two-sphere reference sample, and the drawing of the two sphere

Table 5-1 The reference data of the two-sphere reference sample calibrated using the Zeiss F25 CMM with a standard uncertainty 50 nm (k = 1) [76].

Sphere 1 diameter (mm)	**Sphere 2 diameter (mm)**	**Unidirectional distance (mm)**
5.081580	5.081850	7.965598
CMM std (nm)	**CMM std (nm)**	**CMM std (nm)**
1	3	6

The sample was measured by a Nikon XT H 225M instrument using the scanning parameter shown in Table 5-2.

Table 5-2: The experimental scanning parameter of the two-sphere sample

Voltage kV	**Current µA**	**Number of projections**	**Magnification**	**Voxel size in µm**	**Filter**
160	100	3142	8	25	0.5 mm Cu

5.1.2 Simulation scanning

A two-sphere phantom reference, shown in Figure 5-2, with the dimensional characteristics listed in Table 5-1, was used in simulations. The CAD file of the phantom reference was generated using aRTist V2.1.0, which is a radiographic

simulation software that simulates the full CT scan with controllable parameters including: voltage, current, noise, material, sample position, etc. [125]. The CAD model of the two-sphere phantom reference had 556,110 triangles.

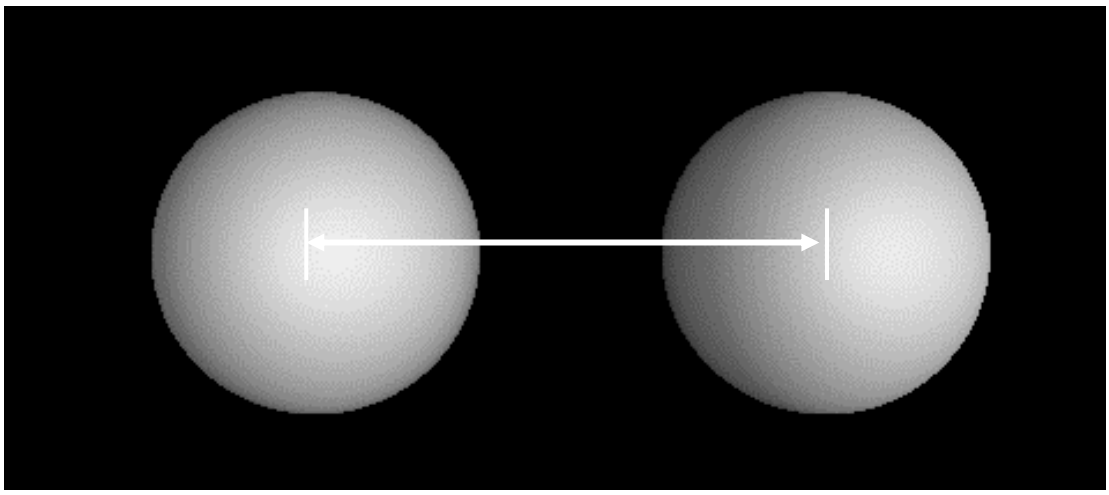

Figure 5-2 The two-sphere CAD model

The simulation input file was a mesh data file of the sample. The mesh surface consists of a set of faces that share edges, or a group of vertices which are connected by edges. A comprehensive review discussing the elements of 3D mesh surfaces is provided in ref. [262].

The parameters listed in Table 5-2 were used for simulations. [283], however, unlike the experimental scanning, the simulations can depict the effect of the spectrum and noise on the SD results separately. Hence, six sets of XCT simulations were considered and shown in Table 5-3. Like the experimental work, the number of projections was set as 3142 over the total rotation angle of 2π. Simulation set 5 fully replicated the XCT experimental scanning conditions.

Table 5-3: Simulation conditions

Trials	Spectrum type	Noise level	Cu filter
1	Mono	0	0
2	Poly	0	0
3	Poly	1.05	0
4	Poly	0	0.5 mm
5	Poly	1.05	0.5 mm

The output projection file type was ‘.tif’ format with 16bit, and each projection image had a resolution of 2000 × 2000 pixels, equivalent to the parameters introduced in the Detector settings user interface.

Lastly, the field correction was enabled to simulate the shading correction process in the experimental CT machine, which is used to eliminate the ghost shadow on the detector from the previous scanning.

For the dataset of Trial 5, the beam hardening correction (BHC) was conducted as described in Appendix A.

5.1.3 Reconstruction

The projection images from both measurement and simulations were reconstructed using the CTPro 3D Version XT 5.4, developed by Nikon Metrology, to get the volume data. The noise reduction and BHC were disabled to test the ability of the SD algorithms to overcome noise and beam hardening effects. The output of the reconstructed volume data included only the information of two spheres, consisting of 700 × 300 × 300, which was trimmed from the original size of 2000 × 2000 × 2000. The output files were exported in VGSTUDIO MAX 3.2.5 project file format, ‘.vol’ file, with a size of 246 MB, and then the data was loaded in MATLAB 2019b for the SD step.

5.1.4 SD implementation

Along with MCW, the other two SD algorithms used in this work were Canny and VG. In all three cases, the operator can influence the results in the thresholding operation stage. To avoid potential errors, here the VG Studio was optimised using a Taguchi scheme. Canny used nine trials using different two-array thresholding settings. The initial threshold and size of struct element for morphological closing and erosion were considered in the MCW implementation.

I VG

VGStudio [284] SD process starts by directly opening the ‘.vol’ file [23, 34, 150, 211, 212]. In the first step, the user sets the initial threshold by selecting a random region of interest within the background and material regions from the

measurement histogram, as shown in Figure 5-3. Note that the VGStudio also has available an automatic starting contour determination, but often the artefact can introduce significant errors, hence not used in this study.

Then the user sets the searching distance and decides whether to use or not the *iterative surface determination* mode.

A summary of the parameters that can be altered during VG studio SD implantation and their potential values are presented in Table 5-4. Here, the Taguchi method, implemented in Minitab software [285], was used to optimise the VG Studio output. The SD process was repeated eight times, with a summary of the trials given in Table 5-5

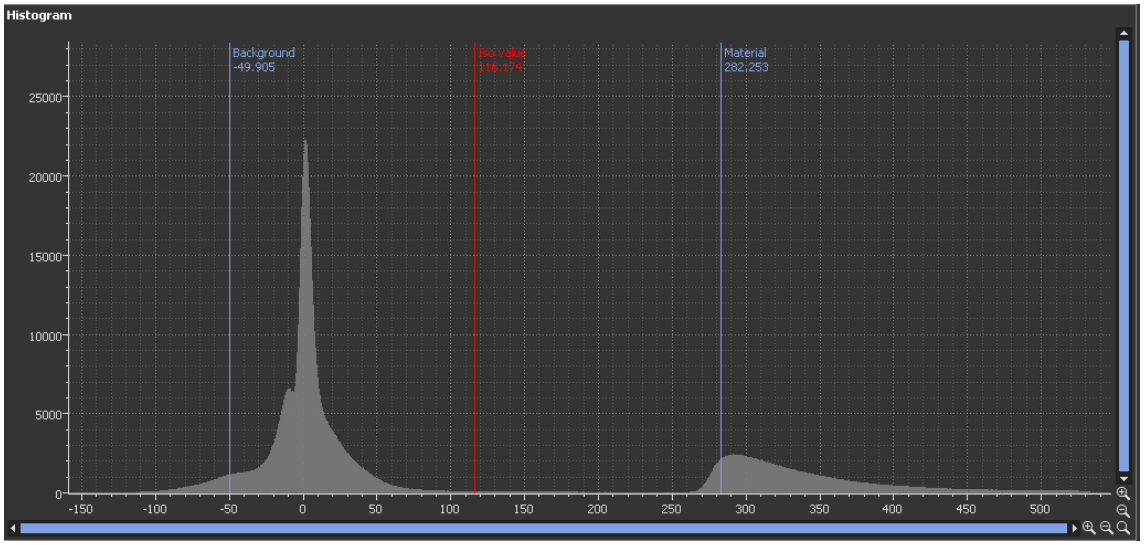

Figure 5-3: The histogram and initial thresholding settings within VGStudio MAX 3.2.5 [284]

Table 5-4: The control parameters and levels for VG

	Levels	*1*	*2*	*3*	*4*
A	Voxel search distance	2	4	10	20
B	Background selection	Away from edge	Close to edge		
C	Material selection	Away from edge	Close to edge		
D	Iterative surface determination	On	Off		

Table 5-5: Taguchi orthogonal array for VG

Trials	Parameters			
	A	B	C	D
1	1	1	1	1
2	1	2	2	2
3	2	1	1	2
4	2	2	2	1
5	3	1	2	1
6	3	2	1	2
7	4	1	2	2
8	4	2	1	1

ii *3D Canny*

Canny algorithm was commonly discussed and used by many researchers [22, 154, 213, 225]. Here, Canny algorithm was implemented in MATLAB using the in-built function of '*BW=edge3(V, 'approxcanny', thresh)'*. The edge3 function returns the edges found in volume data *V* by looking for the local maxima of the gradient of *V*. The threshold value, which consists of *lower* and *upper* values within the range of [0 1], can directly affect the results. There were nine trials used in this work that had different threshold options presented in Table 5-6.

Table 5-6: The threshold settings for 3D Canny algorithm

Trials	Low threshold	High threshold
1	0	0.2
2	0.2	0.4
3	0.4	0.6
4	0.6	0.8
5	0.8	1
6	0.1	0.6
7	0.3	0.9
8	0.1	0.4
9	0.5	0.9

iii MCW

The main factors that can be changed in the 3D MCW are the structuring elements for closing and erosion transformation. For the volume data representing single homogeneous material, the initial threshold can be simply determined using the ISO50 value in the histogram. For cubic morphological structing element for closing and erosion transformation, the size was set as 20

and 40 in one dimension, respectively. Four trials have been implemented in this work with different parameters, which are described in Table 5-7

Table 5-7: Parameter setting for 3D MCW algorithm

Trials	Initial threshold	Structing element size
1	ISO50	20
2	ISO50	20
3	Material Peak	40
4	Material Peak	40

5.1.5 Radius calculation

In VG, the radius calculation was performed using build-in functions, the sphere determination module. The error threshold was set as 0.15 mm, with two iterative processes, to exclude the surface points beyond the error threshold.

For MCW and Canny, the radius was calculated in MATLAB R2019b using a least square fitting algorithm [286].

5.2 Results and Discussions

Figure 5-4 presents the summary (mean radius errors) of the measurement and simulation results. The standard deviation associated with the residual of the point clouds related to Canny and MCW algorithm is 2 µm.

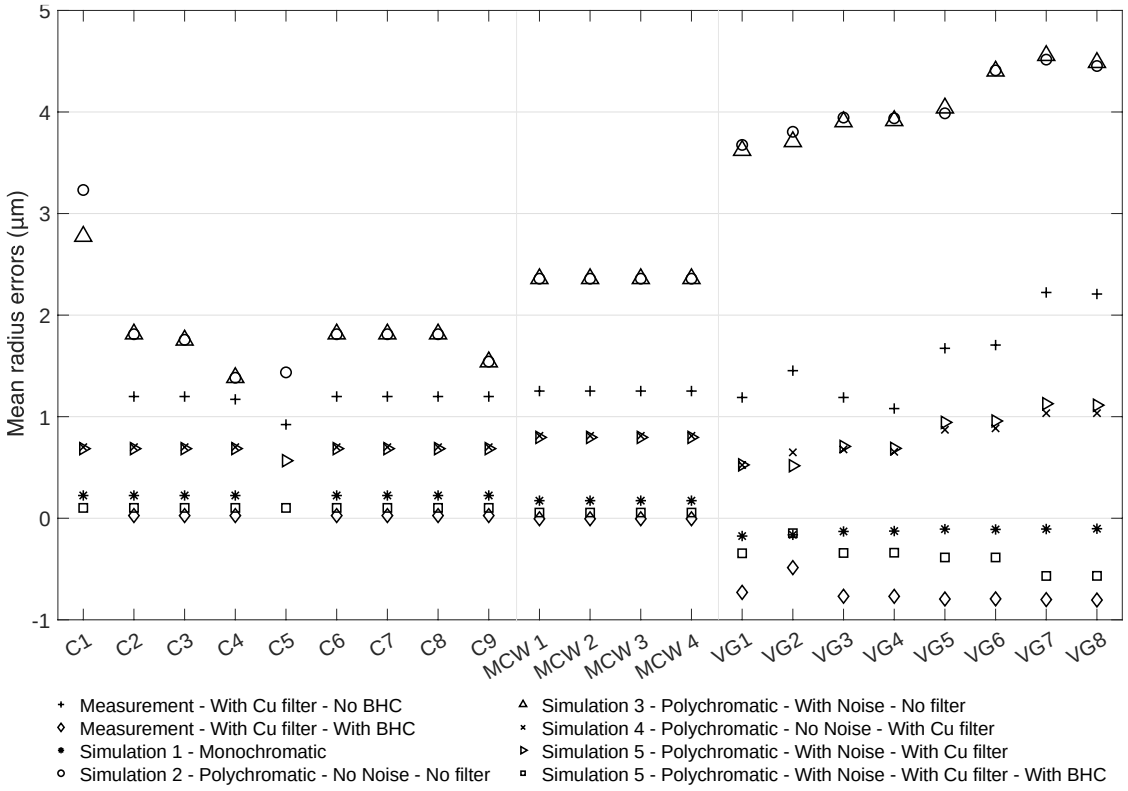

Figure 5-4: Summary of SD optimisation results of S1 (measurement), S2 (simulation)

5.2.1 Measurement data

In all MCW and in most of the Canny trials, the radius measurement errors without BHC, Figure 5-4 (+), were found to be the same, 1.25 µm. In the Canny case, trial C1, did not return the surface of the sphere due to the presence of noise. C5 returned a lower error because it did not include data around the streak artefact (see also the polychromatic simulation discussion). VG trials were sensitive to different user settings, and trial VG4 showed the best performance. An increase in search distance led to larger errors – see trials VG5 to VG8, which contradicted the assumption that VG should not be influenced by an increase in search distance applied to XCT measurement for reconstruction of smooth surfaces.

The radii errors after BHC, Figure 5-4 (◊), were found to be significantly smaller for all SD trials, and VG case reversing sign. This finding is supported by previous research, which concluded that beam hardening caused measurement dilation [2, 43, 154, 287]. From all SD algorithms, MCW yielded the smallest radius error,

-5 nm. Canny algorithms (C2, C3, C4, C6 to C9) yielded a radius error of 27 nm. C1 and C5 failed to detect the surface of the sphere appropriately (see also Figure 5-5). In C1, Canny algorithm was not able to discriminate between the edge of the spheres and the edge of the support platform, because a low value of the high threshold in the normalised gradient image forced the SD to include the surface of different material and/or the noise signal. Large values of the low threshold will omit the data in the gradient image that sit below this threshold, which in the C5 case resulted in no surface detected. Apart from C1 and C5, Canny radius errors were around 27 nm. Canny algorithm was less sensitive to the selected threshold values when applied to the results with BHC compared with no BHC. VG sensitivity to the user threshold also decreased after applying BHC, VG2 providing the lowest magnitude error, -0.49 µm. However, the radius errors between the surface determined by VG algorithm before and after BHC were larger than the ones calculated using Canny and MCW.

The Canny and MCW radius results after BHC were found to be within the uncertainty associated with the CMM measurements (50 nm, $k = 1$). These results were possible after the radius was calculated using the portion of the spheres sitting above the holding plate of the artefact, which coincided with the sphere portion measured by the CMM. Nevertheless, Canny algorithm required trial-and-error tests to find the optimal threshold conditions compared to MCW, which provided an error of -5 nm in all conditions. This suggests that in this case, with proper SD algorithms and correction applied, the result of XCT dimensional measurement can be reliable and can sit within the uncertainty of the CMM.

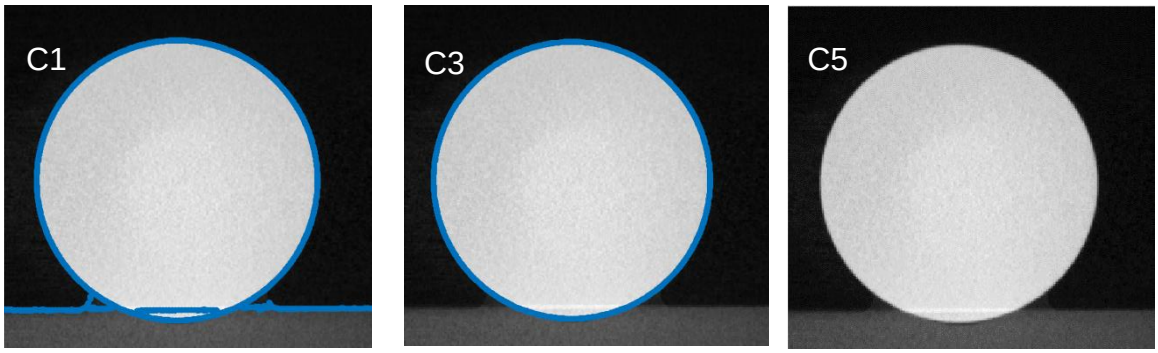

Figure 5-5: Canny optimisation results applied to the measured data.

5.2.2 Monochromatic simulations data

Simulation 1 – Figure 5-4 (✳) – For the monochromatic case, VG slightly outperformed both Canny and MCW in all threshold optimisation trials; VG radius error did not exceed – 0.1 µm whereas Canny and MCW radius errors were levelled at 0.25 µm. It can also be observed that the algorithms were not sensitive to the threshold settings. Interestingly, the Canny and MCW deviations had opposite signs to VG errors, which could be caused by the way the data was manipulated – Canny and MCW were applied using MATLAB. Meanwhile, the monochromatic simulations should not deviate from the nominal dimension of the spheres. These differences from the nominal value could be caused by the voxel size (digitisation).

5.2.3 Polychromatic simulations data – no filters

Simulation 2 – Figure 5-4 (O) – In polychromatic conditions, without noise and without filter, Canny and VG results were dependent on the threshold setting, with errors ranging from 1.4 µm to 3.2 µm and from 3.6 to 4.5 µm, respectively, whereas for MCW a radius error of 2.36 µm was recorded in all threshold optimisation conditions, outperforming VG, and had less sensitive than Canny. In the VG case, the radii errors were affected by the search distance, 0.9 µm difference between the errors calculated for 2 and 20 voxels search distance, which corroborates with the threshold optimisation results performed on the real measurement, which were found to be approximately 1 µm.

Simulation 3 – Figure 5-4 (△) – When noise was applied, no significant change was found except for the Canny trial 1 and 5. This is because applying the noise to the data only increased the dispersion of the surface point cloud, but did not deviate the mean of the point cloud significantly. C1 had the decrease of the radius error compared with simulation 2, whereas C5 failed to detect the surface. As discussed previously, a low value of the high threshold makes the algorithm more sensitive to noise, though the radius error decreased. Case of C5 suggested that high value of the low threshold can result in failure of surface detection.

By comparing simulation 1 (✳) with simulation 2 (O) & 3 (△), it was found that the radius errors increased significantly in polychromatic conditions compared with the monochromatic case, due to the dilation of the material [37, 40, 43, 44, 154]. A popular explanation is that the reconstruction algorithms assume monochromatic radiation for which the attention has a simple linear relationship with the penetration length. However, in the polychromatic conditions, the attenuation coefficient is dependent on the energy, and the relationship between the attenuation and attenuation thickness is more complex (see Appendix A). Still, there are mainly two types of polychromatic errors (beam hardening): cupping effect and 'streak' artefact. Cupping has been discussed in multiple papers [2, 43, 154, 287]. Nathanael [154] concluded that the material dilation was the result of filter smoothing over the cupped edge. The 'streak' artefact has been identified in the literature by Muller [211] for two touching spheres. Nevertheless, Muller used VG only without any optimisation and BHC.

'Streak' artefact usually appears during the measurement of multiple adjacent objects, and here for example, two adjacent spheres. Under the monochromatic condition, there were no 'streak' artefacts, as Figure 5-6-A shows. However, under polychromatic conditions, see Figure 5-6-B, there are two protruding parts on each sphere, showing how the steak artefacts affected the SD result.

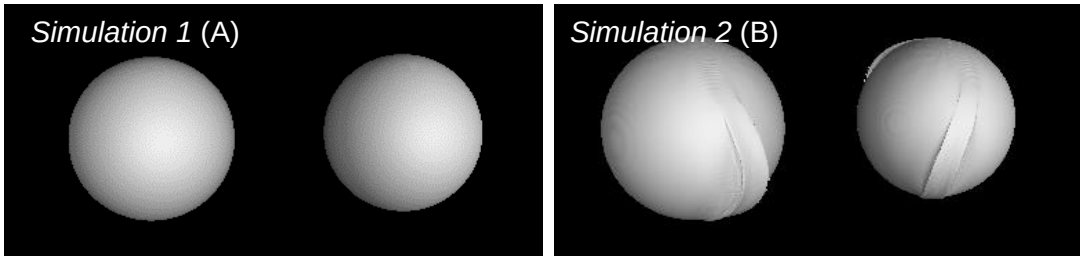

Figure 5-6: (A) Simulation 1 – Monochromatic and (B) Simulation 2 – polychromatic simulations reconstruction result.

Without any filter or BHC, a gradual increase of the lower threshold value in the Canny algorithm leads to an increased loss of surface data around the streak artefacts, as shown in Figure 5-7 (corresponding to C3, C4, C5 and C9). Therefore, C3, C4, C5 and C9 showed a smaller deviation compared with other Canny threshold settings in simulation 2 (O).

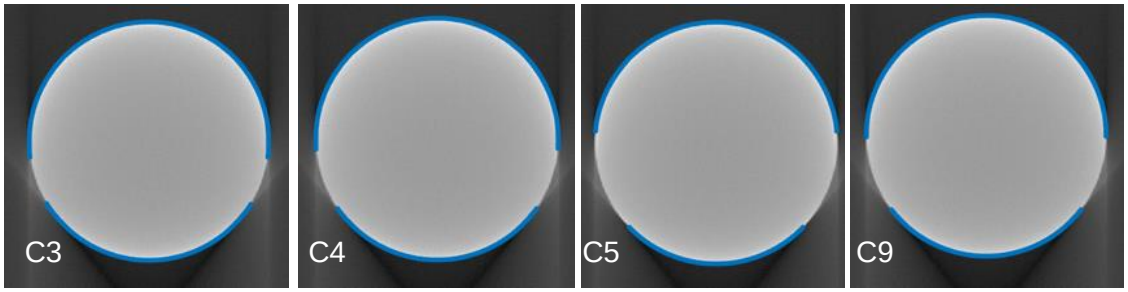

Figure 5-7: Canny trials results on Simulation 2 (O)

As in the measurement case, Some of the VG optimisation trials did not detect the surface of the sphere correctly around the streak artefact, see Figure 5-8. Trials VG1 and VG3 had the background and material ROI away from the edge, such that the surface around the streak artefact was departing from the edge of the sphere. In VG2 and VG4 cases, background and material ROI were closer to the edge, but the results identified an additional boundary which does not belong to the sphere. Only the increase in voxel search distance was able to effectively determine the boundary around the sphere (from VG5 to VG8). Nevertheless, VG radius calculation automatically disregarded the regions affected by large errors (VG1, VG2, VG3 and VG4), leading to lower radius values compared with the rest of the trials, in which the ‘streak’ affected zone was included in the radius calculation.

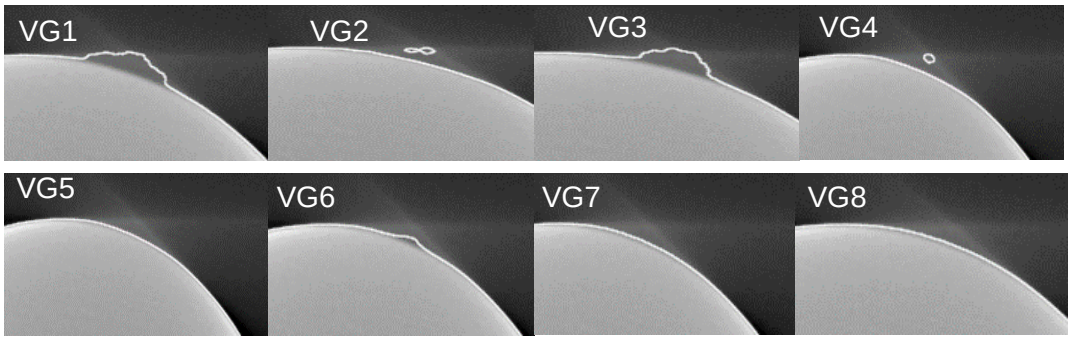

Figure 5-8: VG threshold trials for simulation 3

As shown in Figure 5-9, all MCW trials outperformed both VG1 and C5 when dealing with the ‘streak’ artefact. The best- and worst-case scenarios are summarised in Table 5-8.

Table 5-8Figure 5-9: The comparison between C5, all MCW trials and VG1 on the streak artefact area

Table 5-8: Relative radius errors between the polychromatic and monochromatic simulations in best- and worst- scenarios

Canny		MCW		VG	
Best	Worst	Best	Worst	Best	Worst
+0.04 %	+0.11 %	+0.08 %	+0.08 %	+0.15 %	+0.18 %

5.2.4 Polychromatic simulations data – with filters and BHC

Simulation 4 & 5- Figure 5-4 (✕ & ▷ respectively) – The copper filter results showed a significant decrease in the radius errors compared with simulation 2 & 3, which was down to 0.83 µm for Canny and MCW; and ranged from 0.5 µm to 1.2 µm in the VG case. However, C5 failed to detect the surface under simulation 4.

Simulation 5 with BHC – Figure 5-4 (□) – Both Canny and MCW yielded an error of less than 0.1 µm, while VG radius errors were found to be around -0.4 µm. By increasing the search distance to 20 voxels (500 µm), the VG radius error was found to be -0.5 µm.

Figure 5-10 shows the reconstruction results for polychromatic with Cu filter, with and without BHC. Both figures show the decreased level of ‘streak’ artefact compared with the reconstructed data shown in Figure 5-6.

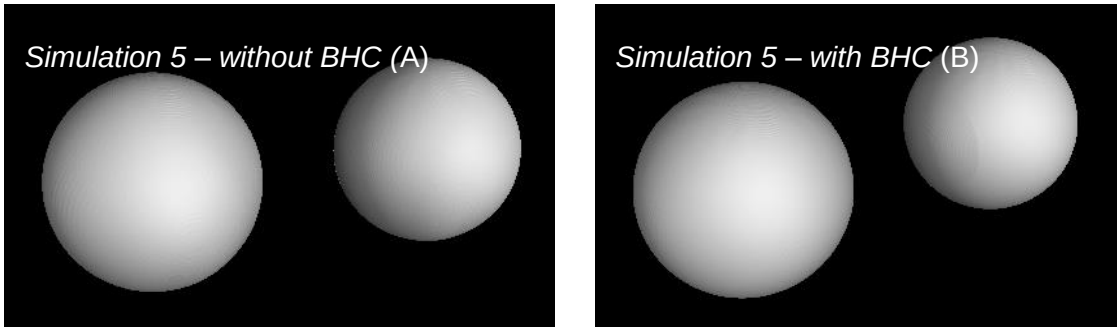

Figure 5-10:A Polychromatic with Cu filter without BHC; B. Polychromatic with Cu filter with BHC reconstruction result

5.2.5 Comparison between measurement and simulations before BHC

The radius errors from the simulation 4 & 5, (× & ▷) in Figure 5-4, were consistently lower compared with the measurement results, (+) in Figure 5-4, but they presented similar trends. Noticeable was the VG increase in material dilation associated with the increase in the search distance. The difference between the simulations and measurements could have been explained by the effect of scattering [45] and the finite focal spot size [27, 143, 288], which were not included in the simulations.

Scattering significantly impacts the measurement of high-density material. Lifton [46] demonstrated that scattering causes material dilation, which leads to an increased size of outer features.

The finite focal spot size influences the resolution of XCT due to the blur generated on the projection image, especially under high magnification [154], resulting in an increase in the sphere. In addition, higher attenuation increases the contrast of the edge and therefore can also cause material dilation [2, 154].

5.2.6 Comparison between measurement and simulations after BHC

BHC reduces the magnitude of the radius error for both measurement and simulation results, (◇) and (□) in Figure 5-4, respectively. However, the difference between measurement and simulation results is noticeably larger in the VG case compared with Canny and MCW.

All Canny trials successfully detected the sphere surface in simulations. One of the reasons is that the simulation only captured the sphere sample, whereas the spheres were placed on a surface during the measurements. Although Canny performs well with simulation data, the measurements still require error-and-trial tests.

5.3 Limitation

In this experimental work, due to the physical limitation of the XCT machine, the sample was only scanned once, hence, the measurement repeatability/reproducibility could be evaluated. Further research should consider repeated scanning of the sample for measurement.

5.4 Summary and Conclusions

In this chapter, the XCT measurement and simulations of XCT scanning of a sample with two smooth spheres were conducted to evaluate the effect of three SD algorithms, including their threshold optimisation, on bidirectional measurements. The high and low threshold values were optimised for Canny; kernel size and initial threshold for MCW; and the background and material ROI, search distance and iterative method option were varied in VG cases. The simulations were used to evaluate the effect of beam hardening, filtering, and noise on SD output.

Most of Canny, apart from C1, and all MCW optimisation trials applied on the XCT reconstructed data before BHC correction provided similar results, radius deviation of 1.25 µm. C1 failed to detect the surface because the higher threshold was too low, hence the edge determination was affected by noise. VG results were sensitive to all user settings, the search distance leading to the largest difference radius value.

Measurement radius errors after BHC were found to be drastically smaller. MCW yielded a radius error of -5 nm and Canny 27 nm, apart from C1 and C5 trials, which did not return the surface of the spheres correctly. This suggests that in this case, if proper SD and BHC are applied, the result of MCW and Canny results sit within the standard uncertainty of the CMM (50 nm, k = 1). VG's sensitivity to

the user settings was also decreased after applying BHC, but the radius errors (-0.49 µm) were larger than the CMM uncertainty.

In the simulated monochromatic conditions, Canny and MCW yielded a radius deviation of 0.25 µm and VG -0.1 µm. The C5 trial failed to detect the surface as well.

Polychromatic simulations without Cu filter and BHC led to an apparent dilation of the spheres, which is consistent with the previous research [22, 43-45, 78] and the measurement results. VG provided the largest errors and was significantly affected by the search distance, leading to radius deviations ranging from (3.6 to 4.5) µm. MCW algorithm showed excellent stability outperforming both VG and Canny. Noise introduced slight differences, except for C1.

In the polychromatic cases, apart from the cupping effect [2, 43, 154, 287], beam hardening could cause ‘streak’ artefacts for adjacent touching spheres. For Canny algorithm with high value of lower threshold settings, loss of surface data occurred around the area affected by ‘streak’ artefact. VG also encountered problems around the ‘streak’ artefact-affected zones when a small voxel search distance (under four voxels, or 100 µm) was applied. In contrast, MCW showed excellent performance when dealing with the ‘streak’ artefact.

The ‘streak’ artefacts should not be mistaken with the Feldkamp effect [19] studied in previous papers [243, 272]. The Feldkamp effect is due to the lack of spatial resolution along the rotation axis, which can be amplified by increasing the cone beam angle [272]. The Feldkamp effect deteriorates with further distance to the detector centre line. Stolfi [243] pointed out that the Feldkamp effect mostly appeared for long workpieces causing longitudinal truncation. For spherical objects, the beam can penetrate the object without significant data truncation.

Polychromatic simulations with the Cu filter and with BHC led to radius errors of 0.09 µm, 0.05 µm and -0.4 µm in Canny, MCW and VG cases, respectively.

These results showed that the MCW algorithm provides accurate and reproducible results in different threshold optimisation conditions. VG was the

worst for both accuracy and reproducibility, with the search distance affecting the accuracy the most. Canny showed great performance in most cases, with proper selection of the threshold conditions. However, appropriate threshold selection can pose difficulties for end users (*i.e.* trial-and-error tests).

As seen in the current results, SD algorithms can have difficulties when the measurements are affected by noise and beam hardening, which for a smooth surface and bidirectional measurements they can overcome. Nevertheless, for rough surfaces, this may not be the case.

At the same time, the results presented here suggest that the SD algorithms and noises were not the major source of errors and uncertainty for bi-directional measurement of the sphere, evidenced by the effect of BHC. The novelty of this work also rests with the adopted methodology, which allowed the researcher to isolate and quantify the contribution of the SD to the XCT bi-directional measurement errors.

6 SD effect on surface texture

The previous chapter has depicted the effect of SD algorithms on XCT bi-directional measurements of smooth surface components, showing that the MCW algorithm outperformed the other two algorithms. This chapter presents the effect of SD algorithms on the measurement of rough surfaces.

CS profilometer is a traceable tool for surface texture profile measurement. However, the non-line-of-sight features (for example, re-entrant features introduced in section 2.3.3), restrict the capability of CS to appropriately measure surfaces with re-entrant features [76]. XCT can measure the non-line-of-sight surface features [76, 150, 289], however the lack of confidence in the measurement is still a problem [76, 150, 289].

Previous research related to XCT and CS comparison is limited compared to the XCT and optical instruments [150, 158, 159, 165]. However, the optical instruments are not regarded as being traceable [76]. All CS and XCT comparisons [76, 150, 289] used VG and did not consider the influence of SD algorithms, see section 2.3.

It has been proven that surfaces based on a single threshold value can be severely affected by artefacts such as beam hardening. Moreover, as is shown in the non-smooth surface example within Figure 6-1-A & B, because of the presence of noise within the 3D volume data, the starting contours based on a single threshold value setting include unwanted signals, which causes additional errors.

The finite search distance setting limits the VG's ability to determine the surface correctly, especially for detecting rough surfaces. This is clearly described in Figure 6-1 A & C. The search distance defines the range where the final surfaces are determined around the starting contour. However, as Figure 6-1-C shows, the VG algorithm searches the surface along the normal direction of the starting surface. This could cause a problem in the rough surface case when the searching distance is set too large, and the search vectors can overlap in some points or cause search vector entanglement. Moreover, a large search distance

can reduce the capability of the VG algorithm to detect the surface with low spatial resolution. A solution is to reduce the search distance, but in this situation, the VG algorithm would not differ from the global threshold algorithms, hence no longer ‘advanced’.

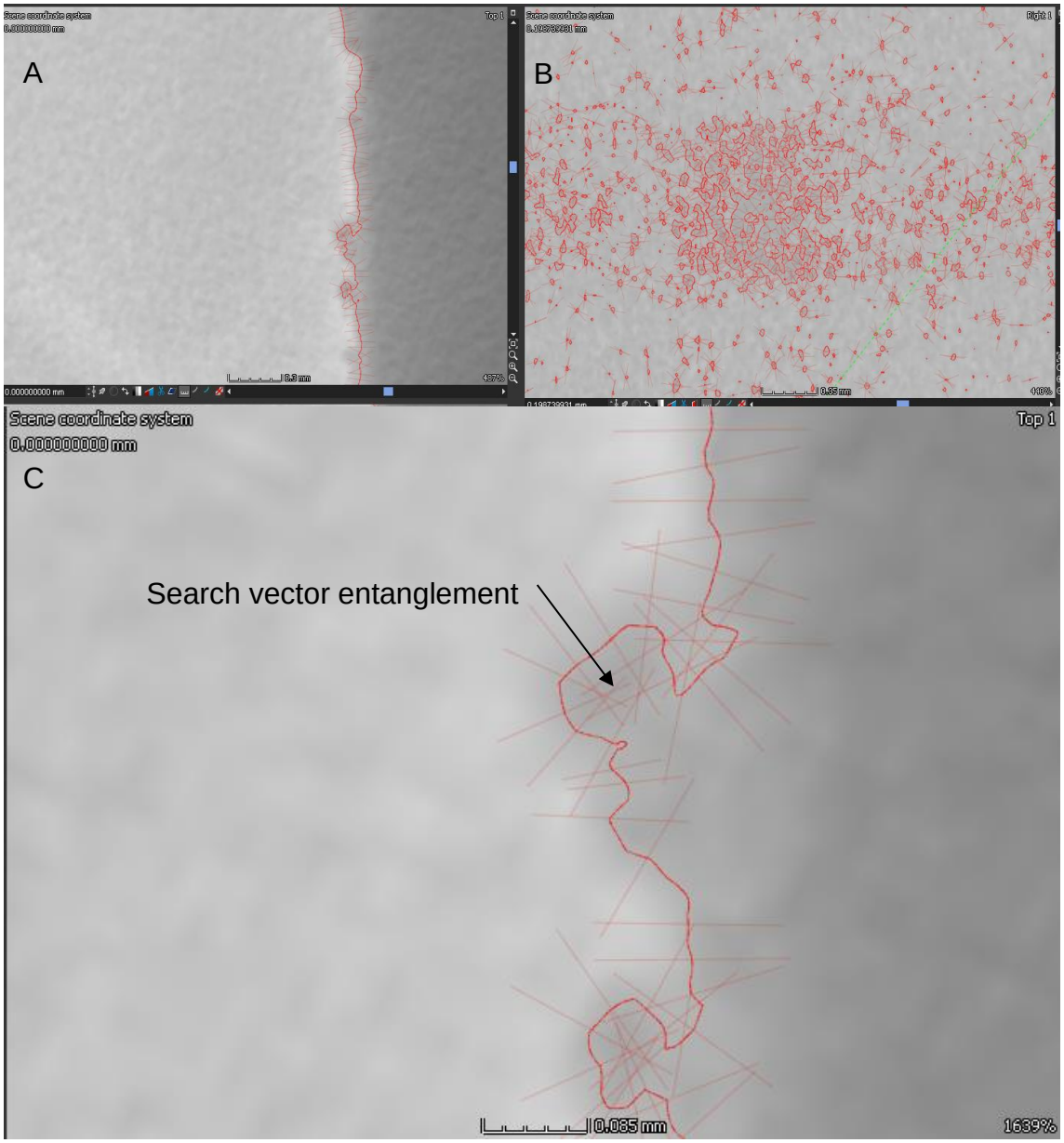

Figure 6-1: The problem of the VG algorithm in non-smooth surface detection. The search distance is set as four voxels, 0.08 mm.

Another challenge of surface texture measurement is the bandwidth limitation of different measurement techniques [76]. Physical components of XCT, such as

the magnification limitation, focal spot size, detector pixel size, etc., limit the XCT to obtain data with high spatial frequencies [76, 83, 158].

Canny and VG's use of a smoothing filter [212, 225] to overcome the noise problems can limit the ability to detect the surface high-spatial frequency components. MCW does not need to prefilter the data and is relatively straightforward to apply, see Chapters 3, 4 and 5, however, it has never been tested for rough surfaces.

This chapter focuses on SD optimisation and comparison by employing experimental scanning and synthetic data. For experimental scanning, CS was used to generate a traceable profile and compare it with the XCT profiles under optimised SD algorithms of VG, Canny and MCW. The synthetic data was used to test SD's capability of the surface with various spatial frequencies (S_a value from 5 µm to 20 µm).

6.1 Materials

This study used both measured and synthetic data sets. The measurements were performed on a three-dimensional roughness standard (3DRS) designed by NPL [76], and the simulations were performed on a set of synthetic surfaces generated using a trained progressively growing adversarial network (PGGAN) [290, 291] representing the down-skin, up-skin and top surfaces of 'bracelet' AM artefact produced using electron beam powder bed fusion (EBPBF) [290, 291].

6.1.1 Measured sample

Figure 6-2 left shows the 3DRS manufactured using electron beam melting [291], a commonly used AM technique. 3DRS was made of Ti64 alloy and has multiple roughness features. In addition, there are five zirconium precision spheres mounted on the sample that help with the registration of the datum. The distance between the centres of the precision spheres mounted on face A was previously calibrated using a micro-coordinate measuring machine [76] and subsequently used to adjust XCT's voxel size.

Only Face A ($\overline{R_a} \pm \sigma_{\overline{R_a}} = (23.36 \pm 1.08)\ \mu m$, when λ_c = 2.5 mm from CS [76]) was used to study the effect of different SD algorithms on the measured surface texture, because CS profiler required spheres S1 and S2 for alignment purpose. A contact stylus instrument (CS) [162], Taylor Hobson's Talysurf (height measurement uncertainty of 50 nm, k=1), fitted with a standard diamond stylus tip (90º angle conisphere and 2 µm [292] radius tip) was used to measure a 5 mm long profile with a 0.25 µm sampling distance on Face A of the 3DRS between the S1 and S2 zirconium precision spheres as shown in Figure 6-2 right.

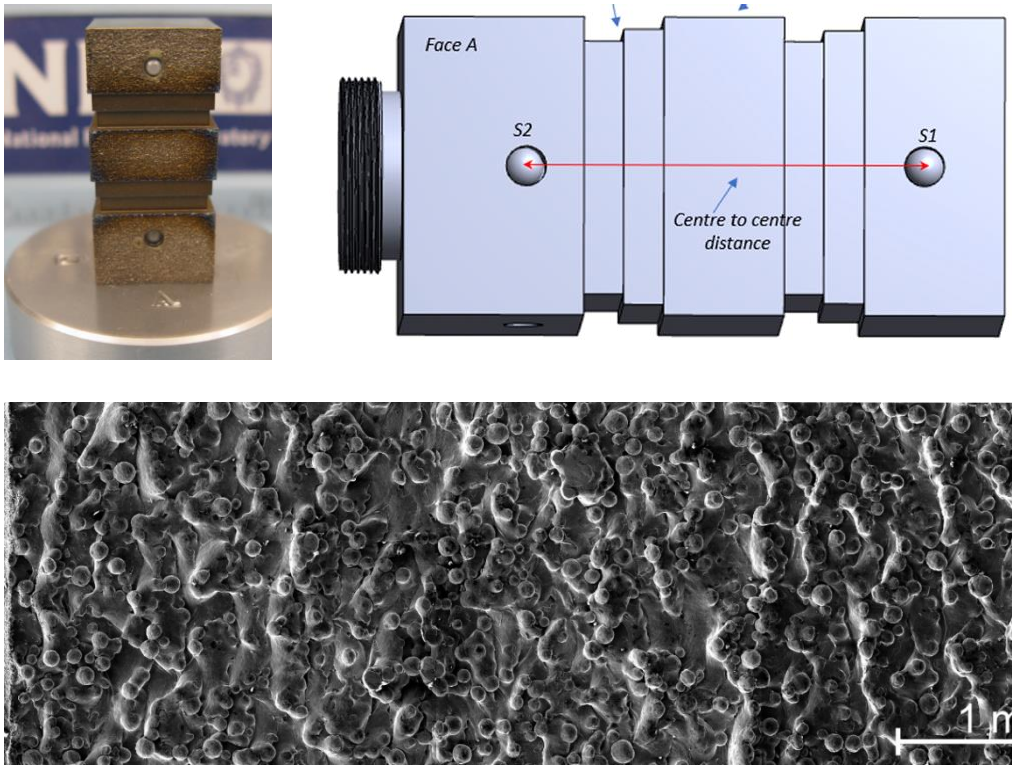

Figure 6-2 The photo of the 3DRS reference sample (left) and the sketch picture, including the CS measuring position. Down: SEM image of the 3DRS surface

The two spheres present on Face A were used to align the CS measurement between the centres of these two spheres using a cresting procedure, which requires a setup composed of a translation and a manual rotation stage. As shown in Figure 6-3, the stylus tip contacted the two spheres separately and crested using the translation stage fitted with a micrometer scale. The micrometer indication served to record the difference between the position of two spheres in the perpendicular direction to the scanning direction of the stylus. Then the

rotational stage was moved to compensate for the miss-alignment between the scanning direction of the stylus and the direction defined by the centre of the two precision spheres. The procedure was repeated until there was no measurable difference in the linear stage's micrometer. This was an important step as it was used collocate the XCT data with the CS data.

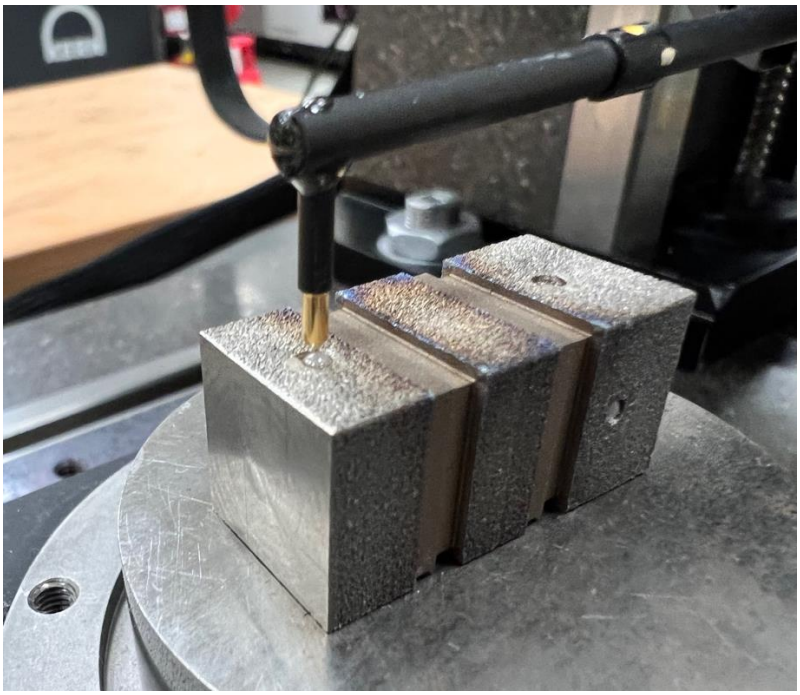

Figure 6-3: Top crest search strategy

The 3DRS sample was scanned using a CT machine, Nikon XT H 225M, using the parameters listed in Table 6-1

Table 6-1: CT scanning parameters of 3DRS (Ti64) sample.

Voltage (kV)	Current (µA)	Number of projections	Magnification	Voxel size in µm	Filter
180	120	3142	10	20	0.5 mm Cu

Prior to reconstruction, BHC described in Appendix A was performed.

The reconstructed data were processed using VG, Canny and MCW (see Sections 2.5.2 and 5.1.4). For Canny and MCW point clouds, voxel refinement was performed, which was described in section 3.5.

Optimisations of Canny, VG and MCW SD were performed using the trials shown in Table 5-4 &

Table 5-5 (VG), Table 5-6 (Canny) and Table 5-7 (MCW), (see also section 5.1.4), for both reconstructed data with and without BHC.

Alignment was needed for the 3DRS sample to extract the profile from the surface point cloud, which makes it comparable with the CS profile measurements. Figure 6-4 illustrates the scattered surface data after alignment.

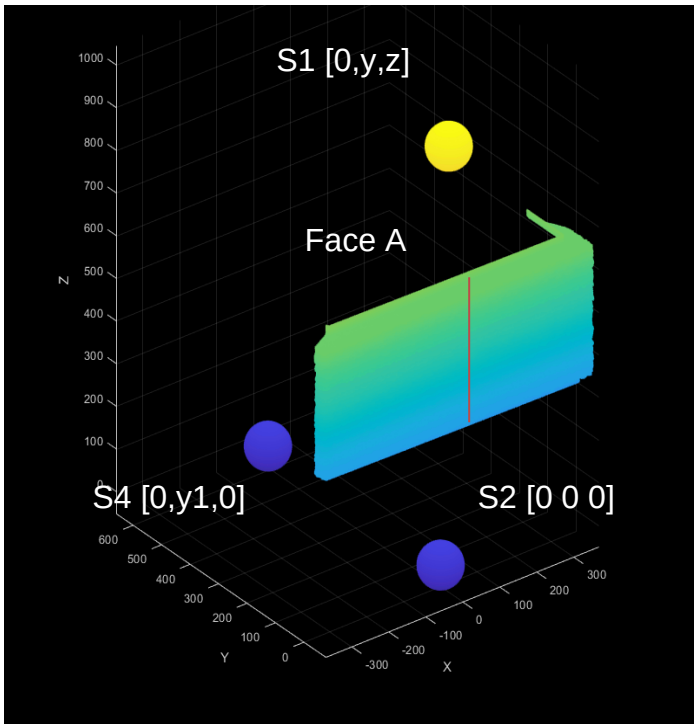

Figure 6-4: The watershed point cloud of Face A, S1, S2 and S4 within the coordinate system before (upper image) and after transformation (lower image). The figure is generated using MATLAB R2019b. Red line indicates the extracted profile position.

All three sphere centre locations were calculated using the *pcfitsphere()*

There are three main steps for 3DRS data alignment, including translation and rotation.

A. Set the origin of the sample coordinate system [0 0 0] to the centre of S2 using a simple translation operation

B. Rotate the data such the centre of S4 to align with the Y axis
C. Rotate the data around the Y axis to move S1 in Y-Z plane, or plane of X = 0.

Voxel size correction [10, 23, 43, 48, 233, 293]. Was based on the calibrated distance between S1 and S2 [76]. The corrected voxel size is shown as follows:

$$v_{cor} = \frac{d_{S1-S2}}{n_{S1-S2}} \quad \textbf{(6-1)}$$

where d_{S1-S2} and n_{S1-S2} denote the calibrated distance and the distance in voxel in CT point cloud data, respectively. Hereby, each position CT data point cloud was calculated by

$$P_r = P_{xyz} \times v_{cor} \quad \textbf{(6-2)}$$

where P_r denotes the dimensional coordinate location in μm, and P_{xyz} is the coordinate position in voxels, assuming that v_{cor} is in μm. Figure 6-4 illustrates the registered point cloud data in micrometres after the voxel size correction and scaling.

After the alignment, the tactile measurement vector was parallel with the Z axis, and the location of the tactile profile on the point cloud surface along X axis was on the plane of X = 0.

The alignment code is presented in 8Appendix C.

6.2 Stylus morphological transformation

The direct comparison between the CT and CS profiles requires a morphological transformation of the CT data [294]. The purpose of stylus morphological transformation is to simulate the movement of the stylus, with a radius of 2 μm and an opening of 90°, on the XCT point cloud profile. Figure 6-5 shows the schematic diagram of the stylus morphological transformation of the XCT point cloud profiles. When measuring a surface, the size of the stylus impedes its access to some features of the surface [162], such as the re-entrant and the deep

valley, which is not the case with XCT [76, 165]. This morphological transformation algorithm transfers the scattered point cloud data (blue dot) into the line profile (solid brown line shown in Figure 6-5). The code is presented in Appendix E.

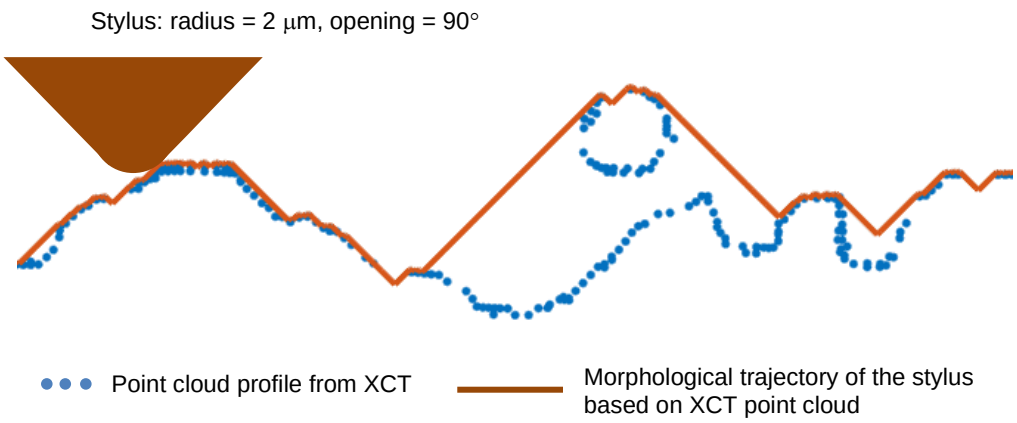

Figure 6-5: The schematic diagram of stylus morphological transformation. The stylus is exaggerated for description only

6.2.1 Synthetic data

The image shown in Figure 6-6 are (512 × 512) pixels artificial surfaces generated by PGGAN [290, 295], with S_a ranging from 5 µm to 20 µm. The image represents a $1\ mm \times 1\ mm$ surface area with a min-max depth value of (-50 to 50) µm.

The synthetic image was transferred to the surface CAD mesh model shown in Figure 6-6 using Image2surface algorithm [296] available in Autodesk Fusion 360 Version 2.0.13618 [297]. The mesh model was processed with the magnification of 1× from image A, therefore the size of the CAD mesh model was (1 × 1×1.1176) mm, with valley depth values of (-50 to 50) µm. The surface was put on the cuboid mesh model for successful simulation scanning. After transformation, the mesh CAD model had in total of 608,462 triangle faces. Images representing three different locations (down-skin, up-skin, top) on the bracelet artefact [290] showing different surface types were transferred into three CAD models, as shown in Figure 6-6. The purpose of employing three different images was the representation of different surface roughness to examine the

capability of XCT and SD algorithms. Especially the top surface had very flat surface roughness with $Z_t = 20\,\mu m$ only, which is the sum of the height of the peak and depth of the valley, as defined in [162].

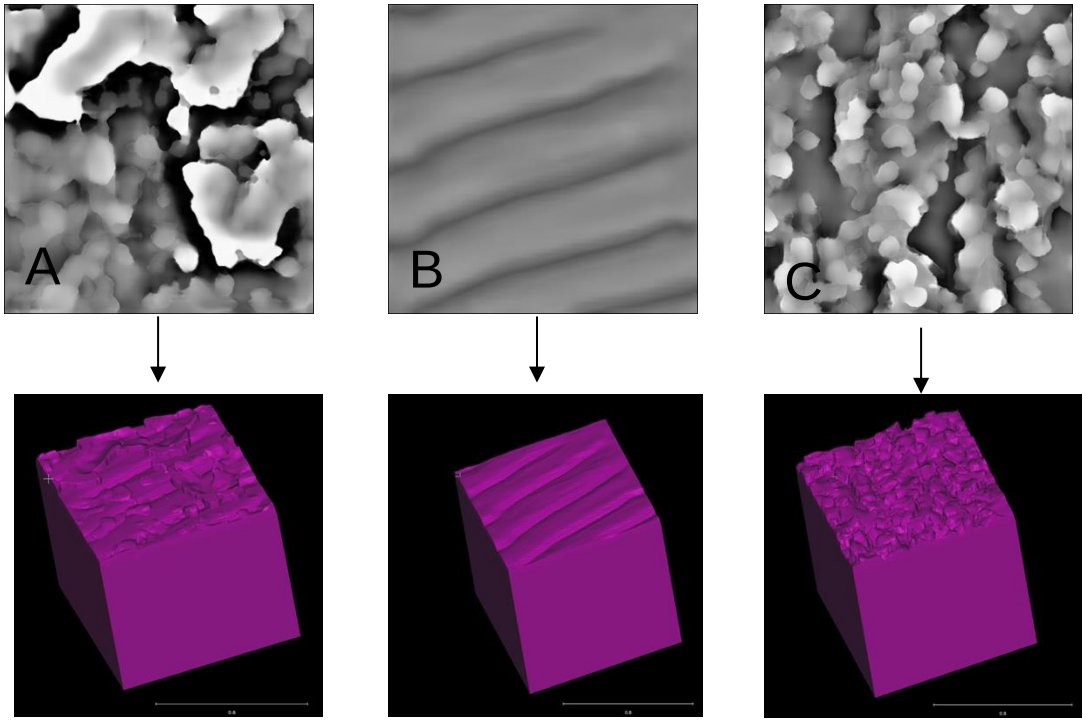

Figure 6-6: The synthetic encoded depth image PGGAN [290, 295] and its corresponding CAD models converted using Image2Surface. A: Downskin surface (S_a = 20 µm); B. Top surface (S_a = 5 µm); C. Upskin surface (S_a = 15 µm)

The CAD model was saved into '.stl' file and imported into aRTist Version 2.10. The general simulation settings are listed in Table 6-2. For each CAD model, four simulation data were obtained with different settings in terms of spectrum and noise, which is described in Table 6-3. The simulated dataset 1 is for benchmark purposes, for analysis of the influence of SD algorithm exclusively without any other influencing factors, such as noise and spectrum. Comparing datasets 1 & 3 and 2 & 4 is to investigate the resilience of SD algorithms to beam hardening caused by polychromatic spectrum; comparing datasets 1 & 2 and 3 & 4 is to study the SD algorithms' resilience to noise in the simulated data.

Table 6-2 The general setting of simulations

Voltage kV	Current µA	Number of projections	Magnification	Voxel size in µm	Multi-sampling	Material
60	70	3141	20	10	3 × 3	Ti64

Table 6-3: Settings for four simulation scanning

Dataset	Spectrum	Noise level
1	Mono	0
2	Mono	2
3	Poly	0
4	Poly	2

For each dataset, VG algorithm, 3D MCW and Canny were applied individually to generate the point cloud data, which were used to compare with the mesh data using the software of CloudCompare V 2.12.0 [298], which is free to use and open source, targeting 3D point cloud and mesh processing.

6.3 Results and discussion

6.3.1 Experimental optimisation results

The complete comparison of XCT profiles with and without the morphological transformation is shown in Appendix B

Figure 6-7 presents examples of XCT profiles without the morphological filter and with all SD optimised.

From Appendix B, it was found that C1, C6 and C8 generated a significant level of noise, with and without BHC. In the optimised case, C7, still generated more errors than MCW and VG, see for example the errors situated at (8700, 10900 and 14000) µm on the horizontal axis. Since the Canny algorithm needs the upper/lower threshold settings prior to computing, incorrect thresholds can lead to unwanted surface errors. This result is supported by Fabijanska [299], where the transition between the sphere and the plane was incorrectly detected when using the Canny algorithm.

VG did not detect some of the surface texture details, such as valleys and the overhang regions at the (9300, 9600, 10200, 10300, 11000, 11800, 12900, 13300, 13900) µm on the horizontal axis. This can be explained by the fact that VG ‘smoothed’ the surface before finding the regional maximum gradient value. However, for surface texture measurement, smoothing data can decrease fidelity.

MCW provided optimal fidelity and minimised surface errors. There were some features that had very good agreement between the MCW and CS, for example, at (11300, 12400, 12500, 13400) µm.

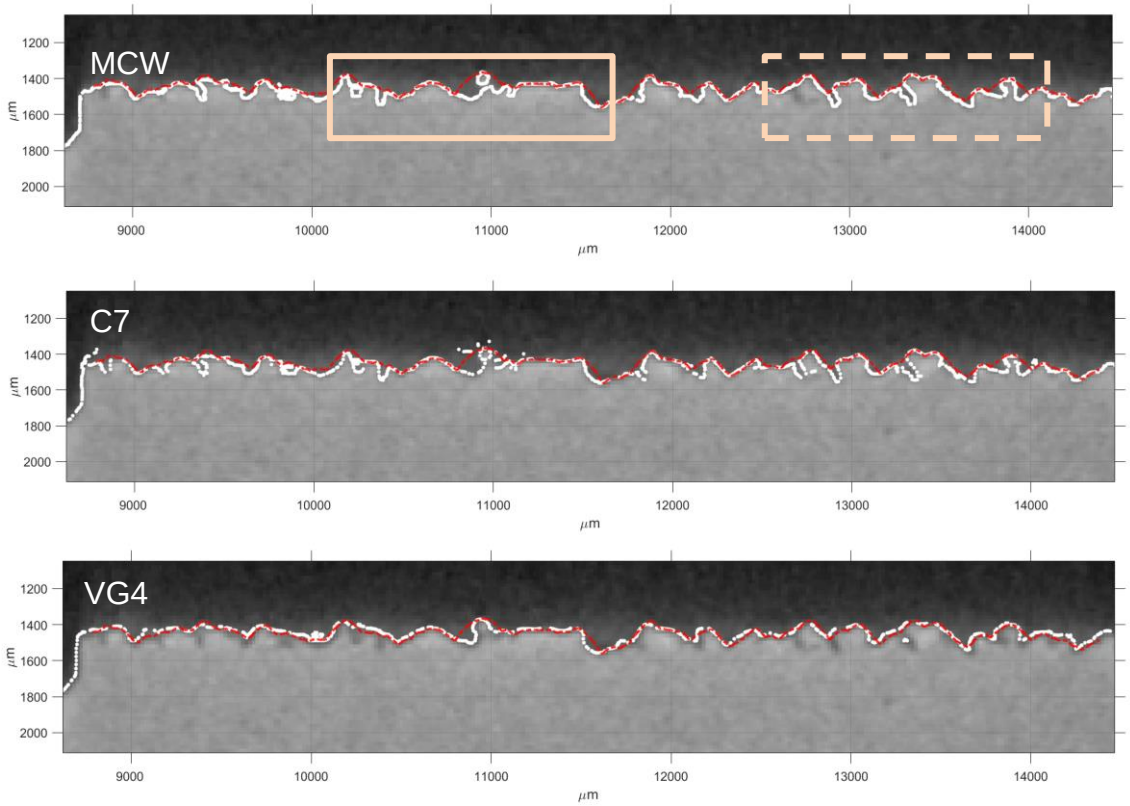

Figure 6-7: SD profiles without morphological filter and without BH (white dots) and CS (red dash line). The solid rectangular indicates the location of Figure 6-13; rectangular dash region indicates the location of Figure 6-14

Figure 6-8 presents the SD results with the morphological filter applied.

Canny presented obvious deviations at (8700, 10900 and 14000) µm due to the presence of surface errors. Many VG profile features were situated above the CS data (towards the background). This showed VG was more likely to be influenced by the material dilation [154] caused by beam hardening. MCW had the best fidelity performance among all three algorithms. However, there are still some locations where there are deviations between MCW and CS, for example, at (10000 and 10800) µm.

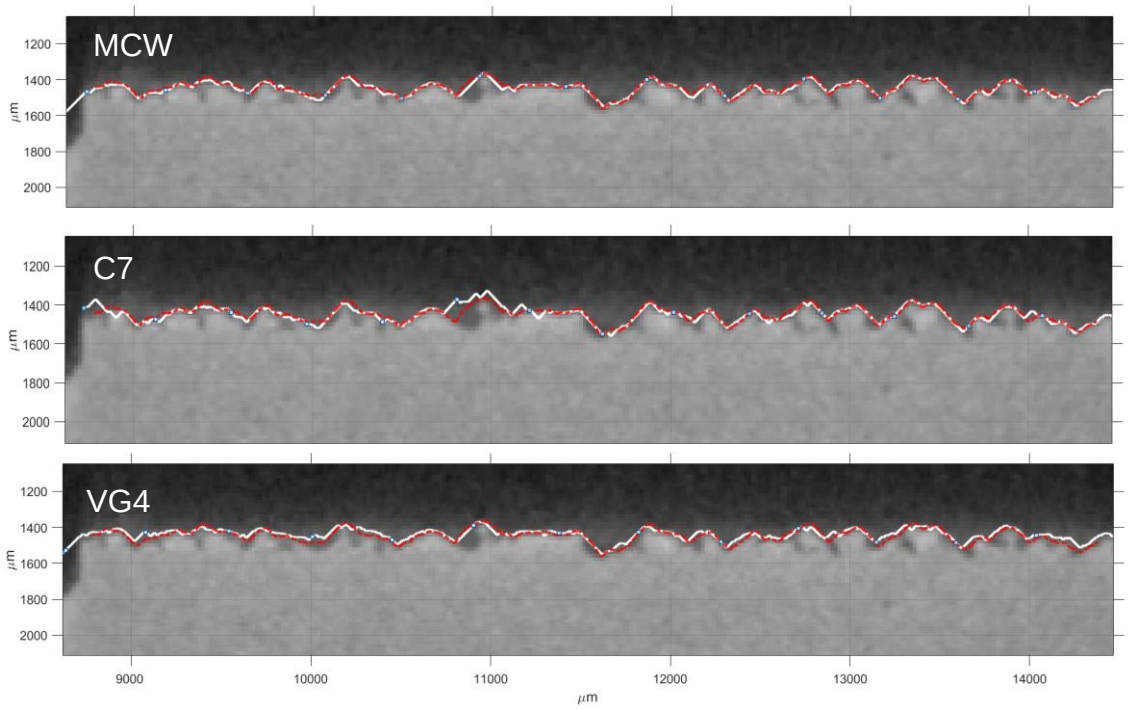

Figure 6-8: SD profiles with morphological filter and without BH (white dots) and CS (red dash line).

Figure 6-9 presents the C7, VG3 and MCW profiles with the morphological filter and without BHC. BHC did not appear to affect the MCW. This finding proved that the MCW algorithm has the robustness to overcome the influence of beam hardening in surface texture measurement, see also Figure 6-12. Before BHC, the VG surface was ‘smoothed’ and therefore had lower Ra and Rq values.

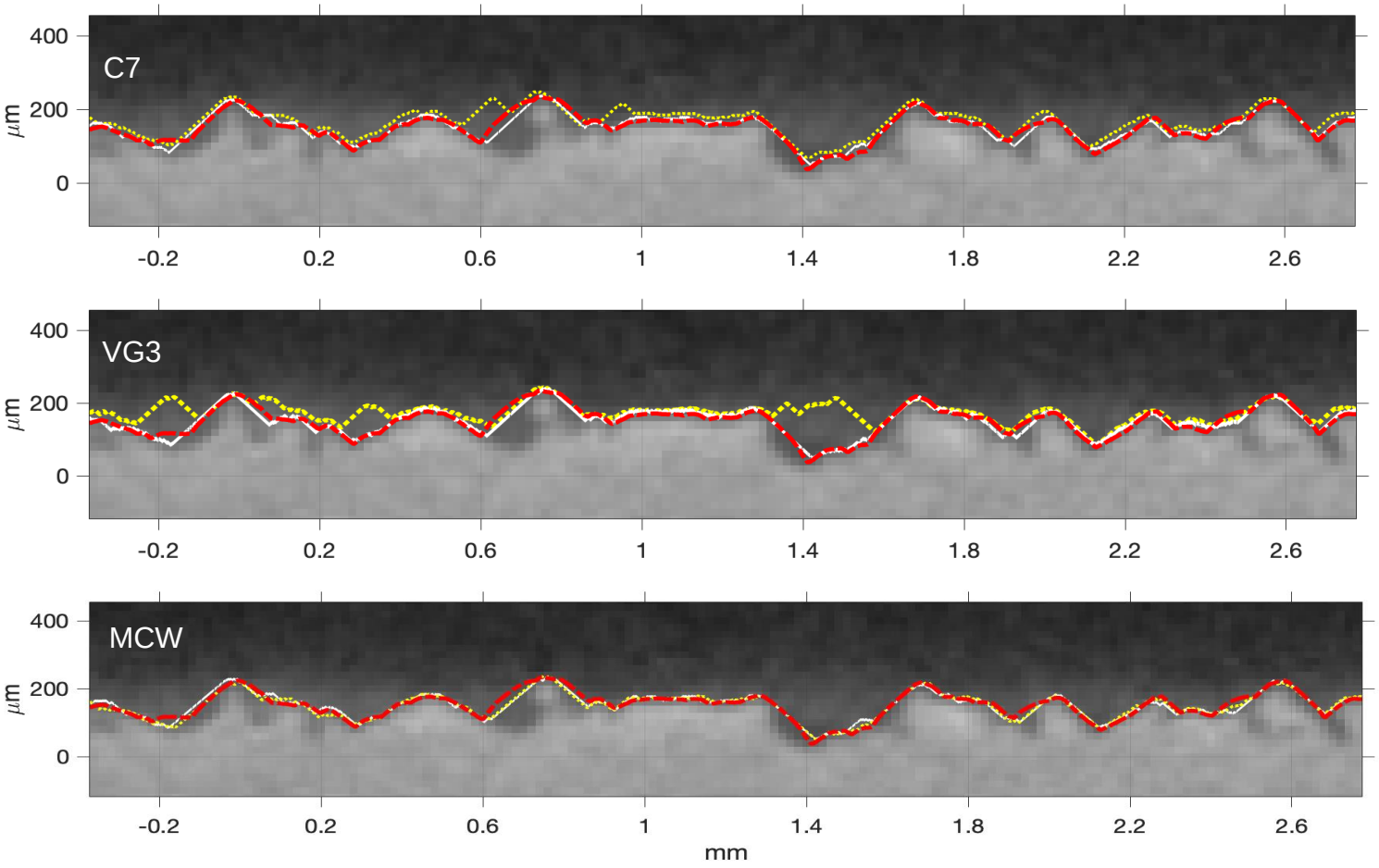

Figure 6-9: MCW and VG roughness profiles (dot yellow: without BHC; solid white: with BHC) and CS profile (dash red).

Figure 6-10 and Figure 6-11 compare the SD algorithms (MCW, C7 and VG3) R_a and R_q values of the profiles presented in (Figure 6-8) without BHC. The CS's R_a and R_q values are 30.38 μm and 37.93 μm, respectively. MCW provides the closest results to CS, with R_a value error of only 0.2 μm, which was only 6 % of the Ra error from Wenjuan's data (3 μm when λ_c = 2.5 μm). Canny results are higher than CS due to the presence of surface errors, and VG results are smaller because it uses a 'smoothing' filter.

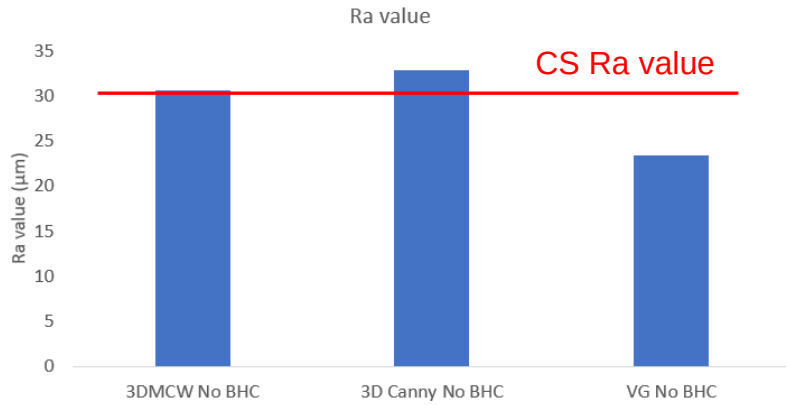

Figure 6-10: The R_a value of the XCT profiles under different surface determination algorithms (MCW, C7 and VG3) without BHC. The red line indicates the R_a value of CS's profile.

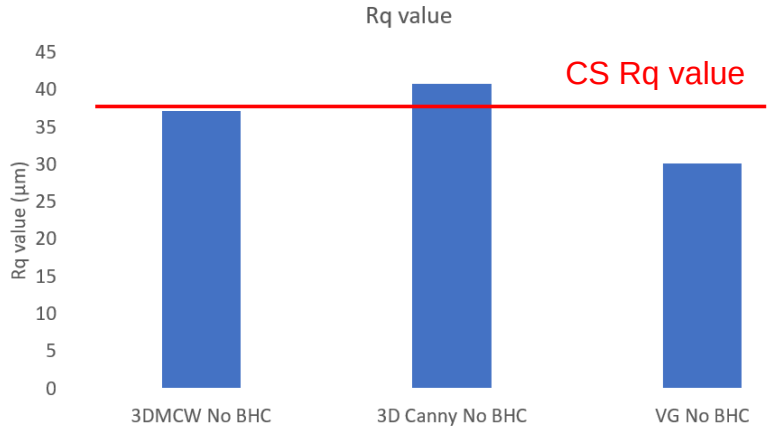

Figure 6-11: The R_q value of the XCT profiles under different surface determination algorithms (MCW, C7 and VG3). The red line indicates the R_q value of CS's profile.

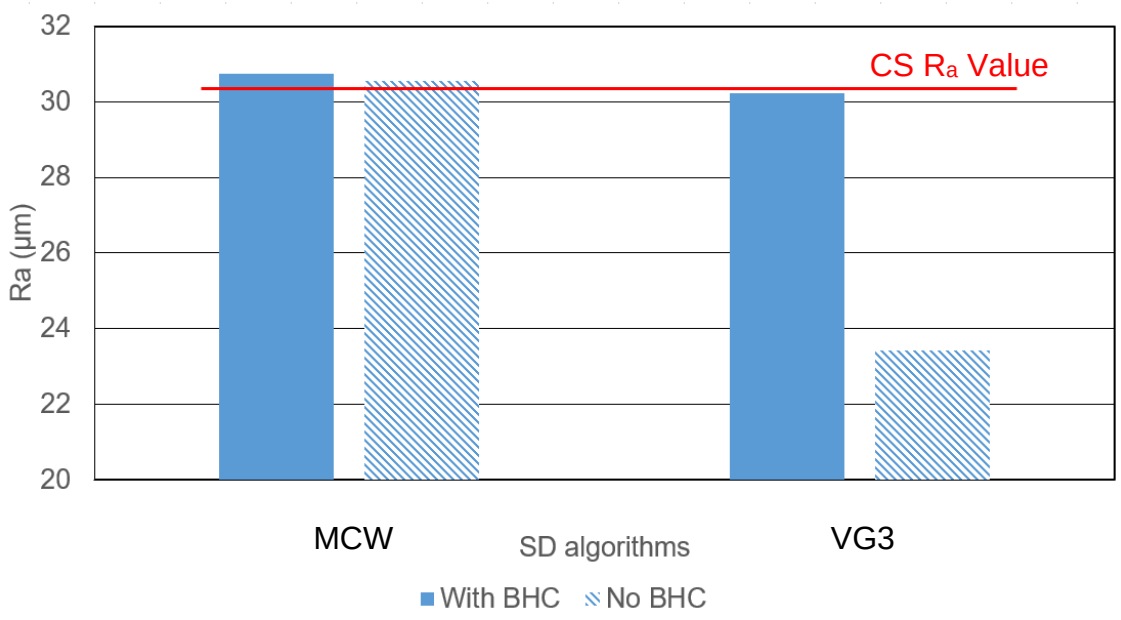

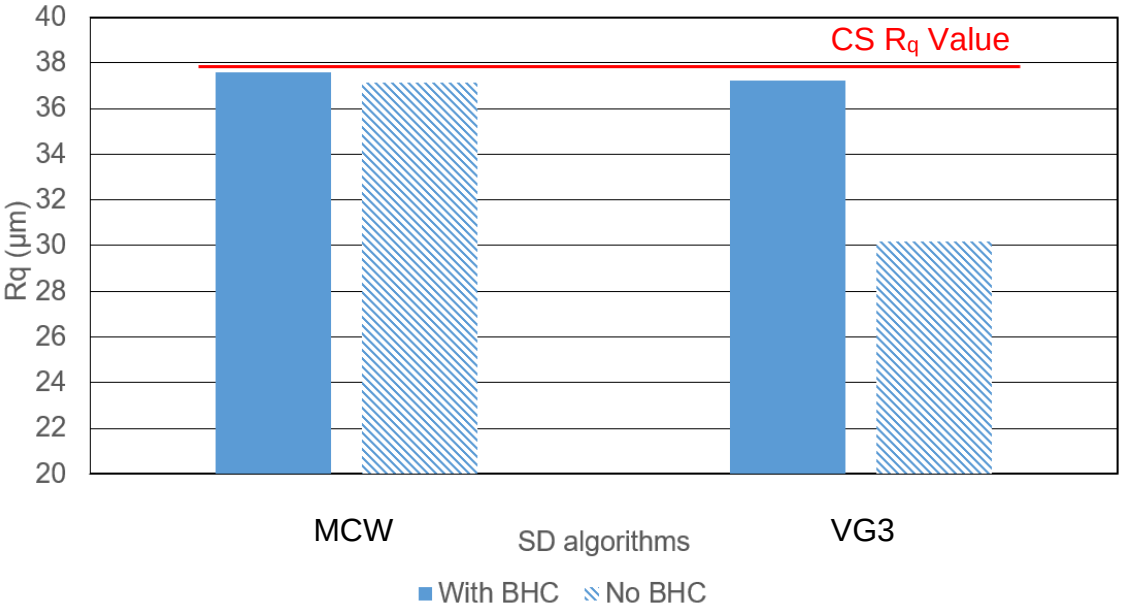

	R_a (µm)		R_q (µm)	
	MCW	VG3	MCW	VG3
With BHC	30.73	23.41	37.58	37.22
Without BHC	30.56	30.21	37.146	30.18
CS	30.376		37.8	

Figure 6-12: R_a and R_q results for MCW and VG, with and without BHC. The red line indicates the corresponding CS values. The table displays the corresponding values.

6.3.2 Discussion of experimental results

Figure 6-13 and Figure 6-14 show the XCT cross sections and the CS measured profile under different optimisation settings with and without BHC at two different positions (the rectangular region labelled in Figure 6-7)

Canny was significantly affected by noise. As shown in Figure 6-13, a significant level of noise was detected in the background region under C2-No BHC. The low-high threshold value of C2 is [0.2 0.4], proving that the high threshold value of 0.4 was set too low. Figure 6-14 shows that C2 – No BHC incorrectly detected the surface within the material range; the errors were not reduced after BHC. C7 shows the optimised Canny trials, however, data loss was found for C7 in some valley areas, such as the valley label with A in Figure 6-13 and Figure 6-14. In all Canny cases, beam hardening pushed the surface profile towards the background region. Overall, Canny performed poorly in the presence of beam hardening and noise.

VG algorithm was unstable in the presence of beam hardening. VG1 led to errors within the background, as shown in Figure 6-13-VG1-No BHC. This is because the lower search distance of 40 µm failed to cover the area of the proposed surface. The VG algorithm with low search distance was significantly influenced by the location of the pre-defined surface with a global threshold, which was largely affected by beam hardening artefact and noise [38, 40, 43, 44]. VG4, with search distance 80 µm, successfully computed the surface with and without BHC, showing good agreement with the CS profile. Interestingly, the VG4 failed to detect the surface within the valley area, as indicated with label B in Figure 6-13 and Figure 6-14. This agrees with previous research [154], which showed that beam hardening limits the capability of XCT to measure surface with high spatial frequencies. Another possible explanation is the smoothing effect of the VG algorithm, which was originally introduced to reduce the impact of noise.

MCW algorithm outperforms all other two SD algorithms with and without BHC and demonstrated excellent agreement with the CS profile. An interesting finding is that MCW detected the material area labelled in C in Figure 6-13, indicating that this region is an overhang area on the surface, while Canny and VG did not

identify a clear overhang region. However, it is difficult to validate this with the CS, because CS could not provide a reference profile for overhung features. MCW, like Canny and VG, failed to detect the valley without BHC labelled by letter E in Figure 6-14, but after BHC, the valley was successfully detected.

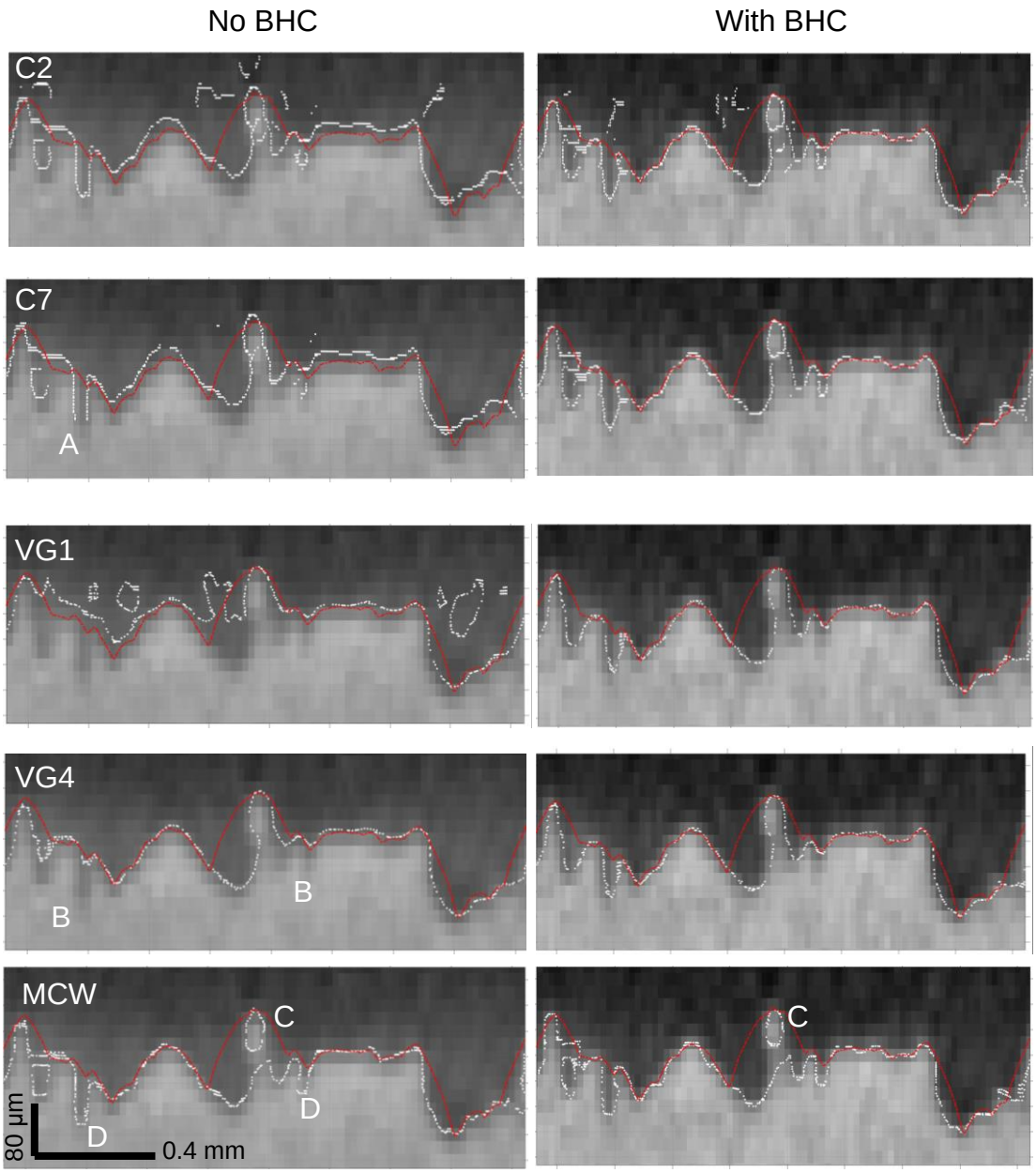

Figure 6-13: The SD results of C2, C7, VG1, VG4, MCW on surface texture before and after BHC. The white dots correspond to SD profiles and red dash line is the CS profile. The XCT reconstructed slices are shown as the background. The image was captured from the solid rectangular region of Figure 6-7

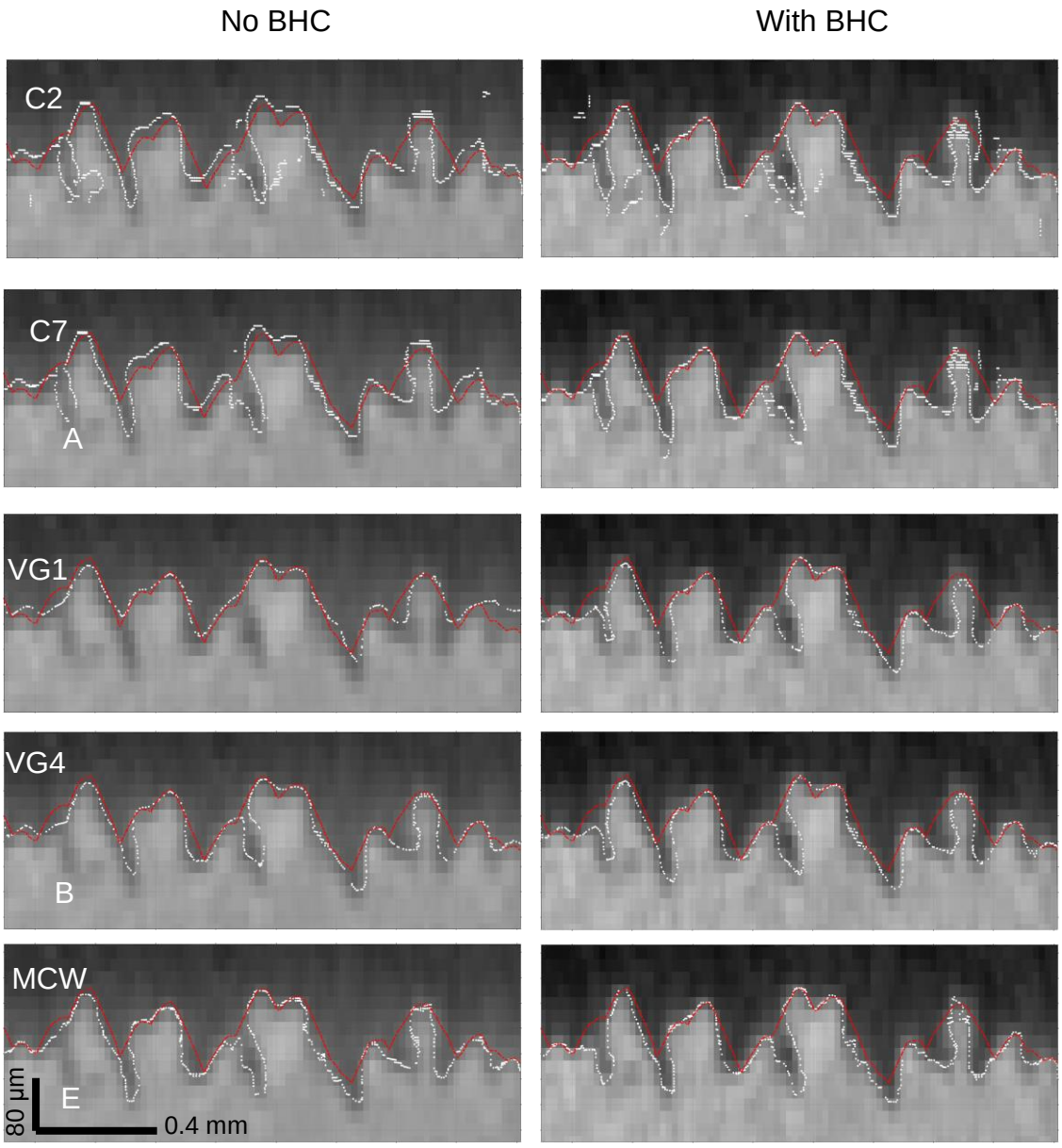

Figure 6-14: The SD results of C2, C7, VG1, VG4, MCW on surface texture before and after BHC. The white dots correspond to SD profiles and red dash line is the CS profile. The XCT reconstructed slices are shown as the background. The image was captured from the dashed rectangular region of Figure 6-7

6.3.3 Similarity comparison

The similarity between the XCT and CS profiles was studied after applying the morphological transformation of the XCT point cloud data. The similarity employed the metric of *diff* calculated by

$$diff = \sqrt{\frac{\sum_{i=1}^{n}(y_i - \overline{y}_i)^2}{n}} \quad \textbf{(6-3)}$$

where n is the number of sampling points on the CS data, y_i and $\overline{y}_i$ are the vertical location of the XCT and CS profile at the same horizontal location *I,* respectively. A lower *diff* value indicates higher similarity between the XCT and CS profiles. Figure 6-15 compares two different XCT plots after morphological transformation and the CS profile with different *diff* values.

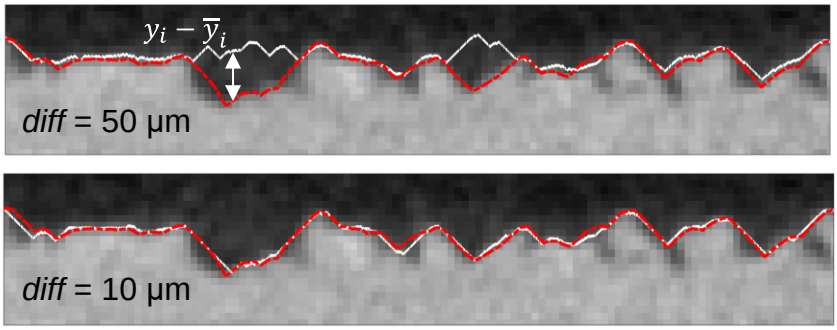

Figure 6-15: The systematic sketch of *diff* metric between XCT (while solid line) and CS profile (red dash line). The morphological profile of high and low *diff* corresponds to VG1 and MCW without BHC individually.

Figure 6-16 presents the similarity results between SD optimisation results and the CS profile with and without BHC.

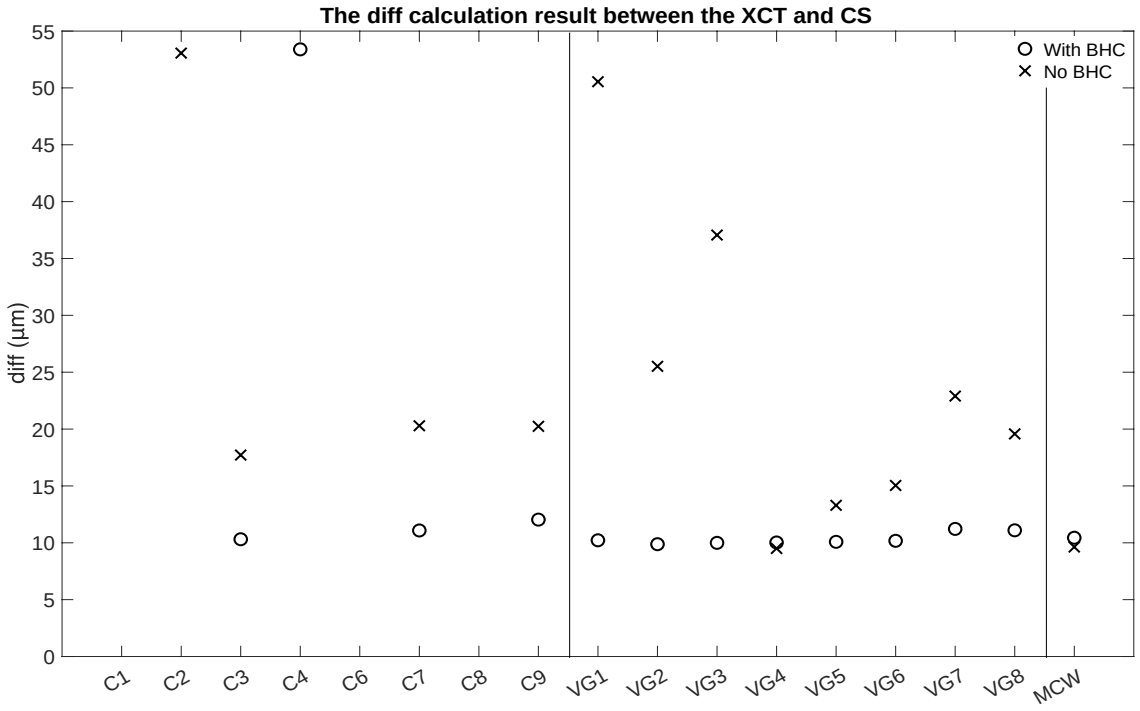

Figure 6-16: The similarity comparison results between XCT and CS profiles. The *diff* range is limited to (0 to 55) µm.

Canny had the worst performance. C1 had a very low 'higher threshold' value, which led to a high level of noise that deterred the morphological filtration, and C5 (not shown in the chart) returned no surface because the low threshold was set higher than 0.8. Only C3, C6 and C7 successfully detected the surface with and without BHC, and the similarity values with BHC were approximately 11 µm lower than the one without BHC. According to Figure 6-13-C7, the profile without BHC deviated towards the background region compared with the scanning with BHC, hence a larger *diff* value without BHC. The best result from Canny was C3 under BHC, with the *diff* equal to 10.5 µm only.

All VG algorithms successfully detected the rough surfaces, and most of the VG *diff* values were found to be below 30 µm, except for VG1 and VG3 without BHC. The VG algorithm performance varied without BHC: the average *diff* with the low search distance (40 µm for VG1 and VG2) was higher than those with the higher search distance (80 µm for VG3 & VG4 and 200 µm for VG5 and VG6); VG4 obtained the best *diff* value of 9.7 µm. The initial threshold for starting contour of

the VG algorithm could deviate from the proposed surface, and a lower search distance limited the VG's ability to find the maximum gradient value around the proposed surface area, resulting in a high *diff* value. By increasing the search distance to up to 200 µm, the search range from the initial threshold could cover the proposed surface. Therefore, the *diff* presented a significant decrease. Interestingly, further increasing the search distance (400 µm for VG7 & VG8) did not help to decrease the *diff* value. This is because a larger search distance reduced the capability of surface detection with high spatial frequency or resulted in a more 'smoothed' surface. Moreover, according to Chapter 5, VG's search distance setting is sensitive to beam hardening artefact. When BHC was applied, a significant decrease of *diff* was observed, in an average 11 µm, and proved to be less sensitive to the user settings.

All MCW trials applied for profile extraction with or without BHC showed the lowest *diff* results among all the investigated algorithms, where the MCW without BHC had a *diff* of only 9.2 µm, and the *diff* difference between with and without BHC was not obvious. This result strongly demonstrated that MCW algorithm outperformed all SD trials from VG and Canny, showing robustness to beam hardening and noise.

It was interesting to find that none of the SD algorithms achieved a *diff* value below 9 µm (or around ½ of the voxel size). This could be due to the CS noise [163], finite pixel size of the XCT detector and the finite focal spot size [2]. Finite focal spot size can cause blur on the projection image, which can be detrimental to the measurement of small features, such as valleys [2].

6.3.4 Residual comparison

Figure 6-17 presents the residual profiles between the optimised SD algorithm results and CS. The means and standard deviations of the residual profiles are presented in Table 6-4. The maximum residual error (40 µm) was half of the one reported in a previous study by Wenjuan [76]. This was facilitated mainly by the measurement colocation strategy (see the methodology section of this chapter).

Also, in [76] a mesh transformation built in VG towards the XCT surface was applied. Leach [130] stated that the mesh transformation could incorrectly correlate adjacent XCT point clouds, causing potential errors in the SD [130]. This work only used the raw XCT data for evaluation to avoid additional errors from mesh conversion.

MCW after BHC showed the least errors, outperforming the other algorithms. MCW was able to form the connected single surface with the help of geodesic and watershed transformations and avoided over-segmentation. An important concept of MCW is connectivity, which was set as six in this study. This means that only the voxels connected by face were considered as connected. Therefore, MCW considered the regional maximum gradient, which can be influenced by beam hardening, and forced all points belonging to the watershed surface to be connected.

VG algorithm residual error before BHC was 1.853 µm and after BHC -0.69 µm, which was in accordance with previous studies [110]. Another explanation is that beam hardening limited the ability of SD to detect the narrow valley area, which also can be regarded as material dilation. Optimised Canny (C3) showed the worst result, with a mean of residual -1.34 µm, even with BHC.

At some particular horizontal locations, such as 1.3 mm, 2.1 mm, and 2.3 mm, there were significant residual errors of up to -35 µm, meaning that the CS data were higher than XCT. A possible explanation is the limitation of the 2D morphological transformation, as shown in Figure 6-5. However, in stylus tip can be influenced by the adjacent structure along the movement path.

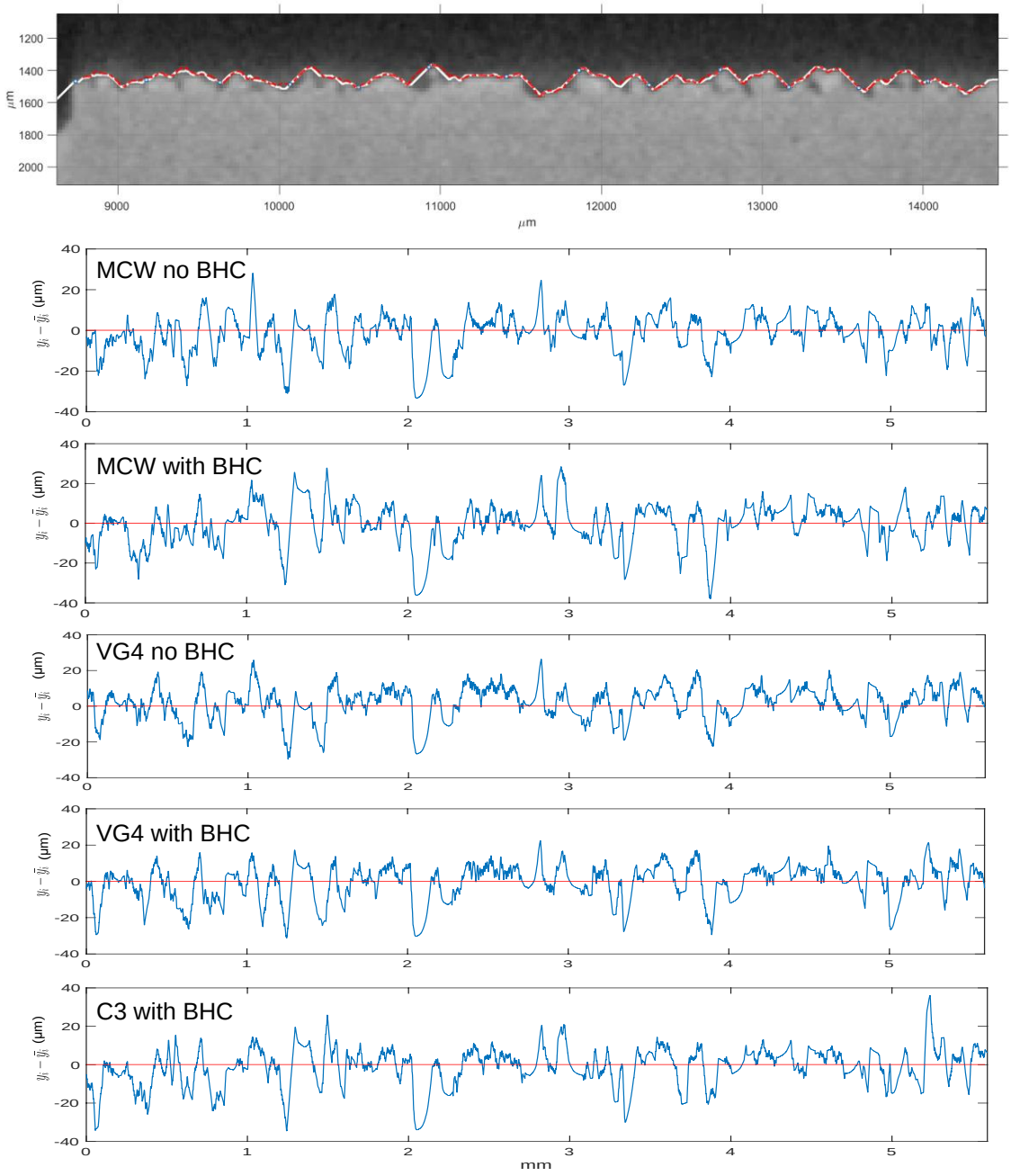

Figure 6-17: First image: The superimposed image containing the morphological profile of XCT with MCW SD algorithm (solid white line), CS profile (red dash line), without BHC. The second to the sixth image: the plot of $y_i - \overline{y}_i$ with the selected optimised SD algorithms. All images are aligned horizontally.

Table 6-4: The mean and standard deviation of residual, where minus means towards the material

	MCW no BHC	MCW with BHC	VG4 no BHC	VG4 with BHC	C3 with BHC
Mean of residual (μm)	-1.4	-0.48	1.853	-0.69	-1.34
σ (μm)	9.5	10.43	9.32	10	10.2

6.3.5 Limitation

It is worth mentioning that this experimental work only included one XCT scanning, therefore the surface texture measurement repeatability/reproducibility was not evaluated. This work only considered the repeatability due to surface determination process. Further research should include repeated XCT scanning for surface texture measurement.

6.3.6 Synthetic Result

The complete comparison of the residual of the surface against the nominal mesh surface is shown in Appendix D. All reported mean values of the residual errors were below 0.15 μm, for down-skin and top-skin synthetic data, and below 0.02 μm, for top surface. The average standard deviations of the residual for down-skin, top and up-skin synthetic data were 1.5, 1.1 and 1.5 μm, respectively. Unlike the experimental data, where SD's performance could vary significantly, no significant differences were found for the surface data generated by MCW, VG and Canny. This proves that XCT is in good agreement with the optical measurement of AM surfaces with different roughness.

Figure 6-18 to Figure 6-20 present the distribution of the deviation of the point cloud to the mesh surface for down-skin, top and up-skin surfaces individually. For the down-skin surface, it can be observed that the point cloud generated by MCW algorithm had the least outlier range.

When VG was applied to the polychromatic data with noise factor = 2, the outlier range increased to 40 μm. The search distance larger than 5 voxels (100 μm) ensured that the desired surface area was covered, however higher search distance forced VG to be affected by the noise.

Meanwhile, the polychromatic simulations led to a large number of positive outliers in Canny and VG, suggesting that these two algorithms were more sensitive to beam hardening errors and noise.

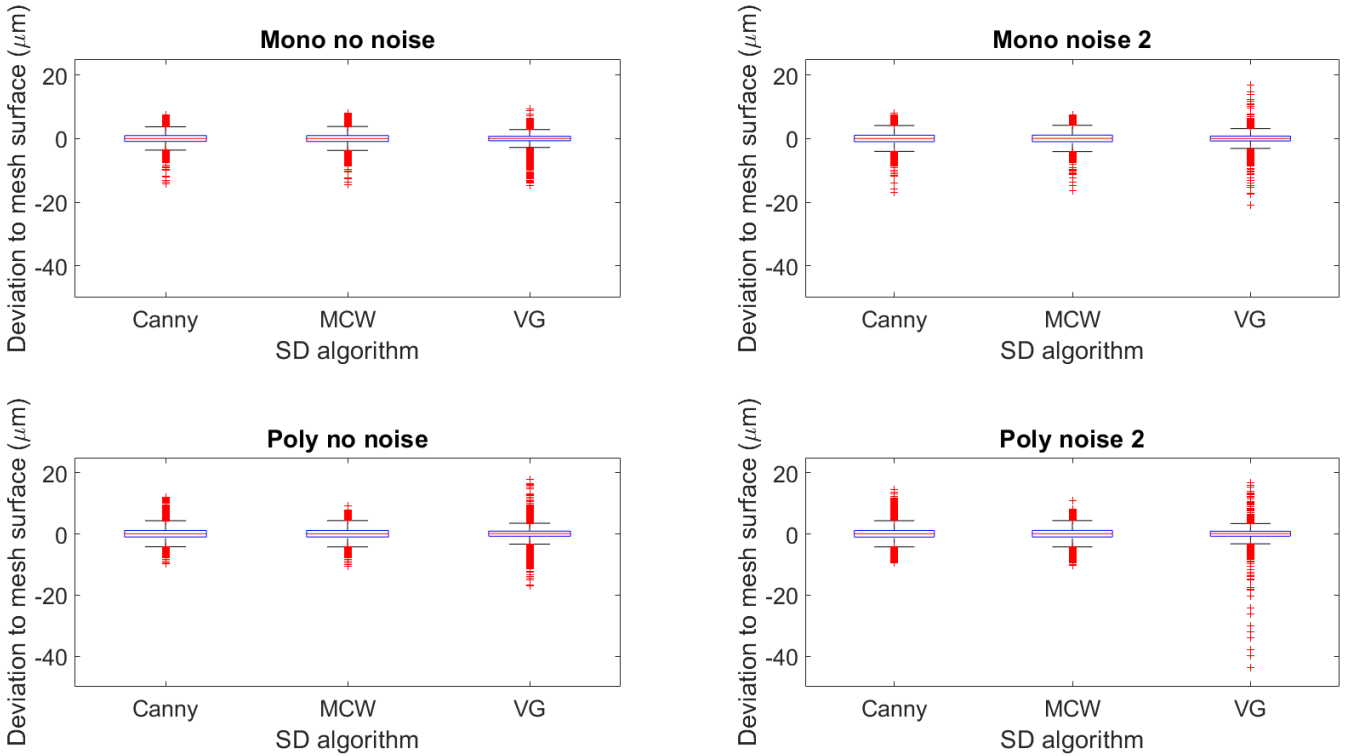

Figure 6-18: The box plot describing the distribution of the deviation of the point clouds from the mesh surface for the down-skin surface (S_a = 20 µm). Each box plot reports the median, interquartile range, whiskers, and outliers (red plus sign).

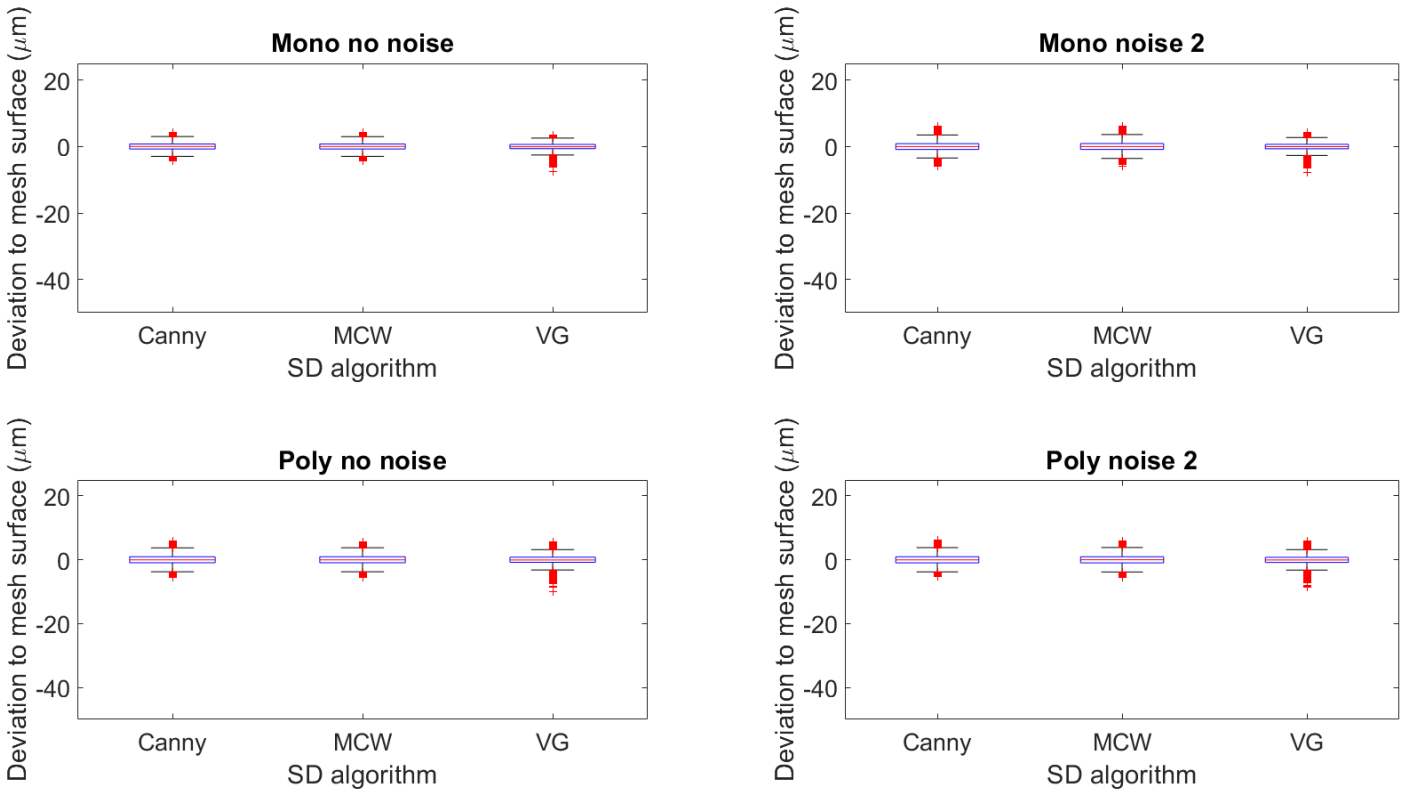

Figure 6-19: The box plot describing the distribution of the deviation of the point clouds from the mesh surface for the top surface (S_a = 5 µm). Each box plot reports the median, interquartile range, whiskers, and outliers (red plus sign).

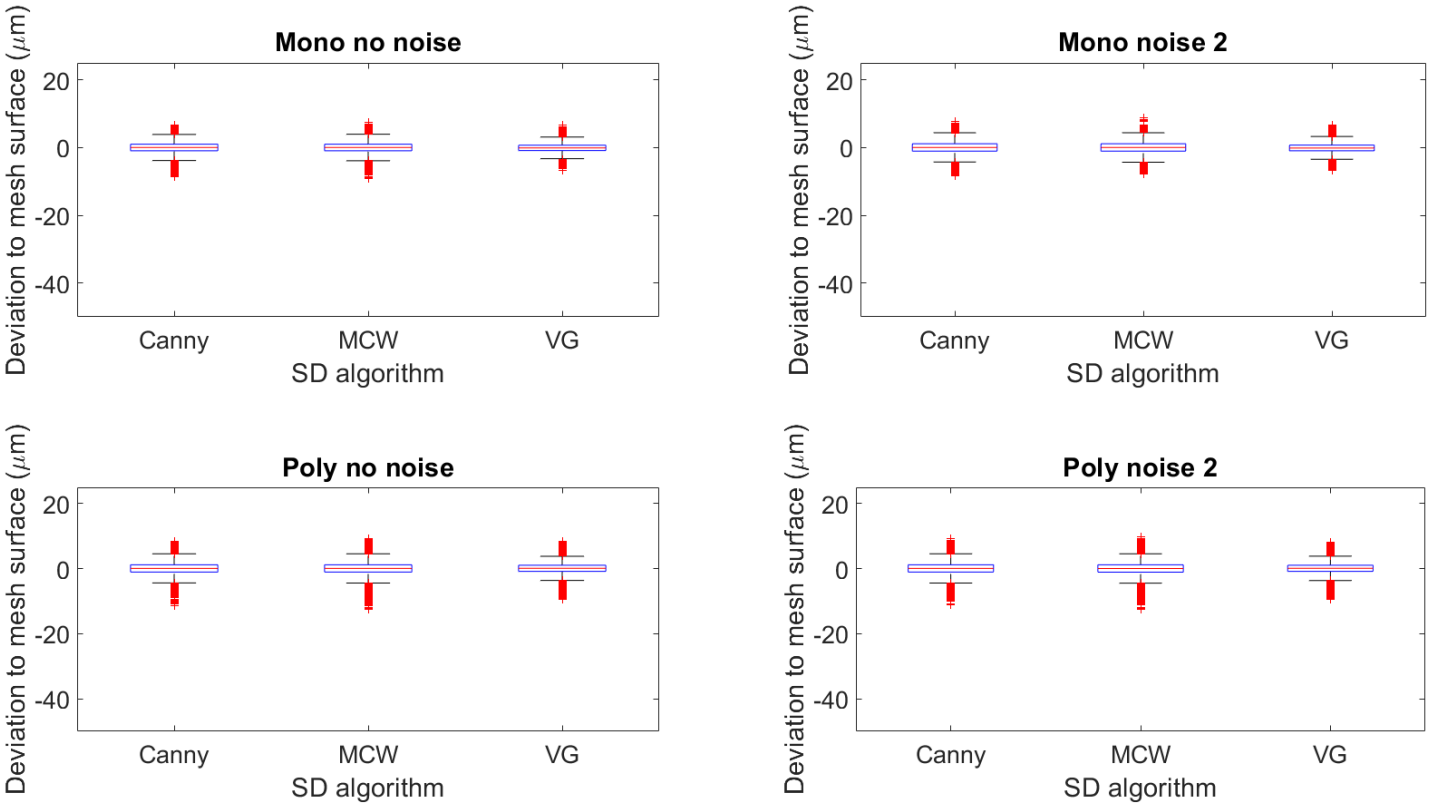

Figure 6-20: The box plot describing the distribution of the deviation of the point clouds from the mesh surface for the up-skin surface (S_a = 15 µm). Each box plot reports the median, interquartile range, whiskers, and outliers (red plus sign).

6.4 Conclusion

In this chapter the performance of SD algorithms on surface texture measurement using XCT was reported. The methodology used both experimental and simulation work. Previous research [76, 83, 150, 157] only applied the VG algorithm to determine the surface, without considering the effect of SD algorithms on surface texture measurements.

The experimental work used a CS to measure a roughness at a well-defined position, which allowed for the first time the colocation with the profile extracted from XCT measurements of an AM manufactured sample. The artificial surfaces (S_a from 5 µm to 20 µm) generated using PGGAN [290] were employed, to evaluate the SD algorithms on different types of surfaces.

A summary of the experimental work findings is listed below:

- MCW algorithm provided the best surface profile fidelity and did not need special threshold optimisation. The difference of CS vs XCT (MCW) Ra values of 0.2 µm was 6 % of the error recorded previously [76].
- Canny had the worst performance. Only three trials of Canny algorithm successfully detected the surfaces even after BHC.
- VG showed excellent performance under BHC. Without BHC, VG1 generated surface errors due to the short search distance. VG also ‘smoothed’ the surface and managed to reduce the number of surface errors, but sacrificed the ability to detect more ‘detailed’ surface texture features, causing lower roughness values.

The result from synthetic data showed that XCT is capable of measuring a wide variety of surfaces with different levels of roughness. There were no significant differences between the SD algorithms, however, the simulated data was generated using prior optical measurements, which did not have out-of-sight type features.

In conclusion, the MCW algorithm outperformed Canny and VG, especially in the presence of beam hardening errors and noise. MCW provided the surface texture with good fidelity, since MCW did not need to perform smoothing prior to

application. Smoothing effect from VG limited its ability to detect the narrow valley with widths less than 60 μm.

The XCT surface texture advantage ability to detect features that traditional CS cannot measure has been proved.

Future work should include the following:

- Development of 3D morphological transformation to allow better comparison with the CS.
- The non-line-of-sight measurement traceability.
- The comparison between the simulation and experimental data for surface texture measurement should be considered. The simulation should consider other complex factors, such as scattering, focal spot size, etc.

7 Conclusion, thesis summary and future work

Conclusion of the work

In conclusion, this work contributes to existing knowledge of XCT dimensional metrology. The thesis studies the influence of SD algorithms on XCT for dimensional metrology. An advanced algorithm has been established based on MCW. Together with the other two popular SD algorithms, these three SD methods were studied in a few cases representing the most common applications in industry. Especial consideration has been given to both smooth and rough surface measurements.

The key strength of this study rests with the application of the MCW algorithm for both bi-directional and surface texture measurement, allowing end users to control the SD process conveniently without compromising accuracy and fidelity.

Thesis summary

The overall aim of this work, to evaluate the impact of the SD algorithms in the uncertainty associated with the XCT dimensional measurements, contributes to the development of traceability XCT dimensional measurements, which includes form, waviness and roughness.

XCT is a promising tool for dimensional metrology [2, 10] because unlike the traceable conventional measurement techniques, such as CMM and CS that depend on the mechanical contact of their probe with the surface of the component and cannot measure complex features and the internal structures [10, 294], XCT offers a non-destructive way to visualize out-of-sight geometrical features [10]. However, there are no dedicated dimensional measurement international standards for XCT [10], mainly because XCT is a complex system that lacks a comprehensively validated measurement model.

SD is an essential mathematical process that directly influences the measurement result of the XCT [3, 10]. SD aims to find, often with a sub-voxel resolution, the boundary situated in the transition area between the object and the background [3]. To achieve traceable and accurate XCT dimensional

measurements, a robust SD algorithm is needed. However, SD algorithms are often sensitive to systematic errors, such as beam hardening and noise, and can be largely influenced by the input parameters selected by operators [2, 3, 10, 22, 43].

Beam hardening is an error related to the incorrection assumption during reconstruction, which assumes that the X-ray source ejects monochromatic photons while in reality, the X-ray beam has a polychromatic spectrum [43]. Previous research demonstrated that beam hardening causes material dilation [43, 154]. Noise effect can originate from various factors, such as detector noise, scattering, etc. [300, 301]. Therefore, both beam hardening and noise can introduce errors in the measurement results.

The main goal of the current study was to investigate the influence of SD on the accuracy of the XCT dimensional measurement and develop and evaluate a new transparent and automated SD method that eliminates the operator-induced errors and reduces the impact of beam hardening and noise.

To clarify the gaps in knowledge, Chapter 2 reviews the following aspects: the basic concept of dimensional measurement, including the new SI system and uncertainty budget; the basic concept and components of XCT, which introduced the error from beam hardening; XCT traceability and basic concepts of CMM and CS, which are two main measurement techniques to provide traceability for XCT dimensional metrology in terms of form and surface texture measurement, respectively. The review found that previous interlaboratory comparison work did not take SD algorithms into account adequately, especially regarding bi-directional and surface texture measurement.

Most industrial users and researchers use commercial software, such as VG [37, 41, 43, 45, 74, 78, 150-153, 221, 226-239], containing several parameters that allow users to optimise/change the SD results. Often the effect of those parameters on the measurement result is not clearly understood [154]. Another common SD algorithm, mostly used in research, is based on the Canny algorithm [31], which again needs a trial-and-error optimisation process [22, 29, 43, 44, 100, 224]. The review of global threshold and local adaptive methods highlighted

the complexity of the control factors within those SD algorithms and that they can influence the measurement results, especially under the influence of beam hardening and noise, and hereby review explored the potential advantage of watershed algorithms. The review points out a gap: a need for a robust SD algorithm. It was found that MCW was successfully applied in the medical field. However, its use for the XCT dimensional work, which requires high energy to penetrate higher-density material, was not explored.

In response to the highlighted gaps, this study developed a procedure for 3D automatic MCW that meets the requirement of a transparent and automated SD algorithm, which is presented in Chapter 3. There are four steps in the MCW implementation: 3D marker generation, gradient transformation, 3D geodesic transformation, 3D watershed transfer function, and voxel refinement. The foreground and background markers were determined automatically by combining the closing and erosion operators, and the geodesic transformation eliminates all regional catchment basins to overcome the over-segmentation problem. The contribution of this work is that the MCW and sub-voxel refinement was integrated into MATLAB software, and there is only one parameter for an end user to adjust: the struct size for marker erosion and dilation. By applying this function, the end user does not need to select various parameters, and the MCW SD algorithm can be applied in one step.

MCW algorithm was then tested and validated using real and simulated data and then compared with other SD algorithms in Chapters 4 to 6. A range of reference samples was carefully selected to assist the investigation. In Chapter 4, a stack tube sample was used to study the SD algorithms in 2D slices. In Chapter 5, a two-sphere sample was selected, which enables the study of uni-directional and bi-directional measurement in the 3D range. In Chapter 6, an AM sample with surface texture was measured, which allows the investigation of the capability of SD algorithms for determining small features.

A preliminary study of the MCW application has been published in NDT & E [3] and presented in Chapter 4. This study used the phantom stack tube sample to enable the measurement of inner and outer diameters simultaneously. It was

identified that, unlike the Canny algorithm which needs trial-and-error tests to optimise the SD results, MCW algorithm could effectively compute closed inner and outer edges and avoid the error from the user settings. Data interpolation was still necessary to obtain sub-pixel surface point clouds, however, subdividing the pixel below 1/25 of its original size did not provide significant improvements. It was also found that under polychromatic conditions, measurement of the inner cylinder led to smaller errors of up to 0.4 % of pixel size, whereas outer feature measurement error was as large as 2.5 % of pixel size. Meanwhile, a linear correlation between the RMS of the residual of the point cloud against the fitted circle and the interpolation ratio was discovered. The relevance of the relationship between beam hardening and outer material dilation is clearly supported by the current findings. The research demonstrated the resilience of the MCW algorithm to beam hardening effect and noise.

The study In Chapter 5 aimed to conduct a comprehensive Investigation of the influence of SD algorithms on bi-directional measurement, which is related to the first gap. The measurement and simulation of XCT of a two-sphere sample were conducted to assess three SD algorithms: VG, Canny and MCW. All SD algorithms were optimised by adjusting the commonly used user settings, and the Taguchi plan was introduced for the implementation of VG. For measurement data, without applying BHC, most of the Canny and all MCW returned a similar result with a radius deviation of 1.25 μm (voxel size = 25 μm). The investigation of VG optimisation has shown that the VG algorithm was sensitive to all user settings, and search distance led to the largest difference in the calculated value of the sphere radius. After applying BHC, the measurement errors using all three SD algorithms were reduced dramatically. MCW and Canny delivered the radius error of -5 nm and 27 nm, respectively. The findings of this research provide insights into the confidence of XCT measurement: if proper SD and BHC are applied, the result from MCW and Canny were within the standard uncertainty of CMM (50 nm). VG also showed lower sensitivity to user parameter variations after applying BHC, but the resulting errors (-490 nm) were higher than CMM uncertainty.

The polychromatic simulation case study looked in detail into the influence of ‘streak’ artefacts (Figure 1-4), which has not been studied before [10, 22, 154, 301]. The ‘streak’ artefact often appears between two closed objects. In certain threshold settings, the canny algorithm could not detect the surface data around the area affected by the ‘streak’ artefact. VG algorithm also encountered problems around the ‘streak’ artefact when a lower search distance (lower than four voxels) was selected. Nevertheless, MCW provided exceptional performance when handling data with streak artefacts.

In this case study, the results indicate that SD algorithms are not the major source of errors and uncertainty. For the first time, the influence of SD on bi-directional measurement error was quantified, reinforcing the novelty of the work.

Chapter 5 also highlighted that there are issues regarding missing surface data using certain settings of SD algorithms. For smooth surface and bidirectional measurement, the loss of surface data may not affect the accuracy of the results. However, this is not the case for rough surface measurements.

Chapter 6 explores the influence of the SD algorithm on surface texture measurement using XCT. This work was completely not been investigated in previously known research, as most of the previous studies [76, 83, 150, 157] only applied the VG algorithm to determine the surface. However, no study of the influence of the SD algorithm was undertaken.

Both experimental and simulation studies were conducted. For experimental work, a roughness sample [76] designed by NPL was used. CS profilometer measured the surface at a well-defined position on the sample and compared it with the profile extracted from the XCT measurement results with all three SD algorithms.

The fidelity estimate demonstrated that MCW was extremely good robust to beam hardening and noise, with a R_a value difference between XCT (MCW) and CS of 0.2 µm only, 6 % of error recorded previously [76], and outperformed the other two algorithms. Canny recorded the worst performance, and only three trials of the Canny algorithm successfully detected the surfaces even with BHC, whereas

some returned very large surface errors. All VG data showed excellent performance with BHC. Without BHC, VG1 generated noise data due to insufficient search distance around the ISO global threshold, which could be largely affected by beam hardening. All standard deviations of the residual were around 10 μm, which is half of the voxel size. This may be due to the digitisation of the volume data, CS noise, and finite focal spot size of XCT.

Three sets of artificial surfaces generated by PGGAN [290] were used to represent the rough surface with different spatial frequencies. Results from synthetic data demonstrated that XCT is capable of measuring a wide variety of surfaces with different levels of roughness (Sa ranging from 5 to 20 μm). There were no significant SD differences in the simulated XCT data.

In summary, these findings in Chapter 6 suggest the important role that XCT can have in measuring the surface texture, including non-line-of-sight features, which CS has restricted access to. Also, these findings contribute to the increased understanding of the difference between CS and XCT. The roughness profiles were presented in a novel way of overlapping them on associated slices extracted from XCT reconstructed images, enabling a better qualitative fidelity assessment.

Based on the results from Chapters 5 to 6, the results clearly provided the influence of SD algorithms on dimensional measurement in both smooth and rough surface measurement. Canny performed worst in experimental surface texture measurement, which makes it difficult for the end user to properly select the required threshold in the first instance. VG performed worst in bi-directional measurement under the influence of beam hardening. Increasing the search distance can be detrimental to the measurement results in both bi-directional and surface texture measurement, because it reduces its ability to detect small-size features.

The contributions to knowledge are:

- A robust SD algorithm was proposed enabling fewer control factors in a transparent script, allowing end-users to operate the SD process in XCT

dimensional metrology conveniently while reducing the error from beam hardening and noise.

- Direct comparison between the CS and XCT profiles is applicable, with the implementation of the colocation strategy of the XCT profile written in script and proper data alignment.
- This work demonstrates that with proper SD and BHC implementation, the measurement error of XCT can sit within the uncertainty of CMM (50 nm when k = 1)
- This work comprehensively compared the different SD algorithms with the outcome of optimised measurement results with the influence of beam hardening and noise for both smooth and rough surface measurements.
- The work related to the preliminary MCW results was published in NDT & E [3].
- The work related to the SD performance in smooth surfaces will be published in Precision Engineering.
- The work related to the SD performance in rough surfaces will be published in Additive Manufacturing.

Future works

Finally, future work should investigate the following:

- The effect of scattering [43] and focal spot size [143], which have been proven to deteriorate the measurement result and SD's performance.
- The MCW's validation for the measurement of inner features.
- A 3D morphological filter applied to the XCT profile to address the potential systematic errors between XCT and CS profiles.
- The effect of a wider range of textures using additional synthetic data to clearly pinpoint the limitations of XCT roughness measurements.
- The comparison between the simulation and experimental data for surface texture measurement should be considered. The simulation should consider other complex factors, such as scattering, focal spot size, etc.

REFERENCES

1. Wenig, P. and S. Kasperl, *Examination of the Measurement Uncertainty on Dimensional Measurements by X-ray Computed Tomography*. 2006.

2. Sun, W., S.B. Beown, and R.K. Leach, *An overview of industrial X-ray computed tomography*. 2012: National Physical Laboratory.

3. Yang, X., W. Sun, and C.L. Giusca, *An automated surface determination approach for computed tomography.* NDT & E International, 2022. **131**: p. 102697.

4. Sun, W., et al., *Review of high energy x-ray computed tomography for non-destructive dimensional metrology of large metallic advanced manufactured components.* Reports on Progress in Physics, 2022. **85**(1): p. 016102.

5. Seifi, M., et al., *Progress Towards Metal Additive Manufacturing Standardization to Support Qualification and Certification.* JOM, 2017. **69**(3): p. 439-455.

6. Thompson, A., et al., *X-ray computed tomography and additive manufacturing in medicine: a review.* Int. J. Metrol. Qual. Eng., 2017. **8**: p. 17.

7. Vogeler, F., et al., *Positional Stability of 2D X-ray Images for Computer Tomography*. 2011.

8. Siewerdsen, J.H. and D.A. Jaffray, *Optimization of x-ray imaging geometry (with specific application to flat-panel cone-beam computed tomography).* Medical Physics, 2000. **27**(8): p. 1903-1914.

9. Carmignato, S., et al., *Dimensional artefacts to achieve metrological traceability in advanced manufacturing.* CIRP Annals, 2020. **69**(2): p. 693-716.

10. Villarraga-Gómez, H., E.L. Herazo, and S.T. Smith, *X-ray computed tomography: from medical imaging to dimensional metrology.* Precision Engineering, 2019. **60**: p. 544-569.

11. Youssef, S., E. Maire, and R. Gaertner, *Finite element modelling of the actual structure of cellular materials determined by X-ray tomography.* Acta Materialia, 2005. **53**(3): p. 719-730.

12. Leach, R., et al., *Metrological characteristics for the calibration of surface topography measuring instruments: a review.* Measurement Science and Technology, 2020. **32**(3): p. 032001.

13. Moylan, S., et al., *PROPOSAL FOR A STANDARDIZED TEST ARTIFACT FOR ADDITIVE MANUFACTURING MACHINES AND PROCESSES.* 2012.

14. Moylan, S., et al., *An Additive Manufacturing Test Artifact.* Journal of research of the National Institute of Standards and Technology, 2014. **119**: p. 429-59.

15. Rivas Santos, V.M., et al., *Design and characterisation of an additive manufacturing benchmarking artefact following a design-for-metrology approach.* Additive Manufacturing, 2020. **32**: p. 100964.

16. Senin, N., A. Thompson, and R.K. Leach, *Characterisation of the topography of metal additive surface features with different measurement technologies.* Measurement Science and Technology, 2017. **28**(9): p. 095003.

17. Teeter, M.G., et al., *Metrology test object for dimensional verification in additive manufacturing of metals for biomedical applications.* J Engineering in Medicine, 2015. **229**(1): p. 20-27.

18. Reimers, P. and J. Goebbels, *New possibility of nondestructive evaluation by X-Ray computed tomography.* 1983.

19. Feldkamp, L.A., L.C. Davis, and J.W. Kress, *Practical cone-beam algorithm.* Josa a, 1984. **1**(6): p. 612-619.

20. Kruth, J.P., et al., *Computed tomography for dimensional metrology.* CIRP Annals, 2011. **60**(2): p. 821-842.

21. *VDI/VDE 2630 Blatt 1.2, Technische Regel, Entwurf, 2008-12, Computertomografie in der dimensionellen Messtechnik - Einflussgrößen auf das Messergebnis und Empfehlungen für dimensionelle Computertomografie-Messungen* 2008.

22. Lifton, J.J., A.A. Malcolm, and J.W. McBride, *On the uncertainty of surface determination in x-ray computed tomography for dimensional metrology.* Measurement Science and Technology, 2015. **26**(3): p. 035003.

23. Gómez, H.V., *Studies of dimensional metrology with X-ray CAT scan*. 2018, The University of North Carolina at Charlotte.

24. Sun, W., et al., *Applications and systematic errors of X-ray computed tomography associated with dimensional metrology.* 2016.

25. Flay, N., et al., *Effects of off-focal radiation on dimensional measurements in industrial cone-beam micro-focus X-ray computed tomography systems.* Precision Engineering, 2020. **66**: p. 472-481.

26. Lohvithee, M., et al., *Ant colony-based hyperparameter optimisation in total variation reconstruction in X-ray computed tomography.* Sensors, 2021. **21**(2): p. 591.

27. Sun, W., et al., *A reference sample for investigating the stability of the imaging system of x-ray computed tomography.* Measurement Science and Technology, 2016. **27**(8): p. 085004.

28. Jcgm, *Evaluation of measurement data-Guide to the expression of uncertainty in measurement Évaluation des données de mesure-Guide pour l'expression de l'incertitude de mesure*. 2008.

29. Yagüe-Fabra, J.A., et al., *A 3D edge detection technique for surface extraction in computed tomography for dimensional metrology applications.* CIRP Annals, 2013. **62**(1): p. 531-534.

30. Jiménez-Pacheco, R., S. Ontiveros, and J.A. Yagüe-Fabra, *A surface extraction analysis in a multi-material test part for computed tomography in metrology applications.* Procedia Manufacturing, 2017. **13**: p. 487-494.

31. Canny, J., *A computational approach to edge detection.* IEEE Trans Pattern Anal Mach Intell, 1986. **8**(6): p. 679-98.

32. Kowaluk, T. and A. Wozniak, *A new threshold selection method for X-ray computed tomography for dimensional metrology.* Precision Engineering, 2017. **50**: p. 449-454.

33. MacAulay, G.D., et al., *Comparison of segmentation techniques to determine the geometric parameters of structured surfaces.* Surface Topography: Metrology and Properties, 2014. **2**(4): p. 044004.

34. Lifton, J.J. and T. Liu, *Evaluation of the standard measurement uncertainty due to the ISO50 surface determination method for dimensional computed tomography.* Precision Engineering, 2020. **61**: p. 82-92.

35. Otsu, N., *A Threshold Selection Method from Gray-Level Histograms.* IEEE Transactions on Systems, Man, and Cybernetics, 1979. **9**(1): p. 62-66.

36. Reinhart, C. and W. Weg. *INDUSTRIAL COMPUTER TOMOGRAPHY - A UNIVERSAL INSPECTION TOOL*. 2008.

37. Hiller, J. and P. Hornberger, *Measurement accuracy in X-ray computed tomography metrology: Toward a systematic analysis of interference effects in tomographic imaging.* Precision Engineering, 2016. **45**: p. 18-32.

38. Ahmed, O. and Y. Song, *A Review of Common Beam Hardening Correction Methods for Industrial X-ray Computed Tomography.* Sains Malaysiana, 2018. **47**(8): p. 1883-1890.

39. Brabant, L., et al., *A novel beam hardening correction method requiring no prior knowledge, incorporated in an iterative reconstruction algorithm.* NDT & E International, 2012. **51**: p. 68-73.

40. Cao, W., et al., *A simulation-based study on the influence of the x-ray spectrum on the performance of multi-material beam hardening correction algorithms.* Measurement Science and Technology, 2018.

41. Dewulf, W., Y. Tan, and K. Kiekens, *Sense and non-sense of beam hardening correction in CT metrology.* CIRP Annals, 2012. **61**(1): p. 495-498.

42. Herman, G.T., *Correction for beam hardening in computed tomography.* Physics in Medicine and Biology, 1979. **24**(1): p. 81-106.

43. Lifton, J.J., *The Influence of Scatter and Beam Hardening in X-ray Computed Tomography for Dimensional Metrology*. 2015, University of Southampton.

44. Lifton, J.J., A.A.M.J.o.X.r.S. …, and undefined, *A simulation-based study on the influence of beam hardening in X-ray computed tomography for dimensional metrology.* content.iospress.com, 2015.

45. Lifton, J.J. and S. Carmignato, *Simulating the influence of scatter and beam hardening in dimensional computed tomography.* Measurement Science and Technology, 2017. **28**(10).

46. Lifton, J.J., A.A. Malcolm, and J.W. McBride, *An experimental study on the influence of scatter and beam hardening in x-ray CT for dimensional metrology.* Measurement Science and Technology, 2016. **27**(1): p. 015007.

47. Rasoulpour, N., A. Kamali-Asl, and H. Hemmati, *A new approach for beam hardening correction based on the local spectrum distributions.* Nuclear Instruments and Methods in Physics Research Section A: Accelerators, Spectrometers, Detectors and Associated Equipment, 2015. **794**: p. 177-184.

48. Tan, Y., et al., *Simulation-aided investigation of beam hardening induced errors in CT dimensional metrology.* Measurement Science and Technology, 2014. **25**(6): p. 064014.

49. Tan, Y., et al., *Beam hardening correction and its influence on the measurement accuracy and repeatability for CT dimensional metrology applications*. 2012.

50. Van Gompel, G., et al., *Iterative correction of beam hardening artifacts in CT.* Medical Physics, 2011. **38**(S1): p. S36-S49.

51. Zhang, X., et al., *Improving the accuracy of CT dimensional metrology by a novel beam hardening correction method.* Measurement Science and Technology, 2014. **26**(1): p. 015007.

52. Boone, J.M. and J.A. Seibert, *An analytical model of the scattered radiation distribution in diagnostic radiology.* Medical physics, 1988. **15**(5): p. 721-725.

53. Chan, H.-P. and K. Doi, *The validity of Monte Carlo simulation in studies of scattered radiation in diagnostic radiology*. 1983. p. 109-129.

54. Chan, H.-P. and K. Doi, *Physical characteristics of scattered radiation in diagnostic radiology: Monte Carlo simulation studies.* Medical Physics, 1985. **12**(2): p. 152-165.

55. Dremel, K. and T. Fuchs, *Scatter simulation and correction in computed tomography: A reconstruction-integrated approach modelling the forward projection.* NDT & E International, 2017. **86**: p. 132-139.

56. Ducote, J.L. and S. Molloi, *Scatter correction in digital mammography based on image deconvolution.* Physics in Medicine and Biology, 2010. **55**(5): p. 1295-1309.

57. Ivanchenko, V.N., et al., *Geant4 models for simulation of multiple scattering.* Journal of Physics: Conference Series, 2010. **219**(3): p. 032045.

58. Johns, P.C. and M. Yaffe, *Scattered radiation in fan beam imaging systems.* Medical Physics, 1982. **9**(2): p. 231-239.

59. Kanamori, H., et al., *Effects of scattered X-rays on CT images.* Physics in Medicine and Biology, 1985. **30**(3): p. 239-249.

60. Kyriakou, Y., T. Riedel, and W.A. Kalender, *Combining deterministic and Monte Carlo calculations for fast estimation of scatter intensities in CT.* Physics in Medicine & Biology, 2006. **51**(18): p. 4567.

61. Leliveld, C.J., *A fast Monte Carlo simulator for scattering in X-ray computerized tomography*. 1996.

62. Maltz, J.S., et al., *Focused beam-stop array for the measurement of scatter in megavoltage portal and cone beam CT imaging.* Medical Physics, 2008. **35**(6Part1): p. 2452-2462.

63. Neitzel, U., J. Kosanetzky, and G. Harding, *Coherent scatter in radiographic imaging: a Monte Carlo simulation study.* Physics in Medicine and Biology, 1985. **30**(12): p. 1289-1296.

64. Peterzol, A., J.M. Létang, and D. Babot, *A beam stop based correction procedure for high spatial frequency scatter in industrial cone-beam X-ray CT.* Nuclear Instruments and Methods in Physics Research Section B: Beam Interactions with Materials and Atoms, 2008. **266**(18): p. 4042-4054.

65. Rührnschopf And, E.-P. and K. Klingenbeck, *A general framework and review of scatter correction methods in cone beam CT. Part 2: Scatter estimation approaches.* Medical Physics, 2011. **38**(9): p. 5186-5199.

66. Rührnschopf, E.-P. and K. Klingenbeck, *A general framework and review of scatter correction methods in x-ray cone-beam computerized tomography. Part 1: Scatter compensation approaches.* Medical Physics, 2011. **38**(7): p. 4296-4311.

67. Schörner, K., M. Goldammer, and J. Stephan, *Comparison between beam-stop and beam-hole array scatter correction techniques for industrial X-ray cone-beam CT.* Nuclear Instruments and Methods in Physics Research Section B: Beam Interactions with Materials and Atoms, 2011. **269**(3): p. 292-299.

68. Sossin, A., et al., *Fast scattering simulation tool for multi-energy x-ray imaging.* Nuclear Instruments and Methods in Physics Research Section A: Accelerators, Spectrometers, Detectors and Associated Equipment, 2015. **802**: p. 60-66.

69. Thanasupsombat, C., et al., *A Simple Scatter Reduction Method in Cone-Beam Computed Tomography for Dental and Maxillofacial Applications Based on Monte Carlo Simulation.* BioMed research international, 2018. **2018**: p. 5748281-5748281.

70. Williams, B., *Compton scattering: the investigation of electron momentum distributions.* 1977.

71. Xie, S.-P. and L.-M. Luo, *Scatter correction for cone-beam computed tomography using self-adaptive scatter kernel superposition.* Chinese Physics C, 2012. **36**(6): p. 566-572.

72. Kraemer, A. and G. Lanza, *Assessment of the Measurement Procedure for Dimensional Metrology with X-ray Computed Tomography.* Procedia CIRP, 2016. **43**: p. 362-367.

73. Kathryn, M., et al., *Quantifying the Contribution of Post-Processing in Computed Tomography Measurement Uncertainty.* Procedia C I R P, 2016. **43**: p. 297-302.

74. Fleßner, M., et al., *Automated detection of artefacts for computed tomography in dimensional metrology.* Digital Industrial Radiology and Computed Tomography, 2015: p. 1-8.

75. Simone, C., D. Wim, and L. Richard, *Industrial X-Ray Computed Tomography*. 2018, Cham: Springer.

76. Sun, W., et al., *Establishment of X-ray computed tomography traceability for additively manufactured surface texture evaluation.* Additive Manufacturing, 2022. **50**: p. 102558.

77. office, G.I.c., *ISO 14660-1*, in *Geometrical product specifications (GPS) — geometrical features —*

Part 1: general terms and definitions. 1999.

78. Zanini, F., S.C.M.S.a. Technology, and undefined, *Two-spheres method for evaluating the metrological structural resolution in dimensional computed tomography.* iopscience.iop.org, 2017.

79. Bartscher, M., et al. *The resolution of dimensional CT-An edge-based analysis*. in *4th Conference on Industrial Computed Tomography*. 2012.

80. Carmignato, S., et al. *CT for industrial metrology-accuracy and structural resolution of CT dimensional measurements*. in *4th conference on industrial computed tomography (iCT)*. 2012.

81. Arenhart, F.A., et al., *Design of a multi-wave standard to evaluate the frequency response of CT measuring systems.* Proc. 10th ISMQC, Cracow-Kielce, Poland, 2013.

82. Izzo, J.R., et al., *Nondestructive Reconstruction and Analysis of SOFC Anodes Using X-ray Computed Tomography at Sub-50 nm Resolution.* Journal of The Electrochemical Society, 2008. **155**(5): p. B504-B504.

83. Thompson, A., et al., *Effects of magnification and sampling resolution in X-ray computed tomography for the measurement of additively manufactured metal surfaces.* Precision Engineering, 2018. **53**: p. 54-64.

84. Siu, W. and K. Hung. *Review of image interpolation and super-resolution*. in *Proceedings of The 2012 Asia Pacific Signal and Information Processing Association Annual Summit and Conference*. 2012.

85. Rosén, S., T.R. Thomas, and B.G. Rosén, *The Stedman diagram revisited.* Surface Topography: Metrology and Properties, 2013. **2**(1): p. 014005.

86. Stedman, M., *Basis for comparing the performance of surface-measuring machines.* Precision Engineering, 1987. **9**(3): p. 149-152.

87. Stedman, M., *Mapping The Performance Of Surface-Measuring Instruments*. Fourth International Symposium on Optical and Optoelectronic Applied Sciences and Engineering. Vol. 0803. 1987: SPIE.

88. Villarraga-Gómez, H., et al., *Representing the specification of industrial X-ray computed tomography with amplitude-wavelength space.* 2018.

89. Yang , T.-H. and J. Jackman *Form Error Estimation Using Spatial Statistics.* Journal of Manufacturing Science and Engineering, 1999. **122**(1): p. 262-272.

90. Thalmann, R., F. Meli, and A. Küng, *State of the Art of Tactile Micro Coordinate Metrology.* Applied Sciences, 2016. **6**(5): p. 150.

91. Stedman, M. and K. Lindsey, *Limits Of Surface Measurement By Stylus Instruments*. 1988 International Congress on Optical Science and Engineering. Vol. 1009. 1989: SPIE.

92. Yester, M. and G. Barnes, *Geometrical Limitations Of Computed Tomography (CT) Scanner Resolution*. Application of Optical Instrumentation in Medicine VI. Vol. 0127. 1977: SPIE.

93. Steffen, J.P. and T. Fröba, *Reducing the Focal Spot Shift of Microfocus X-ray Tubes to Increase the Accuracy of CT-Based Dimensional Measurement*. 2010.

94. Forbes, A.B. and H.D. Minh. *Form Assessment in Coordinate Metrology*. 2011. Berlin, Heidelberg: Springer Berlin Heidelberg.

95. Affenzeller, C., et al., *Measurement uncertainty evaluation of an X-ray computed tomography system.* 2015.

96. Bewoor, A.K. and V.A. Kulkarni, *Metrology and measurement*. 2009: McGraw-Hill Education.

97. Dotson, *Fundamentals of Dimensional Metrology*. 2015: Cengage Learning.

98. Standard, A., *Dimensioning and tolerancing—engineering drawing and related documentation practices.* ASME Y14. 5M-2018, ASME, USA, 2018.

99. Weights, I.B.o. and Measures, *International vocabulary of basic and general terms in metrology*. 1993: International organization for standardization.

100. Flay, N., *An investigation of the factors associated with the X-ray tube and their influence on dimensional measurement in micro-focus cane-beam industrial X-ray computed tomography systems*. 2016, University of Southampton. p. 185.

101. Weights, I.B.o., et al., *The international system of units (SI)*. 2001: US Department of Commerce, Technology Administration, National Institute of Standards and Technology.

102. Meaures, B.I.d.P.e., *The International System of Units*. 2019.

103. Bell, S.A., *A beginner's guide to uncertainty of measurement.* 2001.

104. ISO, B., *14253-2: 2011: Geometrical product specifications (GPS). Inspection by measurement of workpieces and measuring equipment. Guidance for the estimation of uncertainty in GPS measurement, in calibration of measuring equipment and in product verification. 2011.* British Standards Institute.

105. *Guide to the expression of uncertainty in measurement — Part 6: Developing and using measurement models.* 2020.

106. Podgoršak, E.B., *Radiation physics for medical physicists*. 2006: Springer.

107. Harding, G., *Inelastic photon scattering: Effects and applications in biomedical science and industry.* Radiation Physics and Chemistry, 1997. **50**(1): p. 91-111.

108. Acharya, T. and P.-S. Tsai, *Computational foundations of image interpolation algorithms.* Ubiquity, 2007. **2007**(October): p. 4-1.

109. Campilho, A., M. Kamel, and Elsevier, *Image analysis and recognition*. Lecture Notes in Computer Science 7324. 2012.

110. Thompson, A., et al., *X-ray computed tomography for additive manufacturing: a review.* 2016.

111. Zaidi, H. and M.R. Ay, *Current status and new horizons in Monte Carlo simulation of X-ray CT scanners.* Medical & Biological Engineering & Computing, 2007. **45**(9): p. 809-817.

112. *X-Ray Microcomputed Tomography in Additive Manufacturing: A Review of the Current Technology and Applications.* 3D Printing and Additive Manufacturing, 2018. **5**(3): p. 227-247.

113. Allison, J., et al. *Geant4 electromagnetic physics for high statistic simulation of LHC experiments*. in *Journal of Physics: Conference Series*. 2012. IOP Publishing.

114. Babout, L., et al., *Characterization by X-ray computed tomography of decohesion, porosity growth and coalescence in model metal matrix composites.* Acta Materialia, 2001. **49**(11): p. 2055-2063.

115. Azároff, L.V., et al., *X-ray Diffraction*. Vol. 3. 1974: McGraw-Hill New York.

116. Busi, M., et al., *A Monte Carlo simulation of scattering reduction in spectral X-ray computed tomography.* 2017.

117. Ellingson, W.A. and M.W. Vannier, *X-ray computed tomography for nondestructive evaluation of advanced structural ceramics*. 1988: Materials and Components Technology Division, Argonne National Laboratory.

118. Ferrucci, M., et al., *Towards geometrical calibration of x-ray computed tomography systems—a review.* Measurement Science and Technology, 2015. **26**(9): p. 092003-092003.

119. Villarraga-Gómez, H., et al., *Amplitude-wavelength maps for X-ray computed tomography systems.* Precision Engineering, 2020. **64**: p. 228-242.

120. Einstein, A., *The General Theory of Relativity*, in *The Meaning of Relativity*, A. Einstein, Editor. 1922, Springer Netherlands: Dordrecht. p. 54-75.

121. Kalender, W.A., *X-ray computed tomography.* Physics in Medicine and Biology, 2006. **51**(13): p. R29-R43.

122. Bartscher, M., et al. *Industrial computed tomography, an emerging coordinate measurement technology with high potentials*. 2008.

123. *Fundamentals of X-ray Physics*, in *Computed Tomography*, T. Buzug, Editor. 2008, Springer Berlin Heidelberg: Berlin, Heidelberg. p. 15-73.

124. Bethe, H., W. Heitler, and P.A.M. Dirac, *On the stopping of fast particles and on the creation of positive electrons.* Proceedings of the Royal Society of London. Series A, Containing Papers of a Mathematical and Physical Character, 1934. **146**(856): p. 83-112.

125. Bellon, C. and G.-R. Jaenisch, *aRTist – Analytical RT Inspection Simulation Tool.* 2007.

126. Hsieh, J., *Computed tomography: principles, design, artifacts, and recent advances*. Vol. 114. 2003: SPIE press.

127. Ferrucci, M., et al., *Measurement of the X-ray computed tomography instrument geometry by minimization of reprojection errors-Implementation on simulated data.* 2018.

128. Kasperl, S., J. Hiller, and M. Krumm, *X-ray 3D Computed Tomography with Mega Electronvolt Source (CTOMES) View project NanoXCT-Compact X-ray computed tomography system for non destructive characterization of nano materials View project.* 2009.

129. Körner, L., et al. *Sinogram interpolation to decrease acquisition time in x-ray computed tomography measurement of surface topography*. 2019.

130. Leach, R.K., et al., *Geometrical metrology for metal additive manufacturing.* CIRP Annals, 2019. **68**(2): p. 677-700.

131. Norbert Daneke, B.S., *From Microfocus To Nanofocus X-Ray Inspection.* OnBoard Technology, 2004: p. 42-44.

132. Uhlman N, S.M., Burtzlaff S, Porsch F, Johansson W, Nachtrab F and Hanke R, *Components and Methods for Highest Resolution Computed Tomography*, in *International Symposium on NDT in Aerospace December 3-5*. 2009: Fürth, Germany.

133. Klug, H.P. and L.E. Alexander, *X-ray diffraction procedures: for polycrystalline and amorphous materials*. X-Ray Diffraction Procedures: For Polycrystalline and Amorphous Materials, 2nd Edition, by Harold P. Klug, Leroy E. Alexander, pp. 992. ISBN 0-471-49369-4. Wiley-VCH, May 1974. 1974. 992-992.

134. Judy, P.F., *The line spread function and modulation transfer function of a computed tomographic scanner.* Medical Physics, 1976. **3**(4): p. 233-236.

135. Swinehart, D.F., *The beer-lambert law.* Journal of chemical education, 1962. **39**(7): p. 333-333.

136. McNaught, A.D., et al., *Compendium of chemical terminology : IUPAC recommendations*. 1997: Blackwell Science. 450-450.

137. Siewerdsen, J.H. and D.A. Jaffray, *Cone-beam computed tomography with a flat-panel imager: Magnitude and effects of x-ray scatter.* Medical Physics, 2001. **28**(2): p. 220-231.

138. Ewert, U., *New trends in industrial radiology.* NDT. net, 2002. **7**(02).

139. Garboczi, E.J., *Three-dimensional mathematical analysis of particle shape using X-ray tomography and spherical harmonics: Application to aggregates used in concrete.* Cement and Concrete Research, 2002. **32**(10): p. 1621-1638.

140. Patterson, B.M. and C.E. Hamilton, *Dimensional Standard for Micro X-ray Computed Tomography.* 2010.

141. !!! INVALID CITATION !!! [4, 81, 102, 103].

142. Flay, N. and R.K. Leach, *Application of the optical transfer function in x-ray computed tomography-a review.* 2012.

143. Flay, N., et al., *Investigation of the focal spot drift in industrial cone-beam X-ray computed tomography.* Proceedings of the DIR, 2015.

144. Corcoran, H.C., et al., *OBSERVATIONS ON THE PERFORMANCE OF X-RAY COMPUTED TOMOGRAPHY FOR DIMENSIONAL METROLOGY.* ISPRS - International Archives of the Photogrammetry, Remote Sensing and Spatial Information Sciences, 2016. **XLI-B5**: p. 25-31.

145. Kiekens, K., et al., *Parameter dependent thresholding for dimensional X-ray computed tomography.* 2011.

146. Kiekens, K., et al., *A test object with parallel grooves for calibration and accuracy assessment of industrial computed tomography (CT) metrology.* Measurement Science and Technology, 2011. **22**(11): p. 115502-115502.

147. Carmignato, S., A. Pierobon, and E. Savio, *CT audit–interlaboratory comparison of computed tomography systems for dimensional metrology.* Final Report, Abridged version. University of Padova, 2012.

148. Angel, J.A.B. and L. De Chiffre, *Inter laboratory comparison on Industrial Computed Tomography: CIA-CT comparison. Final Report.* 2013.

149. Stolfi, A. and L. De Chiffre, *InteraqCT comparison on assemblies-final report.* 2016.

150. Townsend, A., et al., *An interlaboratory comparison of X-ray computed tomography measurement for texture and dimensional characterisation of additively manufactured parts.* Additive Manufacturing, 2018. **23**: p. 422-432.

151. Carmignato, S., et al., *Testing of x-ray microtomography systems using a traceable geometrical standard.* Measurement Science and Technology, 2009. **20**(8): p. 084021-084021.

152. Müller, P., et al. *Investigation of measuring strategies in computed tomography*. 2011.

153. Aloisi, V. and S. Carmignato, *Influence of surface roughness on X-ray computed tomography dimensional measurements of additive manufactured parts.* Case Studies in Nondestructive Testing and Evaluation, 2016. **6**: p. 104-110.

154. Nathanael, T., *Erosion and dilation of edges in dimensional X-ray computed tomography images*. 2020.

155. Standard, B., *ISO 25178-2:2012: Geometrical product specifications (GPS) — Surface texture: Areal — Part 2: Terms, definitions and surface texture parameters*.

156. Klingaa, C.G., et al., *Characterization of Geometry and Surface Texture of AlSi10Mg Laser Powder Bed Fusion Channels Using X-ray Computed Tomography.* Applied Sciences, 2021. **11**(9): p. 4304.

157. Thompson, A., *Surface texture measurement of metal additively manufactured parts by X-ray computed tomography*. 2019, University of Nottingham.

158. Zanini, F., et al., *New Approach for Verifying the Accuracy of X-ray Computed Tomography Measurements of Surface Topographies in Additively Manufactured Metal Parts.* Journal of Nondestructive Evaluation, 2018. **38**(1): p. 12.

159. Townsend, A., et al., *Factors affecting the accuracy of areal surface texture data extraction from X-ray CT.* CIRP Annals, 2017. **66**(1): p. 547-550.

160. *BS EN ISO 10360-1:2001: Geometrical product specifications (GPS). Acceptance and reverification tests for coordinate measuring machines (CMM). Vocabulary*. 2001.

161. Wilhelm, R.G., R. Hocken, and H. Schwenke, *Task Specific Uncertainty in Coordinate Measurement.* CIRP Annals, 2001. **50**(2): p. 553-563.

162. Leach, R., *The measurement of surface texture using stylus instruments*. 2001: National Physical Laboratory.

163. Leach, R.K., et al., *Calibration and verification of areal surface texture measuring instruments.* CIRP Annals, 2015. **64**(2): p. 797-813.

164. Triantaphyllou, A., et al., *Surface texture measurement for additive manufacturing.* Surface Topography: Metrology and Properties, 2015. **3**(2): p. 024002.

165. Townsend, A., et al., *Areal surface texture data extraction from X-ray computed tomography reconstructions of metal additively manufactured parts.* Precision Engineering, 2017. **48**: p. 254-264.

166. *ISO 15530-3: Geometrical product specifications (GPS). Coordinate measuring machines (CMM). Technique for determining the uncertainty*

of measurement. Use of calibrated workpieces or measurement standards. 2011.

167. 15530-3, I., *Geometrical product specifications (GPS) — Coordinate measuring machines (CMM): Technique for determining the uncertainty of measurement — Part 3: Use of calibrated workpieces or measurement standards.* 2011.

168. Durakbasa, M., et al., *Contact and Contactless Investigations of Manufactured High-Precise Surface Structures.* microscope, 2009. **2**: p. 8.

169. Thompson, A., et al., *Topography of selectively laser melted surfaces: A comparison of different measurement methods.* CIRP Annals, 2017. **66**(1): p. 543-546.

170. Standard, B., *Geometric Product Specifications (GPS) — Surface texture: Profile method — Nominal characteristics of contact (stylus) instruments*, in 1998.

171. Wennerberg, A., et al., *Characterizing three-dimensional topography of engineering and biomaterial surfaces by confocal laser scanning and stylus techniques.* Medical Engineering & Physics, 1996. **18**(7): p. 548-556.

172. Smith, I.M., et al., *Algorithms and software for areal surface texture function parameters.* Measurement Science and Technology, 2017. **28**(10): p. 105008.

173. Standard, B., *Geometrical Product Specifications (GPS). Surface texture: Profile method; Measurement standards. Geometric product specifications (GPS). Surface texture. Profile method calibration. Measurement standards*, in *ISO 5436*. 2001.

174. Zhao, Y.-q., et al. *Medical Images Edge Detection Based on Mathematical Morphology*. in *2005 IEEE Engineering in Medicine and Biology 27th Annual Conference*. 2005.

175. Ying-Dong, Q., et al., *A fast subpixel edge detection method using Sobel–Zernike moments operator.* Image and Vision Computing, 2005. **23**(1): p. 11-17.

176. Ye, J., G. Fu, and U.P. Poudel, *High-accuracy edge detection with Blurred Edge Model.* Image and Vision Computing, 2005. **23**(5): p. 453-467.

177. Xie, S., Q. Liao, and S. Qin. *Sub-pixel edge detection for precision measurement based on canny criteria*. in *Key Engineering Materials*. 2005. Trans Tech Publ.

178. Vincent, L. and P. Soille, *Watersheds in digital spaces: an efficient algorithm based on immersion simulations.* IEEE Transactions on Pattern Analysis and Machine Intelligence, 1991. **13**(6): p. 583-598.

179. Villarraga-Gómez, H., *X-ray Computed Tomography for Dimensional Measurements*. 2016.

180. Trujillo-Pino, A., et al., *Accurate subpixel edge location based on partial area effect.* Image and Vision Computing, 2013. **31**(1): p. 72-90.

181. Tabatabai, A.J. and O.R. Mitchell, *Edge location to subpixel values in digital imagery.* IEEE Transactions on Pattern Analysis & Machine Intelligence, 1984(2): p. 188-201.

182. Steger, C., *Subpixel-precise extraction of lines and edges.* International archives of photogrammetry and remote sensing, 2000. **33**(3): p. 141-156.

183. Singh, T.R., et al., *A new local adaptive thresholding technique in binarization.* arXiv preprint arXiv:1201.5227, 2012.

184. Shan, Y. and G.W. Boon, *Sub-pixel location of edges with non-uniform blurring: a finite closed-form approach.* 2000. **18**(13): p. 1015-1023.

185. Rockett, P. *The Accuracy of Sub-Pixel Localisation in the Canny Edge Detector*. in *BMVC*. 1999. Citeseer.

186. Parvati, K., B.S. Prakasa Rao, and M. Mariya Das, *Image Segmentation Using Gray-Scale Morphology and Marker-Controlled Watershed Transformation.* Discrete Dynamics in Nature and Society, 2008. **2008**: p. 384346.

187. Osma-Ruiz, V., et al., *An improved watershed algorithm based on efficient computation of shortest paths.* 2007. **40**(3): p. 1078-1090.

188. Nixon, M. and A. Aguado, *Feature extraction and image processing for computer vision*. 2019: Academic press.

189. Neubert, P. and P. Protzel. *Compact Watershed and Preemptive SLIC: On Improving Trade-offs of Superpixel Segmentation Algorithms*. in *2014 22nd International Conference on Pattern Recognition*. 2014.

190. Nalwa, V.S. and T.O. Binford, *On Detecting Edges.* IEEE Transactions on Pattern Analysis and Machine Intelligence, 1986. **PAMI-8**(6): p. 699-714.

191. Meyer, F., *The watershed concept and its use in segmentation: a brief history.* arXiv preprint arXiv:1202.0216, 2012.

192. Lyvers, E.P., et al., *Subpixel measurements using a moment-based edge operator.* IEEE Transactions on pattern analysis and machine intelligence, 1989. **11**(12): p. 1293-1309.

193. Kornilov, A. and I. Safonov, *An Overview of Watershed Algorithm Implementations in Open Source Libraries.* Journal of Imaging, 2018. **4**: p. 123.

194. Kisworo, M., S. Venkatesh, and G. West, *Modeling edges at subpixel accuracy using the local energy approach.* 1994. **16**(4): p. 405-410.

195. Deriche, R., *Using Canny's criteria to derive a recursively implemented optimal edge detector.* International Journal of Computer Vision, 1987. **1**(2): p. 167-187.

196. Da, F. and H. Zhang, *Sub-pixel edge detection based on an improved moment.* Image and Vision Computing, 2010. **28**(12): p. 1645-1658.

197. Cheng, S.-C. and T.-L. Wu, *Subpixel edge detection of color images by principal axis analysis and moment-preserving principle.* 2005. **38**(4): p. 527-537.

198. Chan, F.H.Y., F.K. Lam, and Z. Hui, *Adaptive thresholding by variational method.* IEEE Transactions on Image Processing, 1998. **7**(3): p. 468-473.

199. Bleau, A. and L.J. Leon, *Watershed-Based Segmentation and Region Merging.* Computer Vision and Image Understanding, 2000. **77**(3): p. 317-370.

200. Bin, T.J., et al., *Subpixel edge location based on orthogonal Fourier–Mellin moments.* 2008. **26**(4): p. 563-569.

201. Bieniek, A. and A. Moga, *An efficient watershed algorithm based on connected components.* 2000. **33**(6): p. 907-916.

202. Beucher, S. and C. Lantuéjoul, *Use of Watersheds in Contour Detection*. Vol. 132. 1979.

203. Beucher, S. and F. Meyer, *The Morphological Approach to Segmentation: The Watershed Transformation*. 1993. p. 433–481.

204. Beucher, S., *The watershed transformation applied to image segmentation.* Scanning microscopy-supplement-, 1992: p. 299-299.

205. Amoda, N. and R. Kulkarni, *Efficient Image Segmentation Using Watershed Transform.* www.ijcst.com, 2013. **4**.

206. Hermosilla, T., et al., *Non-linear fourth-order image interpolation for subpixel edge detection and localization.* 2008. **26**(9): p. 1240-1248.

207. Jiménez, R., C. Comps, and J.A. Yagüe, *An Optimized Segmentation Algorithm for the Surface Extraction in Computed Tomography for Metrology Applications.* Procedia Engineering, 2015. **132**: p. 804-810.

208. Heinzl, C., J. Kastner, and E. Gröller, *Reproducible Surface Extraction for Variance Comparison in 3D Computed Tomography*, in *Proc. of the 9th European Conference on Non-Destructive Testing*. 2006, Citeseer.

209. Haitham Shammaa, M. and Y. Ohtake, *Segmentation of multi-material CT data of mechanical parts for extracting boundary surfaces.* Computer-Aided Design, 2010. **42**(2): p. 118-128.

210. Heinzl, C., et al. *Robust Surface Detection for Variance Comparison and Dimensional Measurement*. in *EuroVis*. 2006.

211. Müller, A.M., et al., *Automated evaluation of the surface point quality in dimensional X-ray computed tomography.* tm - Technisches Messen, 2020. **87**(2): p. 111-121.

212. Sokac, M., et al., *Improved surface extraction of multi-material components for single-source industrial X-ray computed tomography.* Measurement, 2020. **153**: p. 107438.

213. Torralba, M., et al., *Comparison of surface extraction techniques performance in computed tomography for 3D complex micro-geometry dimensional measurements.* The International Journal of Advanced Manufacturing Technology, 2018.

214. Ontiveros, S., et al., *Computer Tomography 3D Edge Detection Comparative for Metrology Applications.* 2013. **63**: p. 710-719.

215. Lifton, J. and T. Liu, *An adaptive thresholding algorithm for porosity measurement of additively manufactured metal test samples via X-ray computed tomography.* Additive Manufacturing, 2021. **39**: p. 101899.

216. Wellner, P.D., *Adaptive thresholding for the DigitalDesk.* Xerox, EPC1993-110, 1993: p. 1-19.

217. Müller, P., et al. *Investigation on the influence of image quality in X-ray CT metrology*. in *Conference on Industrial Computed Tomography, Wels, Austria*. 2012. Citeseer.

218. Matern, D. and M. Töpperwien. *How much does image quality influence the form error in industrial X-Ray CT*. in *10th conf. Industrial computed tomography*. 2020.

219. Fleßner, M., et al., *Evaluating and visualizing the quality of surface points determined from computed tomography volume data.* Proc. MacroScale, 2014. **2014**.

220. Buratti, A., et al., *Determination of the optimal imaging parameters in industrial computed tomography for dimensional measurements on monomaterial workpieces.* Measurement Science and Technology, 2018. **29**(11): p. 115009.

221. Brunke, O., J. Santillan, and A. Suppes, *Precise 3D dimensional metrology using high-resolution x-ray computed tomography (muCT)*. SPIE Optical Engineering + Applications. Vol. 7804. 2010: SPIE.

222. Heinzl, C., et al. *Comparison of surface detection methods to evaluate cone beam computed tomography data for three dimensional metrology*. 2007.

223. Steinbeiß, H.P., *Dimensionelles Messen mit Mikro-Computertomographie*. 2005: Hieronymus.

224. Jiménez, R., et al., *Experimental approach for the uncertainty assessment of 3D complex geometry dimensional measurements using computed tomography at the mm and sub-mm scales.* Sensors (Switzerland), 2017. **17**(5).

225. Rong, W.B., et al., *An Improved Canny Edge Detection Algorithm.* 2014 Ieee International Conference on Mechatronics and Automation (Ieee Icma 2014), 2014: p. 577-582.

226. Bartscher, M., et al., *Achieving Traceability of Industrial Computed Tomography.* Key Engineering Materials, 2010. **437**: p. 79-83.

227. Hiller, J., M. Maisl, and L.M. Reindl, *Physical characterization and performance evaluation of an x-ray micro-computed tomography system for dimensional metrology applications.* Measurement Science and Technology, 2012. **23**(8): p. 085404.

228. du Plessis, A. and P. Rossouw, *X-ray computed tomography of a titanium aerospace investment casting.* Case Studies in Nondestructive Testing and Evaluation, 2015. **3**: p. 21-26.

229. Bartscher, M., J. Illemann, and U. Neuschaefer-Rube, *ISO test survey on material influence in dimensional computed tomography.* Case Studies in Nondestructive Testing and Evaluation, 2016. **6**: p. 79-92.

230. Borges de Oliveira, F., et al., *Experimental investigation of surface determination process on multi-material components for dimensional computed tomography.* Case Studies in Nondestructive Testing and Evaluation, 2016. **6**: p. 93-103.

231. Carmignato, S., et al., *Influence of surface roughness on computed tomography dimensional measurements.* CIRP Annals, 2017. **66**(1): p. 499-502.

232. Hermanek, P. and S. Carmignato, *Porosity measurements by X-ray computed tomography: Accuracy evaluation using a calibrated object.* Precision Engineering, 2017. **49**: p. 377-387.

233. Kiekens, K., *Contributions to performance verification and uncertainty determination of industrial computed tomography for dimensional metrology.* 2017.

234. Thompson, A., et al., *Measurement of internal surfaces of additively manufactured parts by X-ray computed tomography.* 2017.

235. Townsend, A., et al., *Factors affecting the accuracy of areal surface texture data extraction from X-ray CT.* Cirp Annals-Manufacturing Technology, 2017. **66**(1): p. 547-550.

236. Villarraga-Gómez, H., C. Lee, and S.T. Smith, *Dimensional metrology with X-ray CT: A comparison with CMM measurements on internal features and compliant structures.* 2017.

237. Ametova, E., et al., *A computationally inexpensive model for estimating dimensional measurement uncertainty due to X-ray computed tomography instrument misalignments.* Measurement Science and Technology, 2018. **29**(6): p. 065007.

238. Ametova, E., et al., *Software-based compensation of instrument misalignments for X-ray computed tomography dimensional metrology.* 2018.

239. Chahid, Y., et al., *Optimizing X-Ray Computed Tomography Settings for Dimensional Metrology Using 2D Image Analysis*, N. Shamsaei and M. Seifi, Editors. 2020, ASTM International: West Conshohocken, PA. p. 88-101.

240. Perona, P. and J. Malik, *Scale-space and edge detection using anisotropic diffusion.* IEEE Transactions on Pattern Analysis and Machine Intelligence, 1990. **12**(7): p. 629-639.

241. Körner, L., et al., *Increasing throughput in x-ray computed tomography measurement of surface topography using sinogram interpolation.* Measurement Science and Technology, 2019. **30**(12): p. 125002.

242. Staude, A. *The Influence of Data Filtering on Dimensional Measurements with CT*. in *WCNDT 2012*. 2012. Durban, South Africa.

243. Stolfi, A., *Integrated quality control of precision assemblies using computed tomography.* Department of Mechanical Engineering: Technical University of Denmark, 2017.

244. Friedlander, F. and F. Meyer, *A sequential algorithm for detecing watersheds on a gray level image*. 1991.

245. Levner, I. and H. Zhang, *Classification-Driven Watershed Segmentation.* IEEE Transactions on Image Processing, 2007. **16**(5): p. 1437-1445.

246. Yung-Chieh, L., et al., *Comparison between immersion-based and toboggan-based watershed image segmentation.* 2006. **15**(3): p. 632-640.

247. Couprie, M. and G. Bertrand. *Topological gray-scale watershed transformation*. in *Vision Geometry Vi*. 1997. International Society for Optics and Photonics.

248. Jähne, B., *Digital image processing, 2005*. Springer Verlag.

249. Vincent, L., *Morphological grayscale reconstruction in image analysis: applications and efficient algorithms.* IEEE Transactions on Image Processing, 1993. **2**(2): p. 176-201.

250. Serra, J., *Image analysis and mathematical morphol-ogy.* (No Title), 1982.

251. Wieclawek, W., *3D marker-controlled watershed for kidney segmentation in clinical CT exams.* Biomed Eng Online, 2018. **17**(1): p. 26.

252. Veta, M., et al. *Marker-controlled watershed segmentation of nuclei in H&E stained breast cancer biopsy images*. in *2011 IEEE International Symposium on Biomedical Imaging: From Nano to Macro*. 2011.

253. Lewis, S.H. and A. Dong. *Detection of breast tumor candidates using marker-controlled watershed segmentation and morphological analysis*. in *2012 IEEE Southwest Symposium on Image Analysis and Interpretation*. 2012.

254. Kanitkar, S.S., N.D. Thombare, and S.S. Lokhande. *Detection of lung cancer using marker-controlled watershed transform*. in *2015 International Conference on Pervasive Computing (ICPC)*. 2015.

255. Zhou, X., et al., *Three-dimensional characterization of powder particles using X-ray computed tomography.* Additive Manufacturing, 2021. **40**: p. 101913.

256. Lou, S., et al., *Watershed segmentation of topographical features on freeform surfaces and its application to additively manufactured surfaces.* Precision Engineering, 2020. **63**: p. 177-186.

257. Wang, Y., C. Lin, and J.J.P.T. Miller, *3D image segmentation for analysis of multisize particles in a packed particle bed.* 2016. **301**: p. 160-168.

258. Kim, F.H., et al., *Investigation of pore structure in cobalt chrome additively manufactured parts using X-ray computed tomography and three-dimensional image analysis.* Additive Manufacturing, 2017. **17**: p. 23-38.

259. Eswaran, C., A.W. Reza, and S. Hati. *Extraction of the Contours of Optic Disc and Exudates Based on Marker-Controlled Watershed Segmentation*. in *2008 International Conference on Computer Science and Information Technology*. 2008.

260. Hamdi, M.A., *Modified algorithm marker-controlled watershed transform for image segmentation based on curvelet threshold.* Middle-East Journal of Scientific Research, 2014. **20**(3): p. 323-327.

261. MacAulay, G.D., et al., *Review of feature boundary identification techniques for the characterization of tessellated surfaces.* Surface Topography: Metrology and Properties, 2015. **3**(1): p. 013002.

262. Mangan, A.P. and R.T. Whitaker, *Partitioning 3D surface meshes using watershed segmentation.* IEEE Transactions on Visualization and Computer Graphics, 1999. **5**(4): p. 308-321.

263. Heijmans, H.J.A.M. and A. Toet, *Morphological sampling.* CVGIP: Image Understanding, 1991. **54**(3): p. 384-400.

264. Vincent, O.R. and O. Folorunso. *A descriptive algorithm for sobel image edge detection*. in *Proceedings of informing science & IT education conference (InSITE)*. 2009.

265. Meyer, F., *Mathematical morphology: from two dimensions to three dimensions.* Journal of Microscopy, 1992. **165**(1): p. 5-28.

266. Meyer, F., *Topographic distance and watershed lines.* Signal Processing, 1994. **38**(1): p. 113-125.

267. Hiller, J., et al., *Measurement uncertainty evaluation in dimensional X-ray computed tomography using the bootstrap method.* International Journal of Precision Engineering and Manufacturing, 2014. **15**(4): p. 617-622.

268. Wang, S., *Investigation of X-ray computed tomography for dimensional measurement.* 2019.

269. Pratt, V., *Direct least-squares fitting of algebraic surfaces.* ACM SIGGRAPH computer graphics, 1987. **21**(4): p. 145-152.

270. *Determination of the measurement uncertainty of computed tomography measurements using a cylinder head as an example.*

271. Schmitt, R. and C. Niggemann, *Uncertainty in measurement for x-ray-computed tomography using calibrated work pieces.* Measurement Science and Technology, 2010. **21**(5): p. 054008.

272. Müller, P., *Coordinate Metrology by Traceable Computed Tomography*. 2013, Technical University of Denmark (DTU).

273. Schmitt, R. and C. Niggemann, *Method for Efficient Identification of Similar Work Pieces for X-Ray Computed Tomography*. 2011.

274. Carmignato, S., et al. *CT for industrial metrology-accuracy and structural resolution of CT dimensional measurements*. 2012.

275. Pauly, M., N.J. Mitra, and L.J. Guibas. *Uncertainty and variability in point cloud surface data*. in *PBG*. 2004.

276. Forbes, A., *Surface fitting taking into account uncertainty structure in coordinate data.* Measurement Science and Technology, 2006. **17**(3): p. 553-558.

277. Forbes, A.B., *Uncertainty evaluation associated with fitting geometric surfaces to coordinate data.* Metrologia, 2006. **43**(4): p. S282-S290.

278. Senin, N., et al., *Statistical point cloud model to investigate measurement uncertainty in coordinate metrology.* Precision Engineering-Journal of the International Societies for Precision Engineering and Nanotechnology, 2021. **70**: p. 44-62.

279. Sun, Q., J. Zheng, and C. Li, *Improved watershed analysis for segmenting contacting particles of coarse granular soils in volumetric images.* Powder Technology, 2019. **356**: p. 295-303.

280. Levine, Z.H., et al., *Scatter Corrections in X-Ray Computed Tomography: A Physics-Based Analysis.* 2019. **124**.

281. Fei, L., et al., *Calibration and uncertainty estimation of non-contact coordinate measurement systems based on Kriging models.* Precision Engineering, 2019. **57**: p. 16-29.

282. Müller, P., *Use of reference objects for correction of measuring errors in X-ray computed tomography.* DTU Mechanical Engineering, Technical University of Denmark, 2010.

283. Duvauchelle, P., et al., *A computer code to simulate X-ray imaging techniques.* Nuclear Instruments and Methods in Physics Research Section B: Beam Interactions with Materials and Atoms, 2000. **170**(1-2): p. 245-258.

284. Graphics, V., *VGStudio MAX 3.0.* Reference Manual, 2016.

285. Alin, A., *Minitab.* WIREs Computational Statistics, 2010. **2**(6): p. 723-727.

286. Jennings, A., *Sphere Fit (least squared)* 2022: MATLAB Central File Exchange.

287. Villarraga-Gómez, H., J.D. Thousand, and S.T. Smith, *Empirical approaches to uncertainty analysis of X-ray computed tomography measurements: A review with examples.* Precision Engineering, 2020. **64**: p. 249-268.

288. Romanov, A.Y., *Measurement of the Parameters of the Focal Spot of an x-Ray Tube Using Kumakhov Optics.* Measurement Techniques, 2004. **47**(7): p. 670-674.

289. Zanini, F., et al., *Characterisation of additively manufactured metal surfaces by means of X-ray computed tomography and generalised surface texture parameters.* CIRP Annals, 2019. **68**(1): p. 515-518.

290. Eastwood, J., et al., *Generation and categorisation of surface texture data using a modified progressively growing adversarial network.* Precision Engineering, 2022. **74**: p. 1-11.

291. Körner, C., *Additive manufacturing of metallic components by selective electron beam melting — a review.* International Materials Reviews, 2016. **61**(5): p. 361-377.

292. Standard, B., *ISO 5436-1:2001 2001 Geometrical product specifications (GPS) — Surface texture: Profile method; Measurement standards — Part 1: Material measures.* 2001.

293. Lifton, J.J., et al. *The application of voxel size correction in x-ray computed tomography for dimensional metrology*. in *Singapore international NDT conference & exhibition*. 2013.

294. Thompson, A., et al., *Comparison of optical and contact surface topography measurement, including uncertainty*. 2020.

295. Karras, T., et al., *Progressive growing of gans for improved quality, stability, and variation.* arXiv preprint arXiv:1710.10196, 2017.

296. *Image2surface*. Available from:

https://github.com/hanskellner/Fusion360Image2Surface.

297. Song, P.P., Y.M. Qi, and D.C. Cai, *Research and Application of Autodesk Fusion360 in Industrial Design.* IOP Conference Series: Materials Science and Engineering, 2018. **359**: p. 012037.

298. project, C., *CloudCompare - 3D point cloud and mesh processing software Open Source Project*.

299. Fabijanska, A., *A SURVEY OF SUBPIXEL EDGE DETECTION METHODS FOR IMAGES OF HEAT-EMITTING METAL SPECIMENS.* International Journal of Applied Mathematics and Computer Science, 2012. **22**(3): p. 695-710.

300. Endo, M., T. Tsunoo, and N. Nakamori. *Effect of scatter radiation on image noise in cone-beam CT*. 2001. International Society for Optics and Photonics.

301. Rodríguez-Sánchez, Á., et al., *Review of the influence of noise in X-ray computed tomography measurement uncertainty.* Precision Engineering, 2020. **66**: p. 382-391.

302. Gollwitzer, C., et al., *On POD Estimations with Radiographic Simulator aRTist.* 2011.

303. Bartscher, Markus, et al. “Current state of standardization in the field of dimensional computed tomography.” Measurement Science and Technology 25.6 (2014): 064013.

304. ISO 15708-2: 2019: Non-destructive testing. Radiation methods for Computed tomography. Principles, equipment and samples

305. ASTM E 1695 : 2020: Standard Test Method for Measurement of Computed Tomography (CT) System Performance

306. ASTM E 1441 : 2019 Standard Guide for Computed Tomography (CT)

307. ASTM E 1570 : 2019 Standard Practice for Fan Beam Computed Tomographic (CT) Examination

308. ISO 10360-11: 2021: Geometrical product specifications (GPS) — Acceptance and reverification tests for coordinate measuring systems (CMS) — Part 11: CMSs using the principle of X-ray computed tomography (CT)

309. Whitehouse, David J. Surfaces and their Measurement. Gulf Professional Publishing, 2004.

8 APPENDICES

Appendix A Fourier Beam Hardening Correction

As discussed in section 2.2 the polychromatic spectrum leads to beam hardening errors, because the reconstruction software assumes a monochromatic beam, *i.e.* X-ray consists of single-energy photons.

Prior to reconstruction, all projection images could be corrected for the effect of beam hardening [44]. The BHC applied in this work was based on linearisation correction method [42], which assumes that the reconstruction process is based on the linear attenuation distance of the photon energy, with the following assumptions:

- The focal spot size was infinitesimal.
- The photon flux did not vary at different projection angle.
- Secondary scattering was not considered. This algorithm only considered the proportion of lost photons in a beam line direction due to Compton scattering. Rayleigh scattering and pair production were not accounted for.
- Effect of noise on the projection image was not considered.
- Attenuation coefficient of air was zero.
- Error due to detector effect was not considered.
- Photon flux and spectrum did not vary during an entire CT scan.

BHC major steps were:

- Calculation of polychromatic beam intensity using integrated Beer-Lambert Law
- Monochromatic photon intensity calculation
- Fourier regression.
- Projection image correction.

A.1 Calculation of polychromatic beam intensity using

Figure 8-1 illustrates the calculation of the polychromatic photon intensity as a function of attenuation distance.

The spectrum was generated using aRTist simulation platform. A comparison between measured and simulated polychromatic spectrum was presented in [302].

W(E) is the proportion of number of photons with energy of E over the total number of photons ejected from the XCT gun in a unit area and unit time.

I_0 is the initial X-ray intensity without any attenuation and is a proportion to the number of photons received by the detector during the exposure time. In other words, I_0 is related to the total number of photons with energy from 0 to $\boldsymbol{E_m}$, while $\boldsymbol{E_m/e}$ is the voltage setting during XCT scan, or the energy of the electron hitting the tungsten target (***e*** is the elementary charge).

$I_0 W(E)$ denotes the X-ray intensity under the given photon energy E.

The attenuation coefficient, μ(E), is energy dependent, and in this case is the sum of attenuation coefficient due to photoelectric effect and Compton scattering. Rayleigh scattering and pair production attenuation coefficients were neglected because they were not dominated factor for low energy photons. The attenuation coefficient was also selected in compliance with NIST.

t denotes the attenuation distance through the material.

Combining $I_0 W(E)$ and $\mu(E)t$, the integrated Beer-Lambert Law equation was obtained to calculate the theoretical intensity of polychromatic photons after attenuation distance of t. The bottom chart in Figure 8-1 shows the relationship between the polychromatic intensity and the attenuation distance.

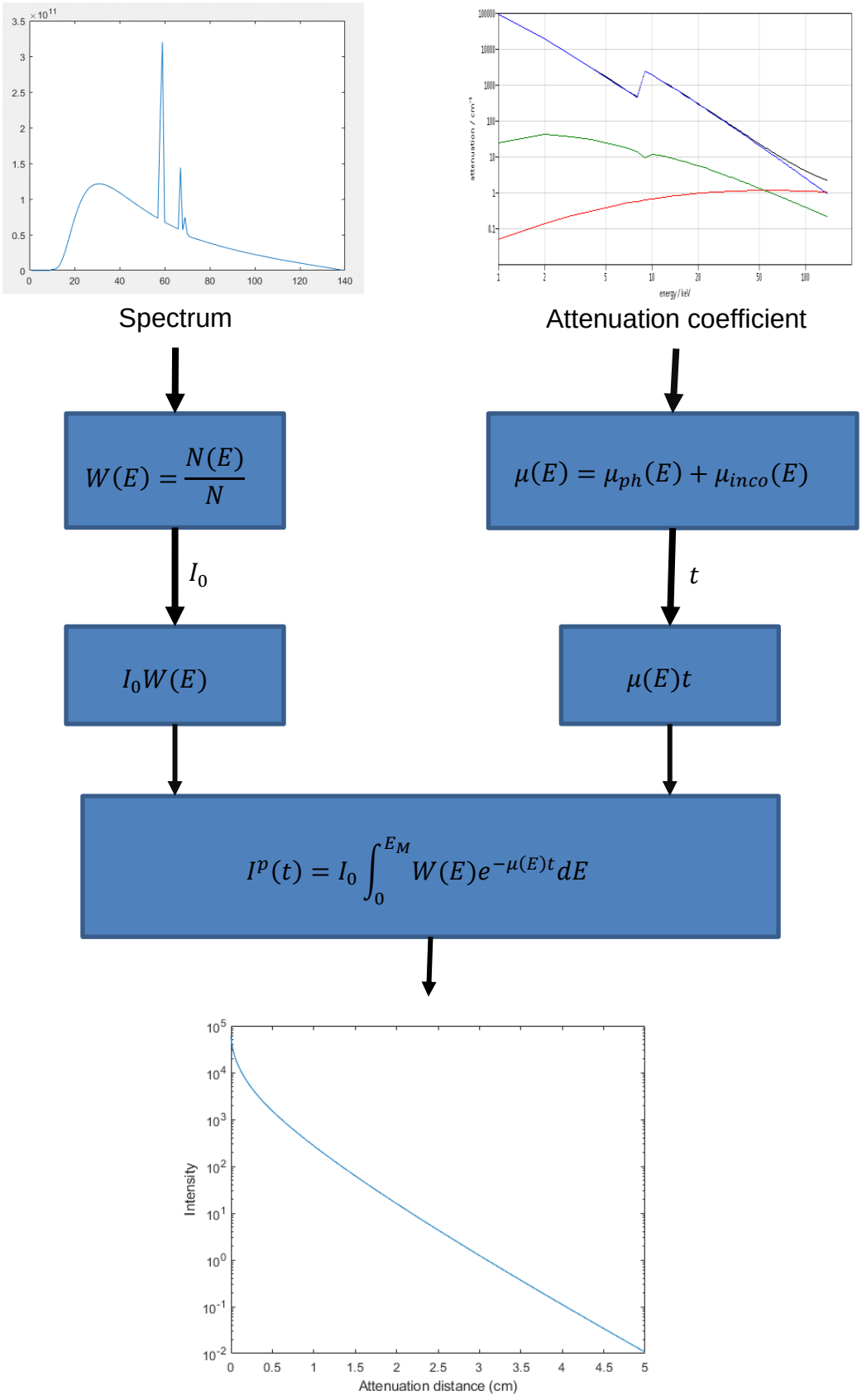

Figure 8-1: The flow chart of calculation of polychromatic beam intensity.

A.2 Monochromatic photon intensity calculation

The monochromatic photon intensity (I^m) is simply calculated using Beer-Lambert Law:

$$I^m(t) = I_0 e^{-\mu t} \qquad \textbf{(8-1)}$$

where μ is the attenuation coefficient and I_0 and t taking the same values as in polychromatic case. Equation (8-1) is only used to linearise the projection image prior to reconstruction.

A.3 Fourier regression

Figure 8-2 compares the $I^p(t)$ (orange dashed line) and $I^m(t)$ (blue solid line) for the spectrum and attenuation coefficient chart (Cu) shown in Figure 8-1 The polychromatic intensity attenuation shows a non-linear relationship (in log scale) only in the first 5 mm. The plot shows that there is a unique regression transfer function that allows to derive the monochromatic response from the polychromatic graph.

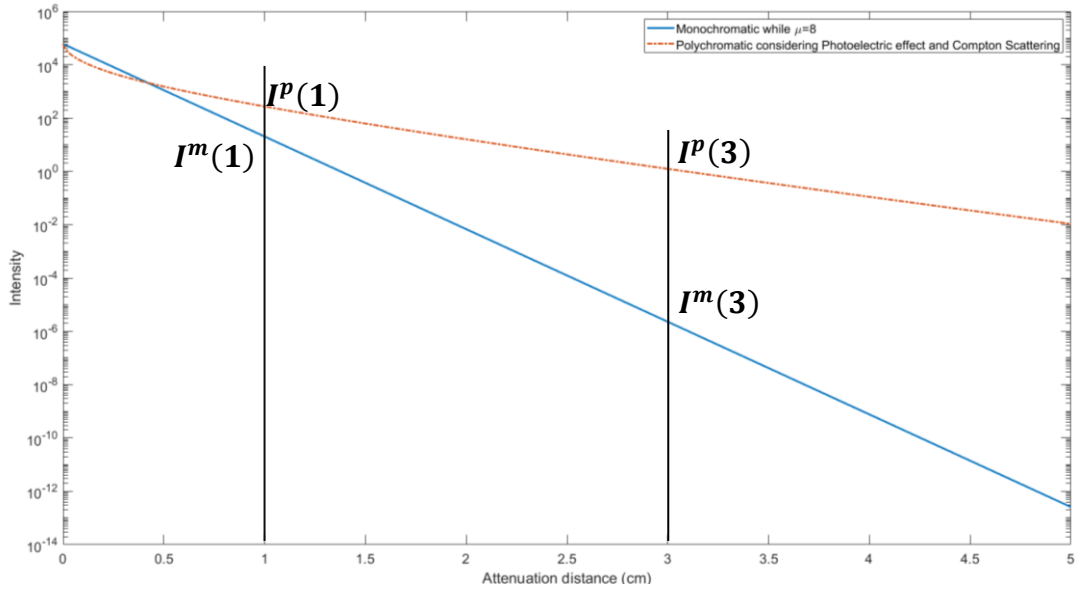

Figure 8-2: The comparison of the intensity of the polychromatic photons with a spectrum between 0 to 140 keV ($I^p(t)$ dashed line) and monochromatic photons μ = 8 ($I^m(t)$ continuous line) after attenuation passing through a Cu.

Most of previous research focused on polynomial regression, which can have between four [41] and eight terms [38]. However, it has been shown that the internal noise can be magnified during BHC polynomial corrections [41, 51]. In general, the optimal polynomial degree difficult to establish. Figure 8-3 shows the sixth-degree polynomial regression for I^p and I^m, and its corresponding residuals fitted to the discrete set of data. The residual here denotes the difference between I^m and $I^{m\prime}$**,** which is the value calculated by polynomial regression expression. Though R-square value was 0.9994, the absolute residual value can reach to the maximum of 1950 with increasing I^p**.** While I^p is in the range of [10000, 50000], the residual can increase to up to 1300. It implies that polynomial regression can introduce the unwanted errors.

In contrast, the sixth degree Fourier regression outperforms the polynomial regression with R-square equal to 1, and maximum residual successfully decreased to only 40, compared with 1900 in polynomial regression. Surely, considering that the domain of $I^p \in [0, I_0]$, the regression curve exceeding I_0 can be neglected during actual beam hardening correction. For simplicity in the following context, the Fourier regression function is recorded as:

$$G^m(G^p) = F^6(G^p) \quad \textbf{(8-2)}$$

while $G^m(G^p)$ denotes the grey value after beam hardening correction from grey value of I^p of the initial projection image pixels, and $F^6(G^p)$ denotes the sixth degree Fourier regression function.

A.4 Projection image correction

After establishing the Fourier regression transfer function, all projection images were transferred to the beam hardening corrected image using the following equation

$$For\ [i,j] \forall \mathbb{R}, {I^m}_{i,j} = F^6({G^p}_{i,j}) \quad \textbf{(8-3)}$$

while $[i,j]$ denotes the coordinate of a single pixel within $\mathbb{R}$, ${G^p}_{i,j}$ is the grey value of the pixel $[i,j]$, and ${G^m}_{i,j}$ is the grey value after correction.

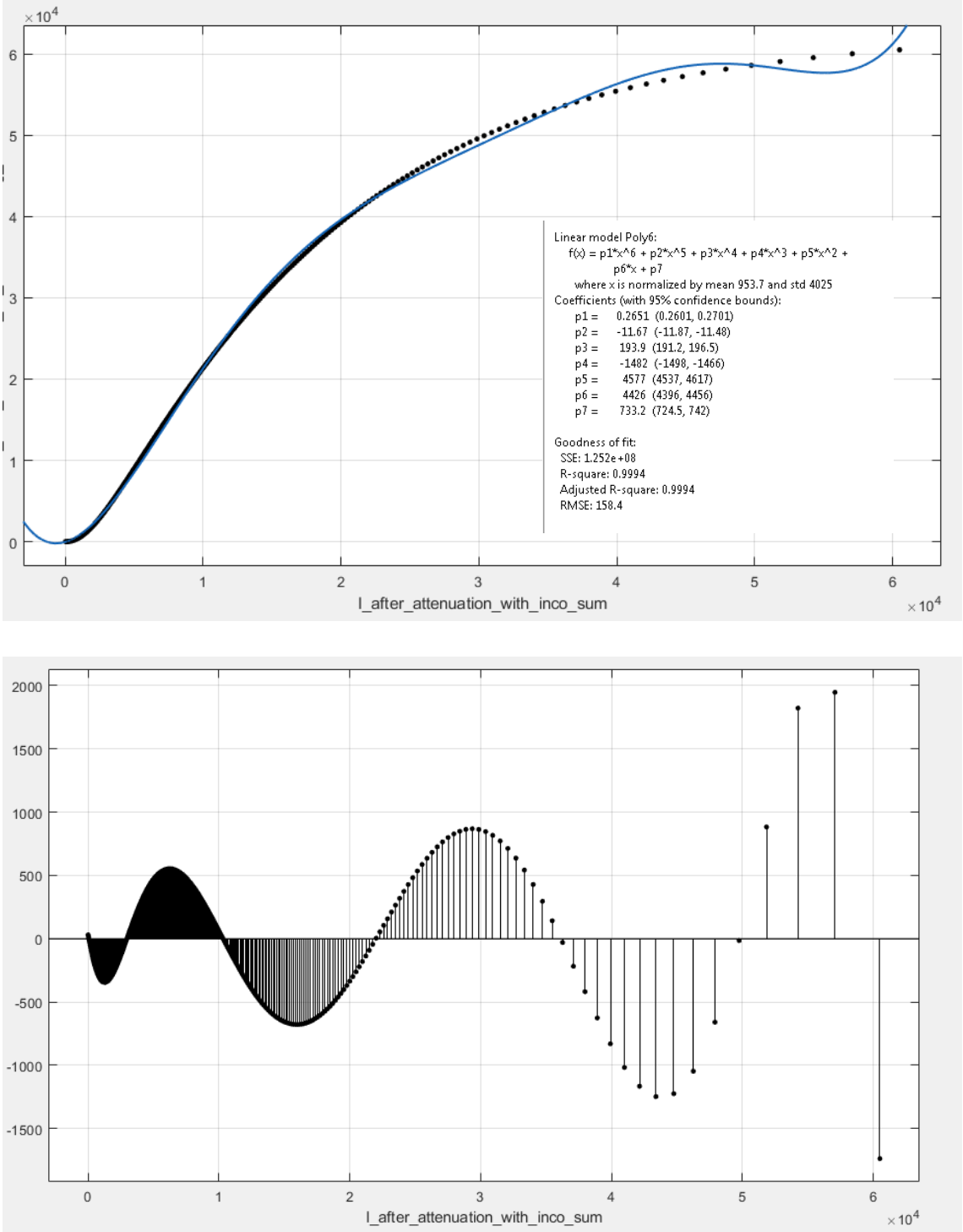

Figure 8-3: Upper: Sixth degree polynomial regression plot. Lower: Regression residual plot, and 'I_after_attenuation_with_inco_sum' is equal to I^p in this plot.

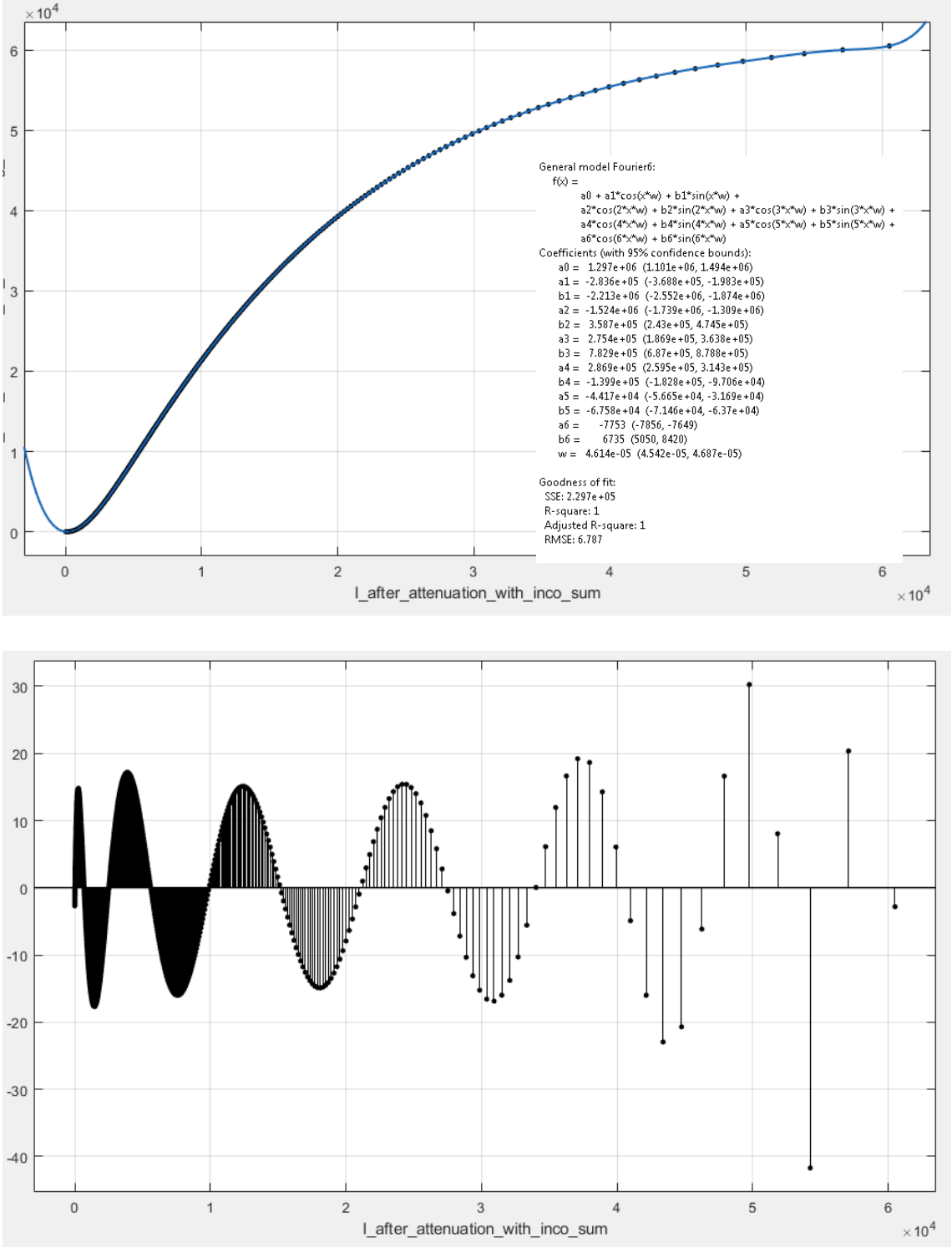

Figure 8-4: Upper: Six degree Fourier regression plot. Lower: Regression residual plot, and 'I_after_attenuation_with_inco_sum' is equal to G^p in this plot.

Figure 8-3 A & B shows an example of the projection image before and after beam hardening correction using F^6 regression function, therefore, the grey value representing the X-ray intensity should be represented by a simple exponential function. Figure 8-3 C & D show the exponential regression result corresponding to the profiles indicated by the yellow lines in A and B, respectively. After beam hardening correction, the R-square value of exponential regression increased from 0.9401 to 0.9959, indicating the effectiveness of the beam hardening correction.

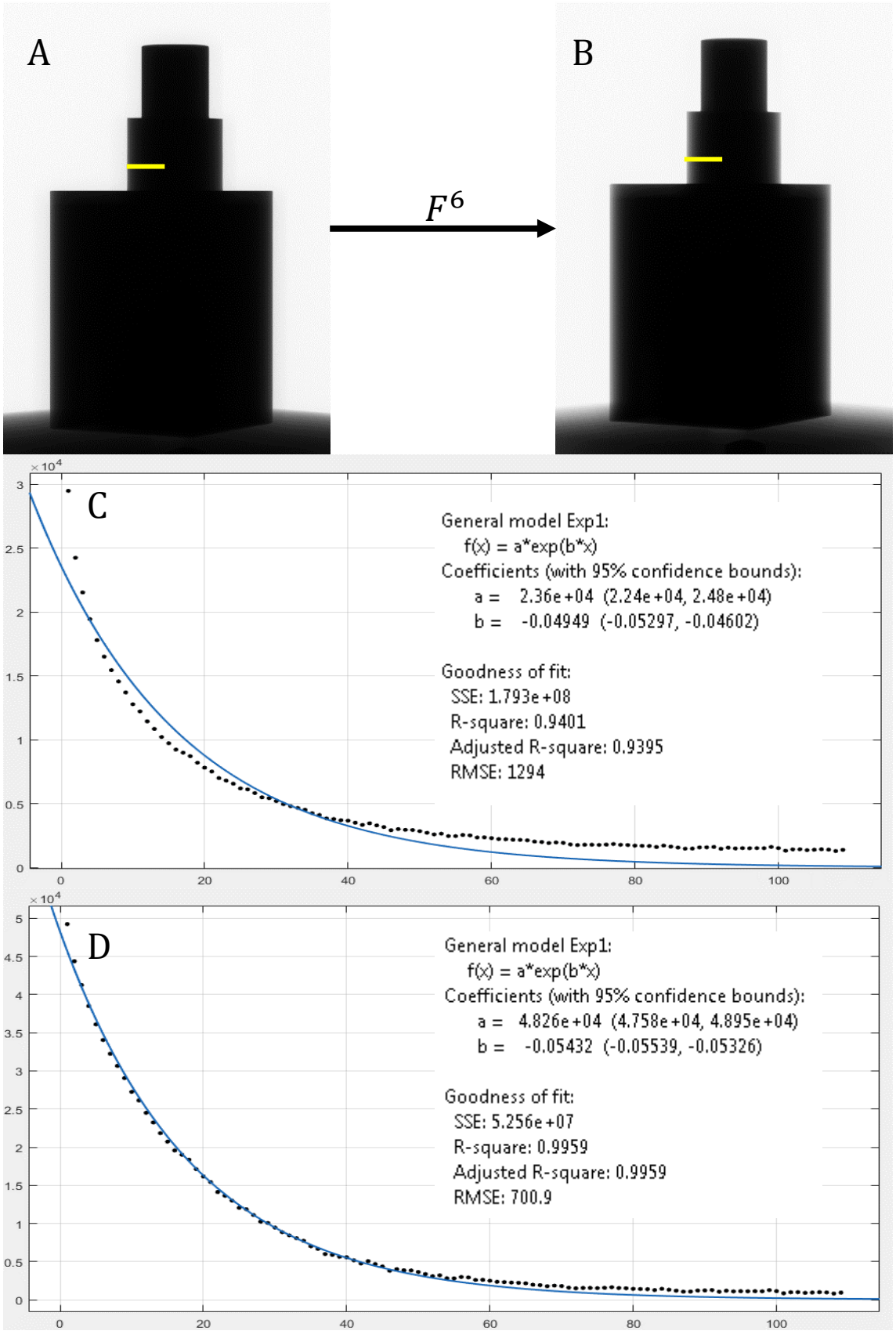
A
B
F^6
C
General model Exp1:
f(x) = a*exp(b*x)
Coefficients (with 95% confidence bounds):
a = 2.36e+04 (2.24e+04, 2.48e+04)
b = -0.04949 (-0.05297, -0.04602)
Goodness of fit:
SSE: 1.793e+08
R-square: 0.9401
Adjusted R-square: 0.9395
RMSE: 1294
D
General model Exp1:
f(x) = a*exp(b*x)
Coefficients (with 95% confidence bounds):
a = 4.826e+04 (4.758e+04, 4.895e+04)
b = -0.05432 (-0.05539, -0.05326)
Goodness of fit:
SSE: 5.256e+07
R-square: 0.9959
Adjusted R-square: 0.9959
RMSE: 700.9

Figure 8-5: A: Projection image without BHC; B: BHC image using F^6 regression transfer function; C. Exponential regression result of the plot indicated by yellow line in A; D. Exponential regression result of the plot indicated by yellow line in B

Appendix B The result of SD optimisation for 3DRS sample

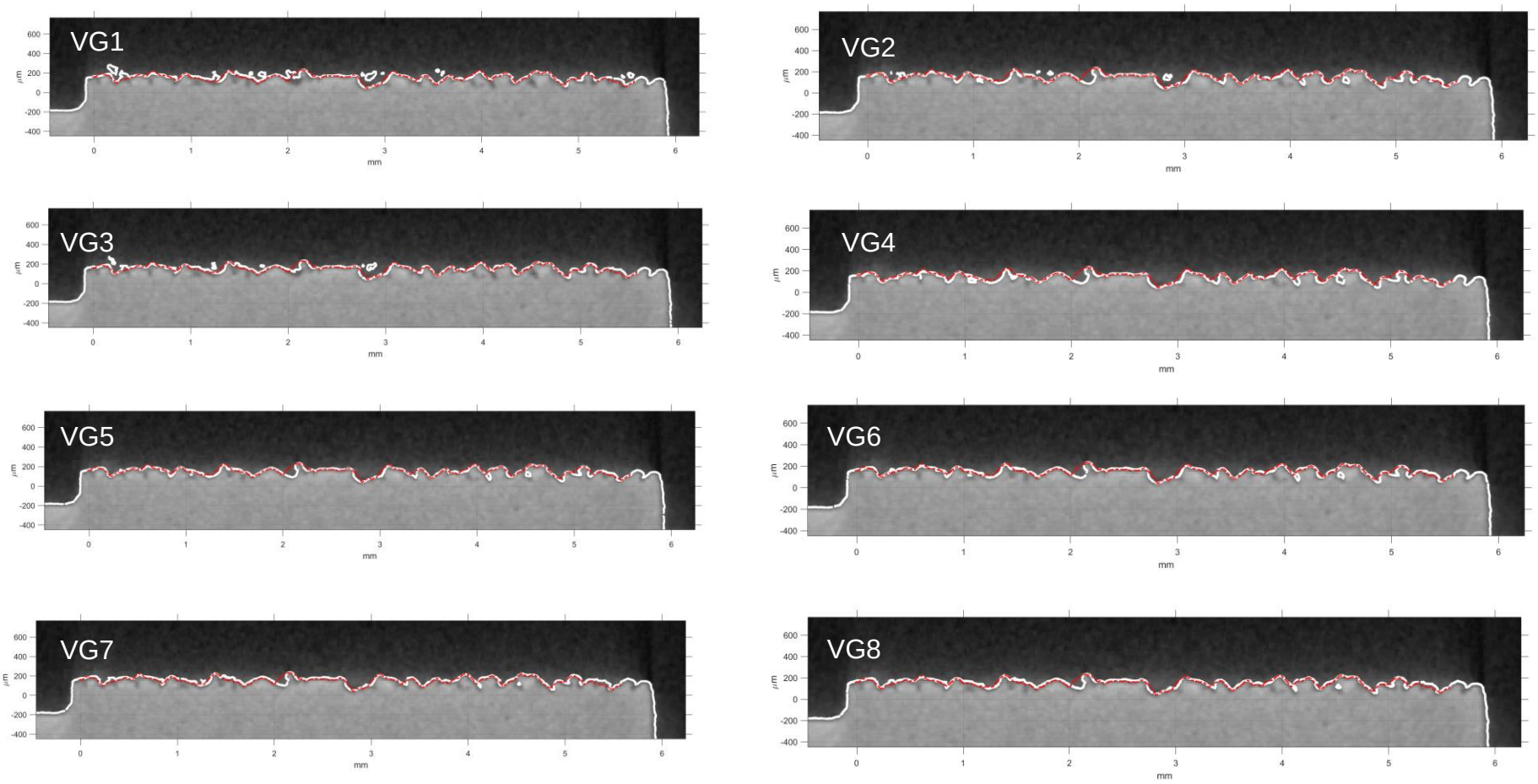

Figure 8-6: The optimisation result without BHC using VG SD algorithm. White dots- XCT surface; red line: CS data

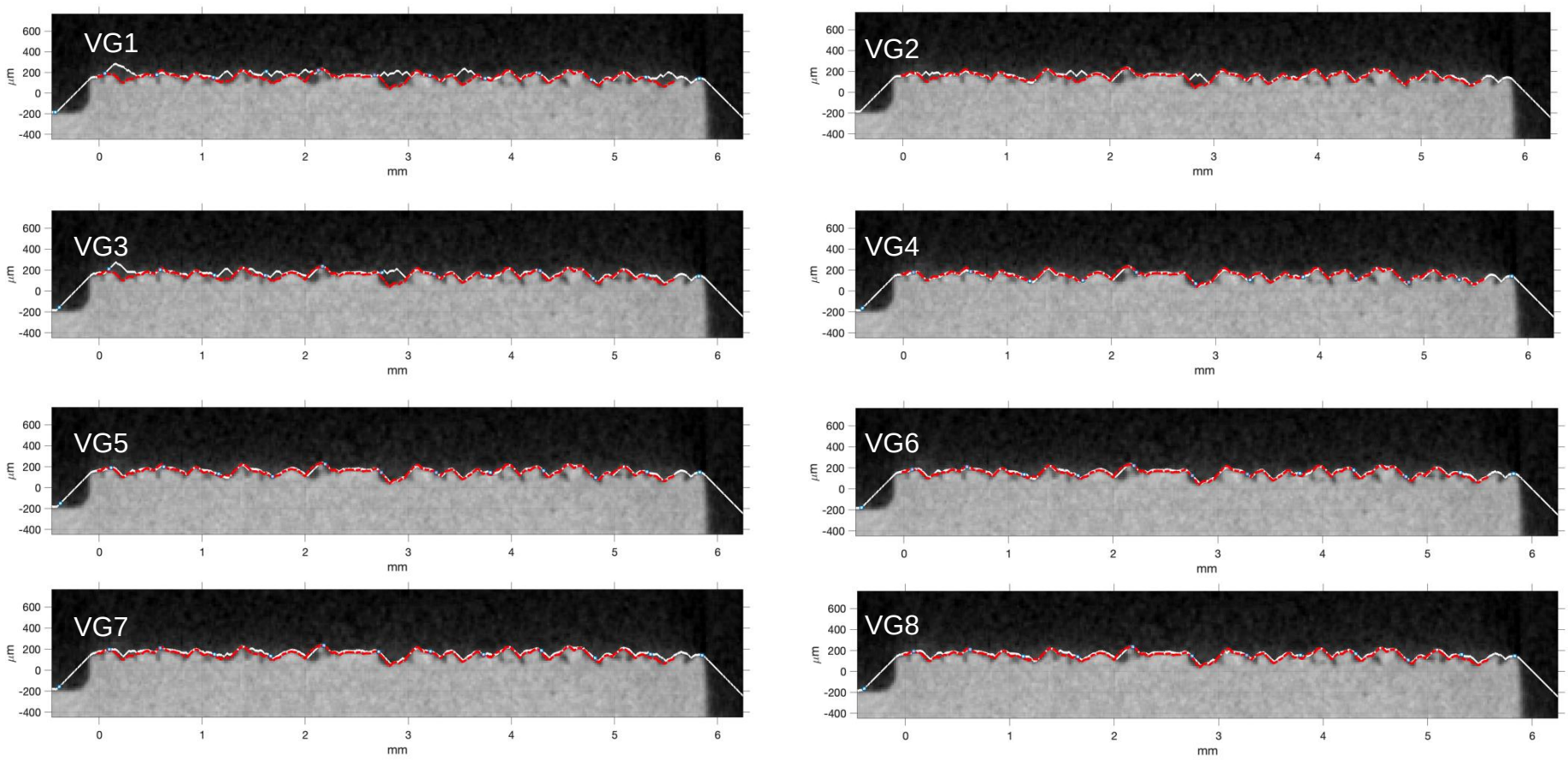

Figure 8-7: The optimisation result without BHC using VG SD algorithm after applying morphological filter. White dots- XCT surface after morphological filter; red line: CS data

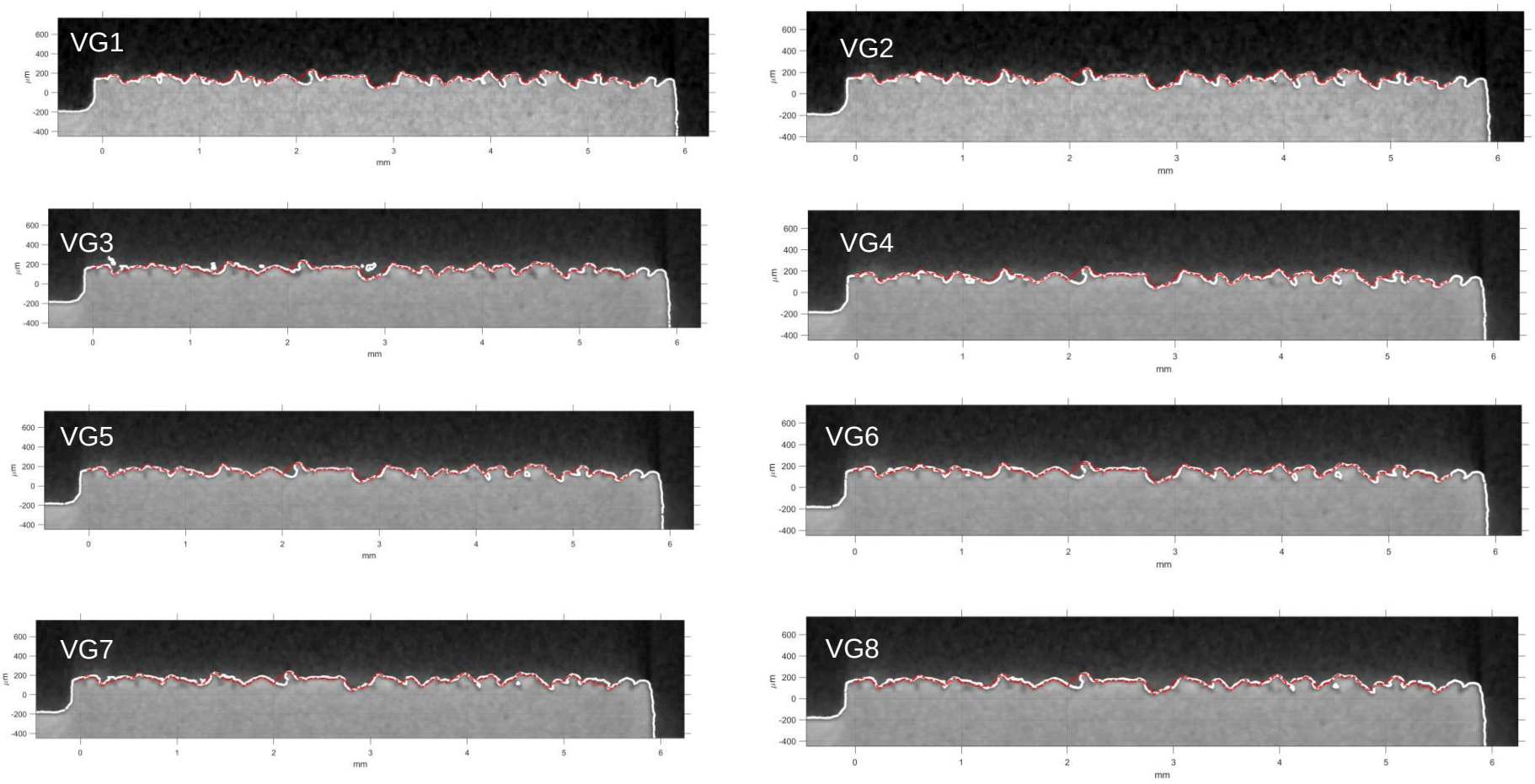

Figure 8-8: The optimisation result with BHC using VG SD algorithm. White dots- XCT surface; red line: CS data

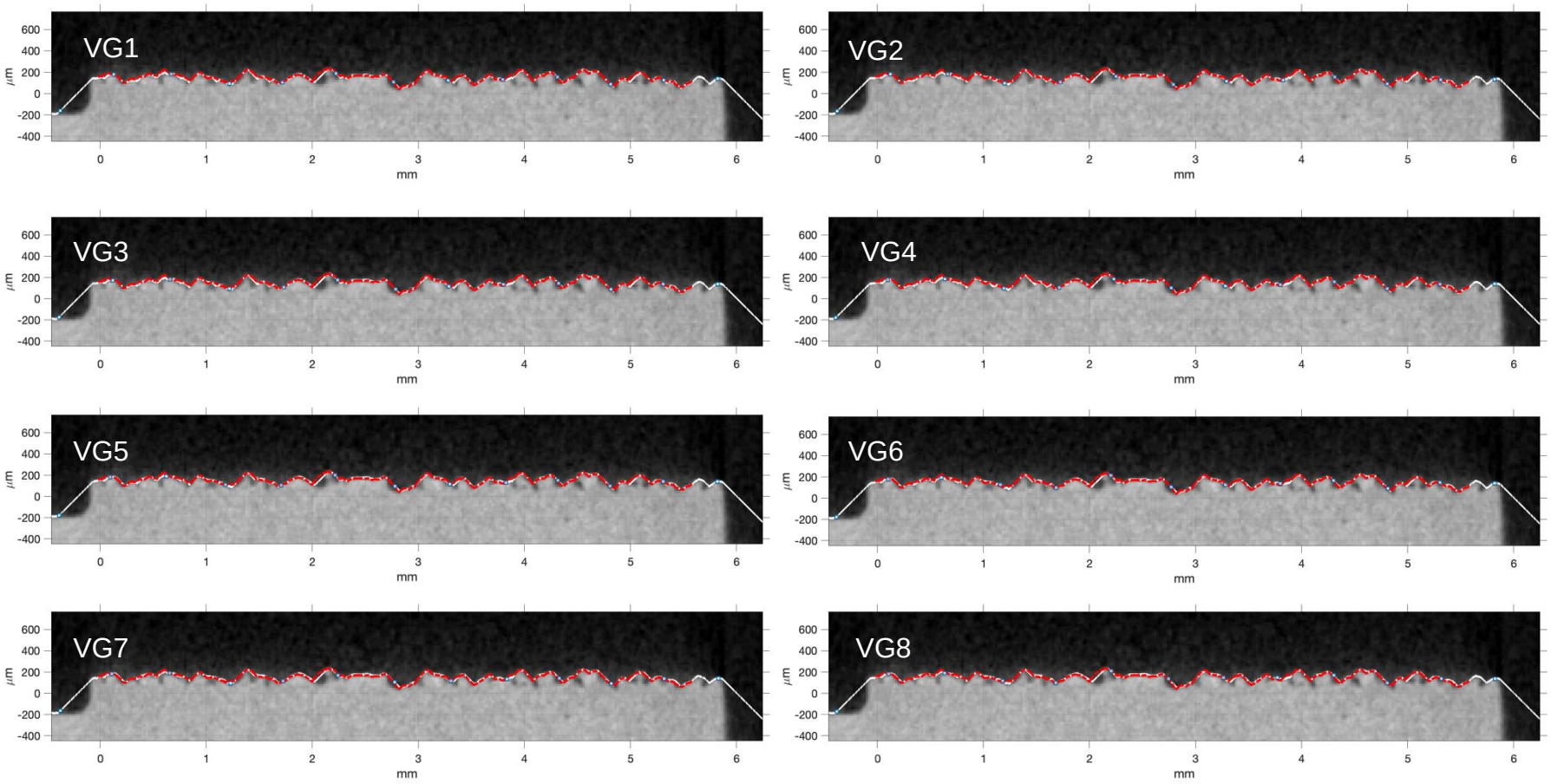

Figure 8-9: The optimisation result with BHC using VG SD algorithm after applying morphological filter. White dots- XCT surface after morphological filter; red line: CS data

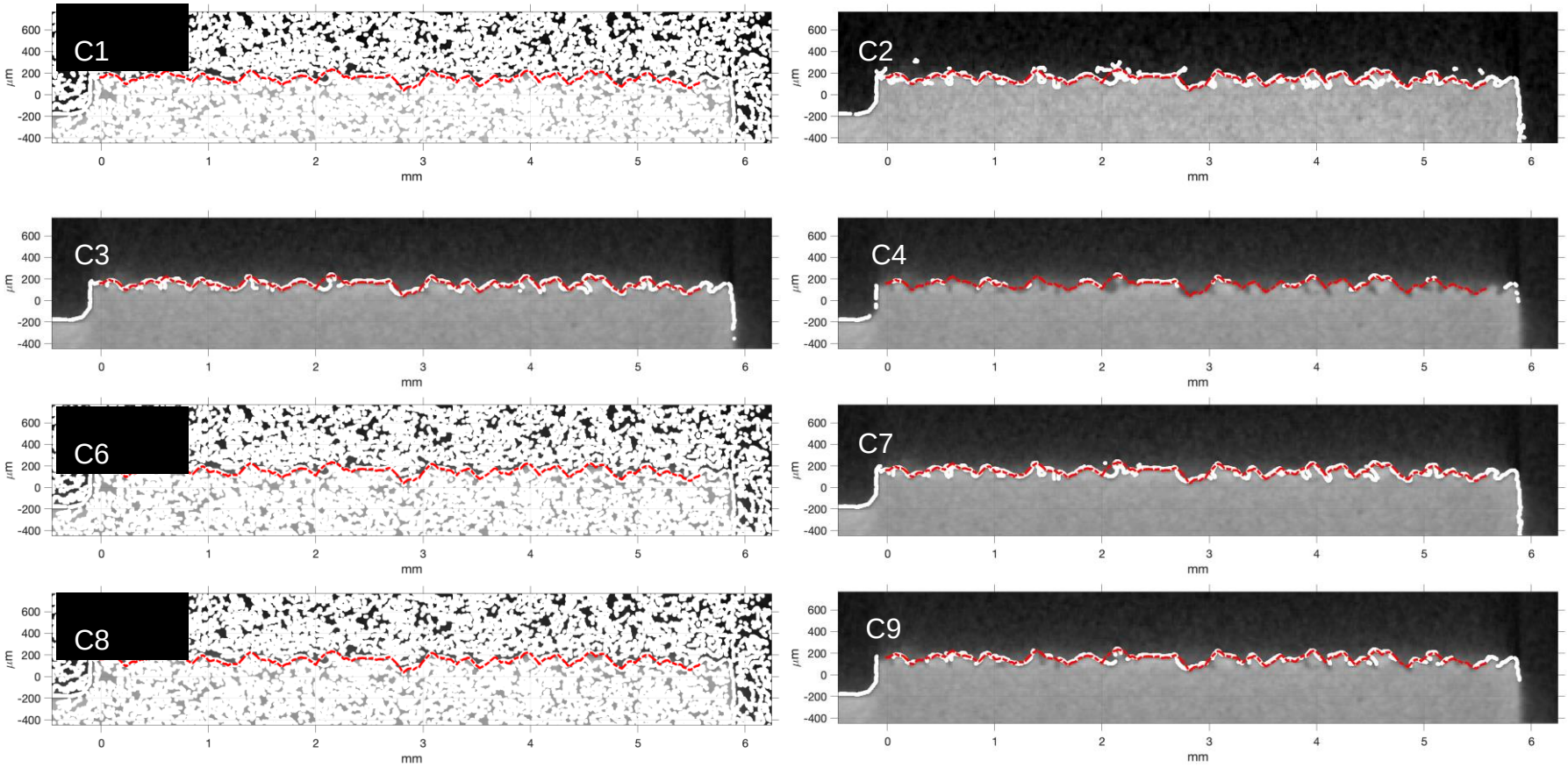

Figure 8-10: The optimisation result without BHC using Canny SD algorithm (C5 returns no surface data and not shown here). White dots: XCT surface; red line: CS data

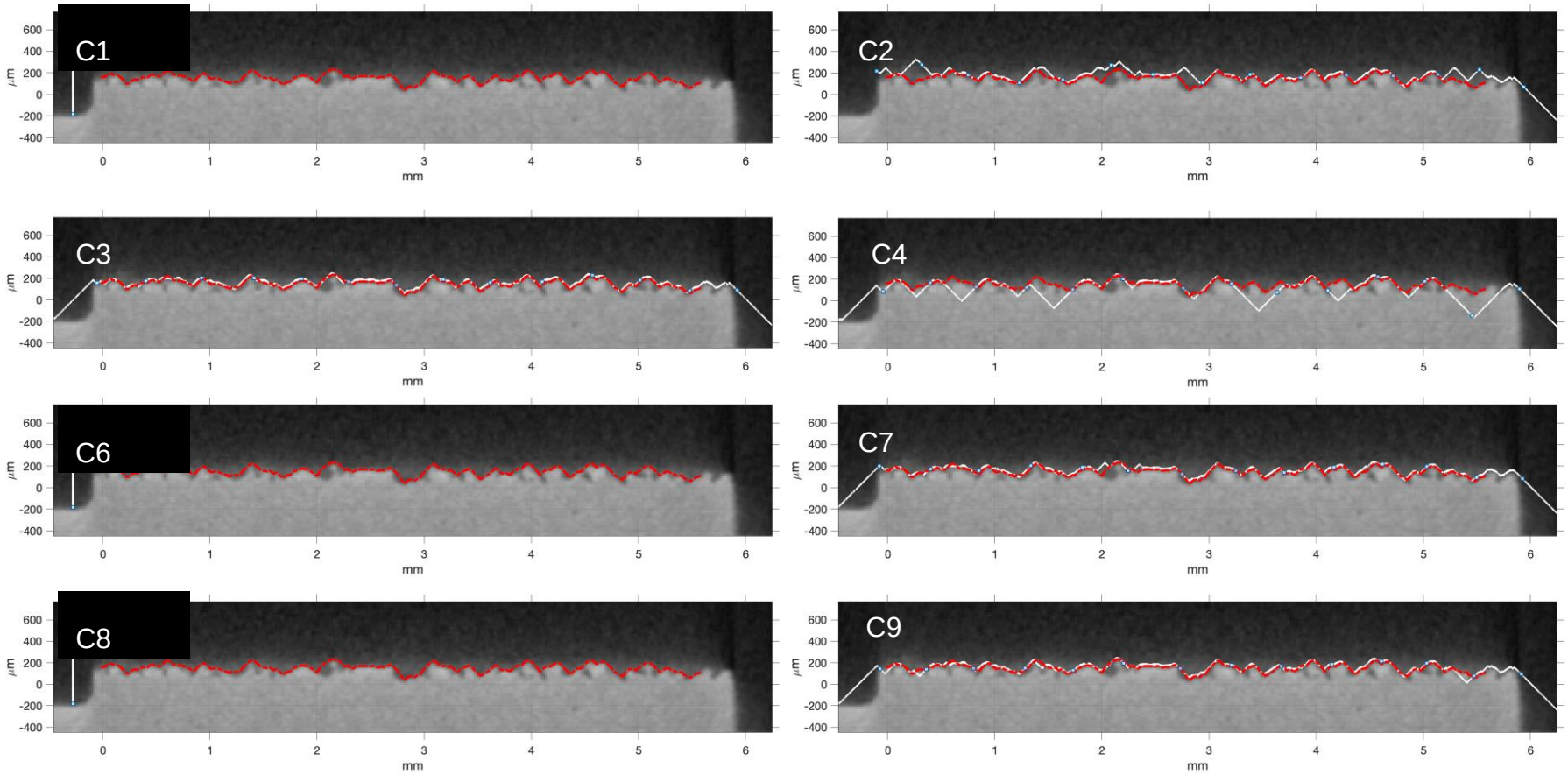

Figure 8-11: The optimisation result without BHC using Canny SD algorithm after applying morphological filter (C5 returns no surface data and not shown here). White dots- XCT surface after morphological filter; red line: CS data

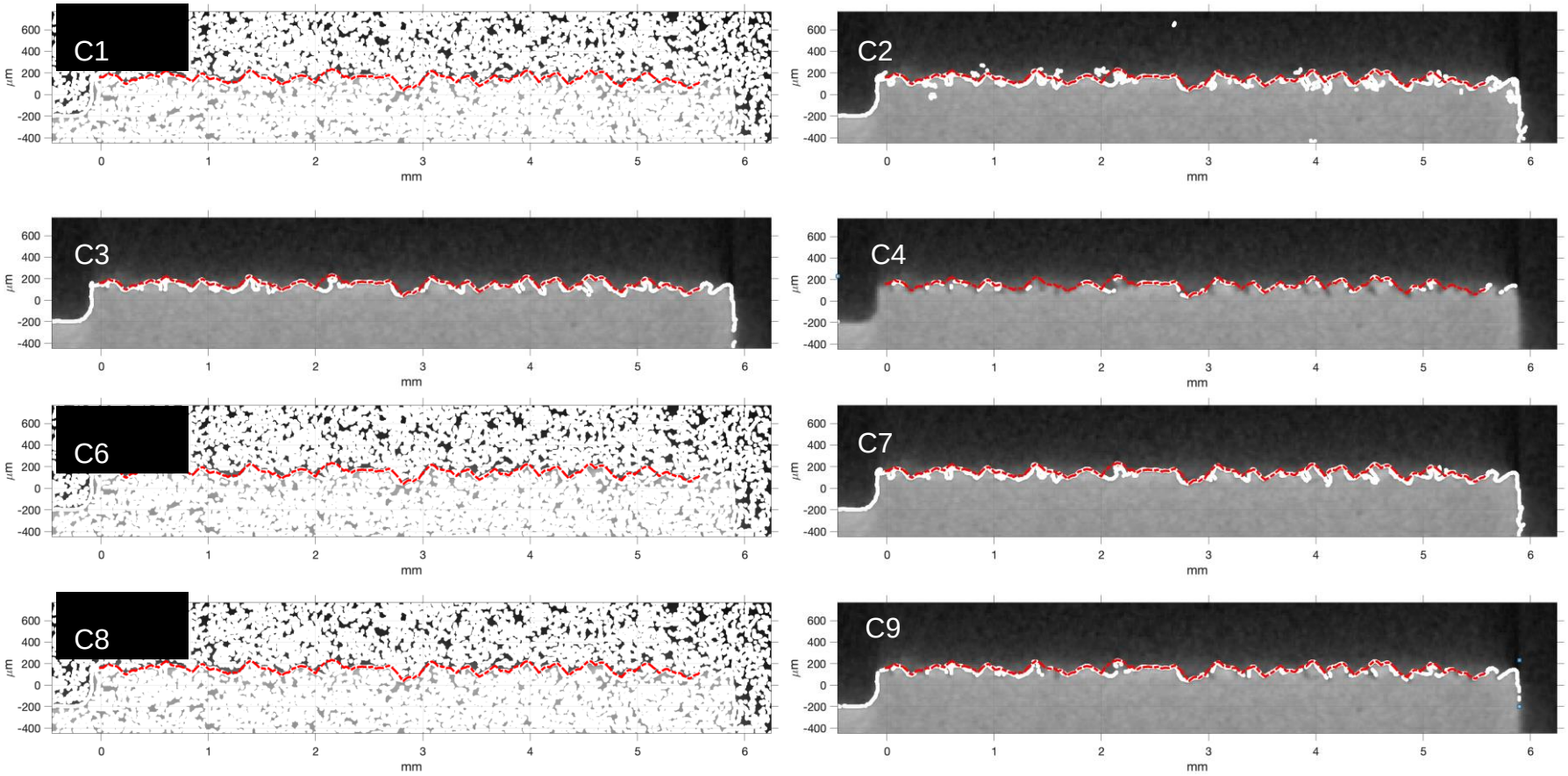

Figure 8-12: The optimisation result with BHC using Canny SD algorithm (C5 returns no surface data and not shown here). White dots: XCT surface; red line: CS data

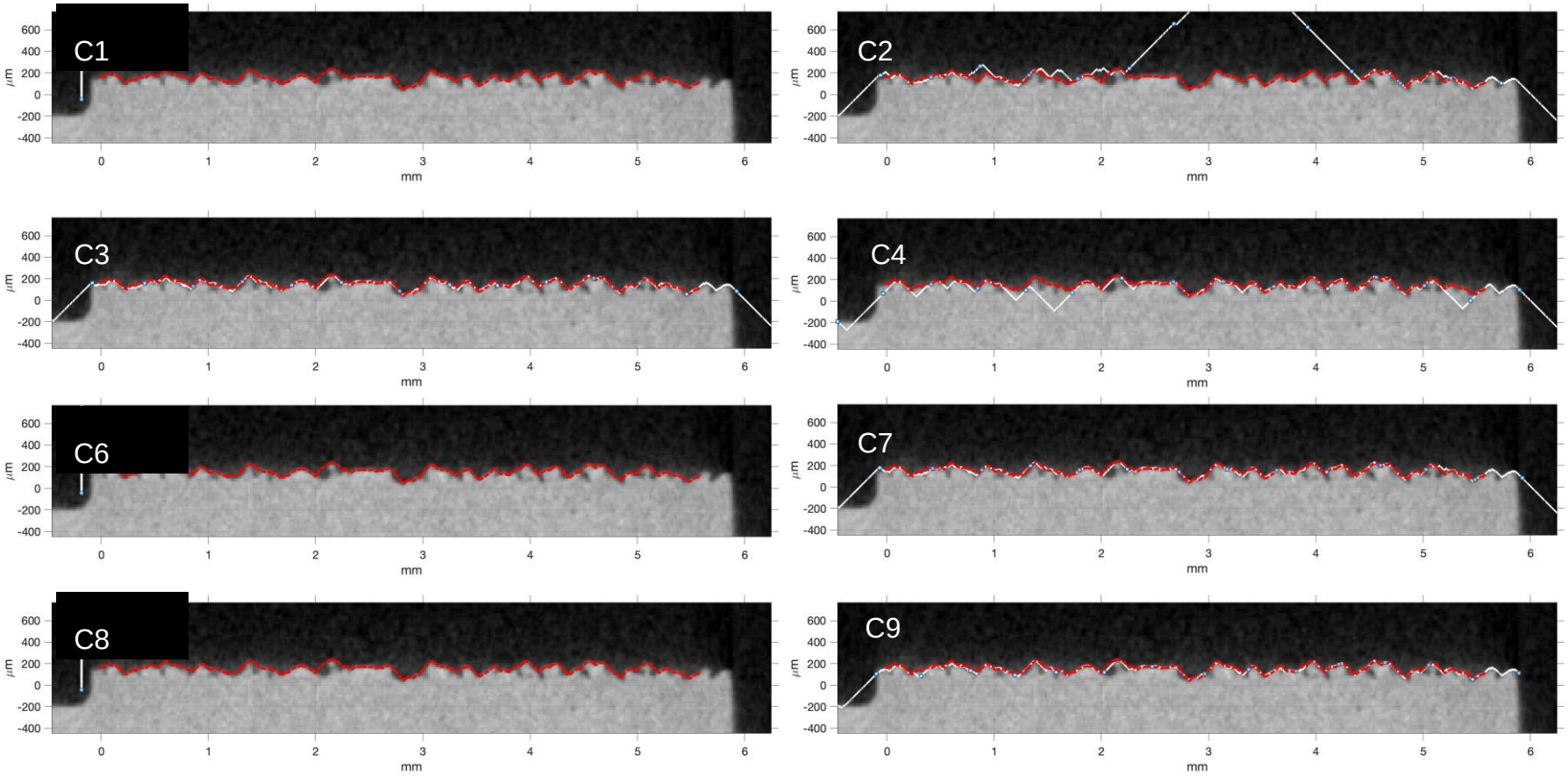

Figure 8-13: The optimisation result with BHC using Canny SD algorithm after applying morphological filter (C5 returns no surface data and not shown here). White dots- XCT surface after morphological filter; red line: CS data

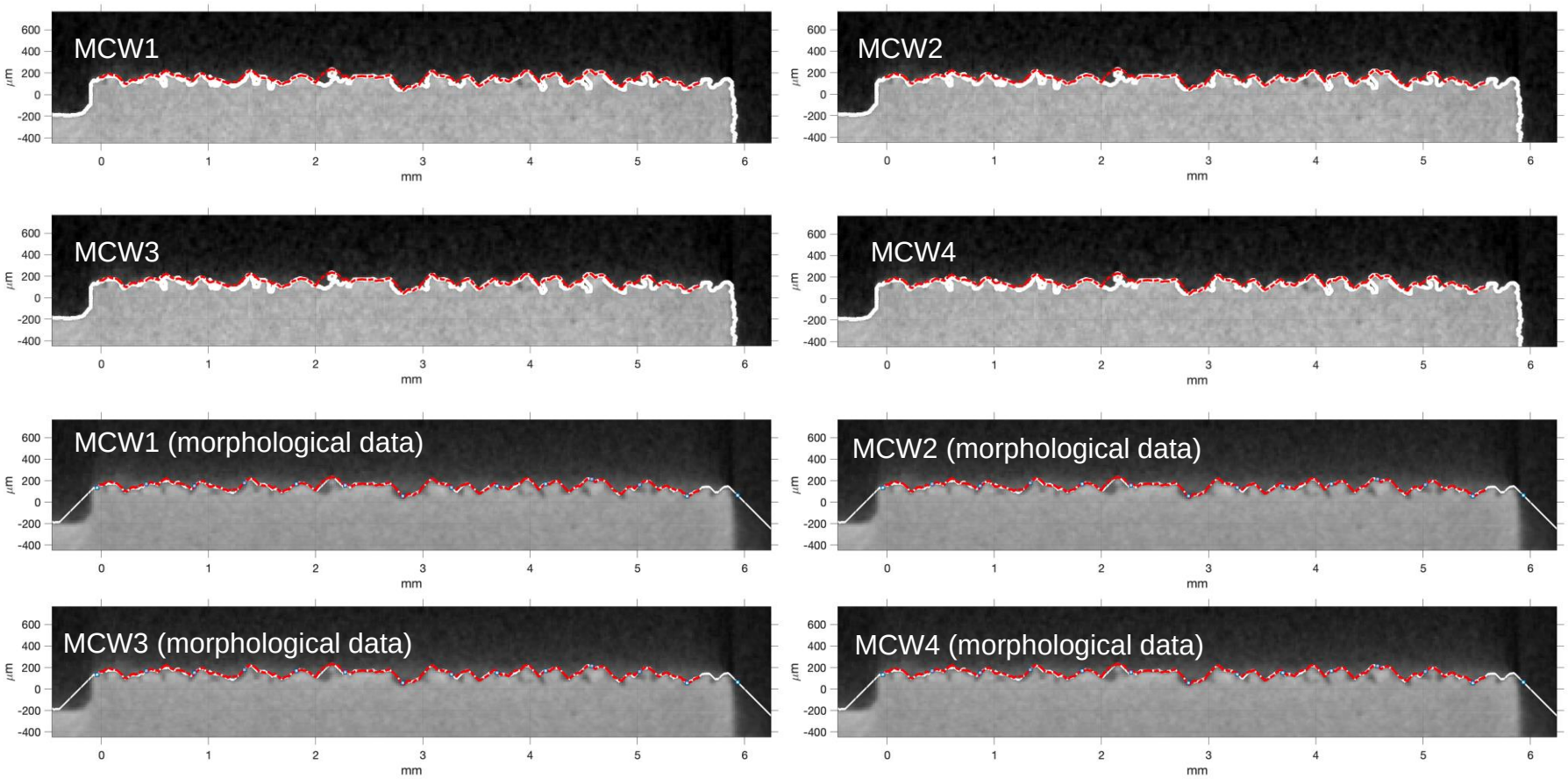

Figure 8-14: The optimisation result without BHC using MCW SD algorithm before and after applying morphological filter. White dots- XCT surface (after morphological filter); red line: CS data

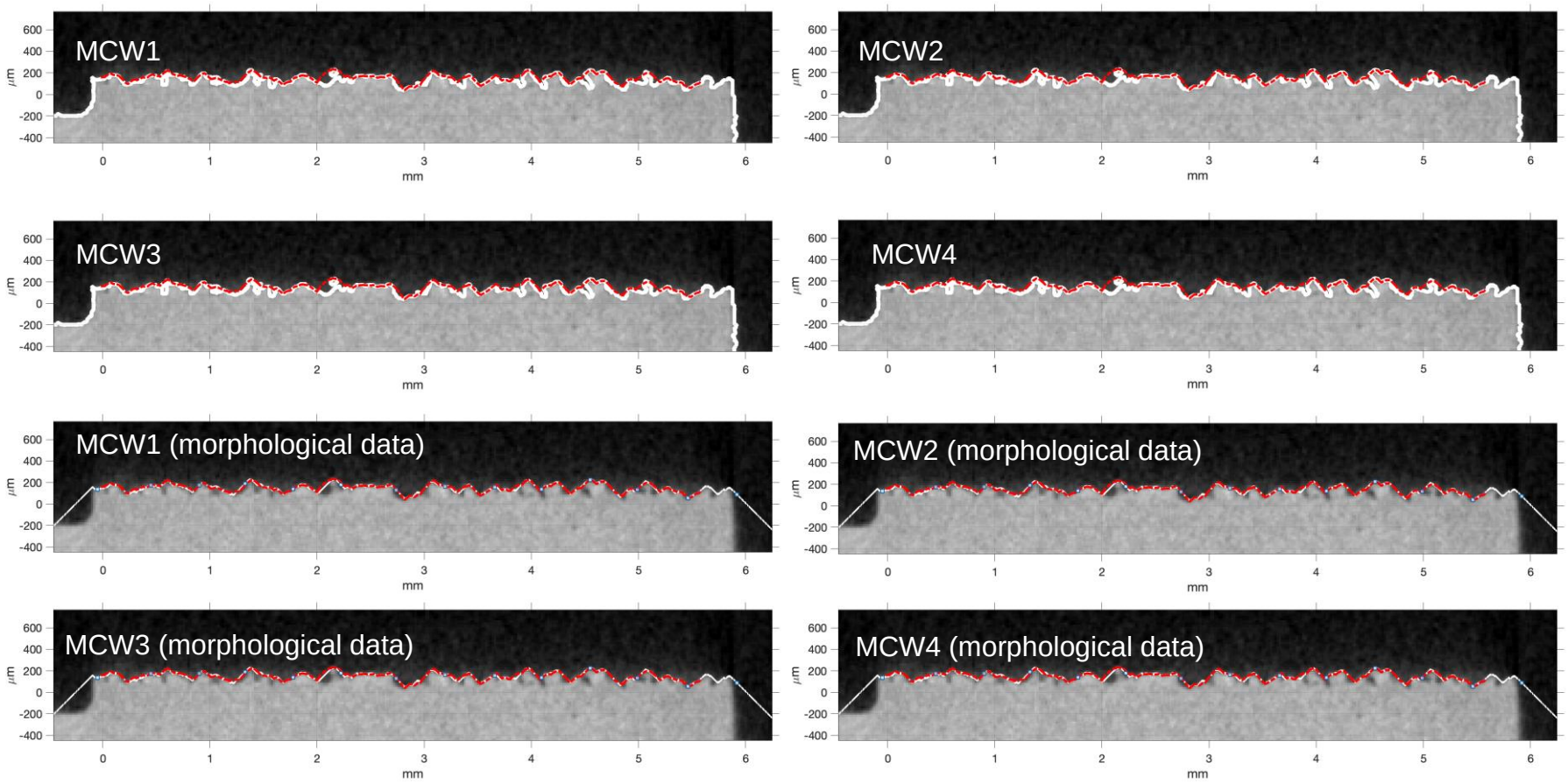

Figure 8-15: The optimisation result with BHC using MCW SD algorithm before and after applying morphological filter. White dots- XCT surface (after morphological filter); red line: CS data

Appendix C 3DRS sample rotation

```
%% 23/03/2022  National Physical Laboratory  Xiuyuan Yang
%  Purpose: rotation and alignment of watershed data based on S1, S2,
S4

% A=load_stack_tif_image_3D;
%
Face_A_watershed=importdata("O:\Xiuyuan\surface_plot_watershed_project
\faceA_Canny.txt");
Face_A_watershed=[surface2.x surface2.y surface2.z];

%% sphere S1
S1_cloud=pointCloud([S1.x,S1.y,S1.z]);
S1_model=pcfitsphereavg(S1_cloud);
% [XXX YYY]=pcfitsphereavg(S1_cloud);

%% sphere S2
S2_cloud=pointCloud([S2.x,S2.y,S2.z]);
S2_model=pcfitsphereavg(S2_cloud);

%% sphere S4
S4_cloud=pointCloud([S4.x,S4.y,S4.z]);
S4_model=pcfitsphereavg(S4_cloud);

%% scatter plot

XXXX=[Face_A_watershed(:,1);S1.x;S2.x;S4.x];
YYYY=[Face_A_watershed(:,2);S1.y;S2.y;S4.y];
ZZZZ=[Face_A_watershed(:,3);S1.z;S2.z;S4.z];
scatter3(XXXX,YYYY,ZZZZ);
axis equal

%% Generate watershed point cloud

%generate watershed point cloud
Face_A_watershed_cloud=pointCloud(Face_A_watershed);
pcshow(Face_A_watershed_cloud);
set(gca,'color','w');
hold on
xlabel('X');
ylabel('Y');
zlabel('Z');
pcshow(S1_cloud);
pcshow(S2_cloud);
pcshow(S4_cloud);

%% transverse S2-> 0 0 0
trans=-S2_model(1:3);
transvertic=[1 0 0 0;...
    0 1 0 0;...
    0 0 1 0;...
    trans 1];
tform=affine3d(transvertic);
Transform.Face_A_watershed_cloud=pctransform(Face_A_watershed_cloud,tf
orm);
```

```
Transform.S1_cloud=pctransform(S1_cloud,tform);
Transform.S2_cloud=pctransform(S2_cloud,tform);
Transform.S4_cloud=pctransform(S4_cloud,tform);
pcshow(Transform.Face_A_watershed_cloud);
hold on
xlabel('X');
ylabel('Y');
zlabel('Z');
pcshow(Transform.S1_cloud);
pcshow(Transform.S2_cloud);
pcshow(Transform.S4_cloud);
hold off

%% record S1 S4 center location
Transform.S1_model=pcfitsphereavg(Transform.S1_cloud);
Transform.S4_model=pcfitsphereavg(Transform.S4_cloud);
%% Put S4 on ZY plane

theta=-atan(Transform.S4_model(1)/Transform.S4_model(2));
transvertic=[cos(-theta) sin(-theta) 0 0;...
    -sin(-theta) cos(-theta) 0 0;...
    0 0 1 0;
    0 0 0 1;]; %rotate around Z axis
tform=affine3d(transvertic);
R1.Face_A_watershed_cloud=pctransform(Transform.Face_A_watershed_cloud
,tform);
R1.S1_cloud=pctransform(Transform.S1_cloud,tform);
R1.S2_cloud=pctransform(Transform.S2_cloud,tform);
R1.S4_cloud=pctransform(Transform.S4_cloud,tform);
pcshow(R1.Face_A_watershed_cloud);
hold on
xlabel('X');
ylabel('Y');
zlabel('Z');
pcshow(R1.S1_cloud);
pcshow(R1.S2_cloud);
pcshow(R1.S4_cloud);
hold off
%% record S1 S4 center location

R1.S1_model=pcfitsphereavg(R1.S1_cloud);
R1.S4_model=pcfitsphereavg(R1.S4_cloud);

%% S4 -> Y axis
theta=-atan(R1.S4_model(3)/R1.S4_model(2));
transvertic=[1 0 0 0;...
    0 cos(theta) sin(theta) 0;...
    0 -sin(theta) cos(theta) 0;...
    0 0 0 1];
tform=affine3d(transvertic);
R2.Face_A_watershed_cloud=pctransform(R1.Face_A_watershed_cloud,tform)
;
R2.S1_cloud=pctransform(R1.S1_cloud,tform);
R2.S2_cloud=pctransform(R1.S2_cloud,tform);
R2.S4_cloud=pctransform(R1.S4_cloud,tform);
pcshow(R2.Face_A_watershed_cloud);
hold on
xlabel('X');
```

```
ylabel('Y');
zlabel('Z');
pcshow(R2.S1_cloud);
pcshow(R2.S2_cloud);
pcshow(R2.S4_cloud);
hold off

%% record S1 S4 center location

R2.S1_model=pcfitsphereavg(R2.S1_cloud);
R2.S4_model=pcfitsphereavg(R2.S4_cloud);
R2.S2_model=pcfitsphereavg(R2.S2_cloud);
%% rotate S1 on YZ plane
theta=-atan(R2.S1_model(1)/R2.S1_model(3));
transvertic=[cos(theta) 0 -sin(theta) 0;...
    0 1 0 0;...
    sin(theta) 0 cos(theta) 0;...
    0 0 0 1];
tform=affine3d(transvertic);
R3.Face_A_watershed_cloud=pctransform(R2.Face_A_watershed_cloud,tform)
;
R3.S1_cloud=pctransform(R2.S1_cloud,tform);
R3.S2_cloud=pctransform(R2.S2_cloud,tform);
R3.S4_cloud=pctransform(R2.S4_cloud,tform);
pcshow(R3.Face_A_watershed_cloud);
hold on
xlabel('X');
ylabel('Y');
zlabel('Z');
pcshow(R3.S1_cloud);
pcshow(R3.S2_cloud);
pcshow(R3.S4_cloud);
hold off
%% record S1 S4 center location

R3.S1_model=pcfitsphereavg(R3.S1_cloud);
R3.S4_model=pcfitsphereavg(R3.S4_cloud);
R3.S2_model=pcfitsphereavg(R3.S2_cloud);

%% distance between S1 and S2 in voxel

dist_S1_S2_vox=sqrt((R3.S1_model(1)-R3.S2_model(1))^2+...
    (R3.S1_model(2)-R3.S2_model(2))^2+...
    (R3.S1_model(3)-R3.S2_model(3))^2);

%% S1_S2 calibrated distance 19896.87 um, with 2.7e-2 sigma

CMS_S1_S2=19896.87;

%% voxel size in um/voxel
Voxel_size=CMS_S1_S2/dist_S1_S2_vox;

%% scale data point cloud
transvertic=[Voxel_size 0 0 0;...
    0 Voxel_size 0 0;...
    0 0 Voxel_size 0;...
    0 0 0 1];
```

```
tform=affine3d(transvertic);
Final.Face_A_watershed_cloud=pctransform(R3.Face_A_watershed_cloud,tfo
rm);
Final.S1_cloud=pctransform(R3.S1_cloud,tform);
Final.S2_cloud=pctransform(R3.S2_cloud,tform);
Final.S4_cloud=pctransform(R3.S4_cloud,tform);
pcshow(Final.Face_A_watershed_cloud);
hold on
xlabel('X in um');
ylabel('Y in um');
zlabel('Z in um');
pcshow(Final.S1_cloud);
pcshow(Final.S2_cloud);
pcshow(Final.S4_cloud);
hold off

function A=pcfitsphereavg(B)
for i=1:20
    C=pcfitsphere(B,0.2);
    D(i,:)=C.Parameters;
end
A=mean(D);
end
```

Appendix D Residual results for synthetic data

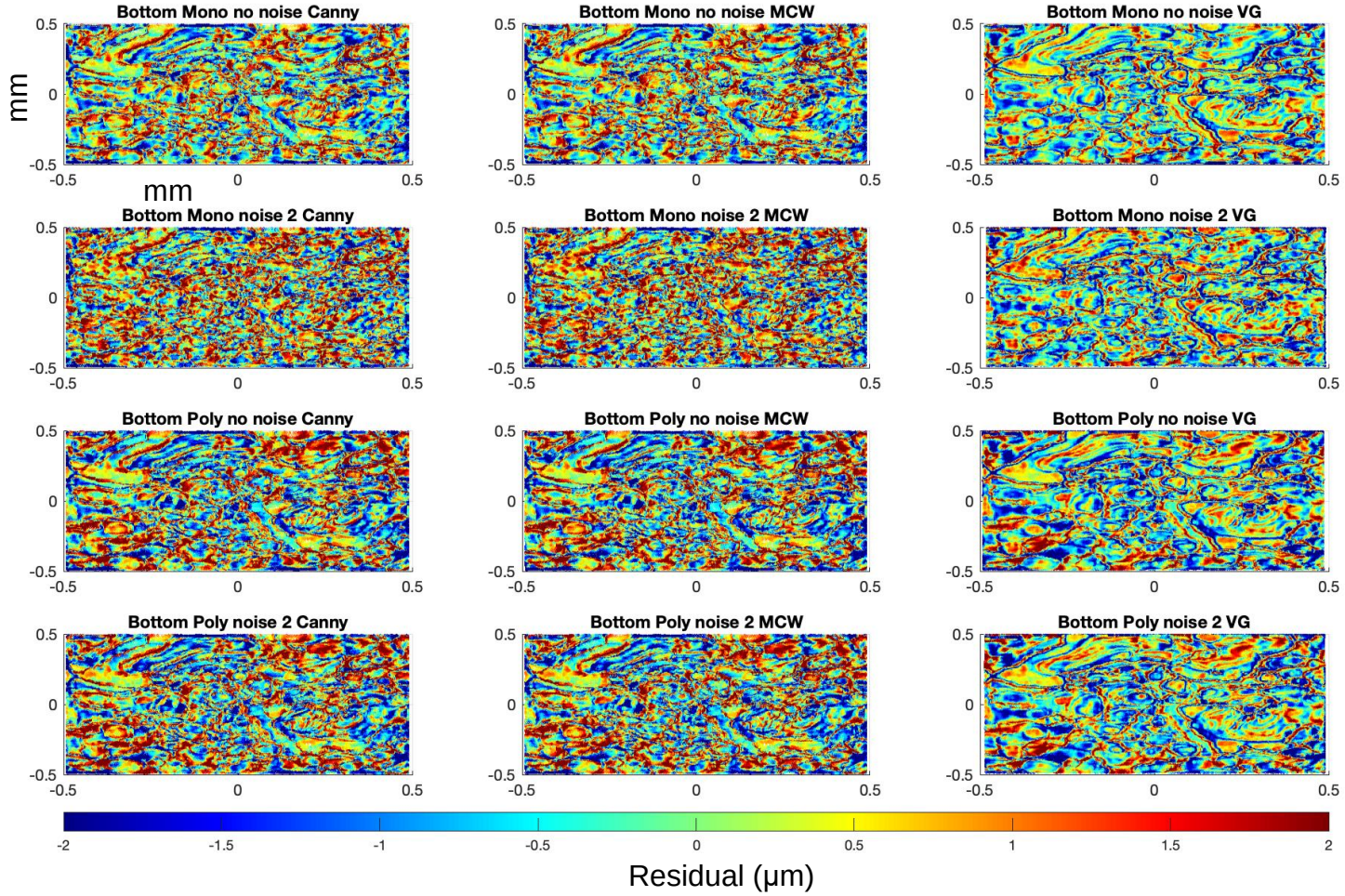

Figure 8-16: The residual of the surface point cloud against the mesh surface of downskin sample

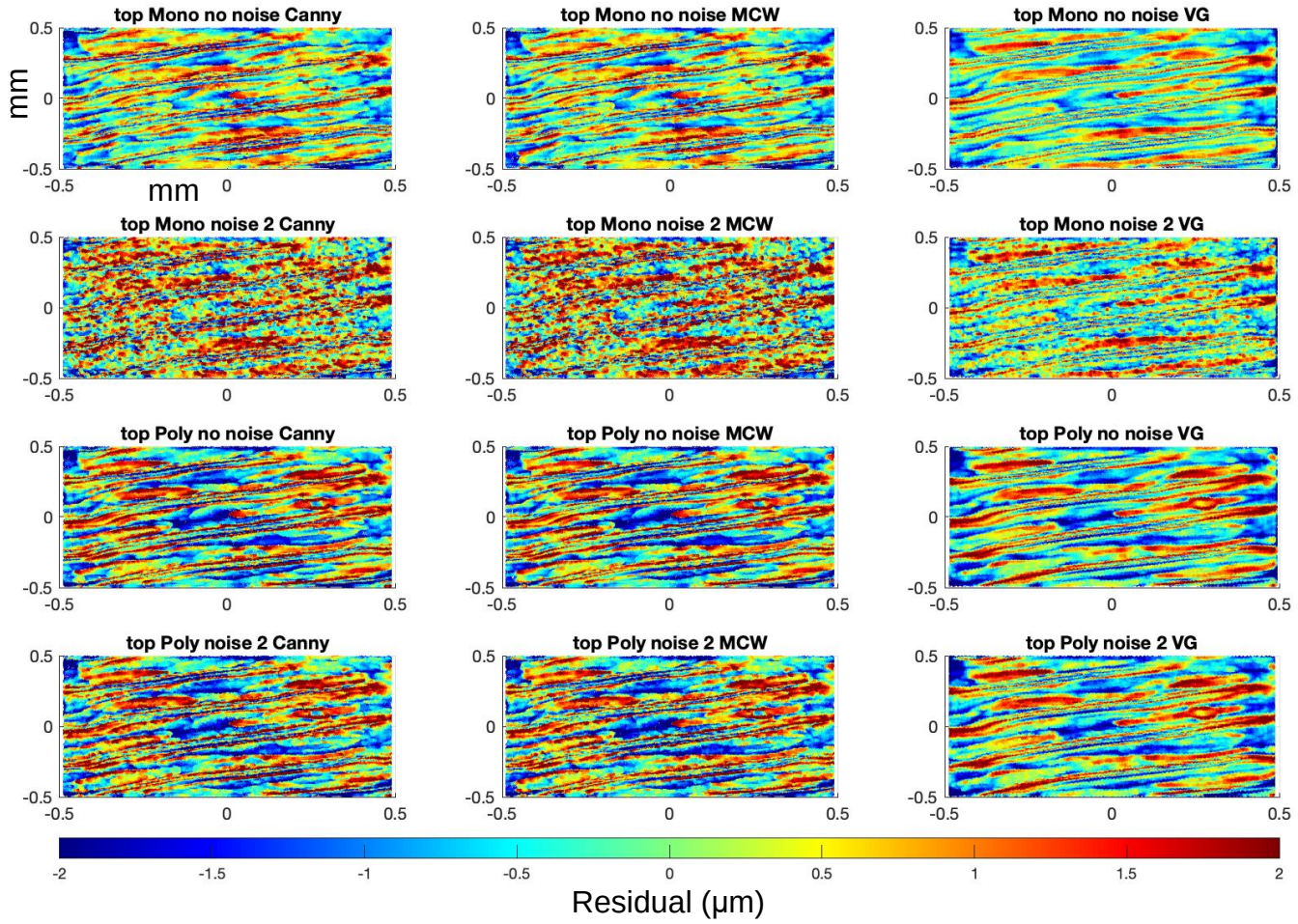

Figure 8-17: The residual of the surface point cloud against the mesh surface of upskin sample

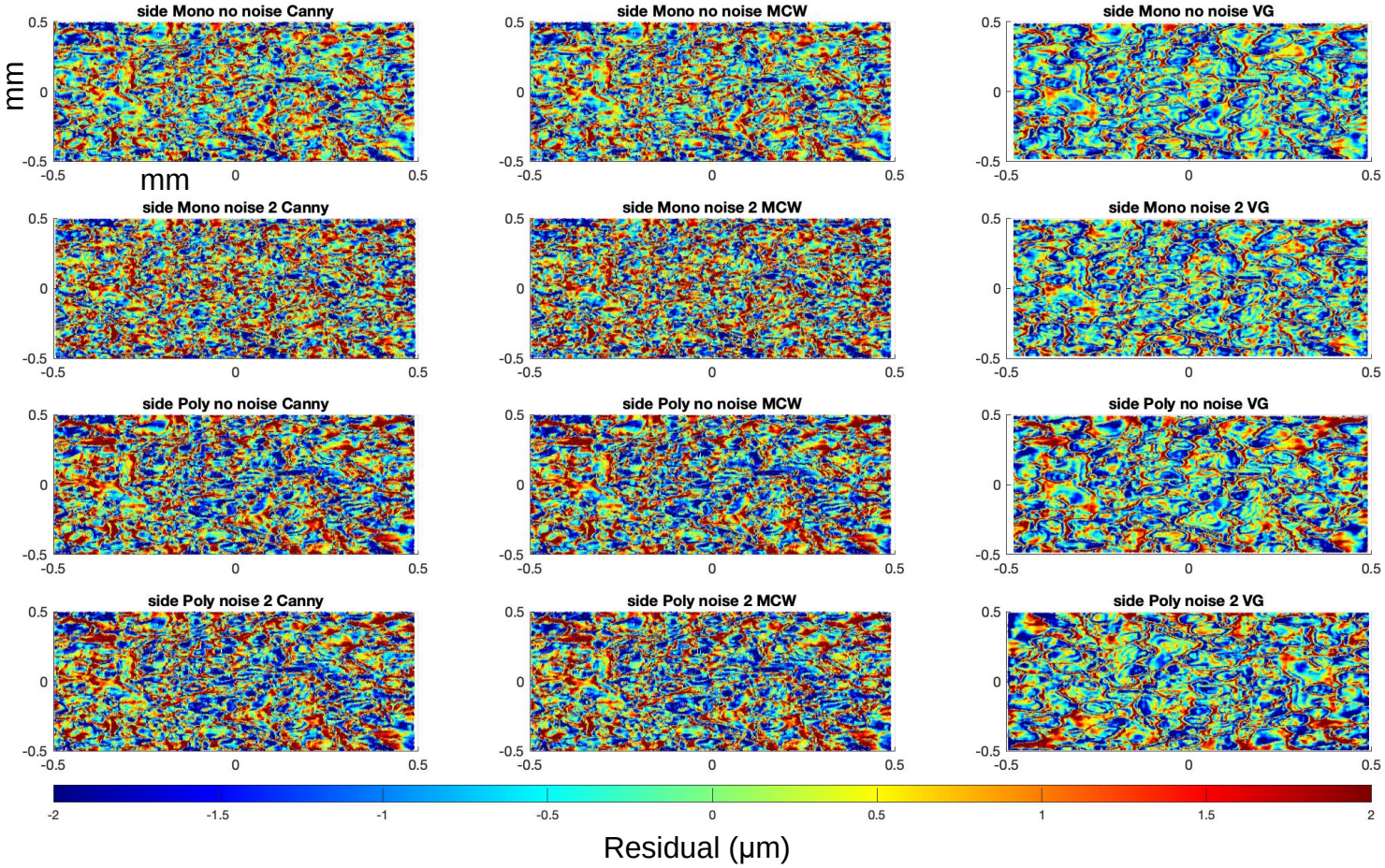

Figure 8-18: The residual of the surface point cloud against the mesh surface of side sample

j

Appendix E Stylus morphological transformation algorithm (written in Matlab)

```
%Version: 19/06/2022, written by Xiuyuan Yang in National Physical

%Laboratory and Cranfield University

%This function is used to simulate the movement of 2um tactile (90 degrees opening) on surface

%point cloud (1D) and register the location of centre of tactile profile.



function Mor_filt=TactileFilter(Profile,bin)

i=1;

%%find the starting point with S=2 (ascending along the contacting point


[~,Start_index]=min(Profile(:,1));


M0=Profile(Start_index,1);

N0=Profile(Start_index,2);

M0=M0-1000;
```

```
Dist=abs(Profile(:,1)-Profile(:,2)+N0-M0)/sqrt(2);
[~,Min_dist_index]=min(Dist);
Cm=Profile(Min_dist_index,1);
Cn=Profile(Min_dist_index,2);
Mor_filt(i,1)=Cm-2;
Mor_filt(i,2)=Mor_filt(i,1)+sqrt(8)+Cn-Cm;

S=2; %This is the status indexing



while Mor_filt(i,1)<max(Profile(:,1))
  i=i+1;

  if S==2
      Mk=Mor_filt(i-1,1)+bin;
      Nk=Mor_filt(i-1,2)+bin;

      if Cm>=Mk+sqrt(2)

   Mor_filt(i,1)=Mk;
    Mor_filt(i,2)=Nk;
    S=2;
```

```
 else
      [P,S]= if_1(Cm,Cn,Mk);
     Mor_filt(i,1)=Mk;
Mor_filt(i,2)=P;
Nk=P;
     [judge_ind,Point_above]=info_stylus(Mk,Nk,Cm,Cn,Profile);
     if judge_ind~=0

 [P,S,Cm,Cn]=if_2(Mk,Nk,Point_above);
 Mor_filt(i,2)=P;
     end
 end

     else if S==1
        Mk=Mor_filt(i-1,1)+bin;
  Nk=Mor_filt(i-1,2)-bin;
   Mor_filt(i,1)=Mk;
   Mor_filt(i,2)=Nk;



 [judge_ind,Point_above]=info_stylus(Mk,Nk,Cm,Cn,Profile);
 if judge_ind~=0
```

```
        [P,S,Cm,Cn]=if_2(Mk,Nk,Point_above) ;
    Mor_filt(i,2)=P;


     end
           else
             Mk=Mor_filt(i-1,1)+bin;
             [P,S]=if_1(Cm,Cn,Mk);
              Mor_filt(i,1)=Mk;
              Mor_filt(i,2)=P;
              [judge_ind,Point_above]=info_stylus(Mk,Nk,Cm,Cn,Profile);
     if judge_ind~=0
        [P,S,Cm,Cn]=if_2(Mk,Nk,Point_above) ;
    Mor_filt(i,2)=P;


     end
end
     end


  end
end
```

```
function [A,B]=info_stylus(Mk,Nk,Cm,Cn,C)
    %A=0 or 1, for logic purpose, B shows the points above the stylus,C:
    %all points after [Cm,Cn]

    index=find(C(:,1)>=Mk-sqrt(2));

    C=C(index,:);
    index1=find(C(:,1)<=Mk-sqrt(2));
    index2=find(C(:,1)>Mk-sqrt(2)  & C(:,1)<Mk+sqrt(2) );
    index3=find(C(:,1)>=Mk+sqrt(2));
    C(index1,3)=-C(index1,1)+Mk+Nk-2*sqrt(2);
    C(index3,3)=C(index3,1)-Mk+Nk-2*sqrt(2);
    C(index2,3)=sqrt(4-(C(index2,1)-Mk).^2)+Nk;
    index=find((C(:,3)-C(:,2))<0);
    if isempty(index)
        A=0;
        B=0;
    else
        A=1;
        B=C(index,1:2);
    end
end
```

```
function [P,S]=if_1(Cm,Cn,Mk)
if Cm>Mk-sqrt(2)  && Cm<Mk+sqrt(2)
    P=Cn+sqrt(4-(Cm-Mk)^2);
    S=3;
else
    P=-(Mk-2*sqrt(2))+Cm+Cn;
    S=1;
end
end

function [P,S,Cm_New,Cn_New]=if_2(Mk,Nk,B)
[Cm_New,Cn_New]=newCmCn(Mk,Nk,B);
if Cm_New<Mk-sqrt(2)
    P=-(Mk-2*sqrt(2))+Cm_New+Cn_New;
    S=1;
else if Cm_New>=Mk-sqrt(2) && Cm_New<Mk+sqrt(2)
       P=Cn_New+sqrt(4-(Cm_New-Mk)^2);
       S=3;
    else
        P=Mk+2*sqrt(2)+Cn_New-Cm_New;
        S=2;
    end
end
```

```
end

function    [Cm_New,Cn_New]=newCmCn(Mk,Nk,B)

    dist=abs(B(:,1)-B(:,2)+Nk-Mk-2*sqrt(2))/sqrt(2);
    [~,index]=max(dist);
    Cm_New=B(index,1);
    Cn_New=B(index,2);
end
```